Security enhancement in islanded dc microgrids via flexibility resources

Published version
DOI:

Publisher: Politecnico di Bari

Department of Electrical and Information Engineering

Electrical and Information Engineering

Ph.D. Program

SSD: IIND-08/B - Electrical Energy Systems

Final Dissertation

Security Enhancement in Islanded DC Microgrids Via Flexibility Resources

by

Mohammad Rajabinasab

Supervisor:

Prof. Massimo LA SCALA

Coordinator of Ph.D. Program:

Prof. Mario Carpentieri

XXXVIII Cycle - November 1st, 2022 - November 1st, 2025

Contents

List of Figures

List of Tables

Abstract

This doctoral dissertation presents the research conducted by the author during the three-year Ph.D. program (XXXVIII cycle) in Electrical and Information Engineering at Politecnico di Bari. The primary objective was to design methodologies and control strategies for energy management in DC microgrids, with a particular focus on fostering the development of stand-alone modern microgrids that integrate significant shares of intermittent renewable resources. Another key aim was to enhance the flexibility of isolated DC systems while ensuring secure and stable operation.

The thesis provides a comprehensive analysis of islanded microgrid control and operation, addressing the behavior of grid components. Special attention was devoted to real-time power balancing through advanced actuators for grid management, flexible resources, and energy devices that operated via power converters, sensors, and other enabling smart grid technologies.

Given the inherently low inertia of converter-based microgrids and isolated networks, the research also developed innovative solutions for providing fast voltage transient support services at the lowest hierarchical control level, operating on time scales of milliseconds to just a few seconds. The proposed methodologies demonstrably improve the reliability and stability of isolated DC systems, while also reducing operating costs and greenhouse gas emissions.

Acknowledgments

The research activities presented in this thesis were made possible thanks to the support and funding of the Next Intelligence Research (NIR srl) company.

I would like to express my deepest gratitude to my supervisor, Prof. Massimo La Scala, and my co-supervisor, Prof. Sergio Bruno, for their invaluable guidance and encouragement throughout my Ph.D. journey. I am also sincerely thankful to all past and present members of the LabZERO Laboratory research group, whose support and collaboration have greatly enriched both my research and personal experience.

A special acknowledgement goes to Prof. Marco Liserre for offering me the opportunity to further explore my research topics at Christian-Albrechts University (CAU). I am equally grateful to the members of his research group for their warm welcome and for contributing to an inspiring and rewarding experience abroad.

My deepest appreciation goes to my family, whose unwavering support and faith in me have been a constant source of strength, regardless of circumstances or decisions made along the way. Finally, I am profoundly thankful to my friends, who stood by me during these three demanding years and helped me face even the most stressful moments with serenity.

Author's Publications

Publications resulting from this research work are listed below in chronological order.

Conferences

1. M. R. Nasab, S. Bruno, M. Liserre, and M. L. Scala, "Adaptive Droop Control for Stability Enhancement in Islanded DC Microgrids with CPLs," in *2025 Power Tech Conference*. IEEE, 2025, pp. 1–6
2. M. R. Nasab *et al.*, "Cost-Based Adaptive Coordination of Battery Energy Storage Systems in DC Microgrid," in *2025 AEIT International Annual Conference (AEIT)*. IEEE, 2025, pp. 1–6
3. C. Iurlaro, M. R. Nasab *et al.*, "Fast frequency support in isolated distribution networks by means of distributed control of V2G electric vehicles," in *2025 IEEE International Conference on Environment and Electrical Engineering and 2025 IEEE Industrial and Commercial Power Systems Europe (EEEIC/I&CPS Europe)*. IEEE, 2025, pp. 1–6
4. M. R. Nasab, R. Cometa, C. Iurlaro, M. M. Islam, S. Bruno, and M. La Scala, "Stand-alone DC Microgrids for Rural Areas: A Decentralized Energy Management and Voltage Regulation Approach," in *2024 IEEE International Humanitarian Technologies Conference (IHTC)*. IEEE, 2024, pp. 1–7
5. M. Menga, C. Iurlaro, M. R. Nasab, S. Bruno, and M. La Scala, "Recursive predictive optimal dispatch for the reduction of fuel dependence in a multi-village power system," in *2024 IEEE International Humanitarian Technologies Conference (IHTC)*. IEEE, 2024, pp. 1–7

6. R. Cometa, A. Velini, M. R. Nasab, S. Bruno, and M. La Scala, “Optimal Transmission Grid Assets Maneuvering for Improving Voltage Profile in RES Scenarios,” in *2024 IEEE International Humanitarian Technologies Conference (IHTC)*. IEEE, 2024, pp. 1–7

7. M. R. Nasab, R. Cometa, P. Ghalebani, S. Bruno, and M. La Scala, “Distributed adaptive droop control method for flexibility enhancement of islanded DC microgrids including electric springs,” in *2024 Energy Conversion Congress & Expo Europe (ECCE Europe)*. IEEE, 2024, pp. 1–6

8. M. R. Nasab, R. Cometa, S. Bruno, and M. La Scala, “Adaptive Scheme for Stability Margin Estimation of Grid-Connected DFIG Based Wind Turbines,” in *2024 IEEE International Conference on Environment and Electrical Engineering and 2024 IEEE Industrial and Commercial Power Systems Europe (EEEIC/I&CPS Europe)*. IEEE, 2024, pp. 1–6

9. R. Cometa, M. R. Nasab, F. Lorusso, A. Velini, M. La Scala, and S. Bruno, “Integration of FDIR Practices in Distribution Optimal Network Reconfiguration Routines,” in *2024 IEEE International Conference on Environment and Electrical Engineering and 2024 IEEE Industrial and Commercial Power Systems Europe (EEEIC/I&CPS Europe)*. IEEE, 2024, pp. 1–6

10. M. R. Nasab, P. Ghalebani, S. Bruno, R. Cometa, and M. La Scala, “Adaptive PI control of PMSM for electric vehicle application based on sliding-mode extremum seeking algorithm,” in *2023 Asia Meeting on Environment and Electrical Engineering (EEE-AM)*. IEEE, 2023, pp. 1–6

11. A. Perrone, M. R. Nasab, and M. La Scala, “Draft animal power versus photovoltaic: A benchmark,” in *2023 AEIT International Annual Conference (AEIT)*. IEEE, 2023, pp. 1–6

Journal

1. A. A. Darban, M. Rajabi Nasab *et al.*, “Anomaly detection in solar farms with a hybrid CNN-ViT model to enhance accuracy and efficiency,” *International Journal of Ambient Energy*, vol. 46, no. 1, p. 2541270, 2025

2. M. R. Nasab, R. Cometa, S. Bruno, G. Giannoccaro, and M. La Scala, "Power systems simulation and analysis: A review on current applications and future trends in DRTS of grid-connected technologies," *IEEE Access*, 2024

3. M. M. Islam, T. Yu, G. Giannoccaro, Y. Mi, M. La Scala, M. N. Rajabi, and J. Wang, "Improving reliability and stability of the power systems: A comprehensive review on the role of energy storage systems to enhance flexibility," *IEEE Access*, 2024

Introduction

Background and Motivation

According to the definition provided by the *Conseil International des Grandes Réseaux Électriques* (CIGRÉ) Working Group C6.22, a Microgrid (MG) is an electricity distribution system that integrates loads and distributed energy resources—such as generators, storage units, and controllable loads—which can be operated in a coordinated and controlled manner, either while connected to the main grid or in islanded mode [24]. MGs may function as grid-connected systems under normal conditions or as permanently isolated systems, as is often the case in remote areas. This thesis specifically addresses isolated entities operated in the form of MGs.

In this specific paradigm, the entire system must be continuously monitored and controlled to guarantee security and operational continuity. In an isolated distribution network, such as an islanded MG, the balance between energy generation and demand must be maintained at all times. Any imbalance could inevitably result in the collapse of the MG. For this reason, the availability and proper dispatch of operational reserves are essential to ensure that the network can continue functioning even in the event of sudden generation shortfalls.

In modern MGs, Renewable Energy Sources (RESs) are increasingly regarded as the cornerstone of system design and operation. This prioritization arises not only from global sustainability and decarbonization goals but also from the practical advantages of exploiting locally available and cost-effective resources such as solar and wind. Unlike fossil fuel-based units, which require continuous fuel supply and maintenance, renewables can be harnessed almost freely, making them particularly suitable for remote or isolated contexts. Furthermore, their natural compatibility with storage systems and power electronic converters facilitates modular, flexible, and scalable architectures, enabling reliable operation even under varying load and generation conditions. Consequently, renewable-based units are positioned as the primary generation assets in modern MGs, while conventional sources and reserves serve mainly as complementary resources to secure stability and continuity of supply.

In this regard, it should be stated that although modern MG can be implemented as either AC- or DC-based, the increasing prevalence of converter-interfaced RESs and storage technologies makes DC architectures attractive approaches. Most RESs, such as photovoltaic panels, as well as battery systems and many modern residential/industrial loads, such as remote telecom sites, data centers and so on, are inherently DC. Consequently, adopting a DC distribution framework reduces the number of conversion stages, thereby improving overall efficiency and lowering system complexity. These features make islanded DC Microgrids (DC-MGs) an effective paradigm for integrating high shares of RESs while ensuring secure and resilient operation.

However, a critical challenge in modern islanded MGs arises from the intermittent nature of RESs and the stochastic profile of local demand. Unlike conventional systems, where dispatchable generators can buffer fluctuations, the variability of solar and wind generation combined with uncertain load profiles can cause frequent and unpredictable power mismatches. To withstand these dynamics and preserve grid's voltage stability, the system must rely on flexibility resources capable of rapidly and adaptively coordinating supply, storage, and demand. In this context, flexibility denotes the ability of the microgrid to accommodate sudden variations in generation and consumption through mechanisms such as distributed storage management, demand-side participation, and adaptive control strategies. Ensuring adequate flexibility is therefore essential to minimize voltage deviations, prevent overuse of storage units, and guarantee reliable operation of islanded MGs under uncertain operating conditions.

Given their critical characteristics, isolated MGs represent a proper framework for testing innovative control strategies and integrating new energy resources. Nevertheless, due to the aforementioned challenges, MGs are generally not intended to operate in islanded mode for extended periods. Disconnection from the main grid is typically limited to short durations, either for testing purposes, research studies, or as a temporary condition following an unintended protection trip caused by disturbances on the utility grid.

There are, however, situations in which the operation of an isolated MG is unavoidable. This is particularly true for islanded systems located on small or geographically remote islands, where establishing a connection to the mainland grid is neither technically nor economically feasible. In such cases, local power supply is often ensured through diesel generator sets, while the integration of RESs remains limited due to hosting capacity and stability constraints.

In this context, the development of methodologies, algorithms, and solutions for isolated MGs that are immediately applicable, simple to implement, and cost-effective is crucial for increasing the hosting capacity of island networks, enhancing the penetration of RESs, and reducing reliance on conventional fuels. On islands, fuel costs have a compounded effect compared to mainland systems: beyond the price of the fuel itself, maritime transport expenses significantly contribute to the overall supply cost. Consequently, the high cost of energy production on islands influences the national energy balance, hindering progress toward decarbonization targets and the reduction of greenhouse gas emissions established by governments and international organizations.

Contributions

This thesis introduces a set of methods and applications designed for enhancing the flexibility and secure operation of isolated DC-MGs. The proposed methodologies aim to enhance the reliability of isolated DC-MGs and to foster their broader deployment within distribution and transmission networks. The main contributions of this work are summarized below.

1. Development of an operational algorithm for the energy management and improvement of voltage transients in small isolated networks;

2. Development of a coordinated framework that employs RESs and flexibility resources to enhance the grid's flexibility, and achieve a uniform and comprehensive control mechanism;

3. Development of a uniform and comprehensive control mechanism across all operating modes, defined with respect to the supply-demand situation;

4. Development of real-time control structures that provide fully controllable responses to uncertainties and cover multiple timescales of power imbalances within the MGs;

5. Implementation of a real-time algorithm that explicitly incorporates balanced operation of distributed storage units, to improve their long-term reliability;

6. Evaluation of the importance of considering generation units' energy-provision capability, to introduce a proper dispatch algorithm for reducing operational costs, load shedding, and generation curtailment in isolated systems;
7. Evaluation of the effect of including the operating constraints of storage systems on the overall operational costs of the network;
8. Assessment of the instantaneous contribution of loads and energy storage systems in providing flexibility while reducing the total size of installed batteries;
9. Evaluation of the impact of countermeasures adopted by current regulations against over-frequency transients and the incidence of acquisition and command delays on these contributions;
10. Assessment of the impact of different control parameters on the stability of the system.

Outline of the Thesis

This thesis is organized into four chapters. It will begin with an overview of isolated MG structure and control, offering the reader the necessary background and context for the methodologies developed in this work. Subsequently, tools and approaches will be presented to address balanced as well as stable power provision at different time scales of the grid.

Chapter 1 - Overview on Microgrids and Autonomous Electric Grids: The concept of the MG and its general structure are introduced, with a primary focus on standalone networks. An overview of the state-of-the-art control schemes regarding small DC-MGs is also provided.

Chapter 2 - Flexibility Resources for Stand-Alone Microgrids: The chapter examines their crucial role in maintaining real-time power balance and in improving the overall reliability and stability of the system. Different categories of flexibility resources are analyzed, including controllable loads, energy storage systems, and advanced control strategies that enable fast and coordinated responses. The discussion highlights how these resources contribute to secure operation under varying conditions, supporting both short-term stability and long-term sustainability of isolated MGs.

Chapter 3 - Stability Analysis and Security Improvement: A small-signal modeling framework for droop-controlled DC microgrids with Constant Power Loads (CPLs) is developed. A state-space model is derived that captures the system's key dynamic behaviors. The droop mechanism was explicitly modeled, and the CPL negative incremental impedance was included to represent its destabilizing influence. Also, the effect of design parameters on system damping and stability has been studied through eigenvalue analysis.

Chapter 4 - Innovative Solutions for Real-Time Energy Management and flexibility Enhancement: This chapter proposes innovative strategies for energy balancing across different time scales of operation. These solutions build upon recent advancements in the literature to enhance the use of flexibility resources for fast voltage regulation, reducing the risk of instability, and improving the efficiency of the whole isolated entity.

Chapter 1

Overview on Microgrids and Autonomous Electric Grids

The rapid evolution of modern electricity generation is being driven by the large-scale integration of Renewable Energy Sources (RESs) and Distributed Generation (DG) technologies. These emerging paradigms offer substantial advantages for electric power systems, including enhanced service continuity, improved resilience, and expanded opportunities for consumer participation in both energy and ancillary service markets. By distributing DG units across geographically diverse locations, portions of the distribution network—at medium-voltage (MV) and low-voltage (LV) levels—can operate in a partially or fully autonomous (*islanded*) mode. Under such conditions, maintaining the balance between generation and demand relies heavily on well-coordinated control and energy management schemes.

The increasing penetration of RES and DG has thus become a cornerstone of modern power system planning, operation, and reliability assessment, particularly in the context of growing global energy demand. According to the U.S. Energy Information Administration (EIA) [25], worldwide energy consumption is projected to increase by approximately 30% by 2030 compared with 2012 levels, and by nearly 50% by 2040, primarily driven by population growth, industrialization, and economic expansion. Similarly, the International Energy Agency (IEA) estimates that cumulative global investment in the energy sector will reach roughly 40 trillion USD by 2035 [26]. These projections highlight the urgent need for efficient, flexible, and decentralized power system architectures capable of accommodating renewable variability while preserving stability, reliability, and power quality.

The integration of RESs into electricity networks has been significantly enabled by DG technologies, which leverage the advantages of decentralization. Over the past two decades, the European Union (EU) has emerged as a global leader in renewable energy deployment. Through long-term targets and supportive legislative frameworks, the region has achieved remarkable progress, with renewable energy consumption rising from about 9% in 2005 to 16.7% in 2015. Building on its initial 20% target for 2020, the recast Renewable Energy Directive 2018/2001/EU [27] established a binding goal requiring at least 32% of total energy consumption to be sourced from renewables by 2030, with provisions for upward revisions by 2023.

In alignment with the ambitions of the European Green Deal [28], the European Commission presented updated 2030 climate objectives on 14 July 2021 [29], proposing to raise the renewable share in the EU energy mix from 32% to a minimum of 40%. Subsequently, on 18 May 2022, the Commission launched the "REPowerEU" initiative [30], aimed at significantly reducing the EU's dependence on Russian fossil fuels before 2030 by accelerating the clean energy transition. The plan focused on three core pillars: improving energy efficiency, expanding clean energy production, and diversifying energy supply sources. Within this framework, the Commission proposed increasing the renewable energy target further to 45% by 2030 to boost adoption across the electricity, industrial, building, and transport sectors.

To facilitate the rapid deployment of renewable projects, the Council adopted a temporary emergency regulation on 22 December 2022 [31], following a Commission proposal from November 2022 [32]. This regulation simplified the permitting process for renewable energy infrastructure and promoted the use of power purchase agreements. Most notably, on 30 March 2023, the European Parliament and the Council reached a provisional agreement to raise the binding renewable energy target to at least 42.5% by 2030, with aspirations to approach 45% [33]. This milestone represents a significant advancement in the EU's renewable energy trajectory.

At the core of this evolving energy landscape lie Microgrids (MGs), which are poised to play a pivotal role in advancing decentralized generation and integrating RES. By enabling localized control and flexibility, MGs represent a cornerstone for building a sustainable, reliable, and future-ready energy system.

Concerning the above outlines, the rest of this chapter begins with a foundational definition and characteristics of MGs. The chapter then examines the operation and control of MGs, describing how hierarchical control layers—primary, secondary, and tertiary—work in coordinated fashion to maintain stability, enable optimal energy management through the Microgrid Controller (MGC), and ensure seamless transitions between grid-connected and islanded operation.

Building on this foundation, the chapter turns to isolated MGs, particularly those located on remote islands, and discusses the technical, economic, and environmental challenges they face due to limited inertia, high dependence on fossil fuels, and logistical constraints. The chapter then introduces cooperative energy management in isolated DC-MGs, explaining how distributed generators, loads, and storage units such as Battery Energy Storage System (BESS) must operate in a coordinated way to maintain voltage stability, manage intermittency, and ensure reliable autonomous operation.

Finally, the chapter highlights the role of Hardware-In-the-Loop (HIL) technologies as essential tools for bridging the gap between simulation and real-world implementation. It outlines how HIL enables high-fidelity validation of control strategies and system behaviors under realistic operating conditions. These capabilities facilitate the development of robust and scalable solutions for modern MGs.

1.1 Definition and Characteristics of Microgrids

Microgrid (MG) represents an innovative paradigm in the modern management and distribution of electrical energy. Although there might be different definitions in the literature, a common set of essential attributes can be identified [24, 34–40]:

- *Generation and Demand Management:* MGs incorporate various generation units (including renewable and conventional) alongside controllable loads and demand-side response mechanisms. This structure fosters a flexible and diversified energy portfolio, improving the system's overall resilience, operational efficiency, and sustainability.

- *Defined Electrical Boundaries:* Each MG functions within distinct electrical limits that differentiate it from the main grid. They are typically implemented at the LV level, though applications at the MV level are becoming more prevalent.

- *Islanded Operation:* A key attribute of MGs is their capacity for autonomous operation (also called islanded, isolated, or stand-alone mode). To achieve this, sufficient local generation and storage must be available to satisfy the maximum load in the absence of a connection to the utilty grid.

The MG concept has undergone substantial evolution. Initially conceptualized as broad subsystems comprising both supply and demand, MGs have progressively transitioned toward distribution-level applications, focusing on localized energy generation, energy storage, and isolated functionalities [40]. Regional interpretations differ as well: for example, in the United States, MGs are often configured to deliver combined heat and power, whereas in Europe the emphasis lies primarily on electrification [38].

Microgrids can be designed for diverse environments and assume multiple configurations. They may be classified according to the type of voltage at their connection bus, namely Alternating Current (AC), Direct Current (DC), or hybrid; or based on ownership, encompassing both public and private grids [41]. Traditionally, large industrial sites served as early examples of MGs, featuring localized electrical networks with limited interaction with the main grid and relying on established internal energy management systems.

In recent years, the deployment of MGs has expanded to include academic campuses, research institutions, residential districts, military installations, commercial centers, and industrial parks. Representative instances of these categories are documented in [42].

A central element of every MG is its control architecture, which supervises distributed generation, storage units, and flexible loads. This control system guarantees operational stability under both grid-connected and islanded conditions, ensuring seamless transitions between modes while maintaining the quality of the grid's main parameters (e.g., voltage and so on) [41].

Microgrids offer numerous tangible advantages that underscore their growing relevance within active distribution networks, even though technical, regulatory, and economic challenges still hinder large-scale adoption of Microgrids. Their main benefits and obstacles are summarized in Table 1.1.

As mentioned earlier, MGs can generally be categorized as either DC or AC systems. In recent years, DC-MGs have attracted growing attention due to their inherent compatibility with the DC nature of most modern energy resources and loads. RESs such as PV panels and fuel cells inherently generate DC power, while energy storage systems, including batteries and supercapacitors, also operate in the DC domain. Moreover, the majority of contemporary electronic and household appliances internally function using DC power, making DC-MGs more efficient by reducing the number of power conversion stages and the associated energy losses [13].

Besides, compared with AC systems, DC-MGs feature simpler voltage regulation and eliminate the need for frequency and phase synchronization, reactive power control,

Table 1.1: Advantages and Drawbacks of Microgrids (MGs).

Advantages	Drawbacks / Challenges
Advantages for Renewable Energy Sources Integration: • Localized integration of RESs close to demand centers, reducing transmission losses. • Promotes clean and renewable energy use, lowering fossil fuel consumption and generation costs. • Mitigates aggregated power fluctuations in distribution networks.	**Regulatory and Economic Barriers:** • Need for coherent policy frameworks and effective market incentives to ensure economic viability. • High initial investment and uncertain return on investment.
Benefits Related to Distribution System Design: • Improves grid reliability, operational efficiency, and adaptability. • Supports both grid-connected and islanded modes of operation, useful during main grid disturbances or in remote areas. • Enables distributed RESs to participate in local and wholesale markets.	**Technical and Operational Challenges:** • Requires advanced control, communication, and optimization systems for real-time coordination. • Must handle renewable intermittency and ensure stable transitions between modes. • Compliance with protection, safety, and power quality standards can be complex.
Advantages for End Users and Environmental Impact: • Encourages consumer participation in generation and energy management. • Enhances supply reliability and allows customized power quality. • Provides ancillary services such as voltage regulation. • Reduces emissions and supports environmental sustainability. • Improves grid resilience and energy security through local renewables.	**Social and Governance Considerations:** • Potential stakeholder conflicts among consumers, producers, operators, and regulators. • Necessity for collaborative governance and clear roles. • Broader socio-economic evaluation needed—e.g., rural electrification, job creation, innovation, and public engagement.

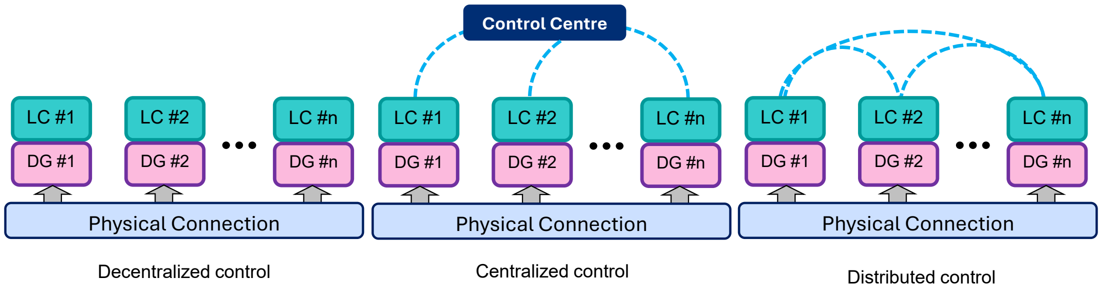

Figure 1.1: Control architectures of MG

and harmonic compensation. These advantages translate into higher overall efficiency, improved reliability, and simplified control and protection architectures, particularly in residential, commercial, and low-voltage industrial applications [43].

Given these technical and operational benefits, it is worth mentioning that since this thesis primarily focuses on DC-MGs, the subsequent sections will further examine their characteristics in terms of typical operating voltage levels, control structures, and power management strategies employed within such MGs.

1.2 Operation and control of microgrids

A MG control system integrates the necessary aspects that define the MG as an intelligent, autonomously managed power system. It can function independently or in coordination with the main grid, maintaining operational flexibility to disconnect, reconnect, and exchange energy in response to network conditions.

Because MGs differ in geographical context, scale, and operational intent, their corresponding control requirements and functionalities also vary. From an implementation viewpoint, a MG control system may comprise hardware, software, and a combination thereof. Its architecture may follow centralized, decentralized, or distributed paradigms, selected according to the desired degree of coordination, scalability, and resilience [43–46]. Fig. 1.1, graphically illustrates these control architectures. Key functions of a MG control system include:

- Coordinating operation under both grid-connected and islanded conditions.
- Managing the transition from grid-connected to islanded operation to ensure an uninterrupted power supply to local loads during grid contingencies, such as blackouts.

- Executing re-synchronization and reconnection procedures when restoring its connection to the main grid.
- Regulating power exchanges to optimize the balance within the MG.
- Delivering ancillary services to the distribution network and, where feasible, participating in electricity markets or utility operations.

It should be stated that not all MGs are equipped with the complete set of these capabilities (particularly, functions related to energy market participation and advanced ancillary services) [47]. The range of control features depends largely on the system's design, available communication infrastructure, and operational objectives (e.g., tasks correlated to grid-connected or isolated operation).

Microgrid control functions can act across several hierarchical layers and timescales, spanning from device-level control (i.e., in the scale of Distributed Energy Resources (DERs)) to system-level coordination (i.e., higher supervisory and grid-interactive operations) [48].

Device-level functions operate on very short timescales, from microseconds to a few seconds, ensuring fast dynamic responses and local stability. Conversely, system-level management tasks act over longer intervals, ranging from seconds to several hours or days, to perform energy scheduling, dispatching, and optimization [49]. Transitions between grid-connected and islanded states must occur rapidly with minimal delay, while dispatch and scheduling functions are performed periodically, typically every 15 minutes or like that. An overview of these hierarchical layers and their respective timescales is presented in Fig. 1.2.

Modern MG implementations commonly adopt a hierarchical control layer composed of three main levels:

- **Primary control**
- **Secondary control**
- **Tertiary control**

The primary layer—often referred to as the local level—guarantees the secure and stable operation of the MG. It is primarily responsible for maintaining stability and supports plug-and-play integration of DERs. This layer is typically implemented through

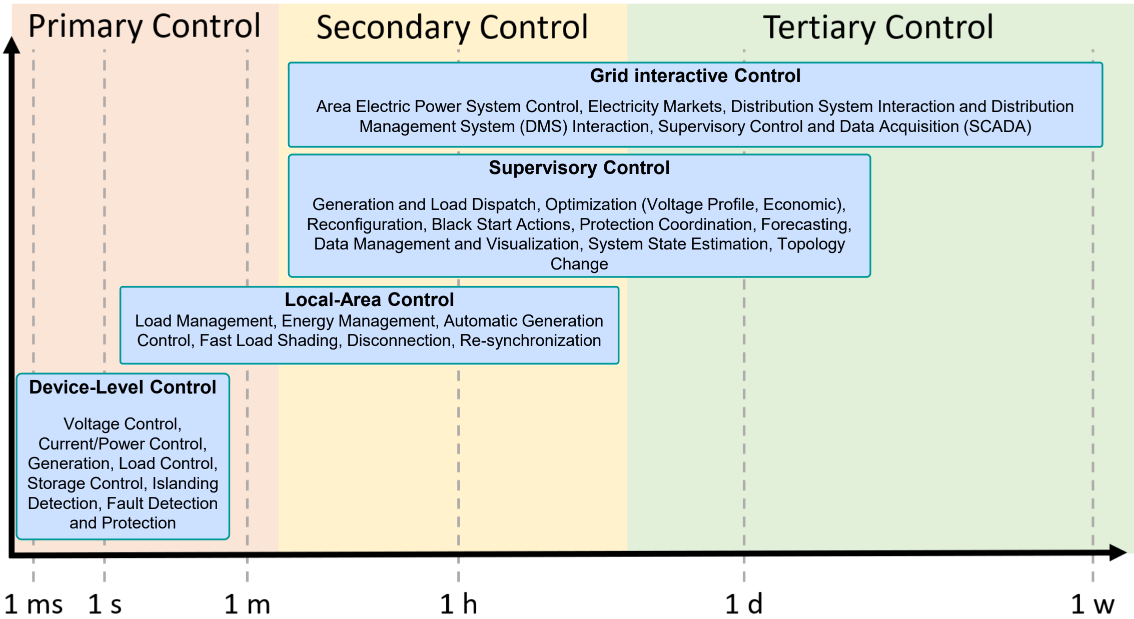

Figure 1.2: Timescales and hierarchical classification of MG control functions

automation techniques such as droop control, which ensure proportional sharing of power among interconnected DERs, providing fast dynamic response and local stability [50].

The secondary layer, sometimes called the management level, restores grids quantities like voltage to their nominal values and facilitates coordination among local controllers, through centralized, decentralized, or distributed architectures [43]. Centralized control schemes offer high precision and effective coordination through a supervisory controller that oversees the overall operation of the MG [1]. These architectures depend on fast and reliable communication networks to transmit measurements and status data from distributed units to the central controller, which then issues coordinated commands for the entire system [44]. While this approach ensures global observability and optimal decision-making, several studies have identified key limitations, including high computational demand on the central controller, the need for system reconfiguration when units are added or removed, and vulnerability to communication failures [51].

To overcome these drawbacks, numerous studies [52, 53] have proposed decentralized control strategies that improve resilience and communication-interruption tolerance. In decentralized architectures, each unit relies primarily on local measurements to perform control actions, allowing for simpler scalability and seamless integration of new units. However, the absence of global coordination can result in suboptimal voltage regulation and unequal current sharing among distributed generators [54].

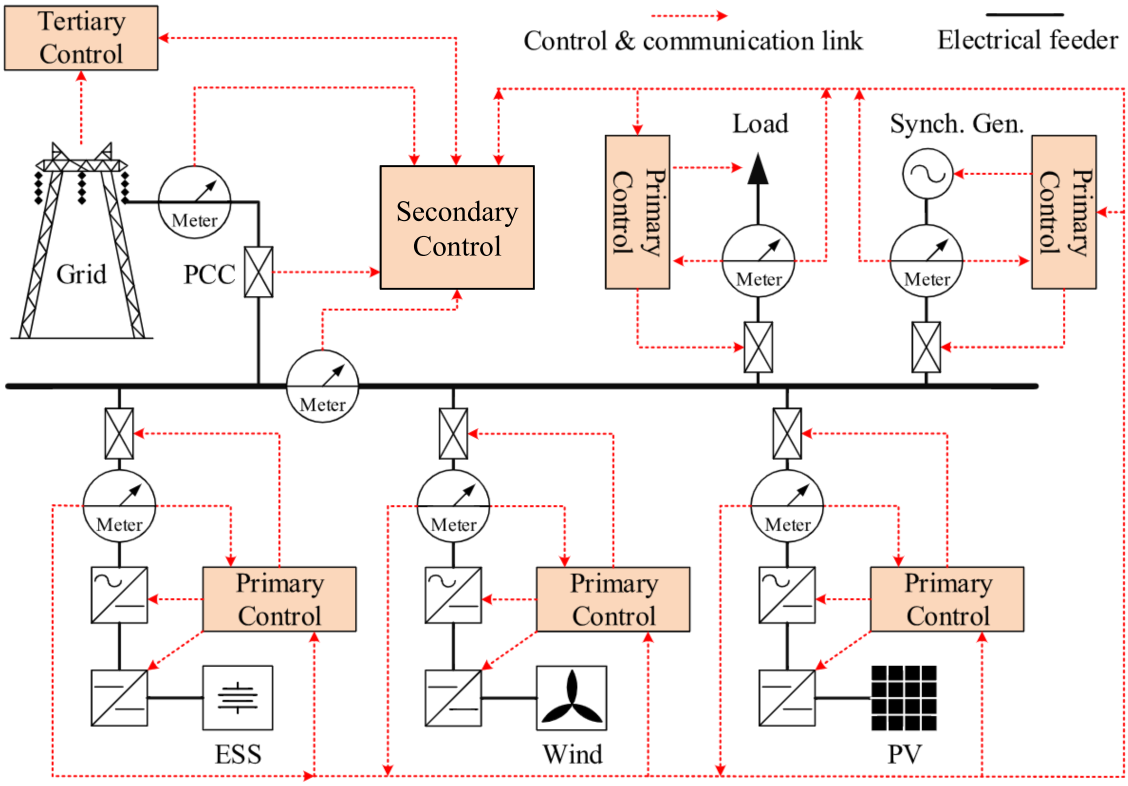

Figure 1.3: Generic control layers of microgrid [1].

To merge the global coordination of centralized schemes with the autonomy of decentralized ones, distributed control frameworks have been developed [45]. These architectures employ partially connected communication networks, where neighboring units exchange information. Each controller combines local measurements with data from adjacent nodes to regulate output voltages. This configuration retains the coordination and system awareness of centralized control while enhancing robustness and eliminating single points of failure in both communication and control layers [45].

At the last of the hierarchy, the tertiary control layer manages the overall economic and operational optimization of the MG. Its functions include energy dispatch, coordination of power exchange with the main grid, and compliance with market and regulatory requirements. As in lower layers, both centralized and distributed implementations have been explored [52], depending on the desired trade-off between global coordination and local autonomy.

According to above explanations, a typical control configuration of MG is shown in Fig. 1.3 [1]. This three-layered control hierarchy aligns with the IEEE 2030.7-2017 standard [40], which also organizes MG functionalities into three levels: Level 1 for local automation and device management, Level 2 for dispatching and transition control, and

Level 3 for system-wide monitoring, control, and optimization. IEEE 2030.7 remains a cornerstone reference in the design of MG control architectures [41, 55], complemented by related standards such as IEEE 2030.8-2018 [56], which specifies controller performance assessment procedures, and IEEE 1547-2018 [57], defining interconnection and interoperability requirements for DERs. IEC 62898-2 [58] addresses operational and control aspects, defining system modes, transitions, EMS functionalities, protection coordination, synchronization, reconnection, and power quality management. IEEE 2030.7 [40] adopt similar hierarchical philosophies, by distinguishing only two modes of operation (i.e., grid-connected and islanded) maintaining consistent dispatch logic across both modes.

Furthermore, the IEC framework introduces differentiated operational and compliance requirements across these categories. During non-isolated operation, distributed resources must comply with national grid codes and continuously monitor grid voltage to ensure readiness for reconnection. In contrast, isolated systems—being disconnected from the external grid—are exempt from such codes but impose stricter internal control demands. These include black-start capability, continuous system monitoring, adaptive energy management with load-shedding mechanisms to preserve power balance, and increased storage capacity to support prolonged autonomous operation.

Turning to the operational aspects of DC-MGs, the common bus voltage is the main parameter, as this quantity serves as a global indicator of power equilibrium within the system. The choice of voltage level directly influences power conversion efficiency, system safety, cost, and interoperability with connected components such as RESs, battery energy storage systems, and loads.

In general, given the nominal voltage levels, DC-MGs are classified into low-voltage and medium-voltage systems. LV grids are predominant in residential and small-scale commercial applications, where safety considerations and compatibility with low-voltage DC appliances are of primary importance [59, 60]. However, not to mention that these systems constrained in power transfer capacity and permissible distribution distance.

For applications requiring higher power capacities and improved transmission efficiency, MV systems are increasingly employed in commercial and industrial prosumers, where higher voltage levels reduce current magnitudes, minimize cable losses, and enhance overall system efficiency [61, 62]. Among various voltages, the 380 V DC bus is a proper value for building-scale and hybrid AC/DC networks, as it achieves an optimal balance between efficiency, safety, and compatibility with existing power electronic interfaces [61].

Table 1.2 summarizes representative DC voltage levels commonly adopted in microgrid

Table 1.2: Typical DC voltage levels in user and industrial prosumer microgrids

Application Type	**Voltage Levels**	**Typical Use Cases**
Residential / User Prosumers	12 V, 24 V, 48 V, 120 V	PV systems, lighting, home storage
Commercial Prosumers	380 V, 1 kV	Data centers, EV chargers, office MGs
Industrial Prosumers	750 V, 1.5 kV	Industrial automation, DC distribution
Utility / Large-Scale Systems	3 kV–10 kV	Long-distance DC links, energy clusters

applications, outlining their typical use cases and corresponding voltage categories across residential, commercial, and industrial domains [59–62].

1.3 Isolated Microgrids

The inherent variability of RESs introduces unpredictable fluctuations in net-load profiles. Large, interconnected power systems are generally resilient to such uncertainties because the high rotational inertia of synchronous machines provides natural stabilization. In contrast, smaller and off-grid systems exhibit much greater sensitivity. In these contexts, high levels of RES penetration often lead to reduced system inertia, thereby increasing the likelihood of voltage instability.

Islanded MGs, especially those located on small islands, serve as ideal environments for testing innovative technological solutions that mitigate stability challenges associated with high RES integration. Globally, small islands share several structural similarities: limited populations, narrow economic bases, and geographic isolation, all of which contribute to logistical, trade, and service-access constraints [63]. Despite these limitations, small islands often possess significant ecological and cultural assets, making them valuable for sustainable development and eco-tourism initiatives.

However, climate change poses an escalating threat to island territories, including European and particularly Italian small islands [64]. According to [65], rising global temperatures, intensified extreme weather events, and shifting precipitation patterns are expected to exacerbate water scarcity and other vulnerabilities. Small Mediterranean islands face multiple challenges, including strong dependence on fossil fuels, high energy production and distribution costs, limited renewable resource utilization, seasonal load variations, water shortages, inefficient waste management, and outdated transport systems [66].

Effective policy frameworks are vital to address these issues, yet small islands often lack the financial resources, technical expertise, and institutional capacity needed for comprehensive energy transition strategies [67]. Recognizing their vulnerability, the 2015 Paris Agreement [68] explicitly identified island regions as both highly exposed to climate impacts and strategically suited for demonstrating sustainable technologies. In response, the European Union has launched several major initiatives, including the NESOI program [69] and the Clean Energy for EU Islands Secretariat [70], aimed at accelerating the clean energy transition in island territories. These programs focus on reducing fossil fuel dependence through the deployment of RES and advanced energy management systems. Successful examples demonstrate that islands can act as living laboratories for achieving high renewable penetration and near self-sufficiency [71, 72].

A holistic approach to island decarbonization should also incorporate waste management, circular economy principles, efficient water use, sustainable tourism, and low-carbon mobility solutions. Nonetheless, research on small Mediterranean islands remains limited, hindering the development of context-specific transition pathways [73]. Recent studies in the Balearic and Canary Islands, together with renewable resource assessments for Lampedusa, have provided valuable insights [73, 74]. Yet, significant gaps persist in high-resolution data collection and climate scenario modeling at the micro-scale—both of which are crucial for accurate energy planning [75].

A detailed assessment presented in [76] highlights the technological and institutional barriers affecting Italian small islands. Although several islands have initiated sustainability programs, progress is often limited by landscape protection regulations, complex connection procedures, and administrative fragmentation among multiple authorities [77]. The European Commission [78] identifies wind energy as a promising renewable option for islands, particularly when combined with energy storage, hybrid generation, or interconnections to nearby grids. Despite this potential, wind energy deployment in Italian small islands remains minimal, restricted to a few micro-wind projects: Pantelleria (32 kW), Sant'Antioco (55 kW), and Ventotene (3.16 kW) [79].

Similar non-technological barriers also limit the expansion of photovoltaic (PV) systems. Although rooftop installations offer a practical way to increase renewable penetration in areas with limited land availability, installed capacities remain well below national averages and the targets set by the Italian Ministry for Economic Development [77]. The Ministerial Decree of 14 February 2017 [80] established installation targets for 20 non-interconnected islands, totaling 12,820 kWp (including 1,000 kWp for Capri, which has since been interconnected). However, progress has been uneven: the Aeolian Islands have reached only 509 kWp of the planned 2,860 kWp, Pantelleria has achieved 872 kWp of its

Table 1.3: PV penetration in Italian islands in 2021 compared with 2020 targets

Island	**Isolated**	**Target** 2020 **[kW]**	**Target reached** 2021 **[%]**	**PV installed** 2021 **[kW]**	**PV installed/habitants** 2021 **[kW/habitant]**	**PV installed/habitants compared with national average** 2021 **[%]**
Capraia	yes	180	19.73%	35.50	0.10	26%
Capri[a]	no	1000	20.63%	206.26	0.02	5%
Ischia	no	-	-	3960.40	0.06	16%
Giglio Island	yes	700	4.96%	34.74	0.03	8%
Elba Island	no	-	-	3623.80	0.12	32%
Aegadian Islands	yes	1060	142.68%	1512.44	0.34	90%
Aeolian Islands (Lipari)	yes	2860	17.79%	508.89	0.04	11%
Pelagie Islands	yes	2310	26.20%	605.12	0.09	24%
Tremiti Islands	yes	240	7.67%	18.40	0.04	11%
La Maddalena	no	-	-	990.50	0.09	24%
Pantelleria	yes	2720	30.89%	840.31	0.11	29%
Ponza	yes	720	40.18%	289.29	0.09	24%
Procida	no	-	-	339.78	0.03	8%
Salina	yes	580	43.10%	250.00	0.10	26%
San Pietro	no	-	-	1547.23	0.26	68%
Sant'Antioco	no	-	-	1934.61	0.14	37%
Ustica	yes	280	155.00%	432.64	0.33	87%
Ventotene	yes	170	77.48%	131.72	0.19	50%

[a]Capri has a target because it was isolated in 2017 when the decree was issued and interconnected to the grid in 2019

2,720 kWp goal, and the Pelagie archipelago has installed 605 kWp compared to a target of 2,310 kWp. Ustica stands out as a positive case, exceeding its target with 432 kWp of installed RES, covering approximately 12% of its electricity demand.

Despite these limitations, the potential for photovoltaic expansion in Italy—particularly in southern regions and islands—is significant due to the country's proper solar irradiation and considerable number of sunny days throughout the year. This favorable climatic condition provides an opportunity to harness solar energy more effectively and reduce dependence on imported fossil fuels. Beyond traditional rooftop or ground-mounted systems, offshore PV installations could also contribute to meeting renewable energy targets, especially in small islands where land is scarce. Recent technological developments in flexible PV arrays have made offshore deployment feasible [81]. These innovative systems can adapt to sea conditions, mitigating the impact of waves and reducing mechanical stress on the panels. As a result, they offer lower maintenance requirements and enhanced overall system longevity, which make them a suitable option for Italy's smaller islands [82].

Currently, PV systems are present across all small Italian islands, although generally at modest scales—for example, 18.4 kWp in the Tremiti Islands and 34.7 kWp on Giglio Island. The largest systems are located on interconnected islands such as Ischia (4,000 kWp), Elba (3,700 kWp), and Sant'Antioco (2,000 kWp). Among the non-interconnected islands, Pantelleria leads with 840 kWp, followed by Lampedusa and Linosa, each with 605 kWp [77]. A detailed summary of photovoltaic penetration across Italian small islands is reported in Table 1.3.

1.4 Cooperative Energy Management in Isolated DC Microgrids

As mentioned in the previous section, the feasible option for electrifying remote islands is to deploy local energy resources, such as solar power. In such case, the control of stand-alone MGs would be crucial due to the increasing penetration of intermittent converter-interfaced RESs. In a typical MG, the interface converters regulate power flow among DGs, loads, and Energy Storage Systems (ESSs), ensuring voltage stability and efficient power sharing [49, 83, 84]. The main objective of microgrid control is to maintain the bus voltage within acceptable limits, achieve proportional load sharing among distributed units, and ensure seamless transitions between operation modes.

As mentioned before, control algorithms can be implemented through centralized, decentralized, or distributed architectures, each offering trade-offs between complexity, reliability, and scalability [85, 86]. Keeping in mind that from the main grid perspective, a MG acts as an aggregated entity that comprises loads, DGs, and ESSs; therefore, its control architecture must ensure cooperative power management, voltage regulation, current sharing, and state-of-charge (SoC) balancing among available resources [85]. While purely local control approaches can reduce implementation cost and enhance modularity, their limited coordination capability may degrade system performance under unbalanced conditions. Conversely, advanced distributed architectures supported by robust communication networks and supervisory control systems, often leveraging IoT-based measurement infrastructures, can significantly improve cooperative operation, enhancing voltage stability and power-sharing accuracy [87–89]. Integrating MGs into the broader grid also demands effective coordination with Distribution System Operator (DSO)s, ensuring that renewable variability and multi-MG interactions do not compromise system stability or power quality [90, 91].

On the other side, in the context of isolated or weakly interconnected systems such as off-grid rural areas or small islands, the need for autonomous operation becomes even more vital. Here, the local coordination between batteries, distributed generators and variable loads must continuously balance generation and consumption [92, 93]. To achieve this, robust local control strategies are essential to maintain stable voltage profiles and ensure secure operation without relying on external support.

It is worth highlighting that the main objective of this PhD dissertation is to investigate and develop device-level and local-area control (see Fig. 1.2), to achieve autonomous operation through coordination mechanisms in stand-alone DC-MGs.

Building on this foundation, the subsequent discussion would be dedicated on the droop control as one of the most fundamental control strategies in this regard. Despite the availability of numerous control approaches [94]), droop control is the most widely adopted technique for ensuring cooperative power sharing among parallel converters in DC-MGs.

Inspired by the droop characteristics the firstly employed for AC systems, droop control for DC systems establishes a direct relationship between the converter's output voltage and current, thereby enabling proportional current sharing with respect to sources power provision capabilities [44]. Its principal merits include simplicity, as each converter operates autonomously using only voltage and current measurements. Furthermore, in the decentralized implementation, it offers scalability and plug-and-play capability, allowing new sources or storage units to be integrated seamlessly without the need to reconfigure the overall control framework. In addition, enhanced stability can potentially be achieved when droop parameters are properly tuned, as they improve system damping and stabilize networks through the introduction of a virtual impedance effect [59, 95].

Nevertheless, conventional droop control involves a trade-off between voltage regulation and current-sharing accuracy. A higher droop gain enhances current-sharing precision but causes larger bus-voltage deviations, while a lower gain achieves the opposite effect. To address these limitations, several enhanced methods—such as adaptive, nonlinear, and communication-assisted droop control—have been proposed [4, 46, 85, 96]. In its standard form, the droop control law is expressed as:

$$V_{n,ref} = V_{nom} - R_{n,c} I_{n,out}, \tag{1.1}$$

where $V_{n,ref}$ denotes the reference output voltage of the n-th converter, V_{nom} is the nominal DC bus voltage, $R_{n,c}$ is the virtual droop resistance (or droop gain), and $I_{n,out}$ is the converter's output current [47, 50].

The droop gain $R_{n,c}$ is typically chosen to ensure that voltage deviations remain within the permissible limit ΔV_{max} when the current reaches its rated value (i.e., maximum continuous current) $I_{n,nom}$:

$$R_{n,c} \leq \frac{\Delta V_{max}}{I_{n,nom}}, \qquad \Delta V_{max} = V_{nom} - V_{per}. \tag{1.2}$$

In (1.2), V_{per} denotes the permissible voltage deviation. In a typical droop control scheme, the introduced formula is applied to the converter's duty cycle via an inner voltage or current control loop to achieve the desired operating point.

This approach enables fully autonomous current sharing among converters in proportion to their rated capacities, eliminating the need for real-time communication. Fig. 1.4 illustrates the conventional droop characteristic, where the DC bus voltage decreases linearly with increasing output current, ensuring balanced load distribution among parallel units.

Although the linear droop relationship provides a simple and effective means of decentralized control, it does not guarantee accurate current sharing in systems affected by unequal line impedances, converter dynamics, or parameter mismatches. To overcome these challenges, recent studies have proposed advanced variants such as adaptive droop,

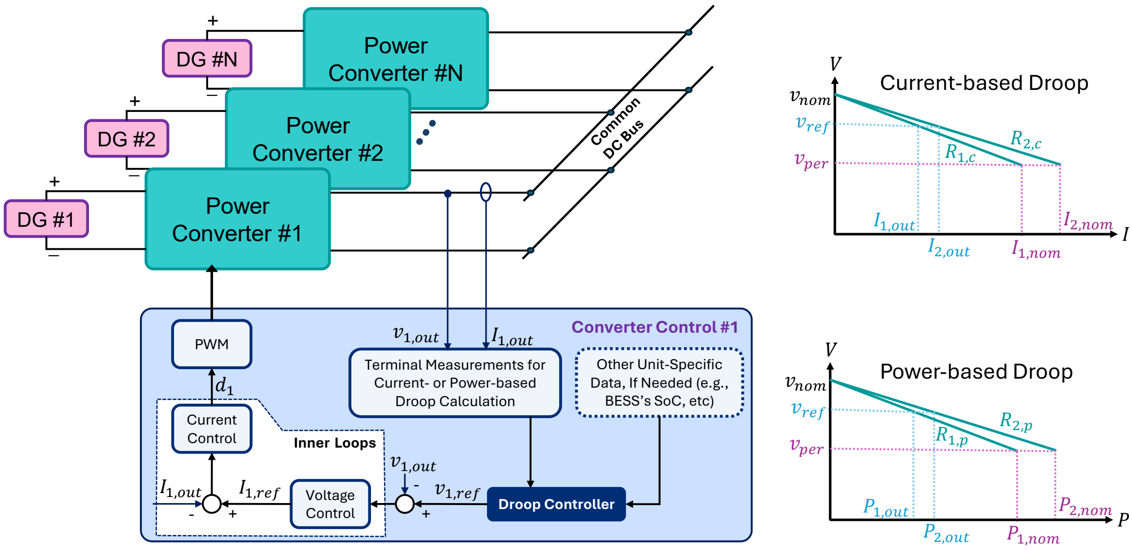

Figure 1.4: Conventional droop control characteristic for parallel converters in a DC microgrid.

low-bandwidth communication-assisted droop, and nonlinear droop schemes, aiming to improve both voltage restoration and current-sharing accuracy [10, 97, 98].

In addition to the conventional current–voltage (I–V) droop method, an alternative control strategy has been introduced based on the converter's output power, referred to as power–voltage (P–V) droop control. In this approach, the output power of each converter is employed as the feedback variable rather than its current, leading to the following control law [50]:

$$V_{n,ref} = V_{nom} - R_{p,n} P_{n,out}, \tag{1.3}$$

where $P_{n,out}$ denotes the output power of the n-th converter, and $R_{p,n}$ is the power-based droop coefficient. Compared with (1.1), this formulation directly couples the converter's power contribution with its reference voltage, thereby achieving proportional power sharing among units with different ratings.

Both current- and power-based droop strategies operate under the same decentralized principle of regulating bus voltage according to converter loading, but they differ in control dynamics and practical suitability [50]. The I–V droop control exhibits linear behavior and straightforward implementation, making it suitable for systems dominated by resistive or constant-current loads [96]. In contrast, the P–V droop control inherently represents the converter's rated power capacity and is advantageous in systems composed of heterogeneous energy sources or constant-power loads, where accurate power coordination is more critical than instantaneous current matching [44, 99].

As in the current-based scheme, the value of the power-based droop coefficient $R_{p,n}$ determines the trade-off between voltage regulation and sharing accuracy. A higher $R_{p,n}$ improves damping and proportional power distribution but results in larger bus-voltage deviations, while a smaller value maintains tighter voltage regulation at the expense of less accurate power sharing [4].

Since Battery Energy Storage Systems (BESSs) are widely employed in the subsequent chapters for enhancing microgrid flexibility and support the voltage stability, it is worth noting that incorporating unit-specific data to droop control provides an effective foundation for coordinated energy management and improved reliability in DC microgrids. In this regard, note that when several BESSs operate in parallel, differences in their capacities or initial SoCs can lead to uneven current or power distribution. If unaddressed, such imbalance can cause certain batteries to cycle more frequently, reducing their operational lifespan [50]. To mitigate this issue, an adaptive droop mechanism considering the state of batteries can be incorporated into the control layer to balance the utilization of distributed storage units.

In this approach, each battery's terminal current follows a droop law similar to (1.1), but the virtual resistance is adjusted dynamically according to the SoC. During discharging, batteries with higher SoC values are assigned smaller droop resistances, allowing them to supply higher output currents and thus discharge more rapidly. Conversely, during charging, batteries with lower SoC levels receive smaller droop resistances, enabling faster charging and gradual SoC equalization over time.

$$\begin{cases} \text{Discharging:} \quad I_{n,out} \propto 1/R_{n,dr} \propto SoC_n \\ \text{Charging:} \quad I_{n,out} \propto 1/R_{n,dr} \propto 1/SoC_n \end{cases} \tag{1.4}$$

This adaptive tuning of the droop coefficient promotes uniform energy utilization among all storage units, thereby extending battery lifespan and maintaining system balance.

To recap this section, the cooperative energy management of isolated DC-MGs fundamentally depends on the integration of robust control mechanisms in both device and local area levels. While droop-based control continues to serve as the cornerstone of primary-level operation, the incorporation of communication-assisted coordination and adaptive control algorithms can substantially enhance voltage regulation and current-sharing accuracy, particularly under islanded conditions with high renewable penetration. Looking ahead, innovations in droop-based strategies are expected to foster resilient, scalable, and self-organizing architectures for next-generation DC-MGs, capable of maintaining stability and efficiency across diverse operating conditions.

1.5 Application of Hardware-In-the-Loop for Real-World Evaluation

Digital Real-Time Simulation (DRTS) represents an advanced approach used to explore how power system components behave dynamically and operationally under real-world conditions. By utilizing modern hardware architectures and parallel computation, researchers employ Real-Time Simulators (RTSs) to solve the differential equations that model power systems in actual real time. This real-time solving capability allows electrical networks to be emulated with high fidelity, effectively reproducing both transient and steady-state characteristics while maintaining minimal latency.

An important extension of DRTS is the Hardware-In-the-Loop (HIL) configuration. In this setup, a simulated or virtual power system interacts directly with a physical device, commonly called the Device Under Test (DUT) or Hardware Under Test (HUT). The DUT may consist of a single converter, a control unit, or an integrated subsystem whose interaction and dynamic response with the rest of the simulated grid are investigated.

Adopting a HIL-based setup offers significant advantages. It allows engineers to perform realistic and repeatable testing in a safe environment. Through this method, control algorithms, protection schemes, and hardware performance can be evaluated across a wide variety of operating scenarios without subjecting the physical equipment to the risks of large-scale experimentation. Moreover, HIL testing provides a cost-efficient route for validating new control and energy management concepts, eliminating the necessity for constructing full-scale prototypes or conducting field trials.

Within this research, the HIL platform functions as an essential link between simulation and physical experimentation for validating the proposed energy management and voltage regulation strategies in DC MGs. By coupling real control hardware with a network simulated in real time, the developed control methods are tested under realistic operating conditions. This configuration captures both computational and electrical interactions, ensuring that the observed results closely reflect the behavior expected in practical power systems.

The idea of HIL-based RTS originated in the mid-twentieth century, initially driven by developments in the aerospace industry. During this period, engineers utilized the technique to design, test, and verify complex control systems under realistic operating conditions. Early realizations of such systems were constructed using analog circuits and simple computing hardware, which offered only limited interaction between physical and simulated elements. As digital computation, parallel processing, and real-time numerical techniques advanced rapidly, HIL simulation evolved into a highly capable and flexible framework that could reproduce system dynamics with true real-time accuracy.

A significant turning point in the industrial application of HIL technology occurred within the automotive field, most notably during Toyota's development of the Prius Hybrid-Electric Vehicle (HEV). Through the adoption of real-time simulation, Toyota's engineers were able to extensively evaluate and refine their powertrain control algorithms and energy management strategies across diverse driving and environmental scenarios. The seamless integration of real and simulated components played a vital role in enhancing the vehicle's energy efficiency, control reliability, and overall robustness.

Beyond its initial aerospace and automotive roots, HIL simulation has become a fundamental approach employed across multiple engineering disciplines—ranging from industrial automation and Renewable Energy Source (RES) to modern power networks. In power system studies, HIL platforms offer a reproducible and secure environment where controllers, converters, and protection mechanisms can be tested effectively, avoiding the risks and costs associated with full-scale hardware experimentation. As a result, this methodology now serves as a cornerstone for validating the design and performance of innovative technologies in Distributed Generation (DG), MG control, and Energy Management System (EMS).

The fundamental difference between DRTS and traditional, non-real-time simulations lies in their temporal synchronization. In a DRTS environment, computation stages—including data acquisition, differential equation solving, and output processing—are executed concurrently with real-world time. This alignment ensures that the simulated system reacts precisely at the same rate as the corresponding physical process it models. Such real-time synchronization is especially critical for developing and testing applications that rely on time-sensitive behavior, such as control and protection algorithms or dynamic energy management in DC-MGs.

Maintaining accurate temporal coordination between simulated and physical components poses one of the primary technical challenges in DRTS. Latency, defined as the time delay between input and output responses, must be minimized to preserve the authenticity of interaction between both domains. Even small timing mismatches can lead to inaccurate results or instability—particularly in systems governed by fast control dynamics, such as voltage regulation and energy management controllers in DC MGs. Therefore, achieving deterministic timing behavior and ultra-low latency is essential to ensure that HIL-based testing reflects true real-world performance and yields dependable insights for control validation and system optimization.

In DRTS-based power system investigations, how the system is modeled critically determines the achievable fidelity, computational performance, and overall suitability of the simulation for a given application. Researchers commonly employ three principal modeling paradigms: the Averaged model, the Phasor model, and the Electromagnetic Transient (EMT) model—or, in some studies, a hybrid combination of these. Each paradigm presents distinct strengths and compromises in terms of accuracy, time-step resolution, and computational intensity, thereby allowing the most appropriate technique to be selected according to the study objectives and performance constraints.

A key challenge in real-time modeling lies in balancing model precision with computational cost. While detailed, component-level representations can enhance realism and better capture system dynamics—particularly valuable in HIL experiments—they also impose heavier computational demands on the simulator. Such complexity can limit the achievable real-time time step, potentially jeopardizing the synchronization needed for accurate execution. Consequently, model choice must judiciously weigh the trade-off between simulation detail and real-time feasibility.

The Averaged model describes the behavior of power system components using time-averaged quantities rather than instantaneous waveforms. By neglecting high-frequency switching effects, it focuses primarily on low-frequency and steady-state phenomena. Because of its reduced computational burden, this approach is particularly effective for steady-state analysis, long-term operation studies, and energy management optimization, where system variables change gradually. Within DC MGs, averaged modeling provides a practical means for evaluating power balance, voltage regulation, and control strategies under quasi-steady conditions, enabling rapid testing of supervisory or high-level controllers in a DRTS framework.

The Phasor model, on the other hand, employs a complex-vector representation to express sinusoidal voltages and currents in terms of their magnitudes and phase angles. This formulation strikes a balance between simplicity and dynamic fidelity, making it suitable for studying medium-term transient behavior. Phasor-domain simulation is widely utilized for small-signal stability analysis, control design, and transient stability evaluation, where the goal is to observe system response to disturbances without resolving fast-switching transients. For HIL-based MGs testing, phasor models support efficient validation of upper-level controllers—such as droop control or coordinated voltage regulation—without imposing excessive computational loads.

Conversely, the EMT model delivers the most detailed and physically comprehensive representation of power system dynamics. EMT-based simulations capture instantaneous voltage and current variations at fine time resolutions, enabling the observation of switching effects, fast transients, and high-frequency oscillations. Such precision makes EMT modeling indispensable for analyzing fault responses, converter switching behavior, communication latency, and protection mechanisms. In DC MGs, EMT real-time simulation is essential for evaluating converter-level control performance, voltage recovery dynamics, and interactions among Distributed Energy Resources (DERs). However, due to its significant computational demand, EMT modeling is often confined to short-duration or event-specific investigations and is frequently combined with averaged or phasor approaches in hybrid frameworks to optimize computational resources.

To summarize, each modeling approach fulfills a specific analytical role within DRTS and HIL-based experimentation. Averaged models enable system-level studies focusing on energy management and steady-state control; phasor models offer a balanced approach for dynamic and supervisory control assessment; and EMT models remain vital for validating converter-level dynamics and protection schemes. Ultimately, the choice—or combination—of models depends on the required temporal resolution, control bandwidth, and level of hardware–software interaction needed to investigate advanced energy management and voltage regulation strategies in DC MGs.

Accordingly, choosing an appropriate simulation model for DRTS studies depends primarily on the dynamic nature of the system or component being analyzed. The relevant temporal scale—defined by the characteristic duration of the physical processes involved—governs the degree of model fidelity and computational detail required. For example, fast phenomena such as converter switching transients or fault-induced oscillations evolve over microsecond to millisecond intervals, while energy management and voltage restoration in DC MGs generally occur on a timescale of seconds to minutes. A clear understanding of these temporal dynamics is therefore essential to develop simulation models that maintain an optimal balance between realism, computational efficiency, and real-time operability.

Apart from model formulation, RTSs play a vital role in model implementation, system prototyping, and concept validation across numerous engineering fields. Prototyping, in this context, refers to the iterative development of simplified or representative system models that facilitate the rapid testing, refinement, and optimization of control strategies and algorithms. The growing practice of Rapid Prototyping (RP) within real-time environments has accelerated the transition from theoretical concepts to hardware deployment. Contemporary RTSs integrate automatic code generation and real-time interfacing functionalities, effectively bridging the gap between software-based simulation and physical controller hardware.

Following the design and development stages, HIL testing provides an efficient and realistic means for assessing prototypes and hardware devices under controlled yet representative operating scenarios. Through this approach, engineers can emulate complex grid behaviors, evaluate controller performance, and validate system interactions without incurring the costs or risks associated with large-scale field trials. Moreover, DRTS and HIL systems are increasingly utilized for education and training purposes, providing learners with practical, hands-on exposure to real-time control, protection, and system integration concepts relevant to modern power and energy infrastructures.

During the past two decades, DRTS methodologies have become increasingly prominent in both transmission and distribution network research. This growth has been propelled by advancements in smart grid technologies, RES integration, and power electronic systems. Although the majority of studies have concentrated on distribution-level MGs, comparatively fewer investigations have addressed the unique challenges of real-time simulation at the transmission level, particularly those involving high-power converters and large-scale dynamic interactions.

As modern power systems grow in scale and complexity, new computational and interface challenges arise for real-time simulation. One notable example is the Modular Multilevel Converter (MMC), whose detailed EMT-level representation involves tracking thousands of switching events within each simulation step. Achieving accurate real-time performance for such systems demands advanced numerical algorithms and high-performance hardware architectures. Similarly, in HIL experiments, the interface subsystem—responsible for delivering voltages and currents to the DUT—must maintain sufficient bandwidth, stability, and synchronization to preserve the fidelity of the real-time interaction between simulated and physical domains.

In addition, the rapid digitalization of modern power systems has introduced cyber-physical considerations into real-time simulation. The widespread use of Internet-based communication infrastructures supports advanced monitoring, automation, and centralized control; however, it simultaneously exposes systems to cybersecurity threats, including data tampering and unauthorized control actions. Therefore, incorporating communication network latency, data flow irregularities, and potential cyber-attack scenarios into DRTS frameworks has become essential to ensure resilient and reliable grid operation.

To address these emerging challenges, current research increasingly focuses on distributed or remote real-time simulation architectures that interconnect geographically separated testbeds via high-speed communication networks. These distributed DRTS platforms enable coordinated HIL experiments across multiple physical sites, allowing the exploration of wide-area control, interconnected MGs, and cyber-resilient operation under realistic communication constraints. Within the scope of this thesis, such developments lay the groundwork for advanced HIL-based validation of DC MGs, supporting the comprehensive evaluation of energy management and voltage regulation algorithms under both electrical and communication-layer disturbances.

1.5.1 Categories of HIL Architectures

Within the field of power system analysis, DRTS techniques are typically divided into two main categories: fully simulated (software-based) real-time simulation and HIL-based real-time simulation. The key distinction between these two approaches lies in the degree of hardware integration and the nature of interaction between the virtual and physical domains.

The first category, commonly known as fully DRTS, includes methodologies such as Software-in-the-Loop (SIL), Model-in-the-Loop (MIL), and Processor-in-the-Loop (PIL). In these configurations, the entire system—comprising the power network, control algorithms, and protection mechanisms—is represented and executed entirely within the digital simulation platform. Because no external hardware components are involved, all signal processing and computational activities remain confined to the software environment. This configuration provides a flexible, safe, and computationally efficient framework for algorithm design, early-stage validation, and control logic debugging prior to physical deployment. Consequently, fully DRTS simulations are widely employed during the initial phases of system development, particularly when analyzing supervisory control performance or optimizing energy management strategies in DC MGs.

Conversely, HIL-based real-time simulation incorporates physical components directly into the simulation loop, collectively referred to as the HUT or DUT. In this setup, selected portions of the power system or control hierarchy are substituted with real hardware that exchanges signals with the simulated environment through high-speed input/output (I/O) interfaces. These interfaces typically include signal conditioning circuits, analog-to-digital (A/D) and digital-to-analog (D/A) converters, and filtering or isolation units that guarantee precise and stable communication between the digital simulator and the physical device.

The real-time simulator continuously computes system variables—such as voltages, currents, and control signals—at discrete time steps and transmits these data to the HUT with a frequency sufficient to preserve both stability and dynamic fidelity. External or user-defined disturbances can also be injected during runtime to evaluate specific operating scenarios, including load fluctuations, voltage sags, or short-circuit faults. This closed-loop configuration enables a highly realistic and repeatable testing environment that mirrors actual operating conditions, effectively bridging the gap between digital simulation and physical experimentation.

Over time, multiple HIL architectures have been proposed and refined, each adapted to the characteristics of the target system, the testing objectives, and the computational resources available. Although implementations differ across sectors such as automotive, aerospace, and electric power, the foundational principles remain consistent. In power and energy applications, HIL setups are generally categorized into three main types: Control-Hardware-In-the-Loop (CHIL), Power-Hardware-In-the-Loop (PHIL), and hybrid or multi-domain HIL configurations. These architectures will be further examined in the following section, with particular emphasis on their significance for DC MGs studies and the validation of the energy management and voltage regulation strategies developed in this research.

1.5.1.1 Control Hardware-In-the-Loop Architectures

A Control-Hardware-In-the-Loop (CHIL) configuration represents a specific form of HIL setup in which a real controller operates interactively with a digitally simulated power system running on a DRTS platform. In this arrangement, no actual power transfer occurs between the controller and the simulator; the exchange is limited to low-power analog and digital input/output (I/O) signals. These signals correspond to system variables—such as voltages, currents, switching states, or reference commands—depending on the control algorithm being validated.

Within a CHIL environment, the entire power network, including its constituent electrical components such as converters, loads, and Distributed Energy Resources (DERs),

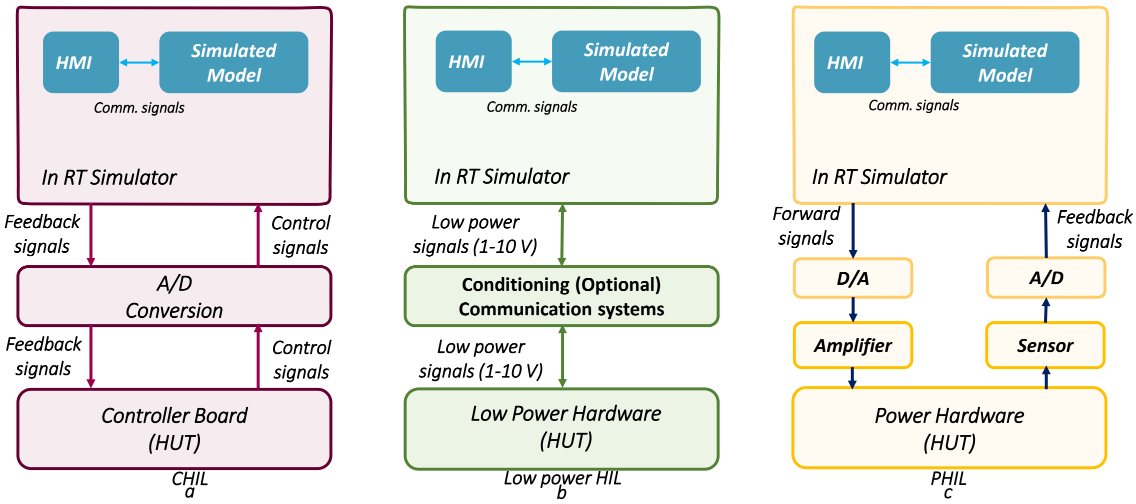

Figure 1.5: Different HIL architectures: (**a**) CHIL architecture. (**b**) Low-power HIL architecture. (**c**) PHIL architecture.

is modeled virtually inside the DRTS. The physical controller, acting as the Hardware Under Test (HUT), is connected to the simulator through dedicated interfacing and signal conditioning hardware. Typical interface components include digital-to-analog (D/A) and analog-to-digital (A/D) converters, isolation amplifiers, and low-pass filters, which ensure precise and stable communication between the virtual system and the physical control hardware. The controller continuously receives simulated measurement signals and transmits control outputs—such as duty cycles, reference voltages, or current limits—back to the simulator in real time.

Through this bidirectional signal-level interaction, the controller perceives the simulated system as a real operating environment. This capability makes the CHIL technique particularly suitable for verifying control algorithms, evaluating embedded hardware performance, and assessing real-time communication behavior under realistic but fully controlled operating conditions. The approach effectively removes the risks and logistical challenges associated with full-scale power testing while preserving high fidelity in control validation.

A visual comparison between the CHIL structure and other HIL configurations—such as Power-Hardware-In-the-Loop (PHIL) or hybrid systems—is typically provided, as illustrated in Fig. 1.5 [22]. In these representations, CHIL can be clearly distinguished by its signal-level interface, whereas PHIL involves physical power exchange between simulated and real components.

To facilitate the selection of an appropriate testing configuration, Table 1.4 presents a comparative summary of the most prevalent HIL architectures. The table outlines key differences in interface characteristics, energy exchange mechanisms, common applica-

Table 1.4: CHIL, Low-power HIL, and PHIL Comparison.

Aspect	CHIL	Low-power HIL	PHIL
Simulation Purpose	Focuses on testing and optimizing control algorithms, usually before the availability of physical instruments.	Validates and analyses proposed algorithms or events using real components under simulated conditions.	Emulates real power system dynamics, components, and interactions.
Application Scope	Used for control algorithm analysis, development, and testing in various aspects.	Applicable to a wide range of power systems engineering domains.	Mainly used for power system and power electronics testing.
Incorporated Hardware	Typically uses lower-power and lower-voltage hardware components.	Includes physical hardware (sometimes reduced-scale) that closely matches actual system components.	Involves actual power components such as generators, transformers, converters, and energy storage systems.
Real-World Interaction	Focuses on RT testing and optimization of control strategies using limited hardware resources.	Simulates the interactions of monitoring, control, or protection algorithms with real or emulated components.	Reflects realistic interactions between power components, allowing accurate analysis of power system behavior.
Complexity of Setup	Setup complexity is generally lower compared to PHIL, due to the focus on control algorithm testing.	Setup complexity depends on the complexity of the proposed algorithms and the required hardware components.	Can be complex due to the integration of real HUT with interface devices and simulation systems.
Use Cases	Ideal for rapid prototyping and early-stage development of control algorithms before the availability of physical instruments.	Suitable for behavior analysis and design algorithm validation in different electrical engineering domains.	Best suited for testing power electronic devices, grid stability, renewable integration into modern grids, and LV/MV power systems.
Resource Requirements (Usually MV-LV applications)	Requires hardware with moderate power for testing and validation of control methods.	Requires components (sometimes scale-down) that sensibly represent the behavior of the actual system.	Requires high-power equipment and specialized hardware for grid emulation, e.g., the amplifier (see Fig. 1.5c).
Flexibility (Compatibility)	Offers flexibility in terms of rapid iteration and optimization of control algorithms.	Flexible in terms of adapting various system configurations and control strategies.	Limited compatibility due to the need to interface with high-power hardware.
Safety	Offers a relatively high level of safety as it interacts with low-power control signals.	Can provide a safe environment for users that is also suitable for training purposes.	Safety cannot be guaranteed since it requires high-power or high-voltage equipment.
Cost Considerations	Generally is a cost-effective option due to the use of lower-power and lower-voltage hardware.	Costs can vary based on the complexity of the hardware components such as HUT, and proposed algorithms.	Typically require higher costs because of the need for high-power and specialized equipment such as amplifiers.

tions, and relative implementation complexity. From a practical standpoint, CHIL offers distinct advantages in simplicity, operational safety, and cost efficiency, making it an optimal preliminary stage for validating the proposed control strategies—particularly those focusing on energy management and voltage regulation within DC MGs.

1.5.1.2 Low-Power Hardware-In-the-Loop Architectures

In this form of HIL configuration, the physical device or HUT exchanges information with the digitally simulated power network through low-power analog and digital signals, as illustrated in Fig. 1.5(b). The RTS continuously transmits and receives these signals, representing key system variables such as voltages, currents, and control references. This real-time exchange enables the component to react to simulated system dynamics as if operating in a physical environment.

In practical implementations, however, the electrical characteristics of the signals exchanged between the simulator and the HUT are not always directly compatible. Differences may arise in voltage or current ranges, logic levels, or signal formats between the hardware and the simulator's I/O interfaces. To ensure accurate and safe communication, signal conditioning hardware is typically inserted between the two systems. Such circuits generally include scaling amplifiers, isolation interfaces, filters, and analog-to-digital or digital-to-analog converters, which align the electrical characteristics and enhance noise immunity, thereby maintaining the fidelity and reliability of the real-time data exchange [5].

In some applications, the HUT may operate at voltage or current levels higher than those natively supported by the simulator's I/O channels. In these cases, power interface modules capable of handling larger signal magnitudes are required. Common examples include two-quadrant (2Q) power amplifiers, which can reproduce voltage levels in the approximate range of 60–200 V and current levels from 5–100 A, depending on the experimental setup. These amplifiers allow the simulated system to excite hardware that demands higher signal levels while preserving real-time synchronization and stability.

Although configurations incorporating such amplifiers technically remain within the low-power signal-based category, the inclusion of power interfaces introduces a limited degree of energy exchange between the simulator and the hardware device. For brevity, the qualifier "low-power" is often omitted in the literature when describing these setups. Nonetheless, the defining feature of this configuration remains the absence of large-scale power transfer, distinguishing it clearly from PHIL systems, which involve direct bidirectional power flow between the simulated and physical domains.

The accurate design of signal conditioning and interface circuits is crucial to ensure proper communication between the real-time simulator and the physical component developed for energy management and voltage regulation in DC MGs. These considerations form the basis for expanding the platform toward PHIL-based validation, enabling comprehensive assessment of converter behavior and power-level interactions under realistic operating conditions.

1.5.1.3 Power Hardware-In-the-Loop Architectures

A Power-Hardware-In-the-Loop (PHIL) configuration, in contrast to HIL setups, enables the inclusion of actual power components—such as batteries, controllable loads, converters, or microgrid subsystems—within the real-time simulation framework. As illustrated in Fig. 1.5(c), this architecture incorporates a power amplifier, typically operating in two- or four-quadrant (2Q or 4Q) mode. Positioned between the RTS and the HUT, the amplifier governs the bidirectional power exchange between the simulated and physical domains.

In this setup, the RTS generates reference or control signals that are delivered to the power amplifier, which, in turn, reproduces the corresponding voltages and currents on the hardware side. The resulting voltage and current responses from the HUT are continuously measured and fed back into the simulator to complete the closed-loop interaction. Through this real-time feedback process, the dynamic behavior of real electrical components—such as DERs, storage units, or loads—can be examined within a controlled and safely simulated network environment.

Moreover, PHIL configurations can be extended to integrate diverse communication interfaces and industrial protocols, including CAN, DNP3, ARINC, and IEC 61850, thereby supporting complex and heterogeneous communication layers within a unified test environment [6, 7]. This capability makes PHIL particularly suitable for testing and validating high-power devices or subsystems under realistic operational and communication conditions [5, 100]. Nevertheless, despite these advantages, certain technical challenges must be carefully addressed to maintain stable and accurate performance.

One of the primary issues arises from the closed-loop time delay between the RTS and the HUT, which can adversely influence system stability if not properly compensated. In addition, as the effective system bandwidth increases, the susceptibility to oscillations and instability tends to rise [6, 100]. These limitations have driven significant research efforts focused on enhancing the precision, robustness, and real-time stability of PHIL platforms. Consequently, various compensation, filtering, and interface algorithms have

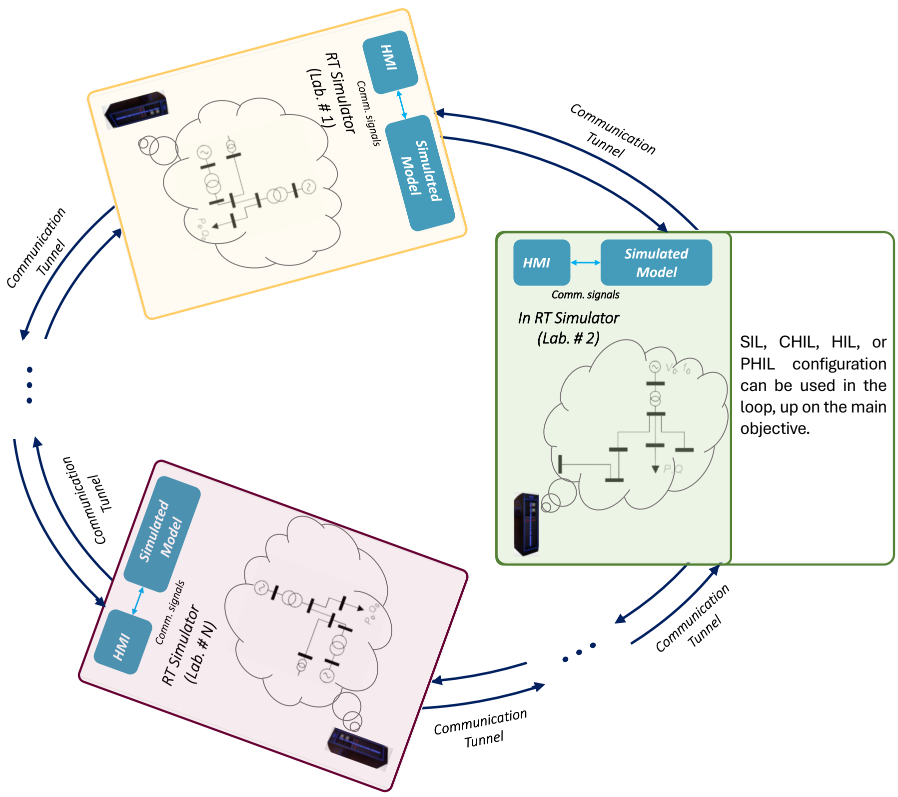

Figure 1.6: Remote architecture, laboratories-in-the-network framework.

been developed and reported in the literature to mitigate delay-induced instability and improve overall system fidelity [5, 101–103].

1.5.1.4 Remote Architecture

It is important to note that the HIL architectures discussed previously can also be implemented in a remote configuration, allowing the testing and validation of real hardware devices located in geographically separated laboratories. This distributed approach enables collaborative experimentation by linking multiple research facilities through a unified “laboratories-in-the-network” framework [103]. Within such a framework, geographically dispersed simulation nodes operate in coordination, allowing institutions to pool their resources and jointly analyze complex power system behaviors that would be difficult to reproduce in isolation. The general concept of this remote architecture is depicted in Fig. 1.6.

Remote HIL configurations are gaining increasing relevance in modern smart power system research. They provide an effective platform for investigating the performance of advanced communication infrastructures that now constitute a fundamental component

Table 1.5: Types of Collaboration of Remote (Laboratories-in-the-Network) Architecture [5–7]

Application	**Description and Purpose**
Model/Data Sharing and Integration	Laboratories would exchange data on various power system aspects in a co-simulation environment to provide a more comprehensive simulation, especially when studying the behavior of large-scale complex systems. This can enhance the realism and reliability of the results.
Facility Sharing	Laboratories could also share their facilities like their measurement instruments or physical electric equipment as HUT. This would be a proper action to avoid constructing expensive fully equipped laboratories.
Testing More Realistic Scenarios	Laboratories can also collaborate to develop and test various scenarios, such as extreme weather conditions or high levels of RES penetration in conventional grids, to explore their impacts and responses more comprehensively.
Coordinated Experiments	Designing and conducting experiments where results from one laboratory's simulations serve as input for another laboratory's model/HUT can pave the way for integrated testing of different system elements.
RT Distributed Analysis	Performing RTS with different components or models provides a suitable platform to analyze the dynamic interactions and time-sensitive events, i.e., allows for a more realistic investigation about how various elements of the grid interact and respond to varying conditions.
Smart Grids Challenges	Remote collaboration in areas such as smart grid integration with communication and IT infrastructure models can facilitate a holistic approach to ensure that interdependencies between power systems and communication networks are fully understood and managed.
Education and Training	Remote educational programs, such as training or workshops can be a proper way to share knowledge and best practices in simulation techniques and tools, enhancing skills and innovation, and also promote collaboration among researchers and practitioners.

of intelligent grid operation. Furthermore, the significant financial and logistical challenges associated with establishing and maintaining fully equipped experimental facilities often limit institutional research expansion. Interconnecting laboratories via high-speed communication links alleviates these constraints by promoting resource sharing, reducing operational costs, and expanding experimental accessibility [100]. Additional examples and applications of remote simulation in power system studies are summarized in Table 1.5.1.4.

From a technical standpoint, implementing a remote HIL setup requires real-time exchange of electrical and control variables between participating laboratories over the Internet while maintaining precise temporal synchronization. To ensure secure and reliable data transfer, Virtual Private Network (VPN) tunnels are commonly employed [6]. Multiple communication protocols can be utilized for this purpose, such as Modbus at the field level and UDP or TCP/IP at the application layer. Together, these protocols enable the continuous and deterministic data transmission necessary for distributed real-time simulation and multi-site hardware testing [101].

1.5.2 Future Trends in the Realm of Modern Grids

DRTS has evolved into an indispensable tool for the study, design, and analysis of modern power and energy systems. Unlike conventional networks, contemporary grids exhibit a much higher degree of interdependence and complexity, primarily resulting from their cyber-physical, multi-domain, and multi-modal characteristics [101]. This section has summarized key developments in DRTS and HIL-based validation approaches, both of which have advanced rapidly in recent years and are now closely aligned with the operational and research needs of emerging power system architectures [5, 102].

Despite these advances, the increasing cyber-physical integration of modern power systems—including DC MGs—calls for further refinement and harmonization in real-time simulation practices. There remains a strong need for standardization across real-time simulation environments and HIL implementation methodologies to improve interoperability, reproducibility, and scalability [22]. At present, most DRTS-based platforms rely heavily on proprietary simulation tools, which constrains model exchange and integration flexibility. Consequently, the development of open and standardized frameworks for simulator coupling, model portability, and hardware interoperability is a research priority to enable comprehensive, cross-domain analysis of power and energy systems. Substantial opportunities therefore exist for continued innovation in this field.

Testing power transmission and distribution equipment at full scale is typically impractical within both industrial and academic laboratories due to the high costs of large-scale testing infrastructure, the financial risks of hardware damage, and the extensive facility requirements. To mitigate these constraints, researchers commonly employ scaled-down prototypes that emulate the essential dynamic characteristics of real systems. While such scaled models effectively reproduce many operational behaviors, conducting full-scale experiments—particularly through PHIL configurations—remains vital for several reasons, summarized below:

- **Scale-Dependent Phenomena:** Certain physical effects in power systems—such as surge voltage gradients, thermal dynamics, current distribution, and electromagnetic interference—depend on system scale and are difficult to reproduce in reduced prototypes [22]. Full-scale testing thus provides a more accurate environment for validating control strategies and ensuring grid stability and performance.

- **Security Challenges:** Modern networks face growing cyber-physical and operational security threats. Full-scale PHIL testing enables the identification and mitigation of vulnerabilities by analyzing the interaction between real hardware and control systems under realistic operating conditions.

- **Complex Interactions:** Power systems comprise multiple interconnected subsystems—such as converters, transformers, and protection devices—that influence one another dynamically. Testing at real scale allows these coupled effects to be accurately captured, which is crucial for optimizing system coordination and stability.

- **Scalability:** As power infrastructures evolve, scalability becomes a fundamental design requirement. Full-scale validation ensures that system expansions and new technology integrations—such as advanced converter topologies or energy management units—can be implemented reliably within DC MGs frameworks.

- **Unexpected Conditions:** Full-scale testbeds provide a means to evaluate system resilience under abnormal or extreme events, including grid faults, blackouts, or adverse weather conditions. Such testing facilitates the development of robust control and protection schemes for enhanced operational security.

- **Informed Decision-Making:** Data obtained from full-scale testing offer high-fidelity insights into system efficiency, reliability, and control performance. These results form the basis for well-informed decisions in design optimization and long-term system planning.

- **Regular Testing and Validation:** Routine verification of protection schemes, control systems, and special functions—such as black-start capability, load-shedding coordination, or Wide-Area Monitoring and Control (WAMPAC)—is essential for maintaining grid reliability. These functionalities can be evaluated within a controlled PHIL environment without jeopardizing actual grid infrastructure.

Selecting an appropriate scale for the HUT requires careful consideration of both modeling accuracy and implementation cost. This trade-off determines whether a scaled prototype or a full-scale device should be utilized. Although establishing PHIL-based infrastructure involves significant upfront investment, it often results in long-term savings and reliability improvements by allowing early detection of design or control flaws in a safe environment. Such proactive validation minimizes costly failures and increases confidence in deploying novel control strategies and equipment in real networks.

Given the growing complexity and expansion of modern energy systems, further investment in advanced laboratory infrastructure is essential to achieve realistic, high-fidelity validation. One promising direction to improve cost-effectiveness and flexibility is the development of mobile, full-scale PHIL units, which can be transported between research facilities for collaborative testing. Alternatively, existing installations—such as STATCOM units—may be reconfigured to operate as PHIL testbeds when not engaged in grid service.

Advancements in DRTS and PHIL technologies are fundamentally reshaping the process of power system validation. These methodologies serve not only to enhance current testing capabilities but also to provide the foundation for the next generation of DC MGs—systems that demand accurate, scalable, and cyber-secure real-time evaluation to ensure dependable energy management and voltage regulation under practical operating conditions.

DC technology plays a pivotal role in facilitating renewable energy integration and improving the reliability and security of modern grids, particularly under complex operational conditions. With continuous advancements in power electronic devices capable of operating at higher voltage and power levels, several critical research areas have emerged within the DC domain [102]. Among these, the development of advanced testing methodologies—especially PHIL techniques—has gained notable importance for investigating complex phenomena such as breaker–network interactions during transient and fault conditions [6].

Practical studies on DC converters' behavior, particularly during high-current interruption events, have also become increasingly significant [7, 100, 102]. Extending the applicability of medium-voltage components to higher voltage domains, whether through improved materials, series connection strategies, or their integration into multilevel converter structures, represents another key research frontier. As the deployment of DC systems accelerates, ensuring the reliability and longevity of power electronic components through condition monitoring and health assessment techniques has become essential [103].

Although numerical simulations provide an economical means of analysis, their accuracy is inherently limited by model assumptions and numerical constraints. Conversely, scaled-down experimental setups offer realistic insights but cover only a narrow range of scenarios. In this context, PHIL testing serves as an effective middle ground, combining physical hardware fidelity with simulation flexibility to achieve comprehensive and accurate validation of DC systems.

Future research on the interaction between RESs, particularly PV generation, and BESS with DC converters is expected to emphasize more accurate and adaptive modeling of RES generation and ESS. Key directions include the incorporation of pitch-angle control for variable solar irradiation conditions and the development of refined solar profile models for enhanced dynamic accuracy [102]. Moreover, aggregated PV arrays representations are anticipated to replace individual unit models to alleviate computational complexity, while modular multilevel and twin-converter topologies will continue to evolve for advanced grid modeling [22].

In the domain of electrothermal analysis of DC systems and power electronic converters, numerous research opportunities remain open [5]. These include the creation of detailed electrothermal models, innovative cooling and thermal management methods, and real-time integration of thermal behavior within control algorithms. Long-term objectives involve improving device reliability assessments, developing real-time thermal simulation techniques, and evaluating the impacts of thermal degradation on converter operation [6].

The inclusion of online thermal monitoring and continuous model validation—together with the consideration of human-in-the-loop decision-making in operational thermal management—will be vital for achieving resilient and efficient DC networks [104]. Coupling electrothermal modeling with HIL-based platforms provides a powerful means for real-time condition assessment and lifetime estimation of power electronic components in

DC-MGs environments.

The integration of Phasor Measurement Unit (PMU) technology is transforming real-time monitoring and control in electrical networks. PMUs provide time-synchronized measurements that enhance situational awareness, enabling operators to make informed and rapid control decisions. The growing deployment of PMUs across utilities highlights their pivotal role in the digital transformation of power grids. However, the full exploitation of PMU data introduces challenges related to large-scale data management, synchronization accuracy, visualization, and interpretation.

One major challenge is achieving seamless integration between PMU data streams and traditional Supervisory Control And Data Acquisition (SCADA) systems. While such integration promises improved coordination and situational awareness, achieving interoperability across multiple vendor platforms demands considerable technical and organizational alignment. Importantly, the use of PMUs is expanding beyond transmission networks into distribution domains, where they can be incorporated into Distribution Management Systems (DMSs) to support localized monitoring and control functions.

Current research efforts are focused on developing standardized WAMPAC frameworks that enhance reliability and system resilience. As power systems become increasingly data-driven and dynamic, PMUs are emerging as core elements of intelligent grid architectures. Consequently, conducting real-time HIL-based testing is essential for validating PMU performance under realistic operating conditions, including dynamic events and system faults. Such experiments provide critical insight into measurement accuracy, communication latency, and data processing performance in real-time scenarios.

The deep integration of communication networks within modern smart grids introduces inherent cybersecurity vulnerabilities that can compromise protection schemes and operational reliability. Cyberattacks may manifest as data breaches, eavesdropping, credential exploitation, or false data injection—potentially coordinated across multiple network layers and time frames.

Ensuring the security and resilience of cyber-physical power systems therefore requires a comprehensive, multi-layered approach encompassing prevention, detection, mitigation, and recovery strategies. The design and validation of such cybersecurity frameworks must occur within realistic, real-time experimental environments that accurately represent both the physical and communication layers. In this regard, HIL and DRTS platforms are invaluable tools for studying system vulnerabilities, testing defense mechanisms, and developing resilient control architectures capable of maintaining grid stability even under cyberattack scenarios.

1.6 Summary of the Chapter

This chapter provided an overview of the evolution, operation, and control of microgrids, focusing on isolated DC configurations. It began by highlighting the global shift toward RESs, driven by decarbonization goals and EU energy policies, positioning microgrids as key enablers of localized, reliable, and sustainable energy systems.

The main characteristics and classifications of microgrids were outlined, emphasizing DC configurations for their efficiency, simplified control, and compatibility with renewable and storage technologies. The hierarchical control structure—primary, secondary, and tertiary—was examined with respect to their objectives, timescales, and control paradigms.

The chapter addressed challenges specific to Mediterranean islands, including fossil fuel dependence and infrastructure limitations, while noting the potential of solar and offshore PV technologies for decarbonization. Droop-based control was discussed as a core method for proper voltage regulation and current sharing, with advanced adaptive and communication-assisted strategies enhancing scalability and resilience.

Finally, HIL testing was introduced as a key validation tool, enabling real-time assessment of control algorithms and bridging theory with practice.

Overall, this chapter established the conceptual, regulatory, and technological foundations necessary for the subsequent research on cooperative control and real-time validation of isolated DC microgrids.

Chapter 2

Flexibility Resources for Stand-Alone Microgrids

This chapter begins with a comprehensive examination of the conceptual foundations and definitions of flexibility, emphasizing its pivotal role in the operation of islanded DC microgrids with penetrations of renewable energy sources. It establishes flexibility as a measurable and controllable attribute that enables microgrids to sustain stability, reliability, and optimal performance under variable and uncertain conditions. Building upon this theoretical basis, the chapter proceeds to classify various Energy Storage Systems (ESSs), which act as primary enablers of flexibility by delivering rapid and adaptive responses to power imbalances. Finally, it introduces the concept of the DC-Electric Spring (ES)—an emerging technology aimed at enhancing system flexibility through instantaneous deployment of load and ESSs.

2.1 The Concept of Flexibility Resources

2.1.1 Definition and Terminology

In modern power systems, microgrids have emerged as a cornerstone for integrating distributed renewable energy sources Renewable Energy Source (RES) and enhancing local energy resilience. However, the growing share of variable RES such as photovoltaic (PVs) introduces substantial variability and uncertainty in power supply, particularly when microgrids operate in islanded mode. Unlike grid-connected operation, islanded microgrids lack external grid support to balance generation and demand, making operational flexibility a critical requirement for maintaining voltage stability, power quality, and supply reliability [105].

In DC microgrids, where energy conversion stages are minimized and system dynamics are inherently rapid due to the lack of high inertia, the need for fast and adaptive flexibility mechanisms becomes even more pronounced. In this context, flexibility refers to the capability of the microgrid to dynamically adjust its generation, storage, and demand in real time in response to fluctuations and disturbances. This adaptability is typically achieved through the coordinated control of Distributed Energy Resources (DERs), Energy Storage Systems (ESSs), and flexible loads, supported by advanced control architectures and energy management strategies.

At the broader system level, the increased integration of intermittent RES across power networks has amplified the demand for flexibility resources and technologies. Flexibility is essential to cope with the inherent uncertainty and variability of renewable generation. While early studies primarily focused on operational reserves to manage short-term fluctuations in variable Renewable Energy Sources (RESs), recent research has expanded the concept to encompass a wider range of challenges, uncertainties, and resources.

Moreover, the islanded grid faces an additional challenge: the usual percentage increase in peak load demand often exceeds that of overall energy demand. As a result, infrastructure designed to meet peak load conditions remains underutilized for much of the times. This situation underscores the importance of deploying flexibility resources as cost-effective alternatives to traditional network reinforcement and expansion.

Over the past decade, flexibility resources have been extensively investigated from multiple perspectives—including the intermittent nature of RES integration, distributed generation, technological solutions, ancillary services, market mechanisms, system operational needs, and the security of electricity supply. So, understanding, defining, and categorizing these flexibility resources is therefore vital not only for enhancing the operational resilience of microgrids but also for enabling optimized planning, techno-economic assessment, and the integration of ancillary services within energy systems.

The concept of "*flexibility*" in power systems requires careful semantic consideration to ensure a unified understanding across research, policy, and industrial practice. Establishing a clear conceptual foundation is essential, given the wide range of contexts in which flexibility is discussed—spanning generation and demand balancing, grid operation, and market participation [106].

According to the *Oxford English Dictionary*, flexibility is defined as “the ability to change to suit new conditions or situations” [23]. In the context of power systems, this implies the capacity to adapt to uncertain or evolving conditions arising from fluctuations in generation, variations in demand, or unforeseen system disturbances. Although future operating conditions may be inherently uncertain, flexibility represents the means by which a system can effectively manage and respond to this uncertainty.

Building upon this interpretation, flexibility in DC microgrids can be viewed not merely as a qualitative characteristic but as a quantifiable and controllable resource. It manifests through the adaptive coordination of Distributed Generation (DG) units, Energy Storage Systems (ESSs), and controllable loads to maintain power balance, voltage regulation, and overall system stability under static and dynamic operating conditions. Consequently, flexibility serves as a core element of energy management frameworks, enabling DC-MGs to respond proactively to the variability and uncertainty associated with renewable generation and stochastic load behavior[81].

Despite widespread use of the term, definitions of flexibility in the literature vary substantially in scope and focus, reflecting the differing priorities of system operation and technology providers. To promote conceptual clarity and harmonization, three fundamental criteria have been identified as essential to any inclusive definition of flexibility:

- **Type of Flexibility Resource:** The definition should encompass all potential sources of flexibility, including both user-side resources (such as controllable loads, and energy storage) and distributed generation resources.

- **Duration of Flexibility Activation:** Flexibility generally refers to a short-term or time-limited capability to alter operation—typically over timeframes ranging from milliseconds to several hours—in response to system needs. It excludes long-term structural measures, such as network reinforcement or energy-efficiency improvements.

- **Incentive for Activation:** Flexibility should be interpreted as a response to an external signal or service request, rather than an autonomous or passive adjustment. This distinction ensures that flexible behavior contributes meaningfully to system-level coordination. For instance, a battery operating solely for self-consumption optimization may exhibit flexible dynamics but does not qualify as a system flexibility provider unless it responds to external control or market signals.

Several international organizations have proposed formal definitions of power system flexibility based on these principles. Representative examples include [105]:

- **CIGRÉ WG (1995):** "The ability to adapt the planned development of the power system, quickly and at reasonable cost, to any change, foreseen or not, in the conditions which prevailed at the time it was planned."
- **EPRI (2016):** "The ability to adapt to dynamic and changing conditions, for example, balancing supply and demand by the hour or minute, or deploying new generation and transmission resources over a period of years."
- **IRENA (2018):** "The capability of a power system to cope with the variability and uncertainty that intermittent renewable energy generation introduces into the system in different time scales, from the very short to the long term, avoiding curtailment of Variable RES and reliably supplying all demanded energy to customers."
- **IEA (2019):** "The ability of a power system to reliably and cost-effectively manage the variability and uncertainty of demand and supply across all relevant timescales, from ensuring instantaneous stability to supporting long-term security of supply."

While these definitions provide valuable insights, many remain limited in either temporal scope or system perspective. To improve previous definitions, [23, 107] proposed an enhanced and unified definition that captures the full conceptual breadth of flexibility across technical, operational, and temporal domains:

> *"The ability of power system operation, power system assets, loads, energy storage assets, and generation units to change or modify their routine operation for a limited duration, in response to external service request signals, without inducing unplanned disruptions."*

In this dissertation, any entity possessing such a capability—whether a controllable source, responsive load, or energy storage unit—is referred to as a *flexibility resource*. This generalized definition provides a consistent basis for analyzing flexibility provision, coordination, and energy management strategies in islanded DC-MGs, where adaptive operation is essential for ensuring stability, reliability, and optimal resource utilization.

It should be noted that, although the concept of flexibility spans multiple domains—including grid operation, market participation, and system planning—the primary focus of this dissertation is on supply and demand balancing within isolated DC microgrids. This focus aligns with the overarching objective of enhancing power balance and security in autonomous DC energy systems, where internal coordination among distributed resources is vital for maintaining resilient and reliable operation [108]. It is worth stating that the broader concept of flexibility that extends far beyond this scope—encompassing dimensions such as market participation, system planning, etc, can be explored in [105].

Several terms are often confused or used interchangeably with *flexibility*, including Demand-Side Response (DSR), Demand-Side Management (DSM), flexible generation, and energy storage on both the supply and demand sides. However, these terms represent only specific subsets of the broader flexibility concept and should not be regarded as equivalent [23, 105]. In [106], DSM is defined as the set of actions such as energy efficiency, energy savings, self-production, and load management. Within this framework, load management techniques and DSR programs are considered specific DSM solutions [109].

Beyond behavioral and temporal aspects, flexibility resources are characterized by their ability to respond to external service requests in terms of volume, timing, availability, and cost. Moreover, their post-provisioning behaviors—such as recovery time and rebound effects—play a key role in determining their practical usefulness for grid operation. Accurate characterization and classification of flexibility resources are, therefore, essential for developing quantitative models that capture their operational capabilities within energy management frameworks.

2.1.2 Taxonomy of Flexibility Resources

The literature presents several approaches for **classifying flexibility resources**, each emphasizing different physical, functional, or modeling aspects. The most common classification dimensions are summarized as follows [105]:

- **Based on position in the electricity suppliers:** Classifies flexibility resources according to their placement within the power system, such as demand-side, supply-side, and network-side flexibility. In demand-side flexibility, end-use consumption patterns and magnitudes are modified through actions such as load shifting, demand curtailment, or controlled scheduling. Supply-side flexibility refers to measures that enable generation units to dynamically adjust their output in response to system needs, thereby supporting real-time power balancing and stability. Network-side flexibility encompasses adaptability originating from the power system infrastructure itself, including network reconfiguration, dynamic line ratings, or wide-area interconnections that enhance operational responsiveness. Finally, other sources of flexibility include ESSs, market mechanisms, and regulatory instruments designed to strengthen overall system adaptability and resilience.

- **Based on functional role in the power system:** Differentiates between actual sources of flexibility—such as generation, load, and storage units that can directly provide flexibility services—and enabling mechanisms, which include grids and potential communication infrastructures that coordinate and facilitate the effective utilization of these flexible resources. In other words, a related distinction can be drawn between technical flexibility, referring to the physical or technological capability of a system to respond to rapid variations in net load, and operational flexibility, which denotes the ability to mange and coordinate assets efficiently within system or economic aspects.

- **Based on direction of load shifting:** Categorizes flexibility resources according to whether they advance, delay, or reduce load consumption, encompassing actions such as load shifting, shedding, and rescheduling. In advance load consumption, electrical loads (include electric storage heaters and water heaters) are operated earlier than their typical schedule to manage energy use or respond to system needs. Delay load consumption refers to the postponement of energy use to periods of lower demand or higher renewable generation availability, as seen in refrigeration, ventilation, and air-conditioning systems. In some cases, loads can be flexibly shifted in either direction—advance or delay load consumption—such as in cold storage units, washing machines, or industrial paper machines, where operational timing can be manipulated without compromising process requirements. Finally, load shedding represents a direct reduction in electricity consumption, typically employed in energy-intensive industries, to provide rapid system support during periods of stress or imbalance.

- **Based on mathematical modeling characteristics:** This perspective focuses on how flexibility resources are represented in analytical or simulation models, particularly in relation to their energy and power constraints. In some cases, the system is modeled as a power- and energy-constrained integrator, typically representing thermal storage, air-conditioning units, or refrigeration systems. Battery-type resources refer to energy-constrained systems that must be charged or discharged within predefined temporal limits, such as electric vehicles or swimming pool filtration systems. Other type of resources may correspond to batch processes that operate at a constant power level and must be completed within a specific time window, as exemplified by large industrial production lines.

- **Based on Availability:** This classification distinguishes flexibility resources based on whether they are fully available and dispatchable assets that can respond to external service requests in real time.

Building upon the unified definition of flexibility introduced earlier and the classifications discussed above, a comprehensive framework for categorizing flexibility resources has been proposed. Table 2.1 summarizes the various groups of flexibility resources identified across the reviewed literature. It should be noted, however, that the underlying classification principles in the cited works are not always explicitly stated, leading to overlap among categories. Consequently, certain resources may appear in multiple groups depending on their technical or operational characteristics. The proposed framework aims to reduce such ambiguities, offering a coherent and unified structure for analyzing and modeling flexibility provision in islanded DC microgrids.

It is worth emphasizing that among the various categories of flexibility resources, ESSs emerge as the most effective and versatile solution for achieving real-time power balancing and enhancing operational security in islanded DC microgrids, particularly those of small scale. Unlike demand-side or generation-based flexibility, which typically depend on user behavior or resource availability, ESSs provide direct, controllable, and bidirectional energy exchange capabilities that enable immediate and precise responses to power fluctuations. Their high controllability, independence from generation or load dynamics, and ability to absorb surplus energy during periods of excess generation and release it during deficits collectively ensure continuous power balance, voltage stability, and supply reliability—all of which are essential for systems operating without external grid support. Furthermore, ESSs play a pivotal role in bridging temporal mismatches between generation and demand, mitigating transient disturbances through their rapid charge–discharge dynamics, and enhancing overall system resilience and reliability. Consequently, ESSs constitute the cornerstone of flexibility provision and energy management in autonomous DC microgrids, directly contributing to the improvement of power quality, stability, and supply security. The following section therefore presents a comprehensive classification of ESSs, highlighting their types, characteristics, and specific roles in enabling flexible, stable, and secure DC microgrid operation.

Table 2.1: Classification of flexibility resources applicable to DC microgrids

Flexibility resource	Sub-groups / examples	References	Comments
Energy storage systems (ESS)	• Pumped hydro • Redox flow batteries • Advanced capacitors / supercapacitors • Superconducting magnetic energy storage (SMES) • Flywheels • Chemical storage (e.g., batteries) • Mechanical storage • Hydrogen systems • Thermal storage	[105, 106, 109]	Charge and discharge rates vary across technologies, determining their service suitability. Electric vehicles (EVs) can also serve as *mobile* storage units, though they are often omitted from conventional ESS classifications.
Demand-side response (DSR)	• Shiftable household loads (e.g., laundry, dishwasher, dryer) • Air-conditioning systems • Commercial refrigeration • Heat pumps • Thermal storage for space and water heating	[105, 106]	DSR involves modifying consumption from its normal pattern in response to price signals or incentive schemes (e.g., during high wholesale prices or reliability events). Heating and cooling loads are particularly suitable due to their inherent thermal inertia.
Distributed energy resources (DER)	• Photovoltaic (PV) generation • Wind generation • Micro-CHP units	[107, 109]	DERs may also be categorized as distributed generation (DG). Some DERs are dispatchable, while ESS and DSR can also be treated as DERs in certain contexts.
Load sector	• Residential / households • Industrial • Tertiary / service sector	[81, 108]	Partially overlaps with the "Customer types" group.
Customer types	• Industrial customers • Commercial and non-residential customers • Residential customers • Electric transport • Data centers	[23, 105]	Data centers may also be grouped under commercial customers. EVs act as mobile loads with embedded energy storage and are not standalone customer types: home charging fits residential, while public charging stations fit commercial categories. The broader term "electric transport" is sometimes used.

2.2 The Role of Energy Storage Systems

As mentioned in the previous section, in addition to uncertainties in the demand profile, relying on RESs for energy provision in MGs introduces significant challenges due to their inherent variability and intermittency—particularly during islanded operation—which can adversely affect system stability and reliability. Consequently, there is a growing need for enhanced flexibility to ensure stable and resilient microgrid performance. This section discusses the critical role of ESSs in mitigating the variability of RESs, supporting voltage stability, and enabling temporal energy shifting to balance generation and demand.

2.2.1 Classification of Energy Storage System Technologies

ESS technologies have undergone substantial development over recent decades and can be classified according to multiple criteria, including storage capacity, operational function, lifecycle characteristics, and response time. Fig. 2.1 illustrates a comprehensive classification of ESS technologies based on their underlying energy form, namely electrical, electrochemical, mechanical, chemical, and thermal. Each category encompasses specific storage technologies that operate according to distinct physical principles and energy conversion mechanisms.

From a functional standpoint, ESS technologies can be broadly grouped into the following four categories:

- Electrical and Electrochemical Energy Storage Systems
- Mechanical Energy Storage Systems
- Chemical Energy Storage Systems
- Thermal Energy Storage Systems

Each category exhibits unique operational characteristics, performance advantages, and limitations, rendering them suitable for different applications within power systems. In particular, within DC microgrids, ESS technologies play a crucial role in maintaining system stability, improving energy efficiency, and providing fast bidirectional power exchange to support voltage regulation, load balancing, and renewable energy integration. Their selection and sizing depend on the specific application requirements, including response time, power-to-energy ratio, and cost-effectiveness.

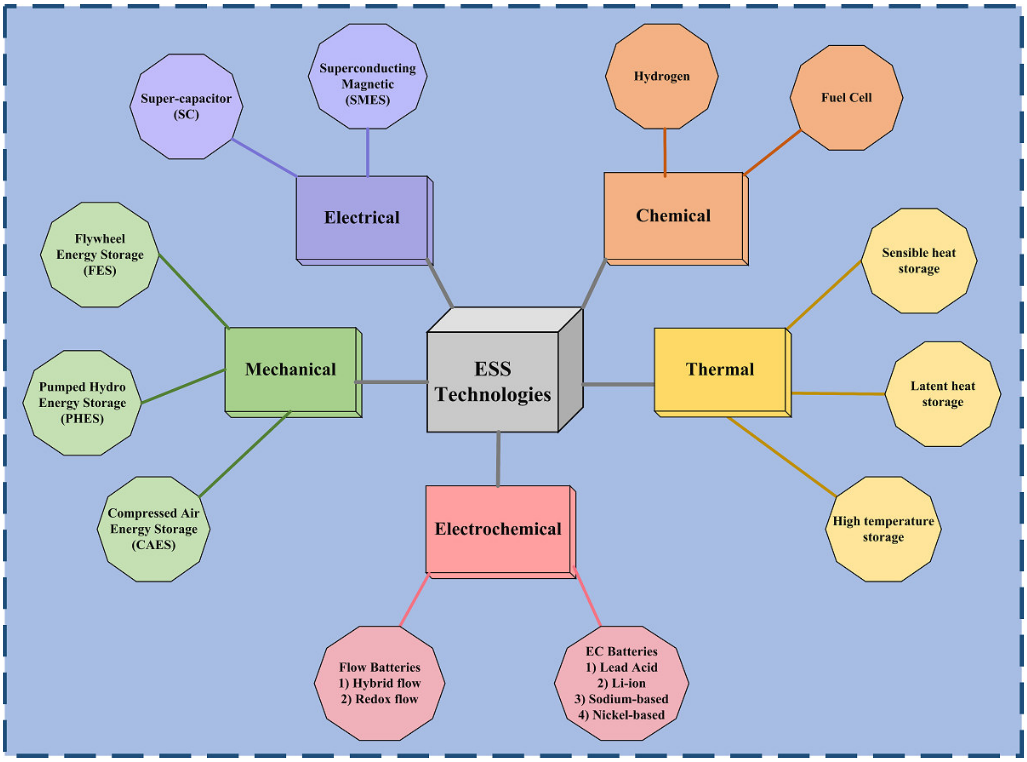

Figure 2.1: Classification of different ESSs.

2.2.1.1 Electrical and Electrochemical Energy Storage

Electrical and electrochemical Energy Storage System (ESS) technologies encompass a wide range of devices capable of storing and releasing electrical energy through electrostatic or electrochemical conversion mechanisms, respectively. Within this category, batteries and Supercapacitors (SCs) represent the two most prominent technologies, each governed by distinct physical principles, dynamic characteristics, and application domains. Batteries operate based on reversible redox reactions that convert chemical energy into electrical energy, whereas SCs store charge electrostatically at the electrode–electrolyte interface. The complementary nature of these technologies makes them indispensable components of modern DC-MGs, where both fast transient support and long-term energy balancing are required.

Superconducting Magnetic Energy Storage (SMES): These systems represent an advanced form of EES that store electrical energy directly in the magnetic field generated by a superconducting coil. The coil operates below its critical temperature and is maintained in the superconducting state through cryogenic cooling, thereby eliminating resistive losses and enabling near-perfect energy retention.

SMES systems exhibit energy densities typically in the range of 0.5–5 Wh/kg and power densities up to 5000 W/kg, positioning them among the highest power-density storage technologies currently available. They offer extremely fast response times—on the order of milliseconds—and very high round-trip efficiencies between 90–95%. Their self-discharge rate is almost negligible (below 0.1% per day), and they demonstrate long operational lifetimes exceeding 20 years, owing to the absence of significant degradation mechanisms common to electrochemical systems.

These characteristics make SMES units particularly suitable for applications requiring instantaneous energy delivery, such as power-quality enhancement, voltage sag mitigation, and transient stability support in DC MGs. The ability to deliver large bursts of power with minimal delay enables SMES to effectively complement slower, energy-dense storage technologies such as batteries or SCs. However, despite their superior dynamic performance and efficiency, the high infrastructure and maintenance costs associated with cryogenic refrigeration systems and superconducting materials currently restrict their deployment to niche, high-value applications, including industrial plants, research facilities, and critical defense infrastructures.

Future advancements in High-Temperature Superconducting (HTS) materials and cryogenic system miniaturization are expected to enhance the techno-economic feasibility of SMES integration within distributed and hybrid DC MGs, further expanding their role in high-performance power stabilization and grid-support operations.

Supercapacitor (SC): These technologies belong to the class of EES devices that store energy through charge separation at the interface between a high-surface-area electrode and an electrolyte. Unlike conventional capacitors, which rely on a solid dielectric medium between two conductors, SCs employ an electrolytic solution that enables the formation of electric double layers and, in certain chemistries, additional pseudocapacitance through faradaic reactions. The combination of these mechanisms significantly increases the effective capacitance and, consequently, the energy storage capability of the device.

The use of highly porous carbon-based electrodes provides exceptionally large surface areas, allowing SCs to achieve capacitance values several orders of magnitude higher than those of traditional capacitors. As a result, SCs exhibit outstanding power density—typically in the range of 1–10 kW/kg—and fast dynamic response on the order of milliseconds. Their specific energy, however, remains relatively low (1–10 Wh/kg), which confines their operation to short-term energy applications. SCs also offer high round-trip efficiencies (95–98%), long cycle life (exceeding 50,000 cycles), and excellent reliability [110]. Owing to these characteristics, SCs are particularly well-suited for applications requiring short-term energy buffering, voltage stabilization, and transient power support within DC MGs.

Despite these advantages, their low energy density and high self-discharge rate limit their use as standalone storage devices [111]. Consequently, SCs are often integrated into Hybrid Energy Storage System (HESS) alongside batteries, where they handle rapid power transients and mitigate current stress on battery units. This complementary configuration enhances system stability, lifetime, and overall efficiency in DC MGs.

Lead–Acid Batteries: Lead–acid batteries are among the most mature and commercially established Electrochemical Energy Storage (EcES) technologies. They exhibit moderate energy densities in the range of 30–50 Wh/kg, power densities of approximately 150–400 W/kg, and round-trip efficiencies between 70–90% [112, 113]. Owing to their simplicity, robustness, and relatively low capital cost, they have been widely adopted in backup power systems, off-grid installations, and small-scale DC networks.

However, their limited cycle life (500–2000 cycles), poor deep-discharge tolerance, and environmental concerns related to lead and sulfuric acid constrain their large-scale sustainability. As a result, their role in modern DC MGs is increasingly limited to auxiliary or standby functions rather than primary system support.

Lithium-Ion Batteries: Lithium-ion (Li-ion) batteries have emerged as the dominant ESS technology due to their high energy density (100–265 Wh/kg), high power density (250–340 W/kg), and superior round-trip efficiency (95–98%). Their electrochemical operation is based on the reversible intercalation and deintercalation of lithium ions between a graphite anode and a lithium metal oxide cathode.

Li-ion systems exhibit fast dynamic response times (milliseconds to seconds) and long cycle life (2000–10,000 cycles), making them particularly suitable for voltage regulation, energy balancing, and frequency support in DC MGs [114, 115]. Although their initial cost and thermal management requirements remain challenges, ongoing advances in cell chemistry and battery management system (BMS) continue to enhance their safety and longevity, consolidating their role as a key enabling technology in high-performance microgrid architectures.

Sodium–Sulfur Batteries: Sodium–Sulfur (Na–S) batteries operate at elevated temperatures (typically 300–350 °C) and utilize molten sodium as the anode and molten sulfur as the cathode, separated by a solid ceramic electrolyte. Compared with conventional lead–acid batteries, Na–S systems offer significantly higher energy and power densities, longer cycle life, and lower maintenance requirements [116].

Their high round-trip efficiency, deep-discharge tolerance, and strong energy-retention characteristics make Na–S batteries well suited for medium- and large-scale stationary storage applications, particularly for renewable energy integration and long-duration energy management in MGs. However, their elevated operating temperature introduces additional complexity in terms of thermal insulation, safety, and system cost, necessitating advanced containment and protection mechanisms for reliable and safe operation.

Nickel-Based Batteries: Nickel-based batteries—including Nickel–Cadmium (Ni–Cd) and Nickel–Metal Hydride (Ni–MH) types—are characterized by moderate energy densities (50–75 Wh/kg), power densities of 150–300 W/kg, round-trip efficiencies around 65–75%, and cycle lives ranging from 1000 to 3500 cycles [117]. Their robustness, wide temperature tolerance, and low self-discharge rates enable reliable operation in demanding environmental conditions.

Nevertheless, their lower energy density compared to Li-ion systems, coupled with the toxicity of cadmium and relatively high cost, has led to a gradual decline in their use for mainstream applications. While Ni–MH variants alleviate some environmental issues, they still lag behind Li-ion technologies in terms of performance and economic viability for next-generation DC MGs.

Vanadium Redox Flow Batteries: Vanadium Redox Flow (VRF) batteries are a prominent category of flow-based electrochemical storage systems that store energy in liquid electrolytes containing vanadium ions of varying oxidation states. They offer specific energy values typically ranging from 20–35 Wh/kg, power densities of 100–150 W/kg, and round-trip efficiencies of 70–85% [118, 119]. Their response times are rapid (less than one second), and their cycle life can exceed 13,000 cycles due to minimal degradation of active materials.

VRF batteries enable the independent scaling of power and energy capacity through separate sizing of the electrochemical stack and electrolyte tanks. This modularity, combined with deep discharge capability and operational safety from non-flammable aqueous electrolytes, makes them highly suitable for long-duration energy management, renewable integration, and voltage stabilization in DC MGs.

2.2.1.2 Mechanical Energy Storage Systems

Mechanical Energy Storage System (MESS) store energy in the form of kinetic, potential, or compressed air energy, which can later be converted back into electrical energy when required. These systems are generally characterized by high power capability, long service life, and fast dynamic response, making them particularly suitable for frequency regulation, transient stability enhancement, and short-term energy balancing in hybrid DC MGs. However, their practical deployment is often constrained by geographical, spatial, or cost-related factors. The most common MESS technologies include Flywheel Energy Storage System (FESS), Pumped Hydro Energy Storage System (PHESS), and Compressed Air Energy Storage System (CAESS).

Flywheel Energy Storage Systems: FESS store energy in the form of rotational kinetic energy using a high-speed rotating mass driven by an integrated motor–generator unit. The stored energy is given by:

$$E = \frac{1}{2} J\omega^2 \tag{2.1}$$

where J is the moment of inertia and ω is the angular velocity.

FESS typically exhibit an energy density of 5–100 Wh/kg, power density between 500–5000 W/kg, and capital costs ranging from 250–2000 €/kW. Their response time ranges from milliseconds to a few minutes, and they experience a self-discharge rate of approximately 20–100% per day, primarily due to bearing and windage losses. FESS units typically operate with round-trip efficiencies between 0.85–0.95 and lifetimes of 15–20 years.

To minimize losses, modern flywheel systems use magnetic bearings and vacuum chambers, allowing high-speed operation (up to tens of thousands of rpm) with minimal friction. The use of composite materials enhances the rotational strength-to-weight ratio. These features grant FESS exceptionally high power density, rapid charge/discharge capability, and long cycle life, making them ideal for power-quality improvement, voltage stabilization, and transient support in DC MGs. However, their low energy density and high self-discharge limit their applicability for long-term storage, confining their use mainly to short-term buffering and dynamic compensation.

Pumped Hydro Energy Storage Systems: Pumped Hydro Energy Storage System (PHESS) represent the most mature and widely implemented large-scale mechanical storage technology. They store energy as gravitational potential energy by pumping water from a lower reservoir to a higher one during periods of low demand and generate electricity when water is released through turbines during peak load periods.

PHESS systems have an energy density of 0.5–1.5 Wh/kg, a power density of 0.5–2 W/kg, and capital costs between 1000–5000 €/kW. Their response time is on the order of minutes, self-discharge is negligible, round-trip efficiency lies between 0.70–0.85, and system lifetime can exceed 40 years.

Owing to their high efficiency, long lifespan, and ability to store energy on a gigawatt-hour scale, PHESS units play a crucial role in peak shaving, load leveling, and grid stabilization. Nevertheless, their implementation is limited by geographical requirements—specifically the need for large elevation differences and substantial water storage capacity—and by long construction times and environmental impacts. Consequently, their integration into MGs is typically indirect, through coupling with other distributed storage or renewable systems.

Compressed Air Energy Storage Systems: Compressed Air Energy Storage System (CAESS) store energy by compressing air into large underground caverns or high-pressure tanks during off-peak hours and releasing it during peak demand to drive turbines for power generation.

CAESS offers an energy density of 2–6 Wh/kg, a power density of 50–150 W/kg, and capital costs between 400–800 €/kW. The response time typically spans from minutes to several hours, with self-discharge losses below 1% per day and round-trip efficiencies ranging from 0.65–0.85. The system lifetime is approximately 20–40 years, depending on configuration and operating pressure.

Traditional CAESS designs rely on gas combustion for air heating during expansion, which decreases overall efficiency and increases emissions. Advanced adiabatic and isothermal CAES configurations eliminate or recover thermal energy, improving efficiency and environmental performance. Although these systems provide long-duration storage capacity and grid-scale flexibility, their large infrastructure requirements and site dependency restrict deployment in small-scale or urban DC MGs. However, when integrated with fast-response storage devices—such as BESS or SC—they can significantly enhance hybrid system reliability and energy management efficiency.

2.2.1.3 Chemical Energy Storage Systems

Chemical Energy Storage System (CESS) store energy in the form of chemical bonds formed via endothermic reactions. When needed, these bonds are broken through reversible processes to release electrical or thermal energy [119]. Due to their high capacity and long-duration storage capability, CESS technologies are well-suited for integrating renewable energy and decoupling generation from consumption over extended periods.

Hydrogen-Based Energy Storage: Among CESS options, hydrogen-based systems are the most developed and promising. They use electrolysis to split water into hydrogen (H_2) and oxygen (O_2) using renewable electricity. The produced hydrogen is stored and later converted back into electricity via a Fuel Cell (FC), generating only water as a byproduct [120].

Hydrogen storage offers high gravimetric energy density, modular scalability, and potential integration across power, heating, and transport sectors. Their self-discharge rates are around 0.2–1% per day [120, 121]. When powered by renewable energy, hydrogen systems operate with zero direct emissions, aligning with global decarbonization goals.

However, key challenges remain, including low round-trip efficiency (30–40%), complex storage infrastructure, and high electrolyzer and FC costs, which currently limit large-scale deployment.

In DC MGs, hydrogen systems can provide long-term energy autonomy. When combined with fast-response storage devices such as BESSs or SCs, they enable multi-timescale flexibility—short-term power smoothing and long-duration energy balancing—enhancing both reliability and sustainability.

2.2.1.4 Thermal Energy Storage Systems

Thermal Energy Storage System (TESS) store energy in the form of heat, which can be extracted and utilized later for power generation, heating, or industrial processes. A typical TESS consists of a thermal storage device and a storage medium that absorbs, retains, and releases heat as required. The storage medium can range from natural soil-based reservoirs to engineered containment systems designed to minimize heat loss and enhance thermal retention efficiency [122].

Thermal energy storage technologies are broadly classified into three main categories—*sensible heat storage*, *latent heat storage*, and *high-temperature thermal storage*—each differing in operational principle, energy density, and application domain.

Sensible Heat Storage: Sensible heat storage involves storing and releasing thermal energy by changing the temperature of a storage material without altering its physical phase. Common storage materials include water, rock, concrete, and molten salts [121]. The amount of energy stored depends on the material's specific heat capacity and the temperature difference between its initial and final states. Typical energy densities range from 30 to 80 Wh/kg, depending on the medium and temperature span [120–123]. Sensible heat systems also exhibit very low self-discharge rates, typically below 0.5% per day when properly insulated [122].

Although conceptually simple and technologically mature, sensible heat storage systems require large storage volumes to achieve significant energy capacity. Moreover, thermal losses and limited operating temperature ranges constrain their overall efficiency and scalability [124].

Latent Heat Storage: Latent heat storage, in contrast, utilizes Phase Change Materials (PCMs) that absorb or release energy during a phase transition—typically from solid to liquid or liquid to gas. This mechanism enables higher energy storage density compared with sensible heat systems, since energy is stored at nearly constant temperature during the phase change process, thereby improving system stability and energy utilization [122]. Typical latent heat storage materials achieve energy densities between 100 and 200 Wh/kg, depending on the PCM type and temperature range [124]. Their self-discharge rates are generally low, around 0.1–1% per day, primarily due to gradual heat losses through insulation [123].

Despite these advantages—such as compactness, high energy density, and near-isothermal operation—latent heat storage presents several engineering challenges. These include managing volume changes during phase transitions, ensuring cycling stability, and maintaining precise temperature control to achieve consistent phase-change behavior [119].

High-Temperature Thermal Storage: High-Temperature Thermal Energy Storage (HT-TESS) systems are designed to operate at elevated temperatures, making them suitable for applications that require intensive thermal energy, such as solar thermal power plants, industrial heat recovery, and high-efficiency power generation [119]. Typical storage media include molten salts, ceramics, or metal oxides, which allow energy retention at temperatures exceeding 500 °C. HT-TESS systems exhibit energy densities ranging from 150 to 300 Wh/kg, depending on the operating temperature and storage medium [23]. The

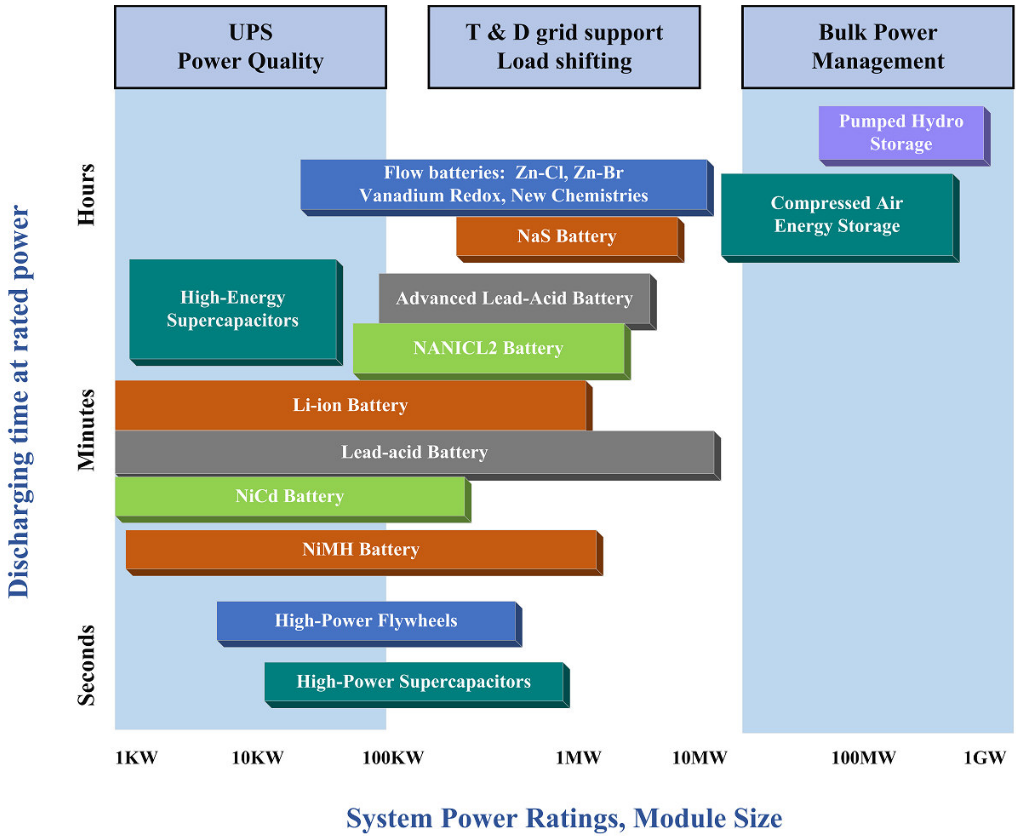

Figure 2.2: Analysis of discharge rates and power ratings of various ESS technologies

self-discharge rate is extremely low, often below 0.1% per day due to advanced thermal insulation [124].

HT-TESS plays a crucial role in facilitating renewable energy integration and enhancing the dispatchability of intermittent sources by storing excess heat from solar or waste energy and converting it into electricity during periods of high demand.

Fig. 2.2 illustrates the discharge rates and power ratings of various ESSs technologies, categorized across small-, medium-, and large-scale applications in power generation, transmission, distribution, and end-user systems. The figure highlights the projected growth in medium- and large-scale deployment of technologies such as CAES, high-power flywheels, and Na–S and zinc–air batteries for bulk power management and grid support, while other ESS technologies increasingly target short-term power quality improvement services [111].

Fig. 2.3 depicts the global evolution of short- and long-term energy storage capacity between 2011 and 2028, as discussed in [114]. The figure underscores the accelerating development of storage technologies and emphasizes their critical role in enhancing power

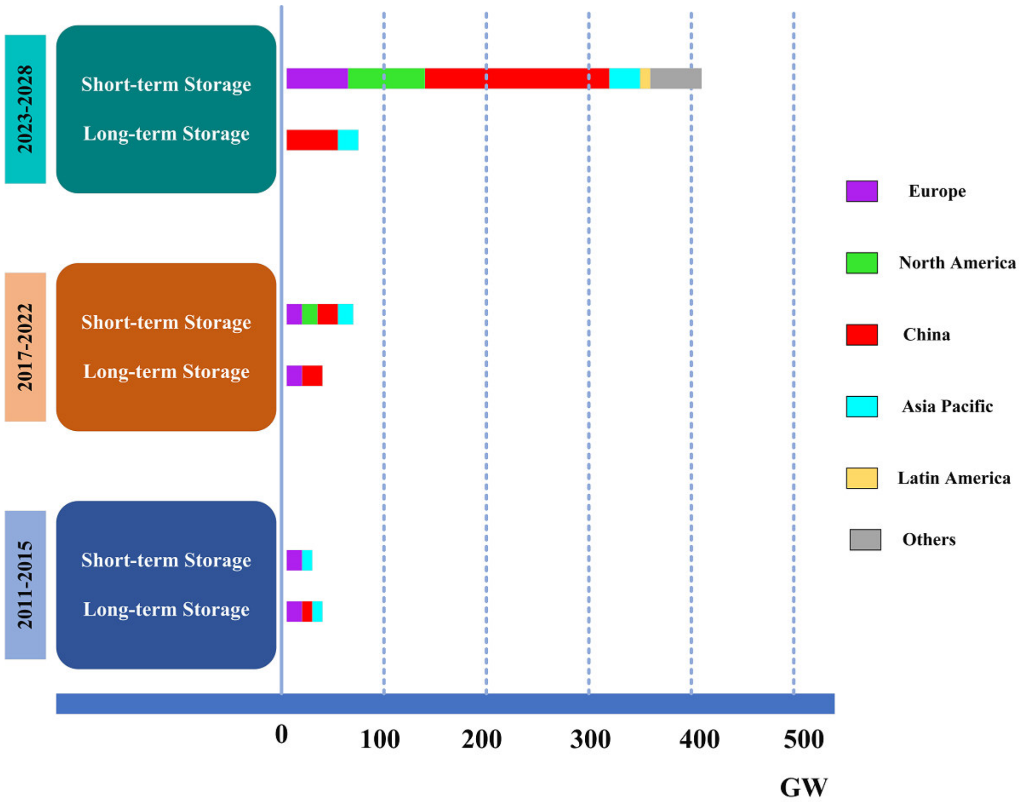

Figure 2.3: Trends in Short- and Long-term storage capacity growth across various regions of the world, from 2011-2028.

system flexibility and supporting sustainable energy transitions.

2.2.2 Discussion on Energy Storage Suitability for Islanded Entities

Table 2.2 presents a comparative summary of the ESSs technologies discussed in this section. It highlights their relative strengths in terms of efficiency, lifecycle, and response characteristics, while also identifying inherent limitations. The table underscores that although no single technology offers a comprehensive solution, the complementary integration of multiple ESS types—across different timescales and capacities—constitutes a promising pathway toward achieving flexible, resilient, and efficient energy management in modern DC MGs.

A rigorous comparison of the technologies in Table 2.2 makes clear that the right ESS for an islanded DC MG must be judged against a small set of non-negotiable metrics: how quickly it can respond to disturbances on the DC bus, whether its energy and power densities are sufficient to cover both fast and sustained imbalances, how much useful life and round-trip efficiency it delivers across heavy cycling, and whether it can be scaled,

Table 2.2: Comparison of various ESSs.

Types of ESSs	Life-Span (Years)	Capacity	Energy-Cost ($/kWh)	Efficiency (%)	Energy-density	Self-discharge (per day)	Limitations
Electrical / Electrochemical							
SMES	≥ 20	10 kW to 10 MW	1000–10,000	85–95	0.5–5 Wh/kg	10 – 15%	High infrastructure & maintenance cost; cryogenic/temperature constraints
Super-capacitor (SC)	≥ 20	up to 300 kW	300–2000	90–95	0.1–5 Wh/kg	20–40%	Low *energy* density, low storage capacity; temperature influence on environment
Lead–acid	≤ 20	0.25–50 MWh	200–400	85–90	30–50 Wh/kg	0.1–0.3%	Environmental issues; risk of thermal runaway with improper charging
Li-ion	≤ 20	0.25–25 MWh	600–2500	95–98	160–260 Wh/kg	0.1–0.3%	High capital cost; thermal management needs
Na–S	≤ 15	$\leq$ 300 MWh	300–500	75–85	(higher than lead–acid; no value)	—	High operating temperature; corrosion/material degradation
Ni–Cd	around 10	–	800–1500	70–90	100–140 Wh/kg	0.2–0.6%	Toxicity (Cd); lower energy density
Vanadium redox flow	≤ 20	$\leq$ 250 MWh	150–1000	75–80	10–30 Wh/kg	(low; qualitative)	Higher design complexity; higher capital cost
Mechanical							
FESS	> 20	kW range	1000–6000	85–90	5–100 Wh/kg	—	Lower energy density; higher capital cost; friction/aerodynamic losses
PHESS	40–60	up to 3 GW	5–100	75–80	—	(negligible)	Geographic constraints; large footprint; ecological impacts; high capex
CAESS	20–40	25–350 MW	2–80	40–60	—	(low; qualitative)	Geological/environmental constraints; high complexity; high capex
Chemical							
Hydrogen-based	5000 cycles in 15 years	–	5–30	45–75	(high; qualitative)	0.2–1%	Low round-trip efficiency; expensive production and transport
Thermal							
Sensible heat storage	10–30	—	15–25	50–94	10–25 kWh/m^3	$< 0.5\%$	Low energy density; limited temp range; high capex
Latent heat storage	10–30	—	25–35	75–90	50–150 kWh/m^3	0.1–1%	Limited suitable PCMs; high capex; low thermal conductivity
High-temperature storage	20–30	—	16–43.6	75–95	120–250 kWh/m^3	$< 1\%$	Insulation maintenance; thermal expansion/contraction issues

safely controlled, and tightly integrated with PECs. When those criteria are applied, lithium-ion BESSs consistently finish ahead. Their converters offer precise, Bidirectional DC–DC converters (BDC) (and AC–DC, where relevant) control, enabling real-time voltage regulation, SI, and dispatchable energy services—capabilities that are foundational for autonomous islanded operation.

Mechanical storage options illustrate the tradeoffs. Flywheel Energy Storage Systems (FESSs) respond in milliseconds and are excellent at riding through sharp transients and mitigating voltage sags. In a DC MG, that speed is valuable during abrupt load steps or renewable power ramps. Yet the same electromechanical attributes that make flywheels fast also limit them: their specific energy is low and self-discharge is high, so they are effective for seconds—occasionally a minute—but not for the multi-minute or hourly balancing that islanded operation routinely demands. CAESS and PHESS succeed at the other extreme. Their energy capacity and cost per kWh are attractive at the bulk level, and lifetimes are long. However, they depend on favorable geography, occupy large footprints, and respond on the order of minutes. These characteristics make them misaligned with the compact, fast-acting, and continuously modulated control that a DC MG requires.

Electrical and electrochemical storage spans the middle ground where MGs actually operate. SCs and SMES deliver unparalleled power density and sub-second response, which is ideal for smoothing converter current, suppressing DC bus ripple, and bridging gaps while other assets ramp. But SCs carry very little energy—often a few Wh/kg or less—so they cannot maintain balance over sustained deficits. SMES is similarly fast and efficient but hampered by cryogenics and cost, which constrains scalability and practical deployment in distributed settings.

Among electrochemical batteries, lead–acid remains inexpensive and familiar, but its specific energy, cycling endurance, and charge acceptance under high rates are modest. In an islanded MG with frequent partial-state-of-charge operation and daily cycling, sulfation and accelerated aging raise maintenance costs and derate usable capacity. Ni–Cd and Ni–MH tolerate abuse better than lead–acid, yet their efficiency is middling and cadmium toxicity is a liability. Flow batteries, notably VRF and zinc–bromine, solve the cycle-life problem and offer energy scalability by decoupling power (stacks) from energy (tanks). Those traits are advantageous for long-duration shifting, but the systems are volumetrically bulky, auxiliary loads reduce round-trip efficiency to the mid-70s–80% range, and response, while controllable, is slower and less granular than that of a tightly coupled battery pack with a fast BDC interface. Na–S pushes energy density higher and operates well for medium- to long-duration support, yet the requirement for 300–350 °C operation introduces corrosion, thermal safety considerations, and enclosure complexity that are generally at odds with distributed, building-scale, or community-scale DC installations.

Lithium-ion resolves most of these compromises. With 160–260 Wh/kg specific energy and high power capability, Li-ion packs can be engineered for both energy and power. Round-trip efficiencies commonly exceed 95–98% at the DC terminals, and self-discharge is very low, so the asset retains stored energy when it is most needed. Electrochemically, Li-ion supports rapid charge acceptance and discharge, allowing converter-level control loops to act on millisecond timescales without being bottlenecked by the cell chemistry. This pairing of a fast, reversible storage element with a bi-directional converter is the essence of why BESSs fit MGs so well: the energy buffer and the control actuator are the same device.

These technology characteristics translate cleanly into functional roles inside an islanded DC MG. The first role is fast transient suppression. Load steps, converter mode changes, or renewable gusts can drive abrupt current excursions and DC voltage deviations. SCs or FESSs can blunt the very first milliseconds of these events, but a BESS keeps the bus stable once the immediate spike passes, absorbing or delivering power for tens of seconds as other resources (PV curtailment, dispatchable DGs) re-schedule. The second role is short- to mid-term balancing. Cloud passages, wind lulls, and stochastic load behavior routinely produce deficits or surpluses on the order of minutes to hours. Here Li-ion BESSs excel because they combine high efficiency with accurate SoC estimation and constraint-aware controls, enabling peak shaving, load following, and spinning-reserve-like support without over-cycling or violating cell limits. The third role is energy management and coordinated dispatch across hours and the diurnal cycle. While Na–S or flow batteries could, in principle, contribute to longer windows, their thermal or system complexity and slower dynamics hinder the kind of tight closed-loop regulation that DC converters depend on. By contrast, a Li-ion BESS, governed by a BMS that communicates limits and gradients to the supervisory controller, provides predictable, repeatable behavior that simplifies optimal scheduling, ensures smooth transitions between generation states, and minimizes renewable curtailment.

Taken together, these roles explain the dominance of BESSs in islanded DC architectures. Their bi-directional energy flow is native: a single converter seamlessly switches between charging and discharging quadrants with commanded current profiles that follow higher-level objectives—maintain the DC bus set-point, enforce droop characteristics for power-sharing, deliver SI, or track dispatch schedules. The same platform naturally covers multiple timescales. Current-mode control and inner loops act within milliseconds to provide stiffness to the DC bus; outer loops handle seconds-to-minutes energy balancing; and supervisory optimizers coordinate hours-ahead dispatch against forecasts and constraints. Because the plant is fully power-electronic, these layers stack without friction: there is no mechanical warm-up, no valve lag, and no geographic lock-in. Moreover, the controllability is precise and model-friendly. Modern predictive or adaptive controllers can enforce SoC guardrails, temperature and cycling rate limits, and degradation budgets, turning the BESS from a passive buffer into an actively managed asset with quantifiable lifetime economics.

Efficiency, form factor, and integration effort reinforce the choice. High round-trip efficiency reduces wasted generation and thermal management overhead—important in islanded sites where every watt-hour is precious. High energy density and modular packaging allow installation in constrained spaces (containers, basements, rooftops) and straightforward scaling from tens of kilowatts for buildings to several megawatts for campuses or remote communities. Maintenance is comparatively light; there are no bearings or rotating seals to wear, no cryogenic systems to service, and safety is addressed through layered protections (cell-level fusing, contactors, pack isolation monitoring, fire detection/suppression). Degradation is predictable and can be co-optimized with operations through condition-based maintenance and calendar/cycle aging models, which is far harder to do for mechanically complex or thermally massive alternatives.

Crucially, BESSs unlock a broader suite of services that islanded MGs increasingly require. They provide black-start capability by forming the DC bus and energizing auxiliary converters; they supply fast reserves and frequency support in hybrid AC/DC sites by emulating inertia and primary control; they implement peak shaving to reduce generator cycling and fuel burn; and they arbitrate energy across the day to minimize curtailed PV while respecting network and device constraints. These services are not simply "nice to have"—they are what turn an islanded system from a fragile ensemble of assets into a resilient, dispatchable power plant.

Looking ahead, solid-state cells promise higher safety margins and energy density; lithium–sulfur targets further gains in specific energy for longer-duration roles; and hybrid configurations that pair Li-ion with SCs or FESSs are maturing, combining ultra-fast buffering with efficient short-term energy support. Such hybrids fit naturally into the layered control hierarchy of MGs: the SC absorbs the first milliseconds, the BESS sustains for minutes to hours, and supervisory optimization coordinates everything against forecasts and constraints.

Other technologies will keep niche roles. Flow batteries remain attractive when footprint is available and very high cycle life at moderate efficiency is acceptable; Na–S suits longer shifts where thermal infrastructure is justified; thermal and hydrogen systems make sense where heat integration or seasonal storage is the priority rather than tight electrical regulation. But none of these, on their own, matches the combination of speed, efficiency, compactness, controllability, and bidirectional power electronics that Li-ion BESSs bring to an islanded DC MG.

In sum, the comparative evidence and operational logic converge: for islanded DC MGs that must continuously balance uncertain renewable generation against variable demand, the most effective solution is a BESS-centric architecture. It delivers fully controllable responses to uncertainty, supports the entire spectrum of power-imbalance timescales from milliseconds to hours, and integrates cleanly with the microgrid's power-electronic fabric. When required, complementary fast buffers (SCs or FESSs) can be added to sharpen transient performance, but the BESS remains the cornerstone that turns flexibility from an aspiration into an engineered, dependable capability.

2.2.3 Challenges of Sole BESS Reliance in Islanded DC Microgrids

Relying solely on BESSs for stability and energy management in islanded DC MGs, although technically attractive, introduces several technical, operational, and environmental challenges that constrain overall system flexibility. While BESSs—especially Li-ion systems—offer superior controllability, bidirectional energy flow, and multi-timescale response capabilities, their integration and long-term operation demand careful consideration of degradation mechanisms, cost, lifecycle management, and system-level coordination. In practice, maintaining MG flexibility while confining excessive battery use is essential for ensuring both economic and technical sustainability.

One of the foremost issues with BESS integration is degradation and aging. Frequent charge–discharge cycling, high cycling rate operation, and exposure to extreme temperatures accelerate capacity fade and internal resistance growth, shortening effective service life. In islanded MGs, where the battery must continuously compensate for RESs intermittency, this degradation is intensified. Maintaining optimal operating conditions—typically within narrow temperature and SoC windows—is crucial to prevent premature wear. However, doing so significantly complicates the MG's control and energy management. Controllers must ensure that charging and discharging patterns remain within rated limits while still providing the required fast transient support and power balancing. This trade-off creates a multi-objective control challenge: maximizing lifetime while maintaining dynamic performance. Advanced control algorithms can mitigate some degradation effects, but they add further complexity, particularly in islanded entities.

Another major constraint is the high capital cost of large-capacity BESSs. In most isolated MGs, batteries represent the single most expensive subsystem, often accounting for more than 40–60% of total installation costs. This cost burden is exacerbated by the need for oversizing to accommodate both energy and power requirements, ensuring sufficient autonomy during long RES deficits or high-load periods. While the cost per kWh of storage continues to decline, the total project economics remain heavily influenced by battery procurement, Power Electronic Converter rating, and associated protection and thermal management systems. Consequently, relying solely on a large BESS not only increases upfront capital expenditure but also reduces economic flexibility and the ability to adapt to future load or generation changes.

Furthermore, the charging demand of large-scale storage systems can exceed the available generation capacity in small or weakly supplied islanded networks. When RESs are intermittent and backup DGs are limited, scheduling the charging of a bulky BESS becomes difficult. During periods of low irradiance or wind availability, directing scarce generation toward battery charging may leave insufficient power for critical loads, resulting in energy shortfalls. Conversely, under high generation, rapid charging can cause converter overloading or DC bus voltage deviations. This delicate energy balance necessitates sophisticated EMS strategies to prioritize essential loads, coordinate charging, and prevent the BESS from imposing excessive stress on the power supply infrastructure.

The efficiency and thermal management of BESSs also present technical constraints. Although round-trip efficiency can reach 95–98% under optimal conditions, it decreases under high-temperature, partial SoC, or high-rate operation—conditions typical in islanded environments with unpredictable renewable profiles. The heat generated during cycling requires effective thermal regulation to avoid runaway risks, further increasing system complexity. These thermal dynamics must be co-optimized with power demand control to avoid cascading effects on performance and safety.

From a materials and environmental perspective, large-scale deployment of batteries raises concerns about sustainability and end-of-life management. The extraction and global supply of critical minerals such as lithium, cobalt, and nickel are subject to geopolitical instability, making future battery production vulnerable to resource scarcity and price fluctuations. In addition, improper disposal or recycling of depleted cells can lead to significant environmental hazards due to toxic electrolyte leakage and heavy metal contamination. Although second-life applications and recycling programs are being developed, their effectiveness depends on the quality of recovered materials and standardized processes that are still evolving. For remote or islanded locations, establishing safe recycling logistics can be particularly challenging.

To achieve long-term sustainability, battery operation must be confined within well-defined boundaries—charging and discharging only when necessary, maintaining SoC within a mid-range band, and leveraging other storage or demand-side flexibility options whenever feasible. So, it can be said that while BESSs remain the cornerstone of energy storage in islanded DC MGs due to their unmatched controllability and efficiency, overreliance on them introduces significant degradation, cost, operational, and environmental challenges.

Given these challenges, incorporating additional flexibility resources and coordinating scheduling across different storage media can substantially reduce battery wear and overall costs. A balanced strategy that leverages supplementary flexibility options—such as demand-side participation—can complement storage-based control and alleviate stress on battery systems. Allowing flexible loads to actively support voltage regulation can greatly improve both the operational resilience and economic efficiency of islanded DC MGs. A promising approach to achieving this is the integration of Electric Spring (ES) technology, an intelligent demand-side energy management framework capable of simultaneously coordinating power exchanges between controllable loads and battery stacks in real time.

Unlike traditional Demand Response (DR) schemes, which require additional infrastructure or extensive communication networks and often introduce further complexity and cost, the ES provides a cost-effective and decentralized means of achieving demand-side flexibility. By simultaneously managing both the power stored in batteries and the power dissipated by loads, the ES can maintain DC bus stability and enhance overall system flexibility without the need for complex grid infrastructure. The detailed working principle and coordination strategy of the ES concept are elaborated in the next section.

2.3 DC Electric Spring: A Technology for Improving the Flexibility

The role of Demand-Side Management (DSM) is becoming increasingly vital as the penetration of RESs continues to rise [125, 126]. Power systems are undergoing a fundamental transformation, from centralized generation scheduling, where a few large power plants were dispatched to meet aggregated demand, toward decentralized coordination of millions of controllable loads that dynamically balance fluctuating generation conditions. This shift represents a transition from generation-centric to demand-centric flexibility, emphasizing the active participation of end-use devices in maintaining system balance. This issue would be even more vital in the realms of RES-dominated islanded microgrids, due to the lack of sufficient inertial, limited local resources, and the absence of grid support [127]. However, realizing such distributed coordination remains challenging due to communication overhead, centralized control complexity, and the substantial infrastructure costs associated with Demand Response (DR) programs [128, 129].

As discussed in the previous chapter, BESSs possess unique characteristics that make them the most effective resource for enhancing flexibility in islanded DC-MGs. In the absence of external grid support, BESSs enable bidirectional energy flow, providing rapid and fully controllable responses to system uncertainties. They can support a wide range of flexibility timescales—from fast transient stabilization (milliseconds to seconds) to short-term energy balancing (minutes to hours). No other single resource in an islanded MG can comprehensively meet these multi-timescale flexibility requirements.

BESSs store surplus energy generated during low-demand or high-RES periods and release it when deficits occur, mitigating renewable intermittency and maintaining supply–demand balance. Nonetheless, as noted in the Introduction of this thesis, there is an increasing emphasis on minimizing the total installed battery capacity in islanded DC-MGs. This approach is driven by several technical, economic, and environmental considerations:

- Batteries require strict charging and discharging conditions to ensure long service life, increasing control and EMS complexity.
- High capital costs make batteries one of the most expensive components in isolated MGs.
- Large-scale charging demand may exceed local generation capacity, posing significant operational challenges in small-scale systems.

- Environmental concerns arise from the disposal and recycling of large quantities of batteries.

Given these constraints, the central question becomes how to sustain adequate flexibility while limiting battery utilization. A commonly proposed approach in the literature is the integration of DR strategies. Nevertheless, implementing DR and achieving effective coordination with battery systems often introduce additional operational complexity and infrastructure costs, primarily due to the need for advanced communication and controller.

To address these challenges and facilitate demand-side participation in flexibility provision alongside batteries, the deployment of *Electric Spring (ES)* technology has emerged. ESs offer a cost-effective and practical solution for demand-side management, as they can operate autonomously without relying on supplementary communication infrastructure. Consequently, the integration of ESs provides a promising pathway to enhance microgrid flexibility while mitigating the dependence on bulky battery systems [126, 127]. This technology was originally proposed for AC systems to introduce a dynamic voltage/frequency compensating device that operates in series with noncritical loads (NCLs). Not to mention that NC loads are those that are not sensitive to voltage fluctuations, such as induction cookers, refrigerators, and water heating systems. By injecting a controlled voltage across the NCL, the ES modulates its power consumption to indirectly stabilize the voltage across Critical Loads (CLs), which are sensitive to supply fluctuations like data centers or communication infrastructures. Through this mechanism, the ESs effectively transforms a conventional passive load into a smart, controllable load capable of contributing to voltage stabilization and local power balancing.

Unlike conventional shunt-connected compensators such as Dynamic Voltage Restorers (DVRs) or STATCOMs, which operate at the system level and typically require centralized coordination, the ES functions in a fully decentralized manner [126]. Each ES-equipped load independently responds to local voltage variations, requiring minimal communication infrastructure—making it particularly suitable for distributed and islanded MGs where autonomy, scalability, and resilience are essential [125].

Building on the success of the AC implementation, the DC Electric Spring (DC-ES) concept has recently been extended to DC power systems to enhance voltage stability, reliability, and flexibility in islanded DC MGs [129]. In DC networks, distributed energy sources such as PV arrays, FCs, and wind rectifiers interface directly through DC–DC converters, resulting in higher efficiency and reduced conversion losses compared with their AC counterparts. Nonetheless, DC microgrids face several unique stability challenges, including:

- Voltage fluctuations and transient dips mainly due to power imbalance between generation and load, which is driven by the intermittent nature of renewable sources or uncertainty in load;
- Constant Power Loads (CPLs)-induced bus oscillations.

These challenges are particularly severe during islanded operation, where the absence of a stiff voltage reference amplifies system nonlinearities and dynamic interactions.

Traditional DC bus stabilization strategies typically rely on hierarchical control frameworks. The primary control layer employs droop control to achieve proportional power sharing among distributed sources [128], while the secondary and tertiary layers handle voltage restoration, power dispatch, and optimization. Although conventional droop control enables proper operation, in terms of good voltage regulation and accurate power sharing, advanced methods—such as gain-scheduled droop control [129] and coordinated hybrid AC/DC control [128]— can offer improved performance. However, they still rely on communication links for coordination.

The DC-ES introduces a fundamentally different paradigm. Rather than acting on the generation side, it operates on the demand side, where each unit autonomously regulates voltage and power consumption at the local level. By injecting a controllable series voltage across the NCL, the DC-ES maintains the voltage across the CL near its nominal value. When renewable generation fluctuates, the DC-ES dynamically modulates the injected voltage, increasing or decreasing the NCL's power absorption to restore local power balance. This behavior enables real-time demand-side regulation, effectively suppressing DC bus voltage oscillations caused by the negative incremental impedance of CPLs [2, 130].

CPL-induced instabilities, which manifest as sustained oscillations or even system collapse, are particularly problematic in DC systems because constant power converters draw increasing current as voltage decreases—further destabilizing the network. The DC-ES mitigates this phenomenon by modulating the NCL's power consumption, thereby providing active damping and enhancing system stability.

The DC-ES can introduce a modular, plug-and-play solution. Each ES autonomously compensates for voltage deviations in its local area, forming a distributed flexibility network where stability and regulation emerge collectively. This decentralized structure inherently enhances resilience and reduces the cyber-vulnerability associated with communication-

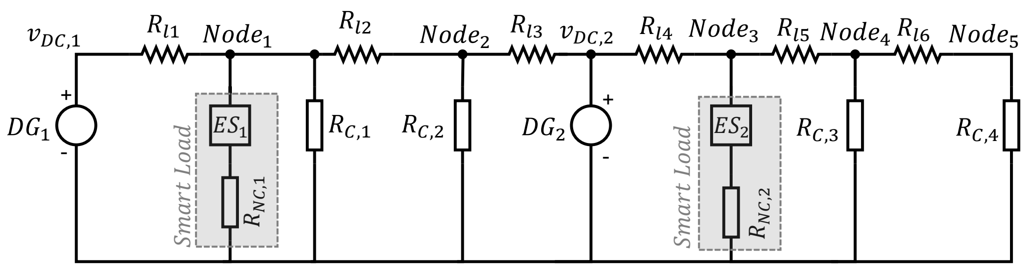

Figure 2.4: A DC-MG including multiple DC-ESs.

based schemes [131]. In essence, the DC-ES embodies a bottom-up flexibility mechanism, where intelligent loads cooperatively maintain system equilibrium.

The principle of operation can be illustrated using the DC network shown in Fig. 2.4, where multiple DG units and loads are interconnected along a distribution bus with finite line impedance. The DC bus voltage, V_{DC}, represents the aggregated output of distributed generation and storage units. Under nominal operation, the DC Electric Spring (DC-ES) maintains the critical load voltage V_{CL} near its rated value by dynamically adjusting the injected series voltage V_{ES} across the NCL. When renewable output varies, V_{ES} is modulated to either absorb surplus power or reduce demand, thereby ensuring local power balance. This autonomous voltage–power regulation ensures bus voltage stability even under substantial renewable fluctuations or transient disturbances [127].

It is important to note that the DC-ES achieves series voltage regulation, directly controlling the voltage across specific loads for localized compensation. This modular architecture scales naturally across large systems, allowing each DC-ES to contribute independently to overall voltage regulation without requiring global synchronization or communication overhead.

Building on previous outlines, it can be stated that the DC-ES represents a transformative advancement in demand-side flexibility management for islanded DC-MGs. By embedding control scheme directly within the load interface, it enables autonomous voltage regulation, distributed power balancing, and local stability enhancement—without reliance on centralized control or high-bandwidth communication. Moreover, when coordinated with BESS or higher-level EMS, DC-ES units can share flexibility across supply and demand, reduce battery cycling depth, and extend storage lifetime.

From a modeling perspective, dynamic representations of DC-ES units facilitate their integration into system-level simulations, enabling evaluation of network-wide stability and control coordination. Parameter mismatches between simulation models and hardware prototypes can be mitigated through refined controller tuning, although this might intro-

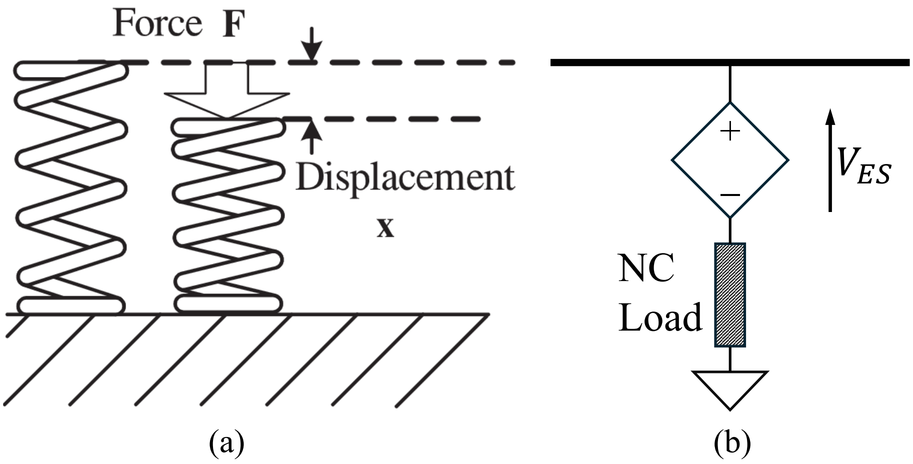

Figure 2.5: Graphical representation of electric spring: (a) Mechanical spring, (b) Electric spring.

duce additional computational complexity. Nevertheless, these models provide a robust foundation for investigating the collective impact of multiple DC-ES units and their role in enhancing grid-wide flexibility. So, the following sections present the mathematical modeling, control architecture, and coordinated operation of DC-ES within islanded DC-MGs, emphasizing its integration with distributed storage and renewable generation units for enhanced resilience and flexibility.

2.3.1 An Introduction to the Concept of DC Electric Spring

The concept of the ES originates from the fundamental behavior of a mechanical spring, which restores equilibrium by exerting a force that opposes the applied disturbance. As illustrated in Fig. 2.5(a), when a force F is applied to a spring with stiffness constant k, the resulting displacement x follows Hooke's law:

$$F = -kx \tag{2.2}$$

The negative sign indicates that the spring generates a restoring force counteracting the external disturbance, thereby maintaining system equilibrium.

This analogy establishes the conceptual foundation of the ES, which can be regarded as the electrical counterpart of a mechanical vibration damper. In mechanical systems, springs mitigate oscillations by elastically absorbing and releasing energy; likewise, ES devices stabilize electrical systems by compensating for voltage and power oscillations arising from renewable generation variability or load fluctuations [132].

Within AC power systems, several versions of ES architectures have been developed

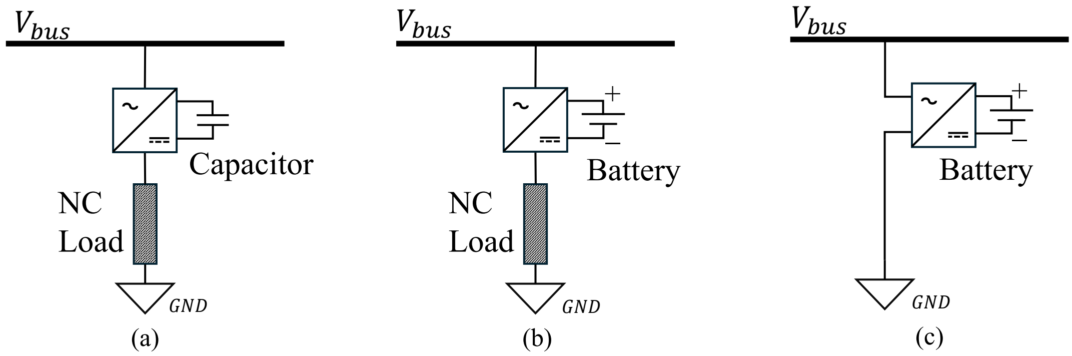

Figure 2.6: Different versions of ESs used in AC grids. (a) ES-1: Series-type without energy storage, (b) ES-2: Series-type with energy storage, (c) ES-3: Shunt-type with energy storage.

to meet distinct operational objectives, as illustrated in Fig. 2.6. The first generation (ES-1) operates in series with the NC load and provides reactive power compensation only [125]. The second generation (ES-2) extends this capability to both active and reactive power compensation [127], enabling simultaneous voltage regulation and active power balancing. Both ES-1 and ES-2 are classified as series-type configurations, in which the ES is connected in series with the NC load to form a "smart load" that dynamically adapts its power consumption according to grid conditions.

In contrast, the third generation (ES-3) adopts a shunt-type topology, implemented as a bidirectional grid-connected AC/DC converter operating independently of any specific load [129]. Among these configurations, ES-2 and ES-3 require integration with an energy storage element to enable bidirectional power flow and to manage the exchange of active power, as depicted in Figs. 2.6(b) and 2.6(c), respectively.

Although extensive studies have validated the performance of these architectures in AC systems [2], their adaptation to DC networks requires more attention. Because reactive power does not exist in DC systems, the ES-1 configuration is inherently unsuitable for such environments. Consequently, this work extends the ES-2 concept to DC networks, proposing a series-type DC-ES integrated with energy storage for autonomous demand-side power management in islanded DC MGs.

The proposed DC-ES dynamically injects a controllable series voltage across noncritical loads to regulate the voltage across critical loads, thereby adjusting their instantaneous power consumption to counteract bus voltage fluctuations. This approach enhances voltage stability, mitigates CPL-induced oscillations, and provides a decentralized, scalable framework for achieving demand-side flexibility within islanded DC microgrids.

The basic configuration of a DC-ES is illustrated in Fig. 2.7. The system comprises a

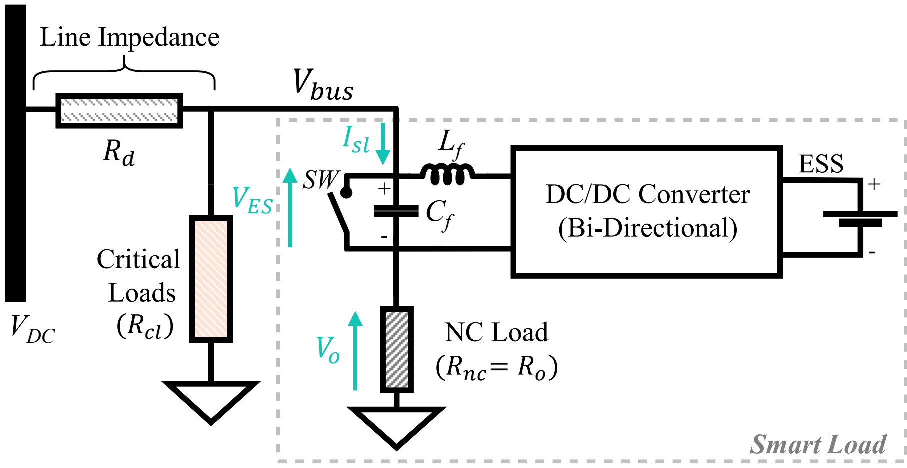

Figure 2.7: Basic structure of DC-ES.

Table 2.3: Electric Spring Characteristics

Description	**Specification**
Resistive Non-Critical Load (R_{nc})	15.6 Ω
Inverter Circuit Topology	Half-bridge
Switching Freq. (f_{sw})	25 kHz
Output Low-pass Filter Inductance (L_f)	600 μH
Output Low-pass Filter Capacitance (C_f)	140 μF

DC common bus voltage V_{DC}, a connecting bus maintaining voltage V_{bus}, and both critical (CL) and noncritical (NC) loads distributed across the network. The DC-ES consists of a bidirectional DC–DC converter that serves as the power interface between the busbar (ES port) and a Battery Energy Storage System (BESS) (battery port). The ES port is connected in series with the NC load, forming a "smart load," while the battery port interfaces with the attached storage element—typically a small Li-ion battery stack. Regarding the converter, a bidirectional DC/DC converter can be employed for this purpose. Various circuit topologies have been explored in the literature, as reviewed in [133]. This thesis, however, focuses on a DC-ES employing the half-bridge circuit, a well-known conversion cell commonly used in this domain [129]. Not to mention that the key characteristics of the proposed ES are outlined in Table 2.3.

When V_{DC} experiences fluctuations due to intermittent RES generation or dynamic load variations, the DC-ES injects an adaptive compensating voltage V_{ES} across the NC load to stabilize the bus voltage V_{bus}. The control objectives are twofold:

Adaptive Load Regulation: The NC load's power consumption is modulated in proportion to the deviation of V_{DC}, effectively performing load shedding or boosting to maintain bus voltage stability.

Energy Balancing via Storage Port: The bidirectional converter channels the surplus or deficit energy to or from the attached energy storage device. Thus, during renewable surpluses, the BESS absorbs excess energy; during deficits, it releases stored energy to support the bus.

Through these mechanisms, the DC-ES ensures that the power drawn by the demand side dynamically follows the fluctuations of the supply, thereby preserving voltage stability at the DC bus and reducing stress on central BESS units or generators.

A key advantage of the series-type DC-ES over conventional shunt-connected distributed ESS systems lies in its dual controllability. Whereas shunt systems can only modulate power flow through the battery interface, the DC-ES can simultaneously control (1) the power consumed by the NC load and (2) the energy exchange with the local storage. This dual control significantly reduces the required energy capacity of the storage component for maintaining supply–demand balance [16]. In essence, the DC-ES uses the controllable elasticity of the NC load to absorb short-term fluctuations, while the attached BESS handles slower dynamics, leading to a more efficient use of energy storages [132].

For reliability, a normally-closed bypass relay is installed across the output of the DC-ES to ensure the continuity of the NC load in case of a converter failure (see Fig. 2.7). In the event of a fault, the relay isolates the converter and allows direct connection of the NC load to the DC bus, thus maintaining operational integrity without compromising system stability [131].

By enabling adaptive demand-side participation through this architecture, the DC-ES transforms traditional passive loads into flexible, self-regulating smart loads. These smart loads autonomously contribute to maintaining the DC bus voltage within prescribed limits, even under severe supply fluctuations or transient disturbances. Furthermore, when multiple DC-ES units are distributed across the network, each operating locally and autonomously, the overall MG exhibits emergent collective stability and enhanced flexibility—without centralized coordination or communication overhead.

Consequently, the DC-ES extends the mechanical spring analogy into the electrical domain, acting as a “virtual elasticity” within DC MGs. It achieves this by dynamically balancing stored and dissipated energy between the NC load and local BESS through a series voltage-injection mechanism. Compared with conventional battery-based stabilization, the DC-ES can achieve comparable or superior voltage regulation with significantly reduced storage capacity and lower operational stress on BESSs. This capability makes it an ideal complementary technology for achieving fine-grained, decentralized flexibility in future islanded MGs.

2.3.2 Investigating the Behavior of DC Electric Spring

To analyze the behavior of series-type DC-ES, consider its basic configuration illustrated in Fig. 2.7. For the sake of simplicity, the DC bus voltage V_{bus} is assumed to remain constant and equal to its nominal value (i.e., $V_{\text{bus}} = V_{\text{nom}}$). Hence, the impedance of the distribution line is ignored in this analysis. Generally, NC loads are classified into two types according to their power–voltage relationships and the direction of energy flow:

- Resistive loads,
- Constant-power loads (CPLs).

For resistive loads, the resistance value does not vary with the applied voltage. Such components, including filament lamps or resistive heaters, naturally adjust their power consumption with voltage magnitude. In contrast, CPLs sustains a fixed power level regardless of voltage changes. This behavior is characteristic of DC–DC converters that operate with tightly regulated power control loops. These converters dynamically modify their input current to maintain constant output power, a property that can lead to negative incremental impedance and potential instability. Not to mention that further information about CPLs is discussed in the next chapter

Because the DC-ES may be associated with any of the two NC load types, each configuration displays distinct steady-state and transient properties governed by the characteristics of the connected load. The subsequent analysis explores how these configurations operate and interact, focusing on their roles in maintaining bus voltage stability, shaping load power dynamics, and influencing overall stability.

A. Resistive NC Loads Connected to DC-ES

Referring to Fig. 2.7, and assuming the noncritical (NC) load is represented by a constant resistance R_o. The DC bus voltage V_{bus}, the ES voltage V_{ES}, the NC load voltage V_o, and the smart-load current I_{sl} are related by:

$$V_{bus} = V_{ES} + V_o = V_{ES} + I_{sl} R_o. \tag{2.3}$$

Here, V_{ES} is the controlled voltage generated by the bidirectional DC–DC converter, while V_o denotes the voltage across the NC load.

From (2.3), the instantaneous powers of the ES, the NC load, and the total smart load can be written as:

$$P_{ES} = V_{ES}I_{sl} = \frac{V_{ES}(V_{bus} - V_{ES})}{R_o}, \tag{2.4}$$

$$P_o = V_oI_{sl} = \frac{(V_{bus} - V_{ES})^2}{R_o}, \tag{2.5}$$

$$P_{sl} = V_{bus}I_{sl} = \frac{V_{bus}(V_{bus} - V_{ES})}{R_o}. \tag{2.6}$$

Equations (2.4)–(2.6) show that the V_{ES} directly determines how current and power are distributed among the ES, the NC load, and the DC bus. Specifically, P_{ES} reaches its maximum value when $V_{ES} = V_{bus}/2$, where the ES either absorbs or delivers maximum power depending on V_{bus}. Equation (2.5) indicates that the NC-load power P_o becomes zero when $V_{ES} = V_{bus}$, meaning that the ES completely compensates the bus voltage. Meanwhile, (2.6) reveals a linear relationship between the smart-load power and V_{ES}, showing that power consumption can be continuously adjusted through voltage modulation.

Defining the nominal smart load power P_{nsl} and nominal smart load current I_{nsl} at $V_{ES} = 0$, the comparative relationships are expressed as:

$$|I_{sl}| \quad \begin{cases} > |I_{nsl}| & \text{if } V_{ES} < 0 \text{ or } V_{ES} > 2V_{bus}, \\ < |I_{nsl}| & \text{if } 0 < V_{ES} < 2V_{bus}, \end{cases} \tag{2.7}$$

$$P_{ES} \quad \begin{cases} > 0 & \text{if } 0 < V_{ES} < V_{bus}, \\ < 0 & \text{if } V_{ES} < 0 \text{ or } V_{ES} > V_{bus}, \end{cases} \tag{2.8}$$

$$P_o \quad \begin{cases} > P_{nsl} & \text{if } V_{ES} < 0 \text{ or } V_{ES} > 2V_{bus}, \\ < P_{nsl} & \text{if } 0 < V_{ES} < 2V_{bus}, \end{cases} \tag{2.9}$$

$$P_{sl} \quad \begin{cases} > P_{nsl} & \text{if } V_{ES} < 0, \\ < P_{nsl} & \text{if } V_{ES} > 0. \end{cases} \tag{2.10}$$

The normalized operating regions derived from (2.7)–(2.10) can be theoretically divided into the following distinct regions:

- **Region I** ($V_{ES} < 0$): The ES supplies power to the bus ($P_{ES} < 0$), causing the load current to rise above its nominal value.
- **Region II** ($0 < V_{ES} < V_{bus}$): The ES absorbs power ($P_{ES} > 0$), leading to a reduction

in both current and total load power.

- **Region III** ($V_{bus} < V_{ES}$): The current through the smart load reverses direction ($I_{sl} < 0$), and the ES begins to inject power back into the bus.

Table 2.4: Modes of Operation of DC-ES with Resistive NC Load

Region	V_{ES} **Range**	$\lvert I_{sl}\rvert$	P_{ES}	P_o	P_{sl}
1	$V_{ES} < 0$	$> \lvert I_{nsl}\rvert$	< 0	$> P_{nsl}$	$> P_{nsl}$
2	$0 < V_{ES} < V_{bus}$	$< \lvert I_{nsl}\rvert$	> 0	$< P_{nsl}$	$> P_{nsl}$
3	$V_{bus} < V_{ES}$	$< \lvert I_{nsl}\rvert$	< 0	$< P_{nsl}$	$> P_{nsl}$

Table 2.4 summarizes the correlations between V_{ES} polarity, current direction, and power flow in each region. These results clearly highlight the bidirectional capability of the DC-ES, enabling it to stabilize the DC bus by either absorbing surplus energy or injecting power when a deficit occurs.

B. Constant Power NC Loads Connected to DC-ES

In addition to resistive NC loads, the DC-ES can also operate with CPLs, which represent many practical DC applications such as tightly regulated DC–DC converters, electric drives, and electronic devices. Unlike resistive loads whose current varies linearly with voltage, CPLs maintain constant output power P_o regardless of voltage variations. This characteristic introduces negative incremental impedance, which can destabilize the DC bus under fluctuating supply conditions (please refer to Chapter 3.4). Integrating a DC-ES in series with such loads provides an effective damping mechanism by adaptively adjusting the series voltage V_{ES} to maintain bus stability.

For the circuit in Fig. 2.7, the voltage relation among the DC bus, ES, and CPL is as below:

$$V_{\text{bus}} = V_{\text{ES}} + V_o = V_{\text{ES}} + \frac{P_o}{I_{\text{sl}}}, \tag{2.11}$$

where P_o is the constant power of the NC load. Using (2.11), the instantaneous powers of the ES and smart load are:

$$P_{\text{ES}} = V_{\text{ES}} I_{\text{sl}} = \frac{V_{\text{ES}} P_o}{V_{\text{bus}} - V_{\text{ES}}}, \tag{2.12}$$

$$P_{\text{sl}} = V_{\text{bus}} I_{\text{sl}} = \frac{V_{\text{bus}} P_o}{V_{\text{bus}} - V_{\text{ES}}}. \tag{2.13}$$

As before, V_{ES} serves as the primary control variable governing current and power sharing among the ES, CPL, and bus. The normalized relations among current, ES power, and total smart-load power are:

$$|I_{\text{sl}}| \quad \begin{cases} > |I_{\text{nsl}}| & \text{if } 0 < V_{\text{ES}} < 2V_{\text{bus}}, \\ < |I_{\text{nsl}}| & \text{if } V_{\text{ES}} < 0 \text{ or } V_{\text{ES}} > 2V_{\text{bus}}, \end{cases} \tag{2.14}$$

$$P_{\text{ES}} \quad \begin{cases} > 0 & \text{if } 0 < V_{\text{ES}} < V_{\text{bus}}, \\ < 0 & \text{if } V_{\text{ES}} < 0 \text{ or } V_{\text{ES}} > V_{\text{bus}}, \end{cases} \tag{2.15}$$

$$P_{\text{sl}} \quad \begin{cases} > P_{\text{nsl}} & \text{if } 0 < V_{\text{ES}} < V_{\text{bus}}, \\ < P_{\text{nsl}} & \text{if } V_{\text{ES}} < 0 \text{ or } V_{\text{ES}} > V_{\text{bus}}. \end{cases} \tag{2.16}$$

Here, I_{nsl} and P_{nsl} also denote the nominal current and power when ES is out of service ($V_{\text{ES}} = 0$). These relations define the transitions between power absorption and injection as V_{ES} varies.

The operating conditions of I_{sl}, P_{ES}, and P_{sl} versus V_{ES} are shown in Table 2.5. The behavior can be divided into three distinct regions:

- **Region I** ($V_{ES} < 0$): The ES delivers power to the bus ($P_{\text{ES}} < 0$) and the smart-load current decreases below nominal, stabilizing the bus.
- **Region II** ($0 < V_{ES} < V_{bus}$): The ES absorbs power ($P_{\text{ES}} > 0$), increasing current and total power to offset voltage rise.
- **Region III** ($V_{bus} < V_{ES}$): The ES voltage dominates, so the current reverses ($I_{\text{sl}} < 0$), and the ES injects power back into the bus to support supply shortages.

Table 2.5: Modes of Operation of DC-ES with NC CPLs

Region	V_{ES} **Range**	$\lvert I_{sl}\rvert$	P_{ES}	P_{sl}
1	$V_{ES} < 0$	$< \lvert I_{nsl}\rvert$	< 0	$< P_{nsl}$
2	$0 < V_{ES} < V_{bus}$	$> \lvert I_{nsl}\rvert$	> 0	$> P_{nsl}$
3	$V_{bus} < V_{ES}$	$< \lvert I_{nsl}\rvert$	< 0	$< P_{nsl}$

When distributed across a microgrid, multiple DC-ES units act asynchronously, each locally adjusting to variations in V_{bus} and P_o.

According to the above, it can be said that in the presence of CPLs, the DC-ES functions as a fast, self-regulating interface that dynamically redistributes power between the DC bus and the load. By modulating its injected voltage V_{ES}, it converts an inherently destabilizing CPL into a grid-supportive smart load capable of real-time power absorption or injection. This adaptive capability highlights the DC-ES as a key enabler of stable and flexible operation in islanded DC-MG with high shares of renewable and constant-power devices.

2.3.3 Dynamic Issues in DC-MGs, and ES as a Privileged Solution

In contrast to the assumption in the previous part, in islanded DC microgrids, the bus voltage does not remain constant but rather fluctuates dynamically over time due to a variety of internal and external influences. As shown in Fig. 2.8, these variations mainly arise from three key factors:

1. The supply-side voltage may become unstable as a result of converter dynamics or weak source inertia.
2. Intermittent renewable generators, such as PV panels or wind turbines, introduce fluctuations since their output power changes with irradiance or wind speed.
3. Rapid load power variations, which stem from the stochastic operation of DC converters, motor drives, and CPLs [2].

The time scales of these disturbances vary substantially—from fast, millisecond-level transients produced by converter switching actions to slower drifts over minutes or hours caused by renewable intermittency. These combined factors continuously alter the DC bus voltage, thereby complicating voltage stability and overall power balance within the microgrid.

A. Droop Effect and Voltage Deviation

A factor that contributes to bus-voltage fluctuation is the inherent droop effect present in DC networks. When current flows through feeders with finite impedance, voltage drops naturally occur along the line from the source to downstream nodes. As a result, the voltage level decreases progressively with distance from the power source. Under heavy loading conditions, this drop becomes severe and can exceed the permissible limits required by sensitive electronic loads.

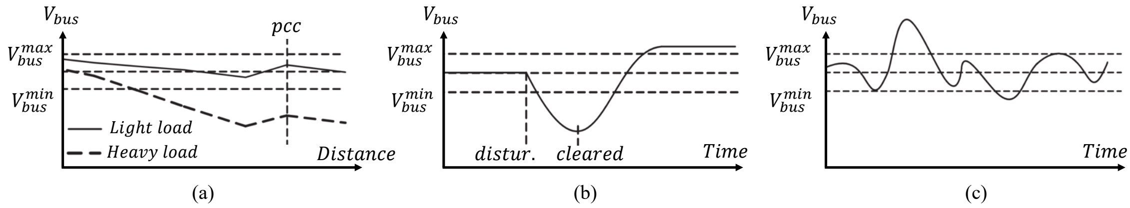

Figure 2.8: Some potential issues in DC-MGs [2]. (a) Droop effect due to distribution line impedance, (b) Sudden voltage drop caused by equipment or system disturbances. (c) Unstable bus voltage caused by the inherent intermittency of RESs.

As depicted in Fig. 2.8(a), the bus voltage remains high under light loading but drops significantly when the line is heavily loaded. In this respect, researchers have proposed various droop-control strategies [16, 128] to mitigate these issues. These schemes intentionally utilize the droop characteristic to autonomously share power among distributed sources. Each converter's output voltage is adjusted based on its current so that proper load sharing is achieved and the overall bus voltage remains within acceptable limits. Despite their effectiveness in coordinating supply sources, these schemes cannot directly correct localized voltage deviations resulting from feeder impedance or load fluctuations. Hence, as a demand-side voltage regulation, the DC-ES can support droop control at the load end.

B. Equipment and System Disturbances

During equipment or system disturbances—such as converter malfunctions or short circuits—a sudden voltage depression can propagate across the DC bus. Such rapid voltage drops may push the bus voltage below safe operational thresholds, as illustrated in Fig. 2.8(b).

Protection mechanisms like electronic circuit breakers and fault-isolation devices are designed to operate swiftly to disconnect the faulty section. After the fault is cleared, transient voltage overshoots often occur because certain loads remain disconnected. These abrupt fluctuations impose significant electrical stress on converters, storage elements, and sensitive devices. When DC-ES units are deployed at critical network nodes, they can absorb or inject compensating power during fault and recovery phases. This action mitigates voltage excursions and preserves stable operation.

C. Implications for DC-ES Control Design

The combined influences of source intermittency (see Fig. 2.8(c)), droop characteristics, and disturbances highlight the importance of real-time voltage control in DC microgrids.

Some energy storage systems—such as batteries and supercapacitors—can compensate for energy fluctuations and addressing rapid voltage transients but as mentioned in section 2.2.3, sole reliance on such ESSs is not rational.

In contrast, the DC-ES operates directly at the load interface, providing rapid and localized voltage compensation. By dynamically controlling its series voltage V_{ES} and interacting with its energy-storage element, the DC-ES immediately counteracts bus-voltage deviations, dampens oscillations, and enhances system resilience during fault conditions—all without high-speed communication or centralized coordination.

2.3.4 Voltage Regulation of the DC-ESs

In practical DC microgrids, both network parameters (line resistance and so on) and device limits (e.g., converter ratings and the admissible range of the NC load) bound the voltage-regulation capability of a DC-ES. To model the system accurately, the MG's distribution-line resistance R_d should be included, while line inductance L_d is neglected under steady-state conditions. This subsection (i) examines how the DC bus voltage, the ES voltage, and the source voltage vary under different smart-load configurations and (ii) determines the DC-ES operating boundaries given electrical and load constraints.

Consider Fig. 2.7, and let the total load-side power be P_{bus}, which equals the sum of the smart-load power P_{sl} and the CL power P_c. Writing the power balance actively yields:

$$P_{\text{bus}} = V_{\text{bus}} I_{\text{bus}} = P_{\text{sl}} + P_c = P_{\text{sl}} + \frac{V_{\text{bus}}^2}{R_c}. \tag{2.17}$$

Because a finite line resistance R_d drops voltage as current flows, the supply and bus voltages satisfy as below:

$$V_{DC} = V_{\text{bus}} + R_d I_s = V_{\text{bus}} + R_d \frac{P_{\text{bus}}}{V_{\text{bus}}} = V_{\text{bus}} + R_d \frac{P_{\text{sl}} + P_c}{V_{\text{bus}}}. \tag{2.18}$$

Here, I_s denotes the line current drawn from the source.

The DC-ES cannot exceed its electrical limits. These constraints could be explicitly stated as follows:

$$V_{ES}^{\text{rated,min}} \le V_{ES} \le V_{ES}^{\text{rated,max}}, \quad V_o^{\text{rated,min}} \le V_o \le V_o^{\text{rated,max}}, \quad I_{sl}^{\text{rated,min}} \le I_{sl} \le I_{sl}^{\text{rated,max}}. \tag{2.19}$$

Accordingly, its effective series-voltage window is summarized by:

$$V_{ES}^{\min} \leq V_{ES} \leq V_{ES}^{\max}. \tag{2.20}$$

In the rest of this part, two NC-load cases: (A) constant-resistive and (B) CPL will be investigated.

A. In Presence of Resistive NC Load

When the NC load is purely resistive with resistance R_o, substituting the smart-load relation into (2.18) gives a source–bus relation that can be written as:

$$V_{DC} = V_{\text{bus}} + \frac{R_d}{R_o\, V_{\text{bus}}}\left[V_{\text{bus}}(V_{\text{bus}} - V_{ES}) + R_o P_c\right]. \tag{2.21}$$

Taking the partial derivative with respect to V_{ES} yields:

$$\frac{\partial V_{DC}}{\partial V_{ES}} = -\frac{R_d}{R_o} V_{\text{bus}} < 0, \tag{2.22}$$

This shows a monotonic and linear decrease of V_{DC} as V_{ES} increases. The feasible V_{ES} is limited simultaneously by the ES ratings, the NC-load voltage range, and the smart-load current bound. Enforcing (2.19) around a nominal bus value $V_{\text{bus}}^{\text{nom}}$ yields the interval constraints:

$$\begin{aligned}
&V_{ES}^{\text{rated,min}} \leq V_{ES} \leq V_{ES}^{\text{rated,max}}, \\
&V_{\text{bus}}^{\text{nom}} - V_o^{\text{rated,max}} \leq V_{ES} \leq V_{\text{bus}}^{\text{nom}} - V_o^{\text{rated,min}}, \\
&V_{\text{bus}}^{\text{nom}} - R_o I_{sl}^{\text{rated,max}} \leq V_{ES} \leq V_{\text{nom}}^{\text{nom}} - R_o I_{sl}^{\text{rated,min}}.
\end{aligned} \tag{2.23}$$

Given (2.21), the minimum and maximum source voltages that still allow regulation at $V_{\text{bus}}^{\text{nom}}$ occur at the upper and lower bands of ES-voltage:

$$V_{DC}^{\min} = V_{\text{bus}}^{\text{nom}} + \frac{R_d}{R_o\, V_{\text{bus}}^{\text{nom}}}\left[V_{\text{bus}}^{\text{nom}}\left(V_{\text{bus}}^{\text{nom}} - V_{ES}^{\max}\right) + R_o P_c\right], \tag{2.24}$$

$$V_{DC}^{\max} = V_{\text{bus}}^{\text{nom}} + \frac{R_d}{R_o\, V_{\text{bus}}^{\text{nom}}}\left[V_{\text{bus}}^{\text{nom}}\left(V_{\text{bus}}^{\text{nom}} - V_{ES}^{\min}\right) + R_o P_c\right]. \tag{2.25}$$

Rearranging (2.21) gives an explicit expression for the bus voltage:

$$V_{\text{bus}} = f_1(R_d, R_c, R_o, V_{ES}, V_{DC}) = \frac{R_o R_c}{R_o R_c + R_c R_d + R_d R_o}\left[V_{DC} + \frac{R_d V_{ES}}{R_o}\right] \tag{2.26}$$

Hence, three operating regions emerge:

$$V_{\text{bus}} = \begin{cases} f_1(R_d, R_c, R_o, V_{ES}^{\max}, V_{DC}), & V_{DC} < V_{DC}^{\min}, \\ V_{\text{bus}}^{\text{nom}}, & V_{DC}^{\min} \leq V_{DC} \leq V_{DC}^{\max}, \\ f_1(R_d, R_c, R_o, V_{ES}^{\min}, V_{DC}), & V_{DC} > V_{DC}^{\max}. \end{cases} \tag{2.27}$$

Thus, when V_{DC} lies inside $[V_{DC}^{\min}, V_{DC}^{\max}]$, the ES holds the bus at $V_{\text{bus}}^{\text{nom}}$; when it does not, the ES saturates and the bus departs from its reference.

Solving (2.21) for V_{ES} yields

$$V_{ES} = f_2(R_d, R_c, R_o, V_{\text{bus}}, V_{DC}) = \frac{R_o}{R_d}\left[V_{\text{bus}}\left(1 + \frac{R_d}{R_c} + \frac{R_d}{R_o}\right) - V_{DC}\right], \tag{2.28}$$

which induces the piecewise ES-voltage behavior

$$V_{ES} = \begin{cases} V_{ES}^{\max}, & V_{DC} < V_{DC}^{\min}, \\ f_2(R_d, R_c, R_o, V_{\text{bus}}^{\text{nom}}, V_{DC}), & V_{DC}^{\min} \leq V_{DC} \leq V_{DC}^{\max}, \\ V_{ES}^{\min}, & V_{DC} > V_{DC}^{\max}. \end{cases} \tag{2.29}$$

Equations (2.27)–(2.29) define the regulation envelope for a resistive NC load. The next part will investigate the voltage regulation procedure in the presence of CPLs.

B. In Presence of Constant Power NC Load

If the NC load behaves as a CPL with power $P_o > 0$, the supply–bus relation changes. Combining (2.18) with the CPL form results in

$$V_{DC} = V_{\text{bus}} + \frac{R_d}{V_{\text{bus}}}\left[\frac{V_{\text{bus}} P_o}{(V_{\text{bus}} - V_{ES})} + \frac{V_{\text{bus}}^2}{R_c}\right] \tag{2.30}$$

Differentiating with respect to V_{ES} gives

$$\frac{\partial V_{DC}}{\partial V_{ES}} = \frac{R_d P_o}{(V_{\text{bus}} - V_{ES})^2} \; > \; 0 \tag{2.31}$$

So, increasing V_{ES} makes V_{DC} increase, opposite to the resistive case. To maintain $V_{\text{bus}} = V_{\text{bus}}^{\text{nom}}$, the admissible V_{ES} interval again follows from the ES ratings, NC-load range, and smart-load current limits:

$$\begin{aligned}
&V_{ES}^{\text{rated,min}} \le V_{ES} \le V_{ES}^{\text{rated,max}}, \\
&V_{\text{bus}}^{\text{nom}} - V_{o}^{\text{rated,max}} \le V_{ES} \le V_{\text{bus}}^{\text{nom}} - V_{o}^{\text{rated,min}}, \\
&V_{\text{bus}}^{\text{nom}} - R_o I_{sl}^{\text{rated,max}} \le V_{ES} \le V_{\text{bus}}^{\text{nom}} - R_o I_{sl}^{\text{rated,min}}.
\end{aligned} \tag{2.32}$$

At the ES limits, the extreme source voltages that still permit regulation become:

$$V_{DC}^{\min} = V_{\text{bus}} + \frac{R_d}{V_{\text{bus}}}\left[\frac{V_{\text{bus}}P_o}{(V_{\text{bus}} - V_{ES}^{\min})} + \frac{V_{\text{bus}}^2}{R_c}\right] \tag{2.33}$$

$$V_{DC}^{\max} = V_{\text{bus}} + \frac{R_d}{V_{\text{bus}}}\left[\frac{V_{\text{bus}}P_o}{(V_{\text{bus}} - V_{ES}^{\max})} + \frac{V_{\text{bus}}^2}{R_c}\right] \tag{2.34}$$

Rearranging (2.30) defines a nonlinear bus-voltage mapping

$$V_{\text{bus}} = f_3(R_d, R_c, R_o, V_{ES}, V_{DC}) = \tag{2.35}$$

$$\frac{R_cV_{DC} + R_cV_{ES} + R_dV_{ES} \pm \sqrt{(R_cV_{DC} + R_cV_{ES} + R_dV_{ES})^2 - 4(R_c + R_d)(R_cV_{DC}V_{ES} + R_dR_cP_o)}}{2(R_c + R_d)}$$

which induces the operating regions, as below:

$$V_{\text{bus}} = \begin{cases} f_3(R_d, R_c, R_o, V_{ES}^{\min}, V_{DC}), & V_{DC} < V_{DC}^{\min}, \\ V_{\text{bus}}^{\text{nom}}, & V_{DC}^{\min} \le V_{DC} \le V_{DC}^{\max}, \\ f_3(R_d, R_c, R_o, V_{ES}^{\max}, V_{DC}), & V_{DC} > V_{DC}^{\max}. \end{cases} \tag{2.36}$$

Solving (2.30) for V_{ES} gives:

$$V_{ES} = f_4(R_d, R_c, R_o, V_{\text{bus}}, V_{DC}) = \frac{(-R_cV_{\text{bus}})V_{DC} + (R_cV_{\text{bus}}^2 + R_dV_{\text{bus}}^2 + P_oR_cR_d)}{(-R_c)V_{DC} + (R_cV_{\text{bus}} + R_dV_{\text{bus}})} \tag{2.37}$$

which can be summarized in the piecewise form, as below:

$$V_{ES} = \begin{cases} V_{ES}^{\min}, & V_{DC} < V_{DC}^{\min}, \\ f_4(R_d, R_c, R_o, V_{\text{bus}}^{\text{nom}}, V_{DC}), & V_{DC}^{\min} \le V_{DC} \le V_{DC}^{\max}, \\ V_{ES}^{\max}, & V_{DC} > V_{DC}^{\max}. \end{cases} \tag{2.38}$$

The derived envelopes reveal how R_d and the load type shape DC-ES behavior. For a

Table 2.6: Parameters of the Electric Spring Under Consideration.

Description	Parameter	Value
Nominal dc bus voltage	$V_{\text{bus,nom}}$	48 V
Distribution line resistance	R_d	0.33 Ω
Critical load resistance	R_c	14 Ω
Resistive NC load	R_o	15.6 Ω
Constant-power NC load	P_o	147 W
ES minimum voltage (for R_o)	$V_{\text{es,min}}$	−24 V
ES maximum voltage (for R_o)	$V_{\text{es,max}}$	60 V
ES minimum voltage (for P_o)	$V_{\text{es,min}}$	−24 V
ES maximum voltage (for P_o)	$V_{\text{es,max}}$	10 V

resistive NC load, V_{DC} decreases with V_{ES} (negative slope); for a CPL, the trend reverses (positive slope under the stated convention), which implies distinct regulation dynamics. In both cases, the effective regulation corridor $[V_{DC}^{\min}, V_{DC}^{\max}]$ defines where V_{bus} is held at $V_{\text{bus}}^{\text{nom}}$. Once V_{DC} leaves this interval, the ES saturates at $V_{ES}^{\min}$ or $V_{ES}^{\max}$ and the bus voltage drifts with the source. These results actively guide DC-ES sizing and controller design: by quantifying the interplay among converter ratings, NC-load constraints, and R_d, they indicate precisely when a DC-ES can sustain stable regulation under varying supply and load conditions.

To investigate how the proposed DC-ES behaves and regulates voltage in practice, the test-bench of Fig. 2.7 can be employed, where its nominal DC bus (V_{nom}) is set to 48 V.

In order to emulate the inherent intermittency of RESs, the supply-side voltage V_{DC} is deliberately varied over time. Two representative operating cases are considered: (i) a resistive NC load and (ii) a constant-power NC load. The electrical parameters of the system are listed in Table 2.6. Considering a resistive NC Load, from the network in Fig. 2.7, the nominal source that supports V_{nom} is obtained as:

$$V_{DC}^{\text{nom}} = V_{\text{nom}} \frac{\left(\dfrac{R_o R_c}{R_o + R_c}\right) + R_d}{\left(\dfrac{R_o R_c}{R_o + R_c}\right)} \tag{2.39}$$

which evaluates to $V_{DC}^{\text{nom}} = 50.18$ V. In the first stage ($t = 0$–200 s), the DC-ES is leaved disabled while the source follows a fluctuating profile. In the second stage ($t = 201$–400 s), the DC-ES will be enabled and reapply the same source profile. Fig. 2.9 displays the waveforms over the entire 400 s window. A magnified view around the enable instant at $t = 200$ s shows that the bus settles to its reference in about 400 ms [2].

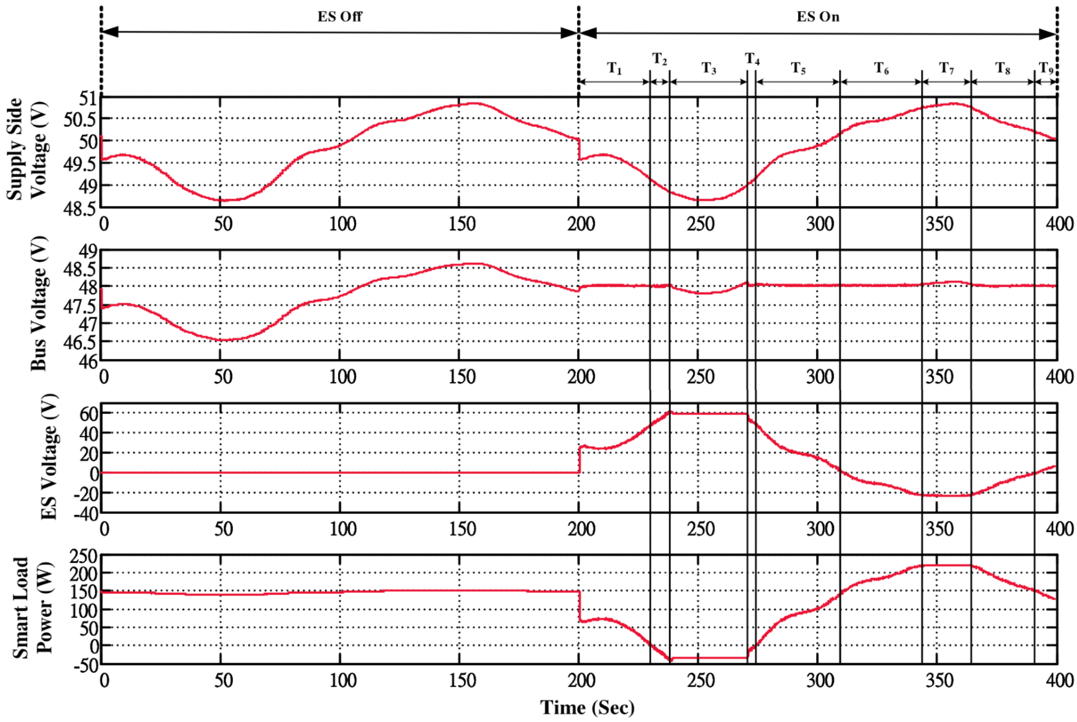

Figure 2.9: The response of ES with a resistive NC load, following random power generation of the intermittent source. ES is activated at t=200 s.

Fig. 2.9 also provides time-domain traces of the instantaneous smart-load. While the DC-ES is off ($t = 0$–200 s), the bus directly mirrors source variations and wanders between 48.5 V and 51 V. Once the DC-ES is *on* ($t = 201$–400 s), it tightly regulates the bus near V_{nom}, except during two brief intervals, T_3 and T_7, where the ES reaches its hardware limits.

Specifically, during T_1, T_5, and T_9, the ES voltage is positive but less than V_{nom}, corresponding to Region 2 of Table 2.4. During T_6, T_7, and T_8, the ES voltage becomes negative (Region 1). In T_2, T_3, and T_4, the ES voltage remains positive and moves between V_{nom} and its ceiling $V_{ES}^{\max}$ (Region 3).

When V_{ES} hits its lower limit $V_{ES}^{\min}$ (i.e., T_3) or upper limit $V_{ES}^{\max}$ (i.e., T_7), the ES saturates and can no longer hold V_{bus} exactly at V_{nom}. These events verify the finite compensation span of an ES, analogous to the stroke of a mechanical spring. In practice, one can reduce such regulation gaps by deploying multiple ES units along the feeder to share the compensation duty and increase voltage support robustness.

Turning to the second scenario, for the constant power NC load with the power P_o, the

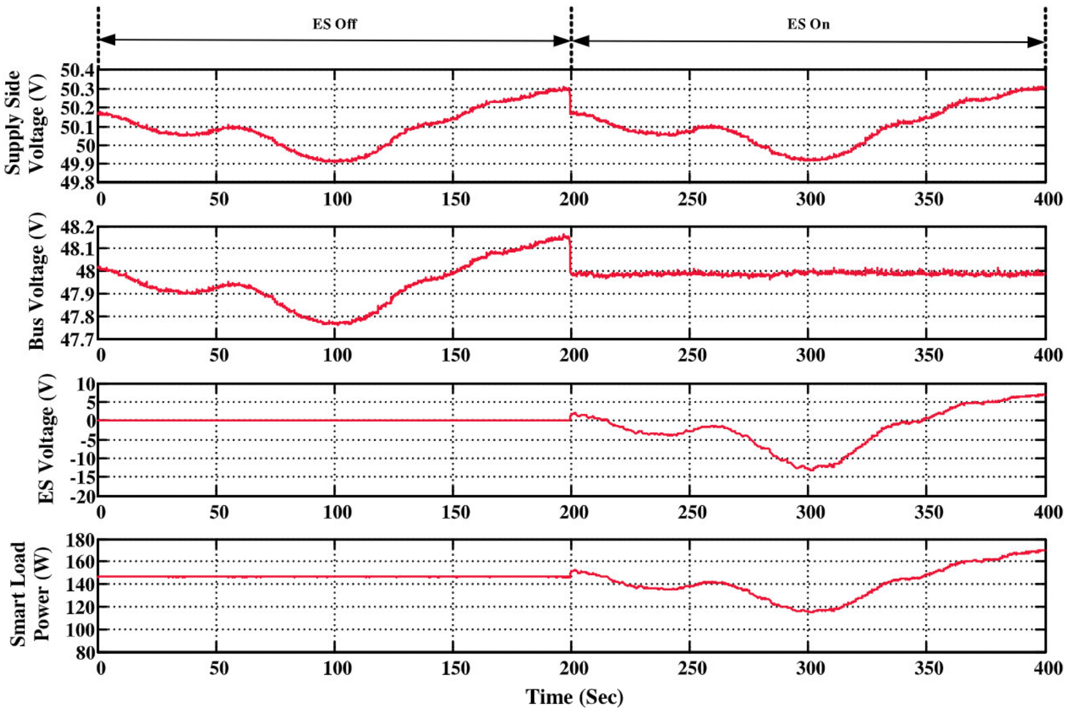

Figure 2.10: The response of ES with a constant-NC load, following random power generation of the intermittent source. ES is activated at t=200 s.

nominal source consistent with V_{nom} follows:

$$V_{DC}^{\text{nom}} = R_d \left(\frac{P_o}{V_{\text{nom}}} + \frac{V_{\text{nom}}}{R_c} + \frac{V_{\text{nom}}}{R_d} \right), \tag{2.40}$$

which yields $V_{DC}^{\text{nom}} = 50.14$ V.

It should be noted that the waveforms here are similar to those in the resistive case (i.e., DC-ES off for $t = 0$–200 s and DC-ES on for $t = 201$–400 s under the same fluctuating source). As before, Fig. 2.10 expands the traces to highlight the full-period response of voltages as well as smart-load power. With the ES disabled ($t = 0$–200 s), the bus oscillates slightly, tracking the source. After enabling the ES ($t = 201$–400 s), the regulation remains effective and compensates source fluctuations dynamically. Unlike the resistive case, however, the CPL implementation uses a unidirectional buck stage for the NC load, so negative ES voltages cannot be applied. Consequently, the ES operates only in Region 1 ($V_{ES} < 0$) or Region 2 ($0 < V_{ES} < V_{\text{bus}}$) [2].

Overall, it can be stated that the DC-ES acts as an *electrical damping spring*: it releases or absorbs energy on demand to counter supply-side fluctuations and load variability. The observed settling and the near-nominal bus under both load types demonstrate the device's suitability as a distributed, demand-side flexibility resource that enhances the resilience of islanded DC microgrids.

2.4 Summary of the Chapter

This chapter explores flexibility as a fundamental attribute for the stable and efficient operation of stand-alone DC (MGs) with high penetrations of RESs. Flexibility is defined as the capability of system components—such as (DGs), (ESSs), and controllable loads—to adjust their operation to fulfill reliable operation. In islanded DC MGs, where no external grid support exists, flexibility is crucial for maintaining voltage stability, power balance, and supply reliability under variable renewable generation and stochastic load conditions.

The chapter first establishes a unified definition of flexibility based on international standards and recent research, identifying three key criteria: (i) the type of resource providing it, (ii) the duration of activation, and (iii) its responsiveness to control signals. These principles enable a systematic characterization of flexibility within isolated MGs, highlighting that flexibility is a measurable, controllable resource that underpins operational resilience and proper energy management.

A comprehensive taxonomy of flexibility resources is then presented, classifying them by system position (supply-, demand-, or network-side), functional role, direction of load shifting, mathematical representation, and availability. This framework supports consistent evaluation of flexibility sources in DC MGs, revealing that while various technologies can contribute, ESS—particularly BESS—are the most practical and effective for islanded configurations.

BESS offer high controllability, rapid response, bidirectional power flow, and independence from generation or load dynamics. They can quickly absorb excess renewable energy and discharge during shortages, ensuring real-time power balance and voltage stability. Their scalability, compactness, and native compatibility with DC systems further strengthen their role in autonomous MGs.

Finally, the chapter introduces the DC-ES as an emerging concept that enhances flexibility through coordinated BESS regulation and load control. By dynamically adjusting non-critical load voltage, the DC-ES maintains bus voltage stability and power balance—offering a fast, distributed means of improving MG flexibility.

Chapter 3

Stability Analysis and Security Improvement

The previous chapter examined the diverse flexibility resources available in MGs, highlighting their contribution to improving reliability, stability, and overall operational efficiency. Both supply-side and demand-side flexibility options were analyzed, encompassing energy storage systems, controllable loads, distributed generation, and demand response mechanisms, emphasizing the importance of the implementation of the ES concept as a flexibility enabler.

This chapter focuses on the modeling and stability assessment of DC-MGs, with particular emphasis on droop-controlled operation and the influence of Constant Power Loads (CPLs). As an emerging class of distributed power systems, renewable-source-based MGs have attracted significant research attention for their capability to integrate local means of generation and energy storage units, thereby delivering reliable and high-quality power to local loads.

The operation of DC-MGs exhibits complex dynamic behavior due to the parallel interconnection of multiple distributed energy sources, the presence of tightly regulated converters that behave as CPLs, inherent uncertainties in renewable generation, and strong coupling among subsystems under varying operating conditions. To ensure stable and efficient performance, it is essential to develop detailed subsystem models and derive an aggregated small-signal representation of the overall system. Such modeling enables a systematic investigation of how control parameters—such as voltage and current references or droop coefficients—as well as system parameters, including line resistances and load characteristics, influence the dynamic response and small-signal stability of the microgrid.

In contrast to AC systems, where frequency naturally reflects load variations, DC systems lack a global variable that indicates load demand. This absence complicates both load estimation and stability assurance, particularly when the load comprises a combination of constant power, constant voltage, and constant current components. Moreover, in applications such as Electric Vehicle (EV) charging infrastructures, the aggregate demand often exhibits pulse-like characteristics, with periods of high instantaneous loading followed by idle intervals. If not properly mitigated, these rapid transitions can significantly degrade system stability.

Small-signal analysis provides a powerful framework for understanding, predicting, and mitigating such instabilities. By linearizing the nonlinear system dynamics around an equilibrium point, small-signal models enable controller design, stability margin evaluation, and parameter sensitivity studies—each critical for maintaining voltage regulation, current sharing, and overall power balance during islanded operation.

Beyond stability analysis, insights obtained from small-signal modeling directly support the development of advanced energy management strategies. These strategies can dynamically coordinate converter operating modes, while accounting for the State of Charge (SoC) of storage units and optimizing current-sharing schemes. Hence, small-signal analysis serves not only as a stability evaluation tool but also as a decision-support framework for improving the efficiency, reliability, and seamless mode transitions of DC-MGs.

Accordingly, the following section introduces the theoretical foundations for small-signal modeling of DC-MGs under droop control, alongside the definition and representation of CPLs. These models form the analytical basis for the subsequent stability assessment and control design presented in the following sections.

3.1 Small-Signal Modeling of DC Microgrids with Droop Control Mechanism

As discussed previously, analyzing the dynamic behavior and stability of droop-controlled DC-MGs requires an accurate small-signal model capable of capturing the key interactions among distributed sources, electrical loads, and network components. Accordingly, this section develops a comprehensive small-signal modeling framework aimed at deriving a reduced-order linearized representation suitable for stability and eigenvalue analysis.

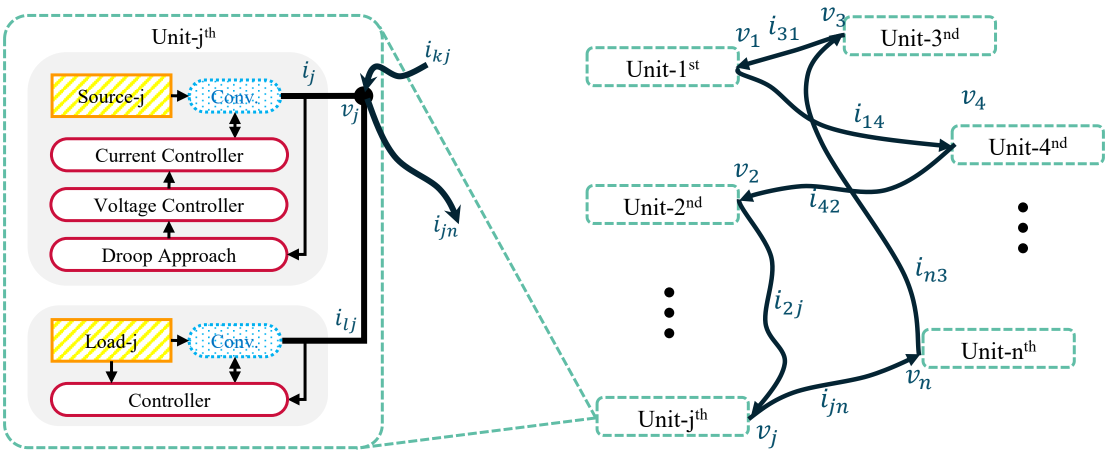

Figure 3.1: DC-MG with several units and loads.

The proposed approach decomposes the DC-MG into its primary functional subsystems—namely, distributed sources, loads (including both resistive and CPLs), and interconnecting lines modeled with lumped *R*–*L* parameters [134]. Controllable units with dissimilar electrical characteristics are interfaced to the MG through Power Electronic Converter (PEC). Each of these components is represented by its corresponding set of linearized dynamic equations. The droop control mechanism, which adjusts each converter's reference voltage in proportion to its output current, is explicitly incorporated into the model to capture its dual impact on bus voltage regulation and current-sharing accuracy among Distributed Generation (DG) units [135].

The electrical coupling among converters, loads, and the common DC bus is formulated using Kirchhoff's voltage law (KVL) and Kirchhoff's current law (KCL), enabling systematic aggregation of all component-level dynamics into a unified small-signal state-space model. This formulation captures both the fast converter dynamics and the slower droop control responses, revealing the coupled electromechanical interactions that govern overall system behavior [136]. The resulting reduced-order small-signal model provides a rigorous analytical basis for evaluating the eigenvalues of the DC-MG, determining stability margins, and performing sensitivity analyses with respect to key physical and control parameters, such as line impedance and droop coefficients. This framework forms the theoretical foundation for the stability assessments and droop controller optimization presented in the following sections.

3.2 Modeling System Stability for Small Perturbations

Before delving into the modeling process, it is first useful to outline the overall architecture of the proposed droop-controlled DC-MG. As it is illustrated in Fig. 3.1, each part in a typical DC-MG generally hosts a local energy source and associated loads, both interfaced to the common bus via PECs, which serve as the primary means of voltage regulation and current control. Depending on the specific type of energy source—such as PV arrays, fuel cells, EESs, or AC-based sources like wind turbines and diesel generators—appropriate power conversion stages (DC–DC or AC–DC) are employed to ensure proper interfacing, voltage adaptation, and bidirectional power flow capability when required [84].

To enable autonomous operation and proportional power sharing among the distributed sources, a droop control mechanism is implemented at each converter. In this control scheme, the reference voltage of each converter is modulated in proportion to its output current, thereby achieving power balance among units (see Fig. 3.1).

Typically, the droop controller operates in coordination with an inner voltage/current regulation loop. This inner loop, characterized by high bandwidth, ensures that the converter output voltage accurately tracks the reference command with minimal transient disparity. The outer droop loop (i.e., the droop control layer in this dissertation), on the other hand, governs the slower dynamics associated with load sharing and voltage regulation across the network.

On the demand side, most practical DC loads—such as electric drives, data center servers, lighting systems, and consumer electronics—exhibit nearly constant power characteristics within their operational range. These loads are modeled as CPLs, which are known to introduce negative incremental impedance behavior. Specifically, when the bus voltage decreases, a CPL draws higher current to maintain constant power consumption, thereby inducing a destabilizing negative damping effect that can significantly impact small-signal stability [130]. Accurately capturing this dynamic phenomenon is therefore crucial for developing a reliable analytical model of the DC-MG. Not to mention that further details in this regard will be discussed in the following section of this chapter (refer to section 3.4).

The electrical interconnections among the distributed nodes are realized through low-voltage DC cables whose resistive and inductive components define the coupling strength between nodes and influence the overall dynamic performance of the system. The network topology can be systematically represented using the relationships between node voltages and branch currents in accordance with Kirchhoff's voltage (KVL) and current laws

(KCL) The architectural overview provided in this section establishes the foundation for the mathematical modeling of droop-controlled DC-MGs. Building upon this structural understanding, the subsequent subsection derives the small-signal equations governing the dynamic behavior of distributed sources, CPLs, and interconnecting lines. These equations are then systematically integrated into a unified reduced-order model, providing a rigorous analytical basis for the stability and sensitivity analyses presented in the following sections.

For clarity, the remainder of Section 3.1 is organized as follows. Subsection 3.2.1 formulates the small-signal modeling of the droop-controlled DC microgrid, including the derivation of linearized equations for sources, loads, and interconnecting cables, which are subsequently integrated into a reduced-order state-space representation. Subsection 3.4.2 focuses on the interpretation of the derived mathematical model by examining the system eigenvalues and establishing sufficient conditions for stable operation based on droop parameters and load characteristics. Subsection 3.3.2 investigates the influence of key physical parameters—such as line resistance and inductance—on the system's dynamic behavior, providing insights into the movement of system poles and their implications for microgrid stability and performance.

3.2.1 Mathematical Representation

A DC-MG generally consists of three primary components:

- Distributed converter-based suppliers,
- Electrical loads,
- Interconnecting distribution lines.

The overall behavior of the system emerges from the coupled interactions among these components, which are governed by the electrical topology of the network and the associated control mechanisms. In the following subsections, the small-signal dynamic equations of each component are systematically derived.

3.2.1.1 Equations of Distributed Generation Units

The block diagram of a droop-controlled Voltage Source Converter (VSC) is depicted in Fig. 3.1. In this configuration, the outer droop control loop generates the reference voltage for the inner voltage controller using locally measured electrical quantities. High-bandwidth voltage regulation techniques for DC–DC converters have been extensively studied in the literature [137]. Since droop controllers generally operate at much lower sampling frequencies than inner voltage control loops, the system order can be reduced by exploiting this time-scale separation. Accordingly, for the purpose of small-signal analysis of the DC-MG and its droop-controlled converters, the fast inner voltage dynamics can be neglected [138]. Under this assumption, each converter is modeled as an ideal controllable voltage source, where the converter output voltage v_j is assumed to instantaneously follow its reference value, i.e.,

$$v_j = v_{j,\mathrm{ref}} \tag{3.1}$$

In a droop-controlled system, each source locally adjusts its reference voltage according to its measured output current. The droop control law for the j-th converter is defined as:

$$v_j^{\mathrm{ref}} = v_j^0 - d_j i_j, \tag{3.2}$$

where v_j^0 denotes the nominal no-load voltage (i.e., the terminal voltage when the output current is zero), and d_j represents the droop coefficient of the converter.

Assuming an ideal voltage-source converter, substituting the control law (3.2) into the converter output equation yields:

$$v_j = v_j^0 - d_j i_j. \tag{3.3}$$

Introducing small-signal perturbations around the steady-state operating point leads to the linearized form:

$$\hat{v}_j = -d_j \hat{i}_j, \tag{3.4}$$

where the symbol $(\hat{\cdot})$ denotes a small-signal deviation from the operating point.

For a system comprising N distributed sources, the small-signal droop equations can be expressed in compact matrix form as:

$$\hat{\mathbf{v}} = -\mathbf{D}\hat{\mathbf{i}}, \tag{3.5}$$

where $\hat{\mathbf{v}} = [\hat{v}_1, \hat{v}_2, \ldots, \hat{v}_N]^T$ and $\hat{\mathbf{i}} = [\hat{i}_1, \hat{i}_2, \ldots, \hat{i}_N]^T$ are the column vectors of small-signal source voltages and currents, respectively. The matrix $\mathbf{D} = \mathrm{diag}(d_1, d_2, \ldots, d_N)$ is diagonal and contains the droop gains of the converters' controller.

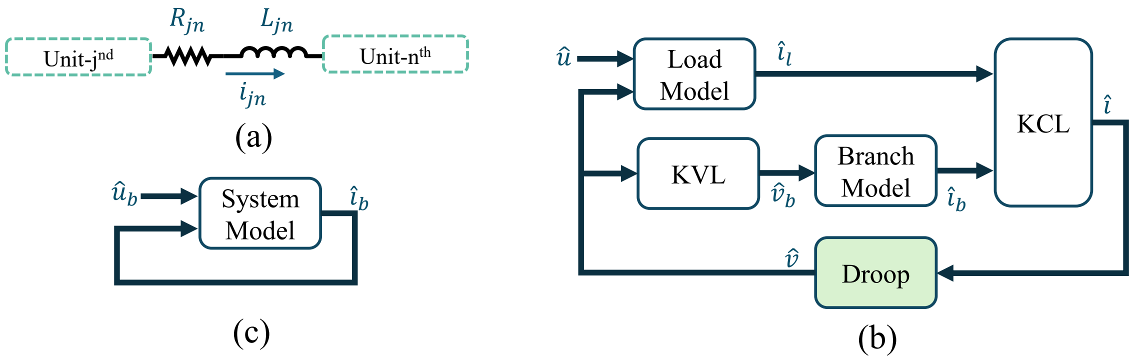

Figure 3.2: (a) Model of connecting lines, (b) Block diagram of the interacted subsystems, (c) System block diagram.

3.2.1.2 Equations of Integrated Loads

As CPLs exhibit a negative incremental impedance characteristic, it can be modeled as negative-resistance components, as described in [139]. In their small-signal representation, each CPL is approximated by a negative conductance $(-g_{lj})$ connected in parallel with a current sink term u_j. Accordingly, the small-signal current drawn by the j-th load can be expressed as:

$$\hat{i}_{lj} = -g_{lj}\hat{v}_j + \hat{u}_j, \tag{3.6}$$

For more explanations about the above formula, please refer to section 3.4.2. By aggregating the contributions of all load buses, the collective CPL dynamics can be expressed in compact matrix form as:

$$\hat{\mathbf{i}}_l = -\mathbf{G}_l\hat{\mathbf{v}} + \hat{\mathbf{u}}, \tag{3.7}$$

where $\hat{\mathbf{i}}_l = [\hat{i}_{l1}, \hat{i}_{l2}, \ldots, \hat{i}_{lN}]^T$ and $\hat{\mathbf{v}} = [\hat{v}_1, \hat{v}_2, \ldots, \hat{v}_N]^T$ are the column vectors of small-signal load currents and bus voltages, respectively. The diagonal matrix $\mathbf{G}_l = \mathrm{diag}(g_{l1}, g_{l2}, \ldots, g_{lN})$ contains the incremental conductance of each load. AS mentioned earlier, since each g_{lj} is negative ($g_{lj} < 0$), $\mathbf{G}_l$ explicitly captures the destabilizing effect introduced by CPLs in the small-signal dynamics of the DC-MG.

3.3 Small-Signal Stability Analysis

3.3.0.1 Equations of Connecting Lines

The interconnecting distribution lines in the DC-MG are modeled as series combinations of resistance and inductance, as illustrated in Fig. 3.2(a). For the j-th line, the small-signal relationship between voltage and current is expressed as:

$$\hat{v}_{bj} = L_{bj}\frac{d\hat{i}_{bj}}{dt} + R_{bj}\,\hat{i}_{bj}, \tag{3.8}$$

where $\hat{v}_{bj}$ and $\hat{i}_{bj}$ denote the small-signal deviations of the branch voltage and current, respectively. The parameters L_{bj} and R_{bj} represent the inductance and resistance of the j-th line segment. By aggregating the dynamic equations of all interconnecting branches, the collective line dynamics can be written in compact matrix form as:

$$\hat{\mathbf{v}}_b = \mathbf{L}_b\frac{d\hat{\mathbf{i}}_b}{dt} + \mathbf{R}_b\,\hat{\mathbf{i}}_b, \tag{3.9}$$

where $\hat{\mathbf{v}}_b$ and $\hat{\mathbf{i}}_b$ are the column vectors of small-signal branch voltages and currents, respectively. The diagonal matrices $\mathbf{L}_b = \mathrm{diag}(L_{b1}, L_{b2}, \ldots, L_{bM})$ and $\mathbf{R}_b = \mathrm{diag}(R_{b1}, R_{b2}, \ldots, R_{bM})$ contain the inductance and resistance values of all distribution lines in the network.

This formulation establishes the electrical coupling among buses and forms the foundation for deriving the network admittance matrix used in the subsequent small-signal and stability analyses.

3.3.0.2 Equations of the Interconnected Network

The electrical interconnection structure of the DC-MG can be represented using KVL and KCL. In matrix form, KVL is expressed as:

$$\hat{\mathbf{v}}_b = \mathbf{M}\,\hat{\mathbf{v}}, \tag{3.10}$$

where $\hat{\mathbf{v}}_b$ is the vector of branch voltages, $\hat{\mathbf{v}}$ is the vector of nodal (bus) voltages, and $\mathbf{M}$ is the network incidence matrix of dimension $m \times n$, with m and n denoting the number of branches and nodes, respectively [134]. It is worth noting that the columns of $\mathbf{M}$ are linearly dependent, as the algebraic sum of all nodal voltages in a connected network is constrained by the chosen reference node.

Similarly, KCL can be compactly formulated as:

$$\hat{\mathbf{i}} - \hat{\mathbf{i}}_l = \mathbf{M}^T\,\hat{\mathbf{i}}_b, \tag{3.11}$$

where $\hat{\mathbf{i}}$ and $\hat{\mathbf{i}}_l$ denote the small-signal vectors of injected source currents and load currents, respectively, and $\hat{\mathbf{i}}_b$ represents the vector of branch currents. Equation (3.11) enforces current conservation at each node, linking nodal and branch current variables through the network topology encapsulated in $\mathbf{M}^T$.

The linearized small-signal relationships governing the different components of the DC-MG are summarized in (3.5), (3.7), and (3.8)–(3.11). The interconnections among these subsystems are schematically depicted in Fig. 3.2(b). As shown, all elements—except for the distribution lines—are described by algebraic equations, whereas the line model includes differential terms arising from the inductive dynamics of the network branches. Consequently, the branch current vector $\hat{\mathbf{i}}_b$ is selected as the system's state variable, while the control input vector is denoted by $\hat{\mathbf{u}}$.

The integrated block diagram representing the complete small-signal model is illustrated in Fig. 3.2(c), explicitly capturing the coupling among the source, load, and network dynamics. The corresponding state-space representation of the linearized DC-MG can be expressed as:

$$\frac{d\hat{\mathbf{i}}_b}{dt} = \mathbf{A}\,\hat{\mathbf{i}}_b + \mathbf{B}\,\hat{\mathbf{u}}, \tag{3.12}$$

where:

$$\begin{aligned}\mathbf{A} &= -\mathbf{L}_b^{-1}\left[\mathbf{M}\left(\mathbf{D}^{-1}-\mathbf{G}_l\right)^{-1}\mathbf{M}^T+\mathbf{R}_b,\right],\\ \mathbf{B} &= -\mathbf{L}_b^{-1}\mathbf{M}\left(\mathbf{D}^{-1}-\mathbf{G}_l\right)^{-1}.\end{aligned}$$

This formulation provides a compact and analytically tractable representation of the DC-MG, in response to small perturbations in the input signal $\hat{\mathbf{u}}$. It provides an effective representation of the system's transient behavior by emphasizing the dominant electrical dynamics associated with the line inductances, while higher-order converter and load dynamics are embedded within the model parameters.

3.3.1 Stability Interpretation Based on Model Parameters

The transient dynamics of the DC-MG are governed by the first-order differential equations in (3.12). The small-signal stability of the system under bounded perturbations is determined by the eigenvalues of the state matrix $\mathbf{A}$. If all eigenvalues lie in the left half of the complex plane—i.e., their real parts are negative—the system is asymptotically stable.

To facilitate the stability assessment, the matrix $\mathbf{A}$ can be decomposed as:

$$\mathbf{A} = \mathbf{H}^{-1}\mathbf{U}, \tag{3.13}$$

where

$$\mathbf{H} = -\mathbf{L}_b, \qquad \mathbf{U} = \mathbf{M}\big(\mathbf{D}^{-1} - \mathbf{G}_l\big)^{-1}\mathbf{M}^T + \mathbf{R}_b.$$

Here, $\mathbf{H}$ and $\mathbf{U}$ are real symmetric matrices encapsulating the effects of the line, droop, and load subsystems. Following the procedure in [140], the eigenvalues of $\mathbf{A}$ are given by:

$$\lambda = \frac{\mathbf{e}^T\mathbf{U}\mathbf{e}}{\mathbf{e}^T\mathbf{H}\mathbf{e}}, \tag{3.14}$$

where $\mathbf{e}$ denotes the corresponding real eigenvector.

Since $\mathbf{H}$ is diagonal with strictly negative entries, it is negative definite, implying $\mathbf{e}^T\mathbf{H}\mathbf{e} < 0$. Therefore, for all eigenvalues to have negative real parts, the numerator in (3.14) must be positive, i.e.,

$$\mathbf{e}^T\mathbf{U}\mathbf{e} > 0. \tag{3.15}$$

Substituting $\mathbf{U}$ from (3.13) yields:

$$\mathbf{e}^T\mathbf{M}\big(\mathbf{D}^{-1} - \mathbf{G}_l\big)^{-1}\mathbf{M}^T\mathbf{e} + \mathbf{e}^T\mathbf{R}_b\mathbf{e} > 0. \tag{3.16}$$

Given that $\mathbf{R}_b$ is a positive definite diagonal matrix, $\mathbf{e}^T\mathbf{R}_b\mathbf{e} > 0$, the sufficient stability condition simplifies to:

$$\mathbf{e}^T\mathbf{M}\big(\mathbf{D}^{-1} - \mathbf{G}_l\big)^{-1}\mathbf{M}^T\mathbf{e} \geq 0. \tag{3.17}$$

Hence, the matrix $(\mathbf{D}^{-1} - \mathbf{G}_l)$ must be positive semidefinite to ensure system stability. This requirement leads to the scalar condition

$$1 - g_{lj}d_j \geq 0, \qquad \forall j \in \{1,2,\ldots,n\}, \tag{3.18}$$

or equivalently,

$$d_j \leq \frac{1}{g_{lj}^{\max}}, \qquad \forall j \in \{1,2,\ldots,n\}.$$

Equation (3.18) specifies the admissible upper bound for the droop coefficient that guarantees stable operation. The result reveals that the stability margin of each converter is directly affected by the maximum incremental conductance of its local CPL. In practical terms, higher load stiffness (i.e., more negative incremental conductance) necessitates smaller droop gains to preserve stable voltage regulation in the DC-MG [10].

3.3.2 Sensitivity Analysis

The permissible range of droop coefficients established in (3.18) serves as a fundamental guideline for ensuring stable operation in DC-MGs. To complement this theoretical result, a sensitivity analysis of the system poles is conducted to evaluate how key line parameters—namely, the branch inductance (L_b) and resistance (R_b)—affect the overall stability margin. This investigation provides insight into how variations in cable characteristics influence the damping and transient response of the network.

To examine the impact of inductance, all branch inductances are uniformly scaled by a positive factor $k_l > 1$, resulting in a modified inductance matrix:

$$\mathbf{L}_b^{\text{new}} = k_l \mathbf{L}_b. \tag{3.19}$$

Since $\mathbf{U}$ in (3.13) is independent of $\mathbf{L}_b$, the updated system matrix becomes:

$$\mathbf{A}^{\text{new}} = \frac{1}{k_l}\mathbf{A}. \tag{3.20}$$

Because $\mathbf{A}^{\text{new}}$ is a scalar multiple of $\mathbf{A}$, the corresponding eigenvectors remain unchanged:

$$\mathbf{e}^{\text{new}} = \mathbf{e}. \tag{3.21}$$

Applying (3.14) to the modified system yields:

$$\lambda^{\text{new}} = \frac{1}{k_l}\lambda. \tag{3.22}$$

Given that $k_l > 1$, the magnitude of the new eigenvalues $|\lambda^{\text{new}}|$ is smaller than that of the original eigenvalues $|\lambda|$. This indicates that increasing the branch inductance shifts the poles toward the imaginary axis, thereby reducing the system's stability margin and slowing its transient response.

The influence of branch resistance is analyzed next. Assuming identical cables are employed throughout the network, the resistance-to-inductance ratio remains constant and can be expressed as:

$$\alpha = \frac{r_{12}}{l_{12}} = \frac{r_{14}}{l_{14}} = \cdots = \frac{r_{jk}}{l_{jk}} = \cdots. \tag{3.23}$$

By rearranging (3.13), the system matrix can be rewritten as:

$$\mathbf{A} = \mathbf{H}^{-1}\mathbf{Q} - \alpha\mathbf{I}, \tag{3.24}$$

where **I** is the identity matrix, and

$$\mathbf{Q} = \mathbf{M}\big(\mathbf{D}^{-1} - \mathbf{G}_l\big)^{-1}\mathbf{M}^T. \tag{3.25}$$

The eigenvalues of **A** are therefore given by:

$$\lambda = \mu - \alpha, \tag{3.26}$$

where μ denotes the eigenvalues of $\mathbf{H}^{-1}\mathbf{Q}$.

To investigate the effect of increasing resistance, all branch resistances are scaled by a positive factor $k_r > 1$, leading to the following:

$$\alpha^{\text{new}} = k_r \alpha. \tag{3.27}$$

Since $\mathbf{H}^{-1}\mathbf{Q}$ is independent of resistance,

$$\mu^{\text{new}} = \mu. \tag{3.28}$$

Substituting into (3.26) yields:

$$\lambda^{\text{new}} = \mu - k_r\alpha = \lambda - (k_r - 1)\alpha. \tag{3.29}$$

Because $\alpha > 0$ and $k_r > 1$, the term $(k_r - 1)\alpha$ is positive, implying that λ^{new} shifts further left in the complex plane. Consequently, increasing branch resistance enhances system damping and improves the overall stability margin of the DC-MG. These mathematical elaborations and their implications on the dynamic behavior of the DC-MG have been quantitatively validated and demonstrated through simulation results in Chapter 4.

3.4 Constant Power Loads Definition and Modeling

Perennial advancements in power electronics, digital control, and energy conversion technologies have significantly broadened the scope of power electronic applications across MG systems [104].

As a result, modern electrical architectures have become highly power-electronics-intensive, integrating multiple converters, inverters, and motor drives operating across various DC voltage levels [97]. These converter-dominated networks exhibit complex

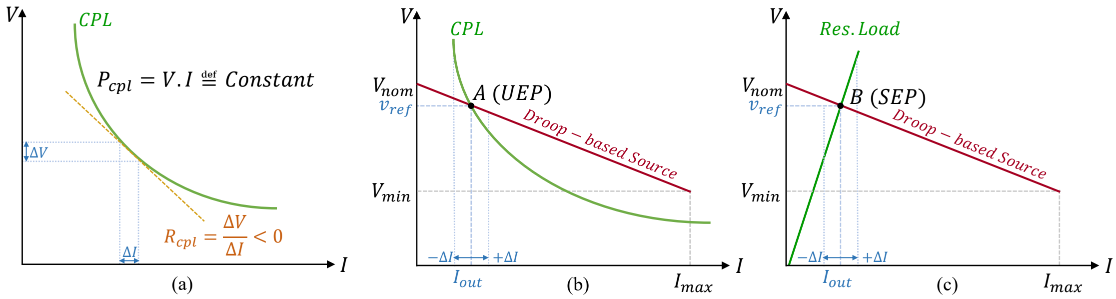

Figure 3.3: CPL and droop-based source characteristics in the voltage-current plane. (a) CPL's negative resistance, (b) Unstable equilibrium point, (c) Stable behavior of typical resistive loads.

dynamic behavior and potential stability challenges due to interactions among tightly regulated converters, nonlinear loads, and feedback-controlled devices. Understanding and mitigating such dynamic interactions are therefore crucial for ensuring the stable and reliable operation of next-generation electrified power systems.

A key factor influencing the stability of these systems is the widespread presence of CPLs. Power electronic converters and electric motor drives, when regulated to maintain constant torque, speed, or voltage, typically draw nearly constant input power from their supply buses [99].

Power electronic converters and electric motor drives could behave as CPLs at their input terminals when tightly regulated. In modern multi-converter architectures, the prevalence of loads exhibiting constant-power characteristics has increased significantly. Many subsystems—such as electric motors for the cooling system, actuators, and regulated DC–DC converters—are designed to maintain constant output power. Assuming negligible conversion losses and near-unity efficiency, the input power drawn from the DC link closely matches the output power, causing these components to exhibit CPL behavior from the perspective of the DC bus [141].

A representative example is an inverter-fed electric motor, when this mechanical load follows a one-to-one torque–speed relationship (e.g., a linear dependence between torque T and angular velocity ω). In such cases, maintaining constant speed implies constant torque. Consequently, the mechanical output power $P = T \times \omega$ remains constant. With approximately constant efficiency, the inverter therefore draws nearly constant electrical power from the DC link, effectively acting as a CPL within the MG.

A similar phenomenon occurs in DC–DC converters supplying regulated downstream loads. When a converter maintains a fixed output voltage for a load with a defined V–I characteristic (e.g., resistive or constant-voltage devices), its input power remains approximately constant, and the converter presents a CPL-type characteristic to the upstream source. Although a CPL exhibits a positive static impedance ($V/I > 0$), its incremental impedance is negative ($dV/dI < 0$). This negative incremental resistance introduces destabilizing dynamics by reducing effective system damping and potentially inducing voltage oscillations on the DC bus. The corresponding small-signal representation is illustrated in Fig. 3.3(a).

The following subsections analyze in detail how CPLs influence the dynamic response and small-signal stability of DC systems, with particular emphasis on their interactions with droop-controlled converters and energy storage interfaces.

3.4.1 Destructive Impact of Tightly Regulated Power Electronic-Based Loads on the Stability of DC Microgrids

The instantaneous power of a CPL—defined as the product of its terminal voltage and current, $P = V \cdot I$—is maintained at a fixed value. Consequently, as illustrated in Fig. 3.3(a), any increase in load voltage results in a proportional decrease in load current, and vice versa. This inverse voltage–current relationship introduces a negative incremental impedance, which can severely affect the stability of an interconnected power system [138].

To better understand this phenomenon, consider the simplified system, where a CPL with a constant power demand P is connected to a generation unit regulated by a conventional droop controller, thereby behaving as a Constant Voltage Source (CVS) with output voltage V. Under steady-state conditions, the system reaches equilibrium when the source voltage equals the load voltage, defining the nominal operating point of the circuit.

When the total load demand exceeds the available generation, the voltage at the Point of Common Connection (PCC) begins to fall. In response, the CPL attempts to maintain its constant power consumption by increasing its current draw. This heightened current demand imposes additional stress on the supply units, further reducing the PCC voltage. This behavior acts like a positive feedback mechanism that amplifies the initial voltage deviation, potentially leading to voltage instability [16].

A similar mechanism occurs in the opposite case, when the aggregate load demand drops below the available generation capacity. The PCC voltage then rises, prompting the CPL to reduce its input current to preserve constant power. This reduction in current causes an additional voltage rise, again reinforcing the deviation and destabilizing the operating point. In both scenarios, the CPL's negative incremental impedance gives rise to adverse dynamic interactions that compromise the voltage stability of the DC MG.

As illustrated in Fig. 3.3(b), the equilibrium operating point corresponds to the intersection of the voltage–current (V–I) characteristics of the droop-controlled source and the CPL, denoted as point A [130]. If a small disturbance reduces the system voltage, the CPL responds by increasing its current by an amount ΔI to sustain constant power. However, since the load voltage remains lower than the source voltage, the current continues to rise, driving the operating point further away from A. The same occurs for a small voltage increase: the current decreases, the load voltage exceeds the source voltage, and the deviation grows instead of decaying. Thus, point A is an Unstable Equilibrium Point (UEP) because the system cannot naturally restore its steady-state condition [10].

When the slopes of the source and load characteristics with opposite signs, small perturbations tend to grow over time, leading to oscillatory or divergent behavior. This outcome reflects the intrinsic destabilizing influence of the CPL's negative incremental impedance.

To illustrate the contrast, Fig. 3.3(c) depicts the V–I characteristics of a conventional voltage source supplying a purely resistive load. The equilibrium point B represents the normal operating condition in this case (i.e., Stable Equilibrium Point (SEP)). Unlike CPLs, resistive loads exhibit a positive incremental resistance, meaning that their terminal voltage increases with current.

If a small perturbation increases the current by ΔI, the source voltage momentarily becomes lower than the load voltage, producing a negative differential voltage that counteracts the current rise [134]. Conversely, if the current decreases, the source voltage exceeds the load voltage, driving the current back up. These restorative effects constitute a negative feedback mechanism that stabilizes the system [138]. Consequently, equilibrium point B is stable, as any small deviation in voltage or current naturally returns to its steady-state condition [141].

In general, an equilibrium point is stable when an increase in current causes the load voltage to exceed the source voltage, and a decrease in current causes the opposite effect. Analytically, this condition corresponds to the combined incremental impedance of the source–load system being positive, ensuring that the system exhibits a restoring—rather than reinforcing—response to small perturbations.

3.4.2 Small-Signal Modeling of Constant Power Loads in DC systems

As mentioned in the previous subsections, some converters in DC systems do not behave like a passive resistor but rather as a CPL, which, when perturbed, exhibits negative incremental impedance that can undermine system stability. Because of the destabilizing nature of that negative incremental impedance, accurately capturing the small-signal behavior of CPLs is essential in any rigorous stability or control design. In particular, a linearized small-signal model lets one place the CPL into classical network-stability tools (e.g., impedance-based Nyquist criteria, eigenvalue analysis, etc.) and thus design damping networks or controllers robustly. This subsection, presents a step-by-step derivation of the linearized model, and finally discusses its domain of validity and practical implications for DC systems.

In order to derive the linearized CPL model, let begin by defining the nominal operating point and then performing a first-order Taylor expansion to obtain the incremental model. Consider v as the instantaneous DC bus voltage seen by the load converter, and i as its instantaneous input current. The converter draws constant power P, so:

$$P = vi \;\Rightarrow\; i = \frac{P}{v}. \tag{3.30}$$

Denote the normal (steady-state) operating point as (V_0, I_0), It can be assumed that the instantaneous quantities are equal to steady-state variables, satisfying

$$P = V_0 I_0. \tag{3.31}$$

Now, given a perturbation around that operating point:

$$v = V_0 + \hat{v}, \qquad i = I_0 + \hat{i}, \tag{3.32}$$

The current–voltage relation of a CPL can be expressed as a first-order Taylor approximation around the operating point:

$$i(v) \approx i(V_0) + \left.\frac{\partial i}{\partial v}\right|_{V_0} (v - V_0) = I_0 - \frac{P}{V_0^2}(v - V_0). \tag{3.33}$$

Expanding and grouping terms, we obtain:

$$i(v) = -\frac{P}{V_0^2} v + 2\frac{P}{V_0}. \tag{3.34}$$

This linear expression represents the tangent line to the I–V curve of the CPL at the operating point, as shown in Fig. 3.3. The above equation reveals that, at a given operating point, a CPL can be approximated by a negative resistance in parallel with a current sink, forming a Norton equivalent circuit:

$$i(v) = \frac{1}{R_{\mathrm{CPL}}} v + I_{\mathrm{CPL}}, \tag{3.35}$$

where

$$R_{\mathrm{CPL}} = -\frac{V_0^2}{P}, \qquad I_{\mathrm{CPL}} = 2\frac{P}{V_0}. \tag{3.36}$$

In this representation, the constant current source I_{CPL} accounts for the steady-state load current, while the parallel branch R_{CPL} models the dynamic (negative resistance) that governs the system's small-signal behavior:

$$\hat{i} = \frac{1}{R_{\mathrm{CPL}}} \hat{v} = -\frac{P}{V_0^2} \hat{v} \tag{3.37}$$

The negative sign indicates that an increase in voltage perturbation $\hat{v}$ leads to a decrease in incremental current $\hat{i}$, i.e., the small-signal slope is opposite to the usual positive-resistance convention, highlighting the destabilizing nature of CPLs in power electronic systems.

3.4.3 An Overview of CPLs' Stabilization Techniques

The fundamental concept behind CPL stabilization lies in enhancing the effective damping of a DC power system by introducing targeted modifications at selected points within the network. These modifications can be implemented at the feeder or source interface, at the load terminal, or through the integration of auxiliary stabilization circuits designed to improve the system's dynamic performance [8]. Such improvements can be achieved either through hardware-based adjustments or by reconfiguring the system's control loops.

Broadly, stabilization techniques are classified into two main categories. Methods that primarily involve hardware modifications are known as passive damping techniques, whereas those based on control adjustments or feedback loop redesign fall under active damping approaches. Although various control-oriented stabilization methods differ in structure and implementation, they are generally grouped within the broader class of active damping strategies. The following subsections summarize the principal techniques developed to counteract the destabilizing influence of CPLs in DC networks.

The stabilization of Constant Power Load (CPL)s has attracted extensive research interest due to their inherent negative incremental impedance characteristics, which can severely compromise the stability of DC distribution systems and microgrids. Over time, a wide variety of stabilization strategies—ranging from passive and active damping to advanced control-based approaches—have been proposed to mitigate these destabilizing effects.

This section presents a concise overview of the most prominent CPL stabilization methods, emphasizing their fundamental principles, operating mechanisms, and relative advantages and limitations. While the scope of existing research is broad, only representative techniques are highlighted here to establish a foundation for the subsequent discussion. For a more comprehensive and detailed review of CPL stabilization strategies, the reader is referred to [9].

3.4.3.1 Passive Damping Strategies

Passive damping seeks to counteract the negative incremental impedance characteristic of CPLs by augmenting the system's inherent damping through the use of passive components such as resistors (R), resistor–capacitor (RC), or resistor–inductor (RL) branches. These elements are typically inserted within the converter's power stage or at the input filter to attenuate oscillations.

While this approach is conceptually straightforward and highly reliable, it inevitably increases system size, weight, and cost. Moreover, passive damping—particularly when implemented with resistive elements—introduces additional power dissipation, thereby reducing overall system efficiency. This loss is especially pronounced when resistors are placed in parallel with filter capacitors, as continuous energy dissipation occurs even during steady-state operation.

To address this efficiency drawback, Loss-Free Resistor (LFR) techniques have been proposed [142]. These emulate the dissipative behavior of resistors without corresponding energy losses, effectively improving damping while maintaining high efficiency. However, LFR implementations often increase system complexity and component count, which can offset their advantages in compact DC MGs applications.

In [143], the small-signal coupling between the negative input resistance of a CPL and the input LC filter was analyzed, leading to the introduction of a series RC damping network connected in parallel with the filter capacitor to enhance stability. Similarly, Cespedes *et al.* [144] proposed three distinct passive damping configurations and formulated an analytical approach for selecting the optimal damper parameters. Further studies, such as [145], investigated DC bus capacitance design using impedance-based stability criteria under various droop control schemes in aircraft power systems composed of parallel sources supplying CPLs.

Overall, although passive damping remains a simple, reliable, and well-understood method for stabilizing DC systems, its inherent disadvantages—namely, increased energy loss and reduced power density—make it less favorable for modern MGs and distributed power systems where compactness, modularity, and high efficiency are key priorities. Consequently, contemporary research has increasingly shifted toward active damping and control-based stabilization methods, which seek to achieve similar damping effects through adaptive, flexible, and energy-efficient means.

3.4.3.2 Active Damping Strategies

The core principle of active damping is to reproduce the damping effect normally achieved by series or parallel resistive elements and DC bus capacitance through modifications in the control structures of the feeder or load subsystems. In certain cases, auxiliary circuits are also integrated at the load terminals to inject compensating currents or emulate variable impedances, thereby mitigating the destabilizing influence of CPLs [138].

Active damping methods can generally be categorized according to their implementation location into three main groups:

1. Feeder-side active damping,

2. Load-side active damping, and

3. Auxiliary-system-based active damping.

The following subsections describe these approaches in detail.

Feeder-side active damping is achieved by embedding compensation loops within the control structure of the feeder converter. These loops modify the converter's output impedance (Z_o) to satisfy impedance-based stability criteria, thereby counteracting the negative incremental impedance exhibited by CPLs [8]. Such techniques are applicable only when the upstream feeder is a controlled converter—such as a DC–DC or AC–DC converter—since uncontrolled feeders (e.g., those comprising only LC filters or rectifiers) lack controllable dynamics.

A key advantage of feeder-side active damping is that it enhances overall system stability without deteriorating load-side performance [9]. For instance, [138] proposed an active damping strategy that emulates a virtual series resistance by feeding back a scaled inductor current ($R_{LA} i_L$) and subtracting it from the control voltage, effectively increasing damping within the converter loop. This method was later extended to isolated DC–DC converters supplying CPLs, though it remains effective only across a limited range of load power levels. In [146], the global dynamics of a DC–DC buck converter were analyzed using phase-plane techniques, employing a hysteresis-based current feedback loop in conjunction with a PI voltage regulator. Similarly, [147] demonstrated that both peak and valley current mode control can stabilize DC–DC boost converters under CPL conditions, with load current feedforward improving system response.

The idea of virtual resistance emulation was revisited in [148] for a source DC–DC buck converter supplying multiple parallel CPLs with input filters. The approach requires the closed-loop bandwidth of the source converter to exceed the resonant frequencies of all input LC filters, which must also be distinct to prevent coupled oscillations.

Shafiee *et al.* [149] introduced the concept of a DC Active Power Filter (APF) for stabilizing DC microgrids with variable loads and interconnections. Their controller, designed using small-signal impedance modeling, employs a damping current loop based on load and tie-line current disturbances. The compensation gain is tuned using root-locus techniques. For comprehensive surveys of feeder-side active damping methods, see [8].

When the feeder subsystem is passive or uncontrolled—such as one containing only an LC input filter or a rectifier—feeder-side compensation is infeasible [9]. In such cases, active damping must be applied on the load side or via an intermediary converter positioned between the feeder and the CPL.

Load-side active damping modifies the input impedance (Z_{in}) of the CPL by injecting compensating currents or voltages within its control loops to satisfy Middlebrook's impedance stability criterion. Although this approach can degrade load performance due to interactions between the compensator and the primary control loop, it remains advantageous because it allows the CPL to self-stabilize.

A Nonlinear System Stabilizing Controller (NSSC) was introduced in [150] to suppress negative impedance instabilities. The controller, validated on both induction motor drives and DC–DC converters with input LC filters, effectively improved stability but at the expense of dynamic performance. Similarly, a Negative Input Resistance Compensator (NIRC) [151] was proposed for brushless DC motor drives exhibiting CPL behavior, improving small-signal stability. To further enhance robustness, a State Feedforward Stabilizing Controller (SFSC) was developed in [152], using input voltage and inductor current as control variables to increase immunity to input disturbances.

Reference Voltage–Based Compensator (RVC) were later introduced in [153], offering improved damping and reduced coupling between the compensator and main control loops. Similarly, Magne *et al.* [154] analyzed a complex system combining inverter drives, converters, and supercapacitor interfaces, introducing a centralized controller to ensure global stability while minimizing filter size. To reduce sensing requirements, an observer-based voltage estimation scheme was proposed in [155]. Additional load-side active damping techniques can be found in [8, 9, 138].

To overcome the inherent limitations of feeder- and load-side compensation, a third category of methods involves the use of auxiliary converters inserted between the feeder and the CPL. These converters—commonly bidirectional DC–DC converters (BDC)—are controlled to inject compensating currents or emulate dynamic damping across a wide range of operating conditions.

Although such configurations introduce additional hardware and cost, they provide enhanced flexibility and strong damping performance. For example, [156] proposed connecting a BDC equipped with a storage capacitor between the CPL and its input LC filter to suppress input voltage oscillations. The controller, designed using pole-placement techniques and a second-order observer, effectively reduced the need for multiple sensors.

Similarly, [157] implemented a PI-controlled BDC with a storage capacitor at the input terminals of a tightly regulated inverter drive, successfully stabilizing the DC bus voltage. A related concept, termed the Smart Active Damper, was presented in [158] for telecommunications and data center DC microgrids. This damper, realized through a non-isolated BDC without dedicated energy storage, emulates a passive RC damper while maintaining communication with both source and load to determine the required damping current. The inner loop operates in fixed-frequency peak-current mode, while the outer loop regulates the inductor's average current to remove steady-state offsets.

Despite its higher cost and circuit complexity, auxiliary active damping provides superior modularity, fast dynamic response, and improved robustness. As a result, it represents one of the most promising approaches for stabilizing future DC microgrids with multiple CPLs and distributed converter systems.

3.4.3.3 Power Shaping Control Method

The Power Shaping Control (PSC) strategy reformulates the system's dynamic equations in terms of instantaneous power—or equivalently, the rate of energy transfer—instead of traditional state variables. This reformulation effectively linearizes the system's nonlinear behavior by transforming it into the power domain, thereby eliminating the destabilizing effects typically associated with CPLs.

By directly expressing and controlling system dynamics in terms of power flow, the controller regulates the instantaneous balance between source, storage, and load components. This power-domain perspective inherently mitigates the negative incremental impedance of CPLs, allowing the system to maintain stability across a wide range of operating conditions.

Compared with other nonlinear control approaches, the design and implementation of PSC are relatively straightforward, as the control law is based primarily on power-feedback relationships rather than detailed energy-function modeling. In addition to achieving accurate DC bus voltage regulation, PSC enhances system damping.

In [159], the PSC framework was applied to stabilize a DC distribution system supplying CPLs. The proposed control scheme successfully maintained voltage stability and attenuated oscillations during load disturbances, demonstrating its effectiveness for practical DC microgrid applications that demand both robustness and implementation simplicity.

3.4.3.4 Pole Placement Control Method

In [160], a pole-placement control strategy was employed to stabilize a buck converter supplying a CPL. The technique functions by relocating the system's unstable right-half-plane poles to desired locations in the left-half-plane of the complex domain, thereby ensuring closed-loop stability. Through appropriate selection of pole positions, the destabilizing influence of the CPL's negative incremental impedance can be effectively mitigated.

The results presented in [9] demonstrated that this control approach enables a reduction in the size of the filter capacitor while maintaining satisfactory stability margins. This characteristic is particularly advantageous in DC-MGs, where compactness and high power density are key design objectives.

However, the successful implementation of the pole-placement method relies on complete state feedback, requiring that all relevant system states be either measured directly or estimated through observers. This necessity increases sensor requirements and computational effort, which can constrain the practicality of the approach in systems with limited measurement infrastructure or processing resources.

3.4.3.5 Feedback Linearization Control Approach

Conventional linearization methods around a specific operating point ensure stability only in the small-signal sense. However, in systems supplying CPLs, the strong nonlinear coupling between voltage and current can give rise to instabilities that cannot be accurately captured by small-signal models. To overcome this limitation, the Feedback Linearization Control (FLC) approach has been developed as a nonlinear control technique capable of compensating the destabilizing effects of CPLs in DC Distribution Power Systems (DPSs) and DC-MGs [8].

The FLC method constructs a nonlinear feedback law that cancels out the nonlinear terms introduced by the CPL, transforming the original nonlinear dynamics into an equivalent linear system with respect to a new set of coordinates. This is achieved via a nonlinear coordinate transformation that channels the system's nonlinearities through the control input, thereby enabling their exact cancellation [161]. Once the transformation is completed, the resulting system exhibits input–output linearity, allowing standard linear control theory to be applied for regulator design.

Unlike conventional active damping techniques, feedback linearization can theoretically compensate for any magnitude of CPL power, ensuring stability rather than limited small-signal robustness. However, the approach is sensitive to measurement noise due to the differentiation involved in the transformation process and may exhibit slower behavior compared to other nonlinear control strategies such as sliding mode or synergetic control [9].

In [161], a feedback linearization controller was implemented through nonlinear coordinate transformation to stabilize a DC–DC buck converter supplying a CPL. Using Lyapunov-based analysis, it was demonstrated that this transformation extends the region of asymptotic stability and effectively suppresses oscillations caused by the negative incremental impedance of the CPL.

Rahimi *et al.* [162] introduced a loop-cancellation technique applicable to basic DC–DC converter topologies (buck, boost, and buck–boost) under resistive and constant power loading. Their approach employed nonlinear feedback to eliminate CPL-induced nonlinearities, where the feedback gain was determined based on converter, source, and load parameters. To ensure robust stability across all operating points, the gain was selected such that the resulting nonlinear term remained strictly positive, effectively yielding a positive equivalent resistance and enhancing system damping.

In [163], a nonlinear coordinate transformation was applied to a buck converter supplying a pure CPL to derive an exact linearized model. Accurate linearization required that the controller's internal inductance (L) and capacitance (C) values match the actual system parameters. To improve robustness, a reduced-order observer was incorporated to estimate both the CPL power and its derivative, ensuring precise compensation over the full operating range. A full-order feedback controller was then designed for the linearized system, and sensitivity analysis was conducted to quantify the impact of parameter mismatches on observer accuracy and closed-loop dynamics.

Further developments were presented in [164], where a Linearization via State Feedback (LSF) strategy was proposed for medium-voltage shipboard DC power systems under CPL conditions. The method employed two transformation functions—one for system linearization and another for pole placement. A Proportional–Derivative (PD) controller was then designed for the linearized model, and sensitivity analysis demonstrated how deviations in the linearizing function affect control accuracy and dynamic response.

In summary, feedback linearization offers a rigorous nonlinear control framework that ensures stability in CPL-dominated DC systems. Despite its reliance on accurate modeling and parameter knowledge, it remains one of the most effective methods for achieving robust voltage regulation and dynamic stability in advanced DC-MGs.

A comparative summary of the discussed CPL compensation techniques is presented in Table 3.1. To the best of the authors' knowledge, within the context of droop-based energy management in DC-MGs, the explicit use of droop VR as a stabilization strategy has not been thoroughly investigated. Nevertheless, as discussed in Section 3.3.2, increasing the droop gains shifts the system eigenvalues toward the left half of the complex plane, thereby enhancing stability and improving network damping. This suggests that proper tuning of droop virtual resistances can provide a decentralized means to mitigate the destabilizing influence of CPLs while maintaining accurate power sharing and autonomous control in DC-MGs. Not to mention that this concept is further utilized in Section 4.2.

3.5 Summary of the Chapter

This chapter developed a coherent small-signal modeling and analysis framework for droop-controlled DC–MGs with constant-power loading. By decomposing the system into source, load, and network subsystems and rigorously enforcing KVL/KCL, a reduced-order state-space model was derived that preserves the dominant electrical dynamics while embedding fast inner-loop converter behavior through appropriate parameters. The

Table 3.1: Comparison of selected CPL compensation techniques for DC distribution power systems (DPS) [8, 9]

Stabilization Technique	Features	Challenges	Damping Improvement in Presence of CPL
Passive Damping	Simple implementation; requires no modification of control loops.	High power dissipation; increases system size and losses.	CPLs introduce negative incremental impedance, reducing system damping. Passive components (*R*, *L*, *C*) are added to improve effective damping.
Active Damping	Maintains high efficiency and reliability; no additional passive losses.	Limited compensation range; may interfere with other control objectives; dependent on switching frequency.	System damping improved by virtual impedance emulation, bandwidth regulation, or stability margin enhancement.
Feedback Linearization	Compensates any level of CPL power; ensures large-signal stability; compatible with linear control design.	Sensitive to measurement noise due to differentiation; slower transient response than sliding-mode or synergetic control.	Feedback law introduces a positive equivalent impedance to counteract CPL-induced negative impedance, resulting in improved stability.
Power Shaping Stabilization	Based on power-domain modeling; achieves large-signal stability; requires lower control bandwidth.	Higher computational demand.	Instability caused by CPLs can be mitigated by reshaping the instantaneous power balance, as stored capacitor energy is proportional to V_c^2.
State-Space Pole Placement	Allows precise relocation of unstable poles; compensates desired CPL power range.	Requires full-state feedback or observers; feedback gains may vary with load.	Properly chosen gain vector shifts unstable poles to desired locations, improving closed-loop damping and stability.

droop mechanism was explicitly represented, revealing its dual role in voltage regulation and proportional current sharing. The small-signal CPL representation—via negative incremental conductance—was integrated to capture the destabilizing effect of tightly regulated power electronic loads.

The stability interpretation linked eigenvalue locations to physical and control parameters, yielding clear, design-oriented conditions on droop coefficients and load stiffness. Sensitivity results showed that increased line inductance weakens damping (poles move toward the imaginary axis), whereas higher line resistance shifts poles leftward, enhancing stability. These insights connect directly to energy management and power balancing in islanded operation: small-signal models enable rapid appraisal of operating margins, informed tuning of droop virtual resistances, and selection of control modes (e.g., Maximum Power Point Tracking (MPPT) vs. voltage control) that maintain feasible equilibria under varying demand.

Finally, principal CPL stabilization strategies—passive, active, and auxiliary-converter-based—were reviewed, positioning droop tuning as a decentralized complement capable of mitigating CPL-induced instabilities without compromising current-sharing objectives. Collectively, the modeling framework and stability tools established here provide the analytical foundation for the controller optimization, robustness evaluation, and case studies presented in the subsequent sections.

Chapter 4

Innovative Solutions for Real-Time Energy Management and Flexibility Enhancement

The growing penetration of renewable energy sources in small islanded systems introduces new challenges for power grid operation, particularly concerning dynamic security and stability issues [165, 166]. The stability and reliability of DC-MGs rely on the capability of the system to regulate voltage deviations and restore them within a narrow band around the nominal value, especially after major disturbances that disrupt the balance between power generation and demand [167]. Conventional control methods, such as droop-based strategies, have been widely adopted to regulate the response of the electrical system by coordinating the contribution of distributed resources and dictating the system's resilience to abrupt changes in the load and generation balance.

In the specific context of islanded DC-MGs, voltage regulation presents additional challenges due to the intermittent nature of renewable-based units and the destabilizing influence of CPLs, which exhibit negative incremental impedance and amplify instability risks [50, 83]. The main challenges in such systems often involve regulating the voltage of the PCC by ensuring appropriate current sharing among heterogeneous sources according to their ratings, and managing the SoC of batteries. Adjusting the common bus voltage is considered the primary control objective because this quantity is a global indicator of power equilibrium across the entire system [34]. However, this task is complicated by the stochastic profile of local demand and the intermittency in RESs generation, which can cause frequent mismatches between supply and consumption.

In this regard, the role of flexibility becomes even more critical in stand-alone operation. As defined in the previous section, flexibility denotes the ability of a DC-MGs to accommodate sudden variations in generation and demand through adaptive coordination of supply, storage, controllable loads, etc. Unlike grid-connected systems, where the main grid can absorb or supply power imbalances, islanded DC-MGs must rely exclusively on their internal resources to preserve voltage stability and ensure continuity of supply. Consequently, the absence of external support amplifies the importance of fast and reliable flexibility mechanisms to mitigate the effects of renewable intermittency and demand uncertainty. A sufficiently flexible system can minimize voltage excursions, reduce stress on storage units, and sustain secure operation even under unforeseen disturbances. This underscores that enhancing flexibility is not only a desirable feature but a fundamental requirement for the stable and resilient operation of islanded DC-MGs.

A further challenge of renewable-based islanded MGs lies in their lack of rotational inertia. In conventional power systems, synchronous generators inherently provide kinetic energy stored in their rotating masses, which acts as a buffer against sudden power imbalances and naturally damps voltage deviations. By contrast, RESs interfaced through power electronic converters are virtually inertia-less. This absence of physical inertia reduces the ability of the system to withstand fast fluctuations, accelerates and amplifies voltage transients, and makes MGs more vulnerable to abrupt changes in generation or demand. The problem is further exacerbated in small-scale isolated systems, where the system is disconnected from the utility grid. The main consequence of reduced system inertia is improper electrification of the DC-MG and, in the most severe cases, an increased risk of blackout [168]. These problems pose a significant threat to both interconnected systems and small isolated networks.

To overcome this obstacle, batteries play a pivotal role in the fast restoration of bus voltage following disturbances in islanded DC-MGs. Thanks to their rapid dynamic response and bidirectional power exchange capability, batteries can instantaneously inject or absorb energy to counteract sudden mismatches between generation and demand [50]. Unlike conventional generators, which are limited by mechanical inertia and ramping constraints, BESS respond within milliseconds, thereby preventing severe voltage deviations that could compromise sensitive electronic loads. This fast-acting support not only stabilizes the common bus voltage but also buys time for slower-acting resources or higher-level controllers to re-establish long-term equilibrium. As such, batteries serve as the primary buffer in modern islanded MGs, enabling reliable operation under highly variable renewable generation and stochastic demand conditions.

Beyond voltage regulation, maintaining balanced SoCs across batteries is equally crucial to prevent overcharging or deep discharging, both of which accelerate degradation and reduce storage lifespan. This aspect becomes even more critical when multiple energy storage units are deployed in the system. In other words, the aggregation of several energy storage systems introduces the need for coordinated SoC management to avoid violations across all battery packs and to extend their service life. To address this issue, several studies have proposed integrating battery SoC information directly into the adaptive droop control law, thereby dynamically adjusting the droop coefficients in response to both electrical and storage conditions [99, 104, 140, 169]. Such SoC-aware control schemes enable more equitable utilization of distributed storages, enhance long-term reliability, and increase the effective hosting capacity of renewable energy resources.

Moreover, ensuring accurate current sharing among distributed sources is of paramount importance for the secure and efficient operation of islanded DC-MGs. Inaccurate current distribution can lead to overloading of certain units while others remain underutilized, thereby accelerating aging, reducing overall system efficiency, and jeopardizing the grid's reliability [170]. This issue is particularly critical when generation units and storage systems possess different ratings, dynamic characteristics, and operational constraints. Proper current-sharing mechanisms not only extend the lifetime of BESSs but also prevent thermal stress on converters of all units, which is essential during transient events and under high-loading conditions. Advanced droop-based strategies, including adaptive and nonlinear extensions, have been proposed to enhance current-sharing accuracy by compensating for line impedance effects and dynamic load variations [16]. By achieving equitable power distribution, these methods increase the robustness of voltage regulation, improve system reliability, and longevity.

To cope with the combined challenges of voltage stability, current-sharing accuracy, and storage management, advanced extensions of conventional droop control have been investigated. Adaptive or nonlinear droop schemes, in particular, offer improved flexibility by dynamically modifying virtual resistances in accordance with load levels and storage conditions. These approaches not only improve current sharing accuracy and reduce line-related power losses but also mitigate the destabilizing effects of converter-interfaced loads and preserve SoC limits of distributed storages [16]. As a result, such control strategies provide a more sophisticated and holistic response to load and generation fluctuations, ensuring secure and reliable operation of islanded DC-MGs under highly uncertain conditions, while simultaneously extending the durability of storage assets and maximizing renewable penetration.

Building upon the challenges outlined above, the remainder of this chapter introduces a set of innovative control solutions specifically tailored for islanded DC-MGs. The proposed methods collectively enhance system security by addressing CPL-induced instabilities, improving flexibility, and reducing battery degradation costs. The chapter first presents a distributed adaptive droop strategy that leverages lightweight communication to coordinate DGs, BESSs, and controllable loads, enabling real-time energy balancing, accurate current sharing, and reduced stress on storage units. It then advances to a fully decentralized adaptive droop scheme that operates without any communication, relying solely on local measurements to maintain voltage stability and fair power sharing—offering a robust and low-cost solution ideal for remote or infrastructure-limited microgrids. Finally, a cost-oriented adaptive droop control is introduced, incorporating battery degradation indicators to allocate power in an economically optimal manner and extend storage lifespan. Together, these approaches form a coherent suite of techniques that strengthen the technical and economic resilience of isolated DC-MGs.

4.1 Distributed Coordination of Generation Units, Battery Storages, and Loads

In this section, the focus is placed on the distributed coordination of generation units, BESSs, and loads in islanded DC-MG, where ensuring a secure and reliable balance between supply and demand is particularly challenging due to the intermittent nature of RESs and the stochastic behavior of local demand. This work employs the ES topology to enhance microgrid flexibility by intelligently managing both battery storage and load consumption. This capability is particularly important when the generation capacity of multiple RESs, operating under the MPPT algorithm, is insufficient to meet demand. In such situations, ES devices dynamically adjust the consumption of non-critical loads, thereby avoiding excessive battery cycling and reducing storage systems usage. This strategy enables a more efficient use of available flexibility resources while preserving voltage stability for critical loads connected to the common bus.

To ensure coordinated operation of heterogeneous units, a distributed adaptive droop-based control scheme is introduced. The primary goal of this strategy is to balance common bus voltage regulation with accurate current sharing among generation units, BESS, and ES devices. The introduced distributed approach employs a low-bandwidth communication layer among active units. Each unit exchanges essential data, such as output current and SoC, which are then used for the adaptive adjustment of droop gains. As a result, system-wide coordination is achieved without dependence on a single, failure-prone controller.

A key innovation of the proposed framework is the explicit use of battery capacity and SoC information in the energy-sharing process. This ensures that charging and discharging stress is evenly distributed across all storage units, preventing overuse of specific batteries and extending their overall lifetime. Maintaining SoC balance during both charging and discharging phases improves long-term reliability and reduces the total storage size required for secure operation. Furthermore, the coordinated approach enables smooth transitions between different operating modes, whether under generation deficit, near balance, or surplus conditions.

Finally, the feasibility and performance of the proposed distributed coordination framework are validated using a PHIL platform. This Real-Time testing environment integrates simulated components with physical hardware, accurately capturing the dynamic behavior of batteries. The PHIL-based validation confirms that the proposed approach improves DC-MG flexibility, maintains bus voltage within acceptable limits, balances SoC across

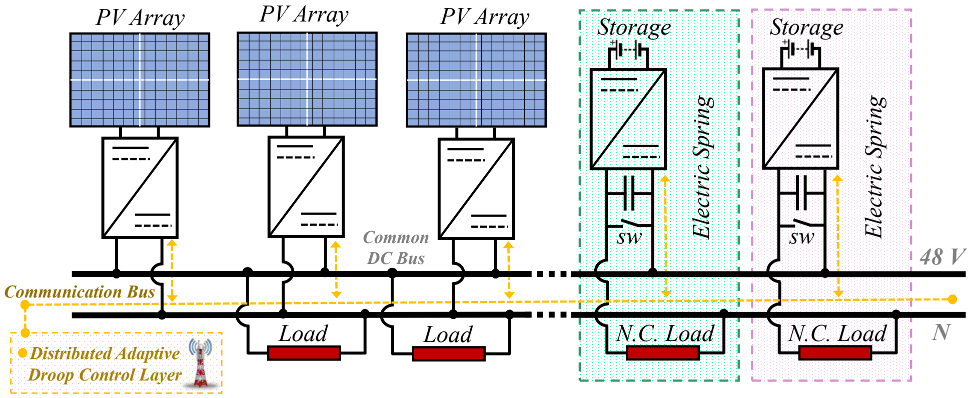

Figure 4.1: The configuration of a DC-MG including electric springs.

distributed batteries, and achieves robust operation under diverse conditions, including supply–demand imbalances and communication delays.

For clarity, the remainder of Section 4.1 is organized as follows. Subsection 4.1.1 describes the system under study. Subsection 4.1.2 outlines the design principles of the proposed distributed adaptive approach under different operating conditions. Subsection 4.1.3 provides a small-signal analysis to assess the relationship between droop gains and system stability. Subsection 4.1.4 reports PHIL-based results that validate the proposed method under realistic scenarios. Finally, Subsection 4.1.5 offers a comparative analysis against alternative approaches from the literature.

4.1.1 The Configuration of the Microgrid Under Consideration

The diagram of the investigated distributed DC system, together with its communication links, is presented in Fig. 4.1. Intermittent generation units based on PV arrays, MGs, and local loads are interconnected through a common bus to form the network. The PV units are installed in a shunt configuration, and their connection to the system is achieved through DC-DC converters. The maximum available power from PV units is typically extracted by employing the MPPT algorithm [170]. In islanded networks, however, the direct use of MPPT may not always be appropriate, since it can generate an energy surplus that cannot be managed, leading to overvoltage or overcharging of storage devices. For this reason, the operation of generation units is controlled either by adopting MPPT as a unit-level strategy or by applying coordinated voltage droop control, depending on the current operating mode of the system.

DC-ESs are employed to mitigate the power mismatch arising from intermittent PV generation and uncertain demand profiles, thereby preserving voltage quality for loads connected to the common bus. While numerous DC-ES configurations have been introduced in the literature [171–173], the present work concentrates on series-type DC-ESs. These devices, as described in [171], incorporate a battery bank and a bidirectional converter, enabling operation in both charging and discharging modes. The designation *"series-type"* originates from the fact that the device is placed in series with the NC load; however, for conciseness, this qualifier will be omitted in the remainder of this section.

As shown in Fig. 4.1, a bypass switch has been integrated at the ES output port so that NC loads can remain supplied whenever the energy storage is unavailable due to a fault in its power converter or similar issues. The main advantage offered by this topology lies in its capability to actively adjust the power consumption of NC loads, which allows supply–demand imbalances to be addressed with reduced storage capacity. Furthermore, as highlighted in [171, 172], transient voltage deviations can be rapidly supported thanks to the fast dynamic response of series DC-ES.

It should also be noted that the classification between NC loads and Critical Loads varies depending on the specific utilization scenario and design priorities of the microgrid. For instance, in some applications, certain loads may shift between critical and non-critical categories depending on operating conditions, economic constraints, or user-defined requirements. Such flexibility is particularly relevant in microgrids that integrate renewable sources, where uncertainty and intermittency may influence the prioritization of loads. In this work, however, a simplified yet conservative assumption is adopted, whereby all loads directly connected to the PCC are treated as critical. This ensures that the continuity of supply at the PCC is always maintained, thereby supporting system stability and reliability under a wide range of conditions.

To facilitate coordinated operation, communication links are established between the sources and ESs, enabling reliable information exchange through a LBC method [83, 174]. The exchanged data consist of output currents from all units and the SoC of batteries, which are then utilized for the adaptive adjustment of droop gains and the computation of voltage references within the coordinated droop-based control layer. This communication-enhanced approach mitigates the drawbacks of conventional decentralized droop methods, particularly under conditions of unequal load sharing or rapid dynamics. Moreover, by incorporating SoC-dependent signals into the control process, the overall energy management strategy is improved, promoting both fair utilization of storage units and extended system lifetime.

4.1.2 Design Principle of the Controller at Different Operating Modes

As discussed in the previous sections, it is advantageous to employ an adaptive droop gain that prioritizes voltage regulation or accurate current sharing depending on the operating point. This adaptive mechanism provides flexibility in maintaining bus stability under light loading conditions while simultaneously ensuring proportional power sharing during heavy load operation. In addition, to effectively exploit the storage capability of ESs and extend their lifespan, the proposed droop formulation must ensure SoC balancing of the batteries during both charging and discharging phases while preventing overcharging and overdischarging. Such considerations are crucial, since unequal utilization of batteries may not only degrade system efficiency but also accelerate the aging process of certain storage units, leading to reduced overall resilience of the MG.

Accordingly, this section introduces a novel droop control strategy designed for the different operating modes of the DC-MG. The proposed formulation incorporates Real-Time feedback of current and SoC information to dynamically adapt droop parameters, enabling coordinated operation of distributed units. By doing so, the strategy enhances both voltage quality and power-sharing accuracy while embedding an inherent energy management mechanism that preserves storage health. This subsection details the control framework, its mathematical formulation, and the specific adaptations required for seamless transition between grid-connected and islanded modes.

4.1.2.1 Operating at Mode I

To address voltage violations concerning the generation–demand equilibrium, the proposed framework explicitly accounts for multiple operating scenarios to guarantee the balance between load and supply, each characterized by distinct objectives and constraints. By adapting the droop parameters and control priorities according to the prevailing conditions, the system can simultaneously preserve reliability, efficiency, and storage health. In the following analysis, four distinct operating modes are therefore considered, providing a structured basis for the design and validation of the adaptive droop control scheme.

In this mode, representing the normal operating condition of the DC-MG, the PV units are operated under the MPPT strategy to extract and deliver the maximum available power to the grid. As a result, they effectively behave as Constant Power Sources (CPS), injecting their full capacity into the common bus. Under these circumstances, the supplied renewable energy is sufficient to satisfy the total demand, and the load is entirely sustained by the PV generation. Consequently, the bus voltage remains regulated within permissible limits without necessitating any compensatory action from the ESs.

This operating condition reflects the desired steady-state scenario, as it ensures efficient utilization of renewable resources while minimizing cycling of storage devices. Since the ES units remain idle, their stored energy is preserved for subsequent modes where fluctuations in generation or demand may occur. Additionally, the absence of frequent charging and discharging cycles under this regime contributes to prolonging battery lifespan and reducing overall system stress.

4.1.2.2 Operating at Mode II

This mode will be activated when the generation units, despite operating with the MPPT algorithm, provide insufficient power to meet the demand. In such situations, the ESs are required to intervene and support the common DC bus voltage by operating in the discharging phase. Consequently, they function as Constant Voltage Sources (CVS) and take responsibility for stabilizing the bus when generation is not sufficient. To align with the notations outlined in the previous sections, the discharge virtual resistors of the droop control should adapt automatically according to both the instantaneous loading level and the individual battery specifications (i.e., SoC, etc.). This ensures that the participation of each ES unit is proportionally coordinated. To this aim, instead of a straight-line approximation, the droop curve can be designed in a nonlinear form by adding an exponential term to conventional droop formula:

$$v_{ref}^{n} = V_{nom} - R_{dr}^{n}\left[e^{\alpha(I_{out}^{n} - I_{max}^{n})}\right] \cdot I_{out}^{n} \tag{4.1}$$

Here, V_{nom} is the grid's nominal voltage, and v_{ref}^{n}, I_{out}^{n}, and R_{dr}^{n} are the reference voltage, output current, and VR (droop gain) of the n-th unit, respectively. I_{out}^{n} is positive in discharging phases of ESs. R_{dr}^{n} is defined based on the maximum continuous current of each unit (I_{max}^{n}) as a unit-specific characteristic, and on the permissible voltage deviation (V_{per}):

$$|R_{dr}^{n}| \leq \frac{\Delta V_{max}}{I_{max}^{n}}, \qquad \Delta V_{max} = V_{nom} - V_{per} \tag{4.2}$$

In (4.1), the shaping parameter α modifies the curvature of the droop characteristic in the voltage–current plane, as illustrated in Fig. 4.2. Note that an increased value of α expands the area under the curve, thereby allowing the unit to enhance its power-exchange capability, while a smaller α makes the unit less aggressive in contributing. Therefore, α

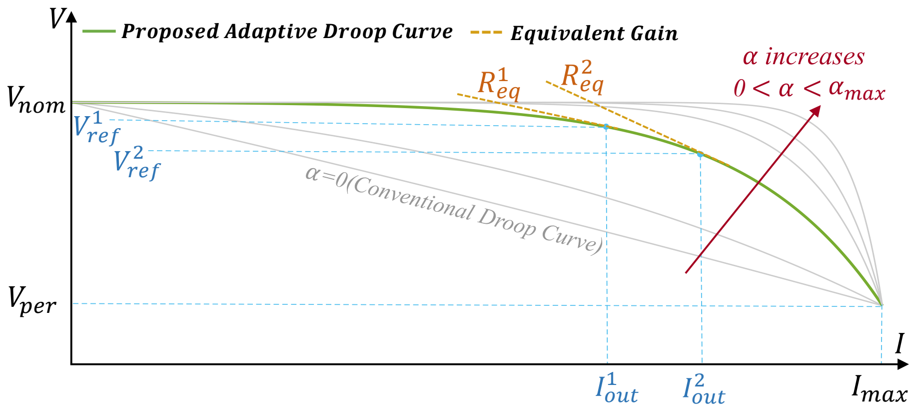

Figure 4.2: The proposed droop curve in the voltage-current plane.

acts as a key tuning coefficient and must be selected carefully based on both system-level requirements and unit-specific constraints. For each unit, α can be expressed as:

$$\alpha = G_{pi} \frac{|I_{des}^n - I_{out}^n|}{I_{des}^n} \tag{4.3}$$

where G_{pi} represents the transfer function of a proportional–integral (PI) controller that improves current-sharing accuracy by mitigating current distribution disparities among units [16]. The second term in (4.3) quantifies the normalized current-sharing error of the n-th droop-controlled unit.

The desired output current I_{des}^n, which serves as a reference for each ES, can be obtained as follows:

$$I_{des}^n = \frac{I_{max}^n \cdot I_{req}}{\sum_{n=1}^{N_u} I_{max}^n} \tag{4.4}$$

In this formulation, N_u denotes the total number of droop-based ES units, while I_{req} corresponds to the required excess current in the grid. Specifically, I_{req} represents the difference between the total load current (I_{load}) and the cumulative contribution of CPSs (PV units in this case). By definition, I_{req} is positive during discharging phases, highlighting the deficit that ES units must compensate:

$$I_{req} = I_{load} - I_{CPS} = I_{out}^n + G_{lat} \sum_{i \neq n}^{N_u} I_{out}^i \tag{4.5}$$

It should be noted that I_{req} inherently depends on measurements from all units. Hence, the performance of the communication layer directly influences its accuracy. To capture this effect, a latency factor G_{lat} is incorporated, modeled as:

$$G_{lat} = \frac{1}{1+\tau s} \tag{4.6}$$

where τ is the delay constant associated with communication latency.

Since α determines the degree of participation of each unit, its calculation must also incorporate the SoC of batteries to avoid imbalance. Otherwise, some units may be overutilized while others remain underused. The SoC of the n-th ES can be estimated using the coulomb-counting method:

$$SoC^n = SoC_0^n - \frac{\eta^n}{C_{BAT}^n} \int_0^T I_{out}^n(t)dt \tag{4.7}$$

where SoC_0^n, C_{BAT}^n, and η^n denote the initial SoC, the rated capacity, and the round-trip efficiency of the battery, respectively. Substituting (4.5) and (4.7) into the proportional rule of (1.4), and differentiating, the dynamic evolution of SoC can be expressed as [99]:

$$\frac{dSoC^n}{dt} = \left(\frac{\eta^n}{C_{BAT}^n} \times \frac{SoC^n.I_{req}}{SoC^n + G_{lat}\sum_{i\neq n}^{N_u} SoC^i} \right) \tag{4.8}$$

The fraction in (4.8) acts as a normalized weighting factor, which determines how each unit participates based on both its local SoC and the SoC states of the remaining ESs. For normalization across heterogeneous units with different capacities, C_{BAT}^n is often replaced by $\kappa^n = C_{BAT}^n/C_{max}$, where C_{max} is the capacity of the largest storage unit.

Considering two arbitrary ESs, ES^n and ES^m, equilibrium is achieved when their SoCs converge to identical rates of change, as reflected in (4.9):

$$\begin{aligned} \frac{dSoC^n/dt}{dSoC^m/dt} &= 1 \\ &= \frac{(\eta^n \cdot SoC^n) / \left(\kappa^n \cdot \left[SoC^n + G_{lat}\sum_{i\neq n}^{N_u} SoC^i\right]\right)}{(\eta^m \cdot SoC^m) / \left(\kappa^m \cdot \left[SoC^m + G_{lat}\sum_{j\neq m}^{N_u} SoC^j\right]\right)} \end{aligned} \tag{4.9}$$

Equation (4.9) confirms that whenever SoC^n exceeds SoC^m, the n-th unit will naturally discharge at a faster rate ($dSoC^n/dt > dSoC^m/dt$). This dynamic accelerates SoC equalization across ESs without requiring external supervisory intervention.

Accordingly, the desired current in (4.4) can be modified to include a contribution factor CF^n, yielding:

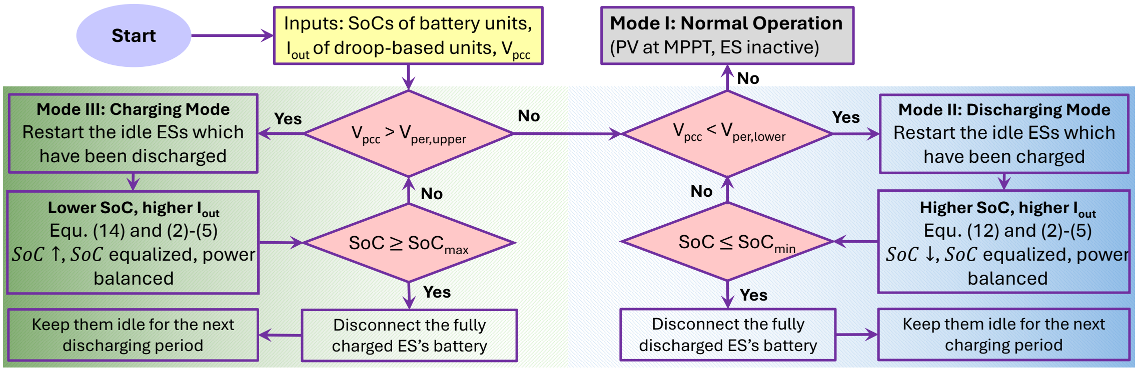

Figure 4.3: Control logic of storage units under charging and discharging phases.

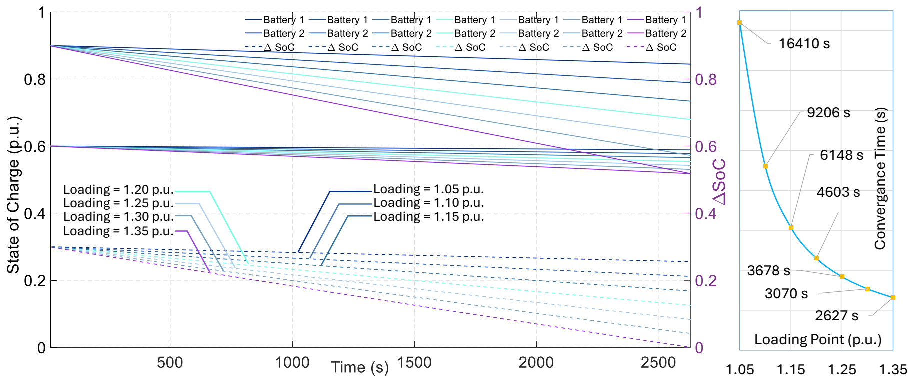

Figure 4.4: SoC behavior of two ESs' batteries to achieve a balanced state in the discharging phase. Note that SoC_0^1 = 90% and SoC_0^2 = 60%. Other specifications of the batteries (e.g., C_{BAT}, etc.) are assumed to be identical.

$$
\begin{aligned}
I^n_{des|_{dis}} &= \frac{I^n_{max} \cdot CF^n}{\sum_{n=1}^{N_u} (I^n_{max} \cdot CF^n)} \times I_{req}, \\
CF^n &= \frac{\eta^n}{\kappa^n} \times \frac{SoC^n}{SoC^n + G_{lat} \sum_{i \neq n}^{N_u} SoC^i}
\end{aligned}
\tag{4.10}
$$

This formulation ensures that ESs with higher SoC levels contribute more aggressively, while depleted units reduce their participation until they reach the lower SoC threshold (e.g., $SoC_{min} = 20\%$), at which point they are disconnected until recharging. Using an exponential droop law instead of a linear approximation accelerates the convergence of SoCs across units, thereby improving system resilience. The operational flow is summarized in Fig. 4.3, while Figs. 4.4 and 4.5 demonstrate the convergence of SoC for two ESs with initially different charge levels.

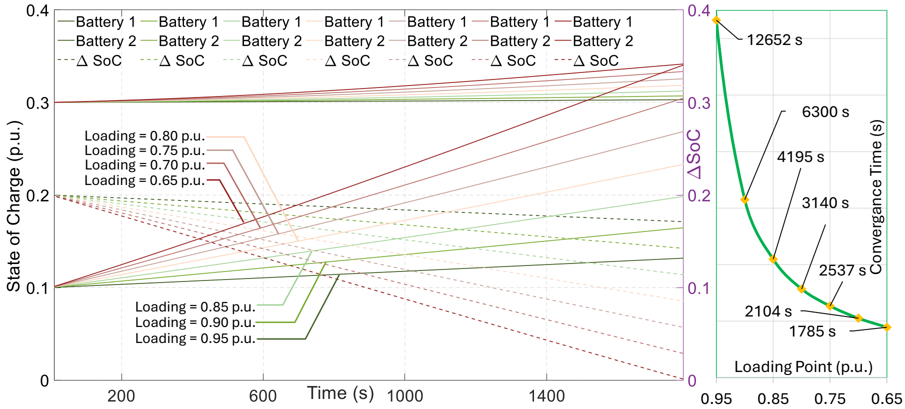

Figure 4.5: SoC behavior of two ESs' batteries to achieve a balanced state in the charging phase. Note that SoC_0^1 = 30% and SoC_0^2 = 10%. Other specifications of the batteries (e.g., C_{BAT}, etc.) are assumed to be identical.

4.1.2.3 Operating at Mode III

In this mode, although the PV units continue to operate under the MPPT algorithm to extract maximum energy, their instantaneous generation exceeds consumption, which in turn causes the PCC voltage to rise above its nominal value. To counteract this effect and maintain voltage stability, ESs equipped with partially charged batteries act as dynamic sinks to absorb the surplus power. By doing so, they effectively behave as additional controllable loads and operate in the charging phase.

To achieve fair and coordinated utilization of storage resources, the charging current must be properly distributed among the ES units. This is accomplished by varying the charge droop resistances according to the loading level and the unit-specific characteristics, following the nonlinear droop curve described in (4.1). It is worth highlighting that the equations defined in (4.3)–(4.6) for Mode II remain valid here as well. The main difference is the polarity of the exchanged current: during charging, I_{req} and I_{out}^n take negative values, reflecting the absorption of surplus power rather than its delivery.

Furthermore, to embed battery specifications into the power-sharing process, (4.7) is combined with (4.9) and the proportional rule in (1.4). As a result, the dynamic rate of change of SoC in the charging mode can be expressed as:

$$\frac{dSoC^n}{dt} = \left(\frac{\eta^n}{C_{BAT}^n} \times \frac{\frac{1}{SoC^n} \cdot I_{req}}{\frac{1}{SoC^n} + G_{lat} \sum_{i \neq n}^{N_u} \frac{1}{SoC^i}} \right) \tag{4.11}$$

Equation (4.11) ensures that units with lower SoC levels are assigned proportionally higher charging currents. This mechanism gradually drives all units toward a common

SoC value and prevents premature saturation of batteries with initially higher SoCs.

To formalize this principle, the storage contribution factor CF^n and the desired charging current $I^n_{des|char}$ for each unit are defined as:

$$\begin{aligned} I^n_{des|_{char}} &= \frac{I^n_{max} \cdot CF^n}{\sum_{n=1}^{N_u} (I^n_{max} \cdot CF^n)} \times I_{req} \\ \forall n \in N_u : CF^n &= \frac{\eta^n}{\kappa^n} \times \frac{\frac{1}{SoC^n}}{\frac{1}{SoC^n} + G_{lat} \sum_{i \neq n}^{N_u} \frac{1}{SoC^i}} \end{aligned} \quad (4.12)$$

Here, CF^n weights the participation of each unit according to both its SoC and normalized capacity κ^n. Consequently, batteries with lower SoCs naturally attract a larger share of the charging current until the fleet converges to a uniform SoC distribution.

The charging control logic is depicted in Fig. 4.3. As illustrated, once a battery is reactivated in charging mode, its droop gain is scaled proportionally to its SoC. When the upper bound SoC_{max} (e.g., 95%) is reached, the unit is isolated from the charging process and transitions to an idle state, waiting for the next discharging cycle. The SoC convergence behavior of two representative ESs initialized at unequal charge levels is shown in Fig. 4.5, where the unit with the lower SoC charges faster. Moreover, under lighter load conditions, the convergence time decreases in an exponential fashion, consistent with the nonlinear droop relation defined in (4.1).

4.1.2.4 Operating at Mode IV

Once the storage units reach full charge, they can no longer act as supplementary loads. If, under these circumstances, renewable generation continues to exceed the demand, the surplus power has no storage path, and the PCC voltage begins to rise beyond the acceptable range. To counter this effect, the PV converters are transitioned from the MPPT phase to the proposed droop control strategy, thereby curtailing their output power in a controlled manner. In this operating mode, the PV units act as Constant Voltage Sources (CVS), regulating the common bus voltage by proportionally reducing their injected power.

Since the ES batteries remain inactive, their SoC-dependent characteristics are excluded from the control scheme in this mode. The responsibility of voltage regulation is therefore fully delegated to the generating units. Consequently, the droop equation governing their operation directly follows equations (4.1)–(4.6) [16], ensuring that the system maintains both stability and voltage compliance despite the absence of storage participation.

This mode highlights the intrinsic flexibility of the proposed control strategy, as it enables a seamless shift in the operational role of PV converters—from maximizing energy harvesting under normal conditions to actively contributing to voltage regulation when storage saturation occurs.

4.1.2.5 Specifying the α limit

As discussed earlier, the PCC voltage reflects the instantaneous power balance condition of the DC-MG. A generation shortfall leads to the discharge of the equivalent DC bus capacitor, resulting in a voltage drop, whereas a surplus of generation charges the capacitor and raises the voltage. This direct coupling between the bus capacitor dynamics and voltage deviations provides a rigorous basis for defining the feasible range of the droop curvature coefficient α, which acts as the dominant parameter in the proposed control method.

It is important to note that when $\alpha = 0$ in (4.1), the conventional linear droop law in (1.1) is exactly recovered, as shown in Fig. 4.2. Thus, α not only generalizes the traditional droop law but also enables a tunable nonlinear mapping that influences both transient and steady-state performance. The derivation of the admissible upper bound of α is provided below.

Depending on the operating mode of the DC-MG, sources may behave either as CPS units (PV generators under MPPT) or as CVS units (storage devices under droop control). When functioning as CVS, the output voltage reference is governed by the nonlinear droop law, and the PCC voltage evolution can be written as:

$$V_{pcc} = \frac{1}{C_{bus}} \int \left(\sum_{n=1}^{N_u} I_{out}^n + (I_{CPS} - I_{load}) \right) dt \tag{4.13}$$

where C_{bus} is the common bus capacitance. By substituting (4.1) into (4.13) and differentiating, the following expression is obtained:

$$\begin{aligned} C_{bus}\frac{dV_{pcc}}{dt} &= \sum_{n=1}^{N_u} \frac{V_{nom} - v_{ref}^n}{\Re_{dr}^n} + (I_{CPS} - I_{load}), \\ \Re_{dr}^n &= R_{dr}^n \left[e^{\alpha(I_{out}^n - I_{max}^n)} \right] \end{aligned} \tag{4.14}$$

Assuming ideal conditions—namely, negligible line voltage drops, ideal battery characteristics (no significant voltage variation across SoC), and perfect control response as in [99]—it follows that $v_{ref}^n \simeq V_{pcc}$ and $\Re_{dr}^n = \beta^1 \Re_{dr}^1 = \beta^2 \Re_{dr}^2 = \cdots = \beta^{N_u} \Re_{dr}^{N_u}$. Under these assumptions, the dynamic response of V_{pcc} reduces to a first-order system with aggregated scaling factor $\lambda^n = \beta^1 + \beta^2 + \cdots + 1 + \cdots + \beta^{N_u}$:

$$V_{pcc}(t) = \left(V_{nom} + (I_{CPS} - I_{load}) \frac{\Re^n_{dr}}{\lambda^n} \right) \left(1 - \exp\left(-\frac{\lambda^n t}{C_{bus} \Re^n_{dr}} \right) \right). \tag{4.15}$$

From (4.15), the PCC voltage time constant is obtained as $\tau_v \approx \frac{C_{bus}\Re_{dr}}{\lambda}$, which directly links the system's dynamic response to the droop parameters. Since $\Re_{dr} = R_{dr} e^{\alpha(I_{out} - I_{max})}$, in the practical operating region where $I_{out} \ll I_{max}$, the exponential term keeps $\Re_{dr}$ relatively small, leading to a faster response.

At steady state ($t \to \infty$), the deviation of V_{pcc} from V_{nom} becomes:

$$\Delta V = V_{nom} - \lim_{t \to \infty} V_{pcc}(t) = (I_{load} - I_{CPS}) \frac{\Re^n_{dr}}{\lambda^n}. \tag{4.16}$$

Equation (4.16) clearly reveals that smaller values of $\Re^n_{dr}$ enhance voltage regulation by minimizing steady-state deviations. Finally, substituting (1.2) into (4.16), the absolute feasible range of α can be determined as:

$$\alpha \leq \left| \frac{\ln\left(I^n_{max} / \left([I_{load} - I_{CPS}] . \lambda^n \right) \right)}{I^n_{out} - I^n_{max}} \right| \tag{4.17}$$

This bound ensures that α is selected such that the exponential droop function does not compromise either bus voltage regulation or system stability. In other words, the feasible range of α provides a direct trade-off between voltage quality, current sharing accuracy, and dynamic response speed.

4.1.2.6 Coordinated Operation Between In-service Units

The common bus voltage deviation can also serve as an information signal to enable seamless transitions between different operating modes, as illustrated in Fig. 4.6. Since the PV units operate in MPPT mode during the first three states, their coordination with the storage systems is achieved through a hysteresis cycle [3, 4]. This mechanism is shown in Fig. 4.7(a), where the voltage band corresponding to normal operation (Mode I) is shaded in red. Whenever the demand exceeds the available generation and the voltage drops below the lower threshold ($V_{per,lower}$), the converters switch from Mode I to Mode II; the reverse transition occurs once conditions are restored.

Although the proposed framework employs the ES concept to maintain continuous electrification with minimal battery use—thereby excluding load shedding from its primary scope—prolonged supply–demand imbalances may reduce the SoC below critical levels. In

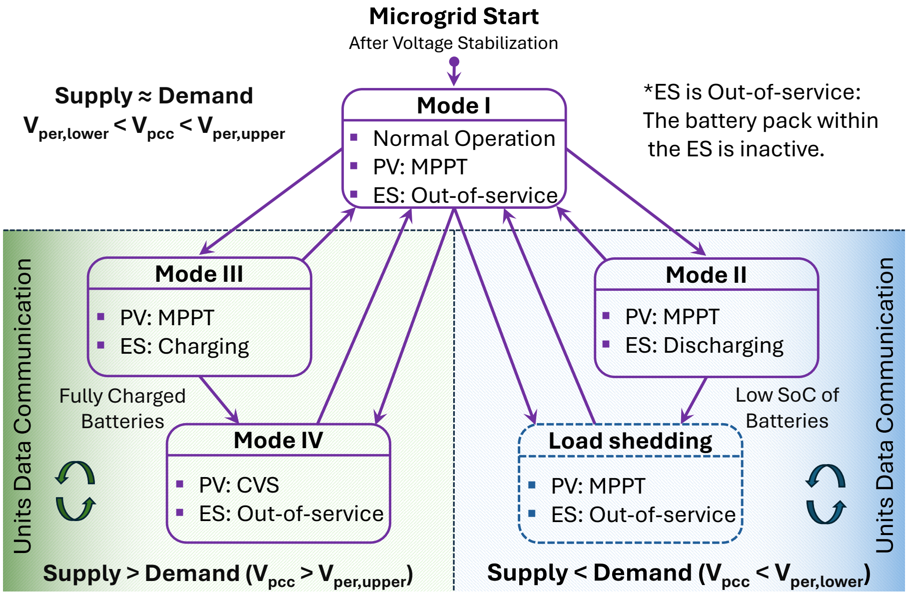

Figure 4.6: Mode transition diagram.

such cases, load shedding becomes unavoidable. Representative strategies for this purpose can be found in [175] and could be integrated into future extensions of the framework to further enhance resilience under severe operating conditions.

On the other hand, the transition from Mode I to Mode III is triggered by over-generation, when the voltage rises above the upper permissible threshold ($V_{per,upper}$), with the reverse transition occurring once the condition is alleviated. If the batteries are fully charged, the converters inevitably switch to Mode IV, where PV units operate in CVS mode to curtail excess generation. As illustrated in Fig. 4.7(b), to mitigate noise-related measurement errors and avoid spurious switching between modes, a cost-effective low-pass filter based on exponential smoothing is employed:

$$V_{\text{filt}}^{t} = \gamma V^{t} + (1-\gamma)V_{\text{filt}}^{t-1}, \tag{4.18}$$

where γ is the smoothing factor, V^t is the observed voltage at time step t, and V_{filt}^{t} and V_{filt}^{t-1} denote the current and previous filtered voltages, respectively. The filtering strength can be tuned by adjusting γ within the range $[0,1]$: maximum smoothing occurs at $\gamma = 0$, while no filtering is applied at $\gamma = 1$. Based on preliminary experiments, $\gamma = 0.1$ is adopted to provide effective smoothing while minimizing delay in mode detection.

Fig. 4.8 presents the complete control framework of the DC-MG units. The output power of both ESs and PVs is regulated through an outer voltage controller combined with an inner current controller. In Fig. 4.8(a), the ES control block is depicted, where the

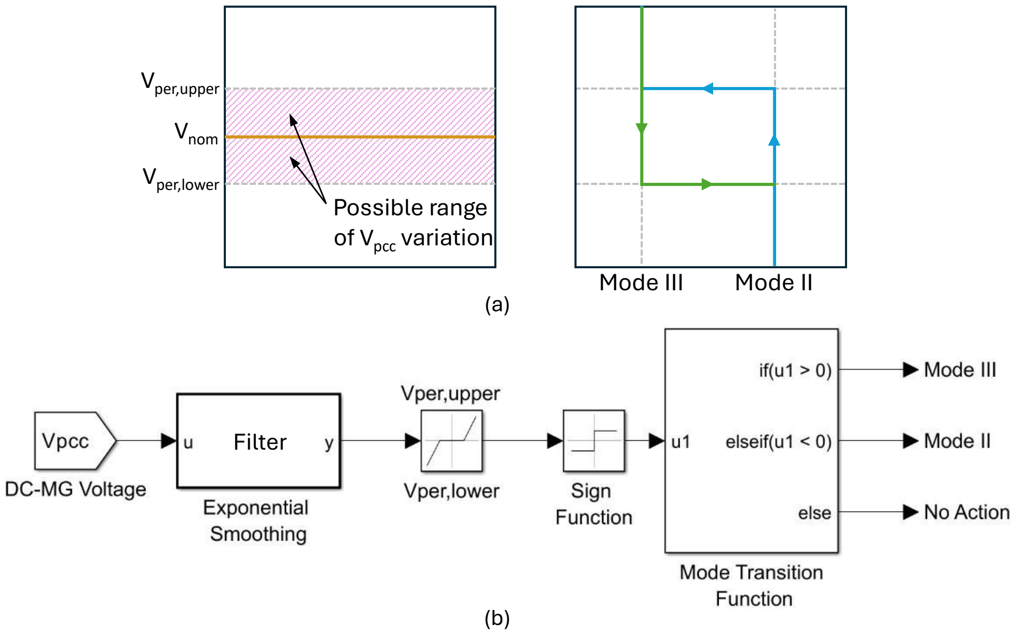

Figure 4.7: Coordinated operation of PV units and energy storage systems under supply–demand imbalance.

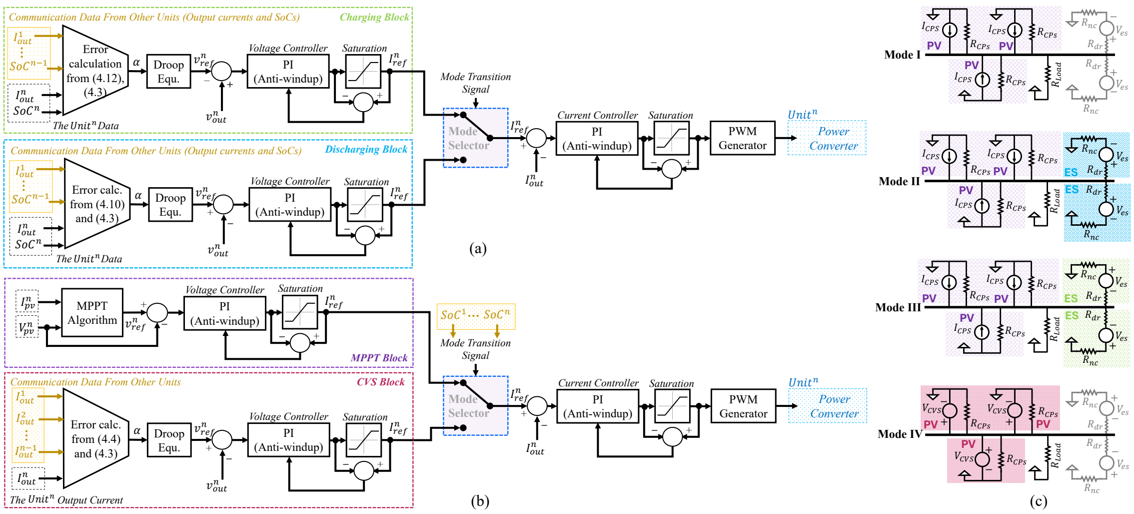

Figure 4.8: Complete control scheme of the units across different modes. (a) ES converter, (b) PV converter, (c) Equivalent circuit of the grid for each mode.

proposed approach generates the reference voltage for the outer loop in Modes II and III based on real-time current data and SoC information exchanged with other active units. This design enables coordinated participation of ES converters, ensuring voltage support and balanced battery utilization.

Fig. 4.8(b) shows the PV converter control structure. As discussed earlier, an MPPT algorithm is used to determine the reference voltage for the outer controller and maximize power extraction under normal operating conditions. In Mode IV, when the SoC thresholds

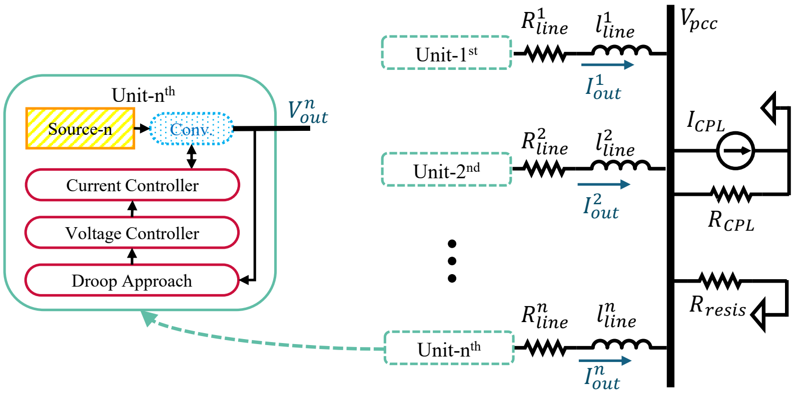

Figure 4.9: DC-MG with several units and different loads at Mode IV.

of the storage systems are reached, the CVS block is activated to regulate the DC bus voltage according to current data from the in-service units. For clarity, Fig. 4.8(c) illustrates the equivalent circuit of the DC-MG under each control mode, highlighting the functional role of each converter.

During over-current conditions, the PI controller integrator may saturate, attempting to increase its output despite the presence of a limiter. To prevent windup, an anti-windup mechanism based on [176] is implemented. This strategy ensures that the controller is released from saturation, restoring stable operation without excessive overshoot. Consequently, the robustness of the system is improved under transient conditions, and reliable mode transitions are maintained.

4.1.3 Stability Evaluation

The stability of the DC-MG can be evaluated using small-signal analysis, which provides valuable insight into the dynamic behavior of the system under perturbations around an equilibrium point. The method adopted in this section follows the reduced-order modeling approach proposed in [134]. Fig. 4.9 illustrates the system model, consisting of generation units, interconnecting lines, and loads, with the main parameters summarized in Table 4.1. As described in Section IV-C, the units can operate either as Constant Power Sources (CPS) or Constant Voltage Sources (CVS), depending on the selected mode.

Loads are classified as purely resistive or CPLs. The latter are particularly critical, as CPLs maintain constant power consumption regardless of the applied voltage. As discussed in [130], an ideal CPL can be linearized around its operating point and represented as a negative resistance (R_{CPL}) in parallel with a current source (I_{CPL}):

Table 4.1: DC Microgrid Parameters in Distributed Control Structure.

Parameters	**Symbol**	**Value**
Nominal Voltage	V_{nom}	48 V
Permissible Voltage Variation	V_{per}	$\pm 5\%\ V_{nom}$
Max. Current (PV_1 & PV_2)	I_{max}	8 A
Max. Current (PV_3)	I_{max}	5 A
Max. Current (ES_1 & ES_2)	I_{max}	10 A
Initial SoC (ES_1 & ES_2)	SoC_0^1, SoC_0^2	%80, %50
Line Res., Induc. (PV_1)	$R_{line,1}$, $l_{line,1}$	$0.15\ \Omega, 0.2$ mH
Line Res., Induc. (PV_2)	$R_{line,2}$, $l_{line,2}$	$0.1\ \Omega, 0.1$ mH
Line Res., Induc. (PV_3)	$R_{line,3}$, $l_{line,3}$	$0.3\ \Omega, 0.3$ mH
Line Res., Induc. (ES_1 & ES_2)	$R_{line,4;5}$, $l_{line,4;5}$	$0.25, 0.3\ \Omega, 0.05$ mH
NC Loads Conn. to ES_1 & ES_2	$R_{nc_{1;2}}$	$15.5\ \Omega$
Other Resistive Loads	R_{resis},	$15\ \Omega$

$$R_{CPL} = -\frac{V_{CPL}^2}{P_{CPL}}, \quad I_{CPL} = 2\frac{P_{CPL}}{V_{CPL}}, \tag{4.19}$$

where P_{CPL} denotes the demanded power.

By contrast, when units operate as CPS, their equivalent model is represented by a current source in series with a positive resistance. While the current source itself does not influence small-signal stability, the resistive term directly affects system damping [170, 177]. Specifically, positive resistance improves stability margins, whereas negative resistance degrades them [136].

Consequently, in the presence of CPLs, the microgrid becomes more vulnerable to instability during Mode IV, since no CPS units are available to inject positive resistance and improve damping. This risk is particularly pronounced under light-load conditions, where the destabilizing influence of CPLs dominates. Because PV units employ the proposed droop-based control in this mode, a detailed stability investigation is essential. It should be noted, however, that practical factors such as finite converter efficiency, limited closed-loop gain, and bandwidth constraints reduce the destabilizing effect of real CPLs compared to their idealized representation [170]. Thus, if stability is guaranteed under the conservative assumption of ideal CPLs, the actual system can also be considered stable.

According to the literature, droop controllers typically operate at relatively low sampling rates, whereas inner current loops and outer voltage controllers exhibit higher bandwidths and significantly faster dynamics [178]. For simplification, these fast dynamics can be neglected in the stability analysis, leading to a reduced-order model [134]. Under this assumption, the n-th converter output voltage can be approximated as $v_{out}^n \approx v_{ref}^n$ [96].

Considering $v_{out}^n = f(I_{out}^n)$ in (4.1), applying a small perturbation at an arbitrarily operating point $(I_{out}^n, v_{out}^n)\big|_{\text{o.p.}}$ gives:

$$\begin{aligned} \widehat{I}_{out}^n &= I_{out}^n - I_{out}^n\big|_{\text{o.p.}} \\ \widehat{v}_{out}^n &= v_{out}^n - v_{out}^n\big|_{\text{o.p.}} \end{aligned} \tag{4.20}$$

where the hat symbol $(\widehat{;})$ denotes perturbed variables. Accordingly, Linearizing (4.1) yields:

$$\begin{aligned} \widehat{v}_{out}^n &= -D^n \cdot \widehat{I}_{out}^n, \\ D^n &= R_{dr}^n \times e^{\alpha(I_{out}^n - I_{max}^n)} \times (1 + \alpha \cdot I_{out}^n) \end{aligned} \tag{4.21}$$

Considering the equivalent inductance and resistance of the interconnecting lines and the lumped load models in Fig. 4.9, Kirchhoff's laws can be applied and linearized to obtain:

$$\widehat{v}_{out}^n - \widehat{V}_{pcc} = R_{\text{line}}^n \widehat{I}_{out}^n + l_{\text{line}}^n \frac{d\widehat{I}_{out}^n}{dt}. \tag{4.22}$$

Substituting (4.21) into (4.22), and sorting the equation with respect to $\widehat{v}_{out}^n$ gives:

$$\frac{d\widehat{v}_{out}^n}{dt} = -\frac{D^n + R_{\text{line}}^n}{l_{\text{line}}^n} \widehat{v}_{out}^n + \frac{D^n}{l_{\text{line}}^n} \widehat{V}_{pcc}. \tag{4.23}$$

To incorporate V_{pcc} dynamics, the DC bus capacitor C_{bus} is included. From (4.21) and Kirchhoff's current law at the PCC, the total output current equals the sum of capacitor and load currents. Applying small-signal perturbation gives:

$$C_{bus} \frac{d\widehat{V}_{\text{pcc}}}{dt} = \sum_{n=1}^{N_u} \left(-\frac{\widehat{v}_{\text{out}}^n}{D^n} \right) - \widehat{I}_{load} \tag{4.24}$$

For the lumped load model, where resistive loads and CPLs are connected in parallel, the small-signal current is:

$$\widehat{I}_{load} = \widehat{I}_{resis} + \widehat{I}_{CPL} = \left(\frac{1}{R_{resis}} - \frac{1}{R_{CPL}} \right) \widehat{V}_{pcc}. \tag{4.25}$$

Substituting (4.25) into (4.24) yields:

$$\frac{d\widehat{V}_{\text{pcc}}}{dt} = -\frac{1}{C_{bus}} \sum_{n=1}^{N_u} \frac{\widehat{v}_{\text{out}}^n}{D^n} - \frac{1}{C_{bus}} \left(\frac{1}{R_{resis}} - \frac{1}{R_{CPL}} \right) \widehat{V}_{\text{pcc}} \tag{4.26}$$

Equations (4.23) and (4.26) can be expressed in compact state-space form as:

$$\frac{d}{dt}\begin{bmatrix}\widehat{v}_{\text{out}}\\ \widehat{V}_{\text{pcc}}\end{bmatrix}=\begin{bmatrix}A_{ii} & A_{iv}\\ A_{vi} & A_{vv}\end{bmatrix}\begin{bmatrix}\widehat{v}_{\text{out}}\\ \widehat{V}_{\text{pcc}}\end{bmatrix} \tag{4.27}$$

with:

$$A_{ii}=\begin{bmatrix}-\frac{D^1+R^1_{\text{line}}}{l^1_{\text{line}}} & 0 & \cdots & 0\\ 0 & -\frac{D^2+R^2_{\text{line}}}{l^2_{\text{line}}} & \cdots & 0\\ \vdots & \vdots & \ddots & \vdots\\ 0 & 0 & \cdots & -\frac{D^{N_u}+R^{N_u}_{\text{line}}}{l^{N_u}_{\text{line}}}\end{bmatrix}\in\mathbb{R}^{N_u\times N_u}$$

$$A_{iv}=\begin{bmatrix}\frac{D^1}{l^1_{\text{line}}} & \frac{D^2}{l^2_{\text{line}}} & \cdots & \frac{D^{N_u}}{l^{N_u}_{\text{line}}}\end{bmatrix}^\top\in\mathbb{R}^{N_u\times 1}$$

$$A_{vi}=\begin{bmatrix}-\frac{1}{C_{\text{bus}}D^1} & -\frac{1}{C_{\text{bus}}D^2} & \cdots & -\frac{1}{C_{\text{bus}}D^{N_u}}\end{bmatrix}\in\mathbb{R}^{1\times N_u}$$

$$A_{vv}=\begin{bmatrix}-\frac{1}{C_{\text{bus}}}\left(\frac{1}{R_{\text{resis}}}-\frac{1}{R_{\text{CPL}}}\right)\end{bmatrix}\in\mathbb{R}^{1\times 1}$$

Fig. 4.10 presents root locus plots under different parameter variations. Since the proposed nonlinear droop modifies the effective gain dynamically, its influence is reflected in all scenarios. In Fig. 4.10(a), increasing line resistance by 10% (in 10 steps) pushes eigenvalues deeper into the left half-plane, thus improving damping and enhancing stability. Conversely, Fig. 4.10(b) shows that higher line inductance shifts poles toward the right half-plane, reducing stability margins.

The impact of load variations is shown in Fig. 4.10(c) and Fig. 4.10(d). In Fig. 4.10(c), when the resistive load rises from 15 Ω (light loading), the eigenvalue locations shift but remain in the stable region, confirming robustness. Fig. 4.10(d) illustrates the effect of increasing CPL power from 50 W to 550 W. As expected, higher CPL shares drive poles closer to instability. However, increasing the droop gain up to eightfold successfully counteracts this destabilizing effect.

These results confirm that CPLs are most detrimental under high-demand conditions, where their relative share is significant. In such cases, large droop gains provide a practical stabilization mechanism, which aligns with the proposed nonlinear droop law in (4.1) (see

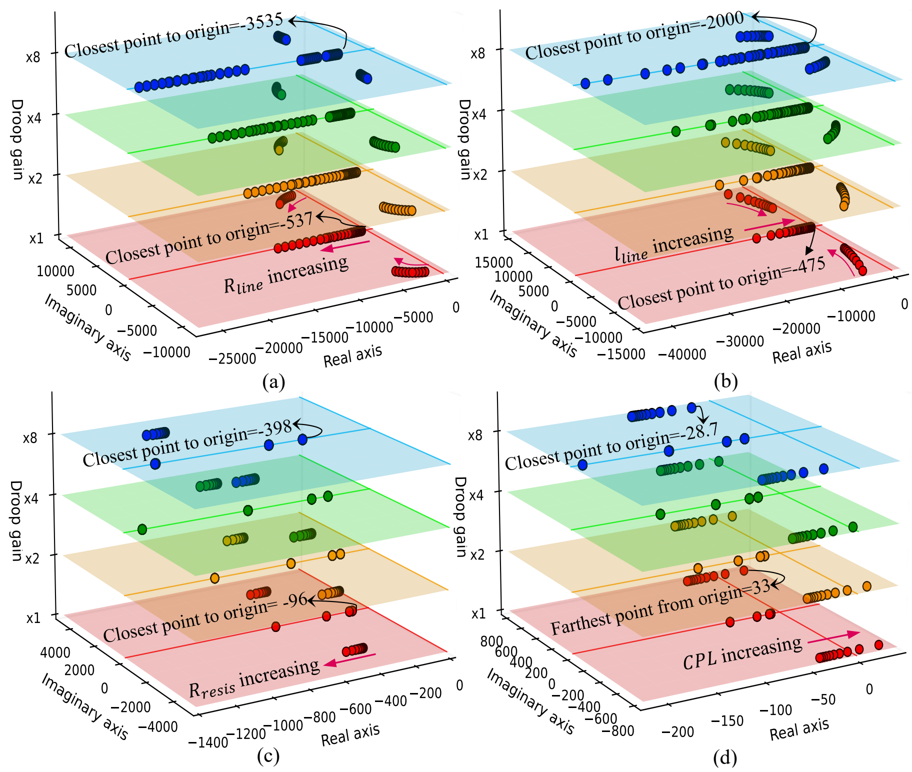

Figure 4.10: Root locus families under different parameter variations: (a) line resistance, (b) line inductance, (c) resistive loads, (d) CPLs.

also Fig. 4.2). Overall, higher droop gains guarantee robust small-signal stability across a wide range of scenarios, validating the effectiveness of the proposed control scheme.

4.1.4 Performance Evaluation based on Power-Hardware-In-the-Loop

To evaluate the effectiveness of the proposed approach, a PHIL-based testbed was developed to model a five-unit microgrid comprising three PV arrays and two ESs, as shown in Fig. 4.1. The main parameters of the DC-MG are reported in Table 4.1: two PV arrays are rated at 384 W, while the third is rated at 240 W. This PHIL platform enables the validation of the control strategy under realistic operating conditions, particularly in handling a physical storage unit [171]. The ES model presented in [171] is adopted here, and a default communication delay of 30 ms is considered to account for data transfer and processing latencies.

PHIL simulation allows the integration of real hardware components with real-time digital environments, thereby reproducing testing conditions that closely approximate those of a physical prototype of the complete system [179]. As highlighted in [180], this technology combines the advantages of numerical simulation and experimental testing,

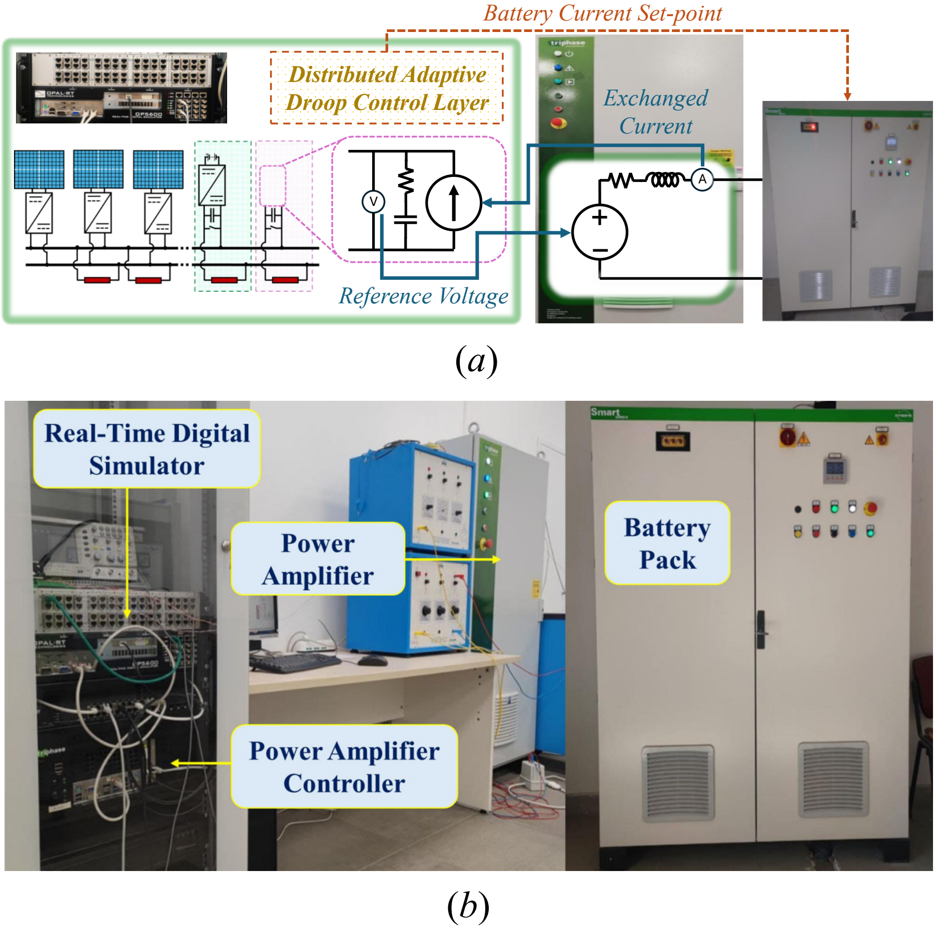

Figure 4.11: PHIL test set-up. (a) configuration, (b) equipment.

offering high-fidelity validation of algorithms and control schemes. Fully simulated tests are useful for verifying the theoretical functionality of the adaptive droop controller, but they may not fully capture the nonlinearities, losses, and dynamic effects of real devices. By incorporating an actual battery into the PHIL loop, electrochemical characteristics and dynamic responses are inherently preserved, leading to more representative and reliable test results [181]. Not to mention that the dynamic network model was created so that it could be integrated into a PHIL-type RT simulation. It was developed in the Matlab/Simulink environment to be connected to the PHIL simulation platform of the Politecnico di Bari, based on the use of an OPAL RT5600 digital RT simulator.

In the present setup, both the DC-MG and the distributed adaptive droop controller were implemented in real time. One of the two ES units was replaced with a physical $LiFePO_4$ battery pack, interfaced through a Triphase PM15A30F60 switching power amplifier. The experimental configuration is depicted in Fig. 4.11. In this arrangement, the amplifier operates as a voltage source, emulating the dynamics of the DC-MG at the PCC, while the real battery injects or absorbs current accordingly. This current is fed back into the real-time simulation, thereby achieving bidirectional coupling between the physical and simulated domains.

To ensure proper integration, appropriate scaling was applied so that the physical battery's capacity and ratings matched those of its simulated counterpart. Signal exchange for PHIL coupling was established via an optical fiber link between the OPAL-RT simulator and the amplifier controller, ensuring fast and reliable communication. The amplifier was managed by a dedicated controller responsible for synchronization and real-time data exchange.

The proposed droop control algorithm was also executed in real time on the simulator, generating current set-points for both the simulated storage units and the physical ES battery. For the latter, the current set-points were transmitted via a wired Ethernet connection to the battery pack. This setup guaranteed accurate implementation of the distributed control logic while subjecting the physical ES unit to realistic operating conditions. Overall, the PHIL platform provided a rigorous and high-fidelity environment for assessing the stability, adaptability, and practicality of the proposed control scheme under conditions closely resembling real-world deployment.

4.1.4.1 Mode I–Normal Operation

In Mode I, the PV arrays operate under the MPPT algorithm, extracting the maximum available energy from the incident irradiance. Under this condition, it is assumed that the generated power approximately matches the load demand, with only a negligible mismatch. As illustrated in Fig. 4.12(a), both the terminal currents and the PCC voltage remain stable, with the bus voltage regulated within its permissible range. Since the power balance is inherently satisfied by PV generation alone, the ES batteries remain inactive and neither charge nor discharge. During this balanced condition, the non-critical (NC) loads are directly supplied by the grid, while the storage units remain on standby, ready to participate whenever a deviation between supply and demand arises.

4.1.4.2 Transition From Mode I to Mode II

When the power generated by the RESs (operating under MPPT) becomes insufficient to meet the load demand (at $t = 3$ s), the PCC voltage begins to decline due to the supply deficit. Once the voltage reaches the predefined threshold of 45.5 V, the DC-MG transitions into Mode II (see Fig. 4.6), where the ESs act as suspension springs by discharging to

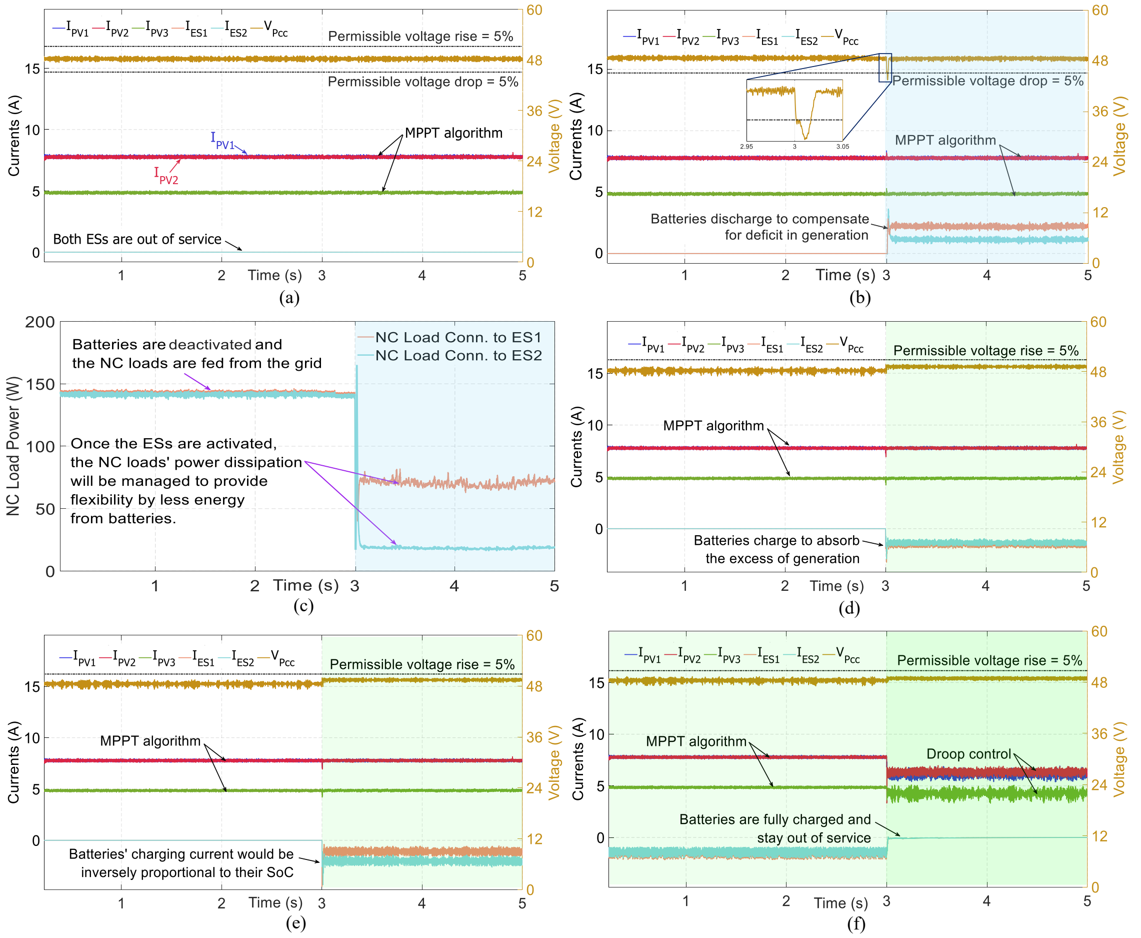

Figure 4.12: Results: (a) Mode I. (b) Transition from Mode I to Mode II. (c) Smart loads power dissipation in Mode II. (d) Transition from Mode I to Mode III with identical SoC of ESs' batteries. (e) Transition from Mode I to Mode III with different SoCs of ESs' batteries. (f) Transition from Mode III to Mode IV.

stabilize the DC bus voltage. As shown in Fig. 4.12(b), this corrective action restores the PCC voltage to approximately 48 V, thereby maintaining system reliability under stressed operating conditions.

The figure also highlights the current-sharing mechanism between two ESs initialized with different SoC levels ($SoC_0^1 = 80\%$ and $SoC_0^2 = 50\%$). In line with the proposed droop-based strategy, the unit with the lower SoC supplies less current than the one with the higher SoC, thus preventing deep discharge and promoting natural SoC equalization. Over time, this process drives the SoCs of both units toward convergence, ensuring long-term balance across the storage fleet.

An additional benefit of the ES concept is illustrated in Fig. 4.12(c). Once the support function is activated, the NC load connected in series with the battery pack dynamically adapts its consumption in response to both the external demand profile and the internal ES dynamics. This adaptive mechanism enhances overall system flexibility while reducing unnecessary battery cycling, which is particularly advantageous during extended supply–demand imbalances in Mode II.

4.1.4.3 Transition From Mode I to Mode III

In the reverse operating condition, when PV generation exceeds the instantaneous demand, the DC bus capacitor accumulates surplus energy, resulting in a rise in bus voltage. Once the PCC voltage surpasses the upper threshold of 50.5 V, the DC-MG transitions into Mode III, in which the ESs operate in the charging phase. In this mode, the ES units act as controllable loads, absorbing excess power to restore system balance and protect the grid from overvoltage.

Fig. 4.12(d) illustrates the case where both ES batteries start with identical SoCs ($SoC_0^1 = SoC_0^2 = 50\%$). Since the units are initially balanced, they absorb equal charging currents, and the PCC voltage stabilizes around 49.5 V while the PV arrays continue operating at their MPPT points. This scenario confirms the effectiveness of the droop-based charging control in evenly distributing surplus energy when the storage units have similar states of charge.

A more practical case is shown in Fig. 4.12(e), where the ES batteries begin with unequal initial charge levels ($SoC_0^1 = 80\%$ and $SoC_0^2 = 50\%$). Here, the unit with the higher SoC is assigned a smaller share of the charging current, while the unit with the lower SoC absorbs a greater portion. This adaptive current distribution promotes gradual convergence of the SoC levels over time, ensuring balanced utilization of the storage fleet and preventing overcharging of already saturated batteries.

4.1.4.4 Transition From Mode III to Mode IV

Once the ES batteries reach full charge capacity, they are deactivated to prevent overcharging, while PV generation continues to exceed the demand. Under this condition, the surplus power must be directly regulated by the PV units themselves. To achieve this, the PV converters switch their control strategy from MPPT to CVS at $t = 3$ s, marking the transition of the DC-MG from Mode III to Mode IV (see Fig. 4.6).

The corresponding system response is shown in Fig. 4.12(f). The two equally rated PV units exhibit effective current sharing, with only minor deviations attributed to line impedance. Meanwhile, the PCC voltage is maintained at approximately 49 V, well within

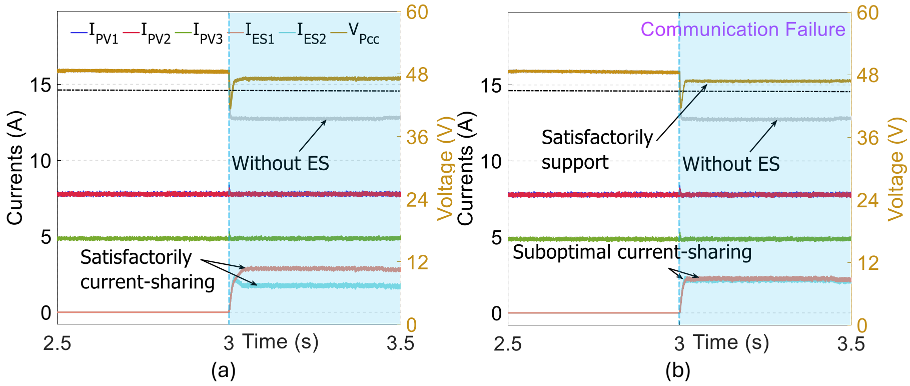

Figure 4.13: Current sharing of droop-controlled units in Mode II under: (a) Normal operation, (b) Communication failure. Note that $SoC_0^1 = 80\%$ and $SoC_0^2 = 50\%$. Other specifications of the batteries (i.e., C_{BAT}, η, and I_{max}) are assumed to be identical.

the permissible deviation band. This confirms that even in the absence of ES participation, the coordinated droop-based operation of PV converters can ensure bus voltage stability and fair load distribution under sustained surplus-generation conditions.

The robustness of the proposed control can also be assessed under communication constraints. Fig. 4.13 compares the current-sharing performance of two ES units in Mode II during (a) normal operation and (b) communication failure. Although a temporary mismatch in current allocation arises in case (b), the system remains stable, and the droop mechanism continues to deliver acceptable performance. This demonstrates the resilience of the proposed approach to practical limitations in communication infrastructure.

4.1.4.5 Evaluation of the Sensitivity to Communication Interruptions

The distributed nature of the proposed control architecture inherently enhances resilience against communication failures. In the event of a low-bandwidth communication loss, each unit seamlessly reverts to local droop control based on its most recently updated parameter values. This fallback mechanism ensures that the PCC voltage remains stable, though it temporarily sacrifices the benefits of optimal current sharing and SoC balancing across the ES fleet.

To validate this feature, an analysis was conducted under a scenario where communication is lost during the transition from Mode I to Mode II. The ES units (operating under droop control) were initialized with different SoCs ($SoC_0^1 = 80\%$ and $SoC_0^2 = 50\%$), while all other parameters (e.g., C_{BAT}, η, and I_{max}) were assumed identical. The corresponding system response is presented in Fig. 4.13.

The results confirm that, even without communication, the proposed control scheme maintains the PCC voltage within the permissible range, thereby ensuring system stability. However, a comparison of Fig. 4.13(a) and Fig. 4.13(b) highlights an important distinction: under normal operation, current sharing adapts to the SoC levels, whereas in the absence of communication, the ESs rely solely on local information. Since all other battery parameters are equal, both units end up sharing the current equally according to (4.10), irrespective of their initial SoC values.

This outcome emphasizes the robustness of the proposed architecture, as stability and voltage regulation are guaranteed even under communication interruptions. At the same time, it illustrates a fundamental trade-off between resilience and optimality: while communication enables fairness and extended battery life through SoC-aware current sharing, its loss leads to a simpler, equal-current distribution that, although less optimal, remains stable and reliable.

4.1.5 Demonstration of Performance privilege

In this section, the performance of the proposed method is further evaluated through a comparative study against three benchmarks: (i) conventional droop control with constant virtual resistances, (ii) the adaptive droop-based method in [3], and (iii) the SoC-oriented approach in [4]. All methods are tested on the sameDC-MG configuration operating in Mode II, where the ES units are active in the discharging phase. The comparison focuses on two critical control objectives for islanded DC-MGs:

- **Bus voltage regulation**, which ensures the PCC voltage remains within the permissible deviation band.

- **Current-sharing accuracy**, which reflects the degree of SoC balancing among active ES batteries with respect to their unit-specific characteristics.

For the conventional droop case, two gain settings are examined to highlight the inherent trade-off: a low gain (0.2 for ESs) and a high gain (2 for ESs). To clearly illustrate current-sharing performance, identical battery specifications are assumed.

The results in Fig. 4.14 and Table 4.2 highlight the intrinsic trade-off between voltage regulation and current-sharing accuracy across different droop-based strategies, under a surplus demand of 550 W beyond the PV generation.

In Fig. 4.14(a), conventional droop control with a high gain achieves excellent current sharing (error of only 0.63%), but this comes at the expense of poor voltage regulation,

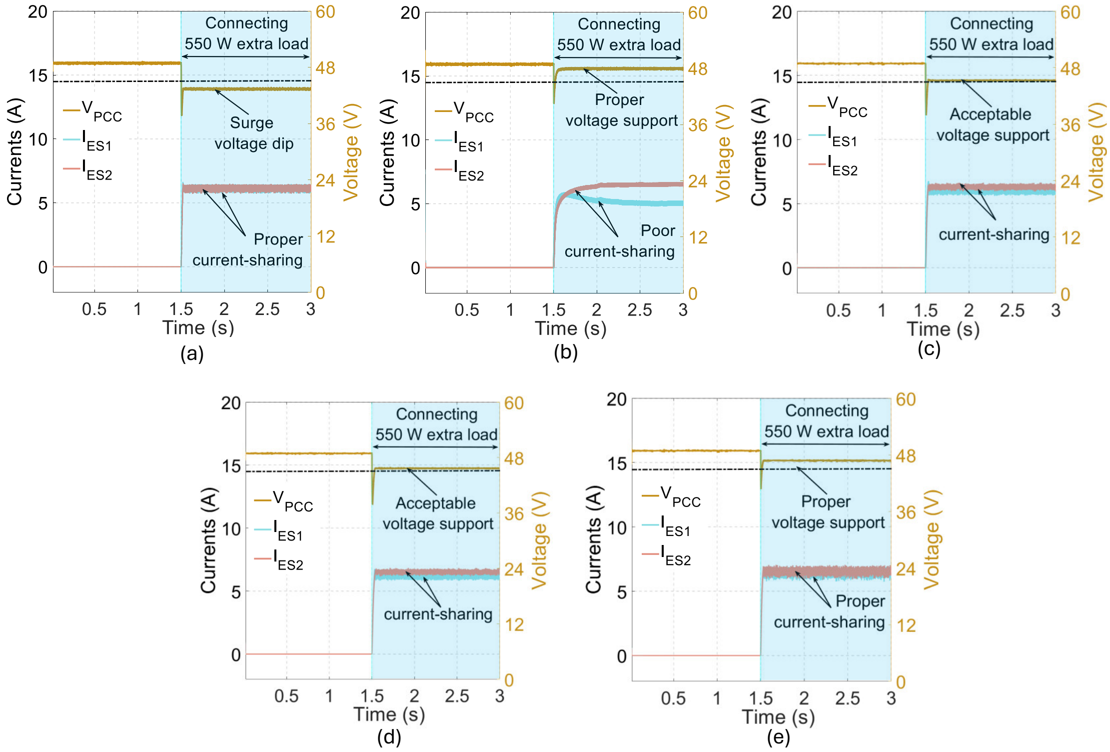

Figure 4.14: Comparison of different droop-based control methods in Mode II under a step-like intermittent operating pattern of theDC-MG. (a) Conventional droop control with high gain, (b) Conventional droop control with low gain, (c) Reference [3], (d) Reference [4], (e) Proposed algorithm.

Table 4.2: Comparison of droop-based control methods in Mode II under a 550 W surplus demand beyond the available power from PVs.

Control Method	**V_{pcc} deviation from V_{nom} (%)**	**I_{out} difference between two units with identical specifications (%)**
Conventional (high gain)	9.74	0.63
Conventional (low gain)	0.54	17.63
[3]	4.28	3.88
[4]	3.64	5.28
Proposed	2.29	1.31

with a deviation of 9.74%. This occurs because, according to (4.1), a large droop gain drives the reference voltage (v_{ref}) significantly away from its nominal value (V_{nom}).

In contrast, the low-gain case in Fig. 4.14(b) results in good bus voltage regulation, reducing the deviation to just 0.54%. However, the price is poor current-sharing accuracy, with a mismatch of 17.63%.

The approaches in [3] and [4] provide a more balanced compromise, with voltage deviations of 4.28% and 3.64% and current-sharing errors of 3.88% and 5.28%, respectively, as shown in Figs. 4.14(c)–(d).

Finally, the proposed distributed method achieves superior results in both objectives simultaneously. As presented in Fig. 4.14(e), it limits voltage deviation to 2.29% while maintaining current-sharing disparity at just 1.31%.

These findings clearly demonstrate that the proposed scheme reconciles the conflicting requirements of bus voltage stability and accurate current distribution, outperforming existing approaches. Its advantage arises from the distributed control structure, which combines local droop control with lightweight communication to adapt droop parameters dynamically. This mechanism, formalized in (4.3)–(4.10), enables the ES units to adjust their contributions according to both their own conditions and system-level demand, thereby ensuring efficient and reliable operation of islanded DC-MGs.

4.2 Decentralized Adaptive Control in the Presence of Constant Power Loads

While distributed control strategies have proven effective in enhancing flexibility and improving supply–demand balancing in MGs, they inevitably rely on communication links among units. This dependency can increase implementation complexity and require costly ICT infrastructure. In particular, in rural or remote areas—where stand-alone DC-MGs are often deployed—such infrastructure is either unavailable or economically impractical to maintain. Consequently, decentralized control schemes emerge as a practical alternative, as they rely solely on local measurements and unit-level decisions without requiring global data exchange.

A decentralized approach offers several advantages in this context. First, it enhances reliability, since each unit can independently regulate its contribution to the common bus voltage and current sharing, eliminating vulnerabilities associated with central controllers or communication failures. Second, it reduces costs and maintenance requirements, which is essential for off-grid MGs in low-resource settings. Third, by leveraging local voltage and current signals, decentralized schemes can still achieve effective power balancing and voltage regulation, especially when adaptive droop control formulations are employed to account for nonlinearities, line impedances, and varying loading conditions. Last but not least, their inherent modularity facilitates the seamless addition to or removal of DG/ESS units from the MG without requiring system-wide reconfiguration or reprogramming.

Therefore, a decentralized strategy is well-suited for rural DC-MGs, where simplicity, robustness, and low deployment cost are crucial. Building on these motivations, the following section presents a decentralized adaptive droop-based methodology designed to enhance flexibility, ensure reliable voltage regulation, and achieve accurate current sharing without relying on communication networks.

Apart from the control structure, as discussed in Section III, the integration of CPLs introduces additional challenges due to their negative incremental impedance characteristic. When the terminal voltage decreases, the load current increases to maintain constant power consumption, effectively exhibiting a negative resistance behavior. This phenomenon reduces system damping—commonly referred to as the *negative damping effect*—and can significantly compromise small-signal stability. In practical terms, the power–voltage interaction of CPLs tends to oppose the natural voltage recovery mechanisms of the sources, thereby amplifying voltage oscillations following disturbances. With the growing use of power electronic interfaces, CPLs have become increasingly prevalent in modern DC-MGs, typical examples being DC–DC converters, motor drives, and information technology equipment.

When CPLs are connected to droop-controlled converters, their negative impedance interacts with the converters' virtual impedance, potentially inducing undesirable dynamic coupling. This interaction can distort the intended droop characteristics and amplify voltage perturbations, resulting in oscillatory or even unstable behavior if not properly mitigated. The severity of this effect increases with both the proportion of CPLs in the load composition and the magnitude of droop gains, as both factors reduce the effective damping margin of the microgrid.

Building upon previous studies on islanded DC-MGs, this section introduces a complementary paradigm—*decentralized control*. The main contribution lies in the design of a cost-effective adaptive droop control scheme that achieves reliable voltage regulation and accurate power sharing without relying on communication links. By removing the dependency on data exchange, the proposed approach simplifies implementation, reduces cost, and becomes particularly suitable for rural or remote stand-alone MGs where communication infrastructure is limited or unavailable.

Addressing the destabilizing influence of CPLs is essential to ensure reliable and stable operation. Hence, the proposed scheme not only adjusts droop gains according to system demands but also explicitly considers stability constraints to guarantee precise voltage regulation, equitable current sharing, and sufficient damping margins in the presence of

CPLs.

In addition to communication independence, the method ensures modularity and scalability, enabling DG units, ESS systems, and ESs to be seamlessly integrated or removed without reprogramming or centralized coordination. The introduction of an adaptive nonlinear droop formulation further enhances robustness under diverse loading conditions and explicitly accounts for line impedance effects, thereby maintaining stable performance even in heavily loaded scenarios.

The effectiveness of the proposed decentralized strategy is validated through detailed simulation studies, demonstrating its ability to balance supply and demand, maintain bus voltage stability, and improve overall system flexibility—all while reducing reliance on large-scale BESS installations.

The remainder of this Section is organized as follows. Section 4.2.1 introduces the system configuration adopted in this study and outlines the proposed decentralized adaptive droop control scheme. It also develops the control formulation in detail, including the voltage regulation mechanism and the adaptive nonlinear droop characteristics. Section 4.2.2 is dedicated to conducting the stability analysis of the proposed approach against small perturbations. Finally, Section 4.2.3 evaluates the performance of the proposed method through simulation studies under diverse operating scenarios, demonstrating its effectiveness in bus voltage regulation, accurate power sharing, and flexibility enhancement in stand-alone DC-MG environments.

4.2.1 The Design Principle on the improved Decentralized approach

Building on the previous Section, which introduced a distributed adaptive coordination framework for enhancing flexibility in stand-alone DC-MGs, this Section examines a decentralized alternative. As in the distributed scheme, the MG under study integrates RES units (e.g., PV arrays), storage devices, and an ES interfaced with NC loads. The *Electric Spring* continues to play a central role by enabling demand-side participation and reducing reliance on large BESS banks, thereby increasing system flexibility. In contrast to the distributed approach, however, the decentralized strategy eliminates the need for communication infrastructure. Each unit operates solely on locally measured signals—specifically, terminal voltage and current.

Conventional droop control provides a simple mechanism for current sharing and voltage regulation by linearly decreasing the reference voltage as current rises. However, its accuracy deteriorates under heavy loading, especially in the presence of line impedance

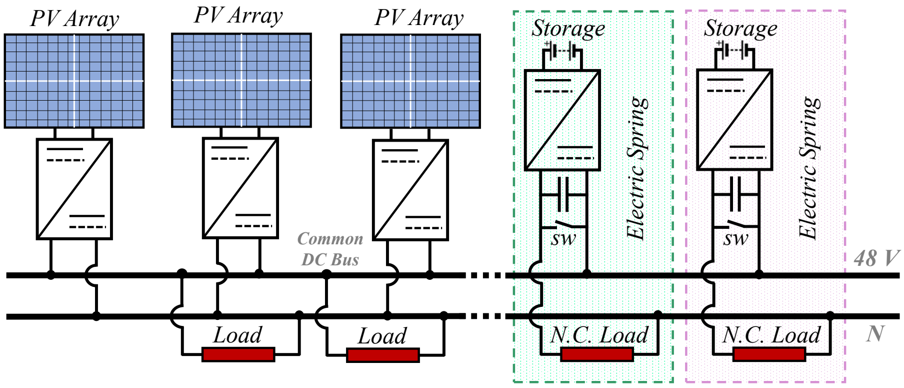

Figure 4.15: Schematic of a standalone DC-MG including some exemplary means of local energy resources, and electric springs.

and CPLs. To address these shortcomings, the proposed method introduces a nonlinear adaptive droop formulation in which the droop slope adjusts dynamically with the load level. Under light loading, the slope remains small, ensuring accurate voltage regulation and reduced power losses. As the load increases and the system approaches its generation capacity, the slope automatically rises, thereby improving current-sharing precision and mitigating the destabilizing effects of CPLs.

Through this adaptive formulation, the decentralized strategy achieves a balanced trade-off between bus voltage regulation and current sharing, while requiring no communication links. Moreover, the control law is applied uniformly across RES generators and the ES, ensuring modularity and scalability: units can be added or removed without global reconfiguration. In this way, the decentralized design almost preserves the same MG configuration presented in the previous Section but offers a simpler, communication-free implementation that enhances flexibility, improves reliability, and provides a cost-effective solution for off-grid applications. This configuration is illustrated in Fig. 4.15.

4.2.1.1 Adaptive Droop control Formulation

To comprehensively assess the performance of a DC-MG, several aspects must be evaluated simultaneously. These include bus voltage regulation, current-sharing accuracy with respect to the rated capacity of individual units, total power dissipation associated with line impedances, and the destabilizing influence of CPLs. The latter are particularly challenging since CPLs attempt to draw fixed power regardless of bus voltage fluctuations, thereby exhibiting a negative incremental resistance that can compromise system stability [16].

Earlier studies [4, 16, 83] have shown that larger droop gains improve current-sharing

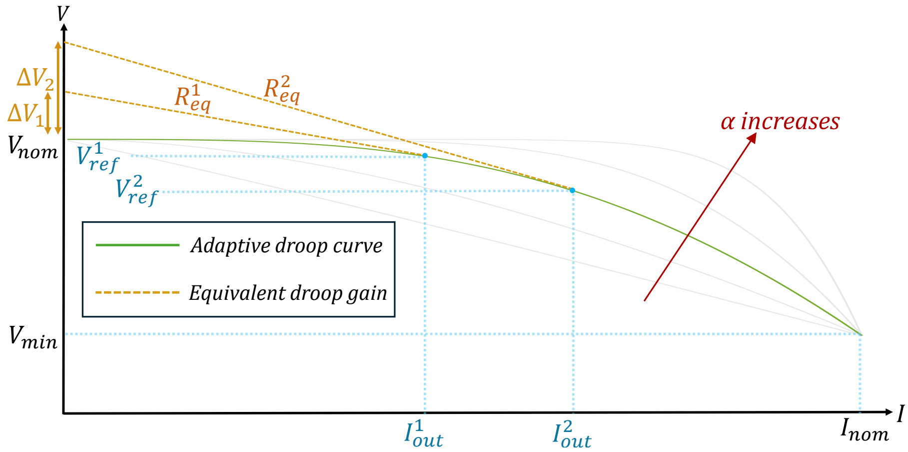

Figure 4.16: The droop curve of the proposed adaptive control approach.

accuracy and mitigate the destabilizing impact of CPLs. Conversely, smaller droop gains enhance voltage regulation and reduce steady-state power losses by keeping the reference voltage closer to its nominal value. From these findings, practical guidelines can be derived. Under light loading conditions, where available generation capacity significantly exceeds demand, CPL effects are negligible and current sharing is less critical. In this case, small droop gains are preferable to achieve accurate voltage regulation and minimize losses. Under heavy loading conditions, when demand approaches the maximum generation capacity and CPLs exert stronger influence, larger droop gains become more beneficial, as they improve current-sharing precision and strengthen overall system stability.

These observations motivate the adoption of an adaptive droop curve instead of a conventional linear droop with fixed slope. The proposed nonlinear formulation preserves low droop gains under light loading and gradually increases them as load rises, thereby combining the advantages of both operating regimes. To achieve this behavior, the Conventional droop formula with a fixed slope can be reformulated by introducing a logarithmic term:

$$\begin{aligned} v^n_{ref} &= V_{nom} - R^n_{dr} \cdot \ln\left(1 + \left(\frac{I^n_{out}}{I^n_{max}}\right)^{\alpha}\right) \cdot I^n_{out}, \\ R^n_{dr} &\leq \frac{\Delta V_{max}}{I^n_{max}}, \qquad \Delta V_{max} = V_{nom} - V_{per} \end{aligned} \tag{4.28}$$

where $\alpha > 0$ is a shaping coefficient that determines the position of the nonlinear droop curve in the v–i plane (see Fig. 4.16). Its value depends on the unit's current-handling capability and the impedance of its connecting line.

For the n-th unit, the equivalent droop gain R^n_{eq} is given by the slope of the tangent to the curve at the operating point. Differentiating (4.28) with respect to I^n_{out} yields:

$$R^n_{eq} = \frac{\partial v^n_{ref}}{\partial I^n_{out}} = -R^n_{dr} \cdot \left[\frac{\alpha \cdot \left(\frac{I^n_{out}}{I^n_{max}}\right)^{\alpha}}{I^n_{max} \cdot \left(1 + \left(\frac{I^n_{out}}{I^n_{max}}\right)^{\alpha}\right)} + \ln\left(1 + \left(\frac{I^n_{out}}{I^n_{max}}\right)^{\alpha}\right) \right]. \tag{4.29}$$

The negative sign reflects the descending nature of the characteristic. For a given loading condition, the intersection of the tangent with the voltage axis defines the voltage shift ΔV^n required to compensate the line drop and maintain the PCC voltage close to nominal. This can be expressed as:

$$\Delta V^n = R^n_{dr} \cdot \left[\frac{\alpha \left(\frac{I^n_{out}}{I^n_{max}}\right)^{\alpha}}{I^n_{max}\left(1 + \left(\frac{I^n_{out}}{I^n_{max}}\right)^{\alpha}\right)} \right] \cdot I^n_{out}. \tag{4.30}$$

It is evident that ΔV^n, which corresponds to the effective voltage drop across the connection line, reaches its maximum under heavy loading when I^n_{out} approaches I^n_{max}. At this operating point, the maximum equivalent droop gain $R^n_{eq,max}$ can be obtained. On the other side, it is highlighted in previous literature that increasing the droop gain enhances current-sharing accuracy among in-service units with unequal power ratings [182]. However, as demonstrated in Section III, this improvement should not reduce system damping or increase the risk of voltage instability. In particular, the stability of a droop-controlled DC-MG with a considerable aggregation of CPLs can be guaranteed if the following condition is satisfied:

$$1 - \frac{R^n_{eq,max}}{R_{CPL}} \geq 0 \tag{4.31}$$

According to this stability criterion and the analytical demonstrations presented in [170, 183], voltage stability within a droop-controlled DC-MG can be ensured by allowing the value of $R^n_{\text{eq,max}}$ to increase with the loading level, provided that it does not exceed the equivalent resistance of the CPLs connected to the microgrid, (i.e., $R^n_{eq,max} \leq R_{CPL}$). This condition guarantees that the system's impedance remains positive, thereby preventing the destabilizing effect commonly associated with CPLs, which behave as negative incremental resistances around their operating point. The detailed mathematical derivation and eigenvalue-based verification of this condition have already been presented in Section III and are therefore omitted here for brevity.

Furthermore, considering the heterogeneous generation capacities among active sources, it follows that the unit with the smallest nominal current capacity (i.e., the lowest $I_{\max}$) must be assigned the highest $R_{eq,max}$ value in order to preserve proportional current sharing across all participating units, as described in (3.18). This ensures that smaller-rated units experience appropriately limited current stress under heavy loading, while higher-capacity units contribute a greater share of the total demand. Consequently, satisfying this condition for the smallest-rated unit inherently guarantees compliance for all other units within the system, thereby maintaining both current-sharing accuracy and voltage stability across the entire DC-MG. Consequently, by substituting this condition into (4.29), the shaping coefficient α can be calculated as follows:

$$\alpha = \left(\frac{R^n_{eq,max}}{R^n_{dr}} - \ln(2) \right) \cdot 2 \cdot I^n_{max}. \tag{4.32}$$

This relation provides a systematic tuning rule, linking the adaptive droop parameter α with the nominal current rating and desired maximum equivalent droop gain of each unit.

4.2.1.2 Contribution of Storage Systems

To maximize the efficiency and lifespan of the ESSs, the proposed droop control strategy must ensure proper SoC balancing during both charging and discharging modes while preventing overcharging and deep discharging. The integration of multiple ESs with different capacities and initial SoCs can adversely affect their long-term performance, as batteries with lower SoC levels are more susceptible to deep discharges, whereas those with higher SoC levels face a greater risk of overcharging [184]. Such imbalance not only accelerates capacity fading but also shortens the overall service life of the energy storage system.

In this work, the stored energy of each battery is regulated through a unified modified droop control principle that operates seamlessly in both charging and discharging modes. As illustrated in Fig. 4.16, the terminal current of each battery is governed by its corresponding droop gain. To promote SoC equalization and enhance the aggregate lifetime of the storage subsystem, the droop gain is adaptively adjusted in real time according to the individual characteristics of each ES unit. Specifically, during discharging, batteries with higher SoC values are required to deliver larger currents and are therefore assigned smaller virtual resistances. Conversely, during charging, batteries with lower SoC levels are given smaller virtual resistances, allowing them to absorb charge at a faster rate. This reciprocal mechanism ensures progressive SoC equalization among all units over time [185]. The corresponding relationship is defined as follows:

$$\begin{cases} \text{Discharging:} \qquad R^n_{dr,dis} = \dfrac{k^n_{dis}}{SoC^n}, \\ \text{Charging:} \qquad R^n_{dr,char} = k^n_{char} \cdot SoC^n. \end{cases} \tag{4.33}$$

Furthermore, employing a logarithmic droop characteristic instead of a linear one accelerates SoC equalization, ensuring smoother convergence among storage units while maintaining robust voltage regulation. This approach mitigates abrupt current transitions and enhances the dynamic coordination of multiple batteries during load variations.

The PCC voltage inherently reflects the instantaneous power balance of the DC-MG: a generation deficit causes the equivalent DC bus capacitor to discharge, resulting in a voltage drop, whereas surplus generation leads to a voltage rise [185]. This relationship can be exploited to define appropriate values for k^n_{char} and k^n_{dis}, ensuring effective SoC balancing under both operational modes.

When the generation capacity of RESs either falls short of or exceeds the load demand, the corresponding current imbalance must be compensated by the ESs. The PCC voltage can therefore be expressed as:

$$V_{pcc} = \frac{1}{C_{pcc}} \int \left(\sum_{n=1}^{N_{es}} I^n_{out} + (I_{RES} - I_{load}) \right) dt, \tag{4.34}$$

where N_{es} denotes the total number of ES units and C_{pcc} represents the equivalent bus capacitance. Differentiating (4.34) and substituting from (4.28) yields:

$$\begin{gathered} C_{pcc} \frac{dV_{pcc}}{dt} = \sum_{n=1}^{N_{es}} \frac{V_{nom} - v^n_{ref}}{\Re^n_{dr}} + (I_{RES} - I_{load}), \\ \Re^n_{dr} = R^n_{dr} \cdot \ln\left(1 + \left(\frac{I^n_{out}}{I^n_{max}}\right)^{\alpha}\right), \end{gathered} \tag{4.35}$$

where $\Re^n_{dr}$ denotes the effective virtual resistance of the n-th ES unit.

Assuming an ideal controller and following the demonstration in [99], where line resistances are designed to render voltage drops negligible, it is reasonable to consider $v^n_{ref} \simeq V_{pcc}$. Furthermore, under coordinated operation, the effective resistances of all ES units can be expressed proportionally as

$$\mathfrak{R}^n_{dr} = \beta_1 \mathfrak{R}^1_{dr} = \beta_2 \mathfrak{R}^2_{dr} = \cdots = \beta_{N_{es}} \mathfrak{R}^{N_{es}}_{dr}, \tag{4.36}$$

where β_n denotes the current-sharing coefficient associated with the n-th ES unit. Under these assumptions, the dynamic behavior of the PCC voltage can be expressed as:

$$V_{pcc}(t) = \left(V_{nom} + (I_{RES} - I_{load}) \frac{\mathfrak{R}^n_{dr}}{\lambda^n} \right) \left(1 - e^{-\frac{\lambda^n t}{C_{bus} \mathfrak{R}^n_{dr}}} \right), \tag{4.37}$$

where $\lambda^n = \beta_1 + \beta_2 + \cdots + 1 + \cdots + \beta_{N_{es}}$.

At steady state ($t \to \infty$), the voltage deviation from the nominal value is given by:

$$\Delta V = V_{nom} - \lim_{t \to \infty} V_{pcc}(t) = (I_{load} - I_{RES}) \frac{\mathfrak{R}^n_{dr}}{\lambda^n}. \tag{4.38}$$

Equation (4.38) indicates that smaller values of $\mathfrak{R}^n_{dr}$ mitigate voltage fluctuations and enhance system stability. Substituting (4.28) into (4.38), the feasible ranges for k^n_{char} and k^n_{dis} ensuring voltage deviation within acceptable limits can be derived as:

$$\begin{aligned} k^n_{dis} &\leq \frac{SoC^n \Delta V_{max} \lambda^n}{(I_{load} - I_{RES}) \ln\left(1 + \left(\frac{I^n_{out}}{I^n_{max}}\right)^{\alpha}\right)}, \\ k^n_{char} &\leq \frac{\Delta V_{max} \lambda^n}{SoC^n (I_{load} - I_{RES}) \ln\left(1 + \left(\frac{I^n_{out}}{I^n_{max}}\right)^{\alpha}\right)}. \end{aligned} \tag{4.39}$$

The above inequalities define the admissible tuning boundaries for the droop coefficients during charging and discharging, ensuring both SoC balancing and voltage stability within the defined 5% tolerance band. These relations serve as practical design guidelines for implementing the proposed adaptive droop strategy in multi-battery DC-MG configurations.

4.2.1.3 Voltage Regulation Mechanism

Building upon the preceding formulation, Fig. 4.17 illustrates the control architecture adopted for the power converters of the DC-MG units, namely DGs and ESS systems. The scheme employs a cascaded arrangement, in which terminal voltages are regulated by an inner current loop combined with an outer voltage loop. The reference signal for the outer loop, v_{ref}, is determined according to (4.28), thereby allowing the droop characteristic to adapt dynamically to varying load and generation conditions. This hierarchical structure enhances robustness by decoupling fast current dynamics from slower voltage regulation,

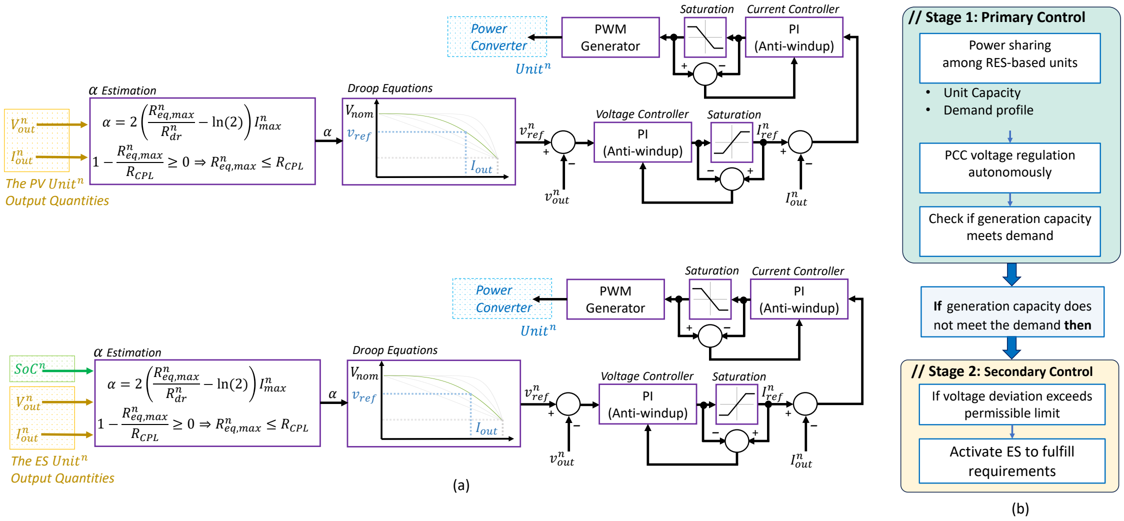

Figure 4.17: Control of in-service units, (a) Control block diagram of power converters, (b) control mechanism.

ensuring stable operation across a broad range of operating points.

During over-current events, the PI controller output may approach saturation as it attempts to restore the voltage, leading to integrator windup, degraded transient performance, and in some cases oscillatory behavior. An anti-windup mechanism, implemented following the approach in [186], is embedded within the loop to address this issue. This strategy prevents the accumulation of error in the integrator state when saturation occurs, thereby releasing the controller once normal conditions are restored and improving both transient response and overall stability.

The overall operation of the proposed adaptive strategy can be interpreted in two sequential stages. In the first stage, the DGs apply the adaptive droop control to regulate the PCC voltage while simultaneously sharing current among the generating units. This constitutes the primary control layer of the DC-MG, ensuring both voltage quality and proportional load sharing under normal operating conditions. In the second stage, if the aggregate DG capacity cannot fully satisfy the demand and the PCC voltage deviates beyond the admissible band, the ESS system is automatically activated. In this mode, the ESS units participate through the same adaptive droop law, thereby reinforcing voltage regulation and contributing to supply–demand balance. This coordinated activation ensures that the storage units are utilized only when strictly necessary, thereby extending battery lifetime and enhancing overall system resilience.

According to Table 4.3, the admissible PCC voltage deviation is limited to 5%. The effectiveness of the proposed scheme in satisfying this requirement, while simultaneously

Table 4.3: DC Microgrid Parameters in Decentralized Control Structure.

Parameters	**Symbol**	**Value**
Nominal Voltage	V_{nom}	48 V
Permissible Voltage Variation	V_{per}	$\pm 5\% V_{nom}$
Max. Current (PV_1 & PV_2)	I_{max}	8 A
Max. Current (PV_3)	I_{max}	5 A
Max. Current (ES_1 & ES_2)	I_{max}	10 A
Initial SoC (ES_1 & ES_2)	SoC_1^0, SoC_2^0	%80, %50
Line Res., Induc.(PV_1)	$R_{line,1}$, $l_{line,1}$	$0.15\ \Omega, 0.2$ mH
Line Res., Induc. (PV_2)	$R_{line,2}$, $l_{line,2}$	$0.1\ \Omega, 0.1$ mH
Line Res., Induc. (PV_3)	$R_{line,3}$, $l_{line,3}$	$0.3\ \Omega, 0.3$ mH
Line Res., Induc. (ES_1 & ES_2)	$R_{line,4;5}$, $l_{line,4;5}$	$0.25\ \Omega, 0.05$ mH
Total Resistive Load, CPL	R_{resis}, R_{CPL}	$15\ \Omega, 10\ \Omega$

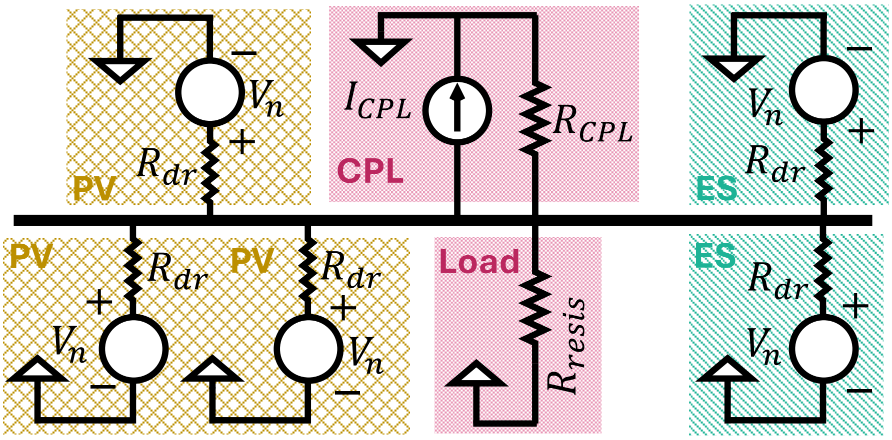

Figure 4.18: Equivalent circuit diagram of the proposed droop-controlled DC-MG.

ensuring reliable current sharing among all active units, is demonstrated through the performance assessment presented in the following section.

4.2.2 Small-Signal Stability Analysis

The situation here closely parallels the stability discussion presented in the previous section. As previously noted, the stability of a DC-MG can be effectively assessed using small-signal analysis. Based on the linearized small-signal model of an ideal CPL given in (3.35), it has been shown in [184] that while the negative incremental resistance of CPLs introduces a destabilizing effect on the grid, the current-source component itself does not significantly affect system stability. It is also important to consider that practical factors—such as converter efficiency, closed-loop gain, and bandwidth—tend to mitigate the destabilizing influence of real CPLs compared to their idealized representations [3, 184, 187]. Therefore, if the system remains stable under ideal CPL conditions, it can be reasonably expected to maintain stability under practical operating scenarios as well.

Furthermore, as discussed in the previous section, droop controllers typically operate at a lower sampling rate than the inner current and outer voltage controllers, which are designed for higher bandwidth and faster dynamic response [185]. Consequently, the dynamics of these faster control loops can be neglected, simplifying the system model by reducing its order [98]. Under such idealized assumptions, the output voltage of the n-th converter can be approximated as equal to its reference voltage (i.e., $v_{out}^n = v_{ref}^n$) [183]. Perturbations around the equilibrium point are then applied to derive linearized system equations, providing analytical insight into the small-signal dynamics. Following the same approach, and considering the same as the Section 4.1.3, the dynamic equations can be expressed by applying a small perturbation to (4.28):

$$\begin{aligned} \widehat{v}_n^{out} &= -D_n \cdot \widehat{I}_n^{out}, \\ D_n &= -R_{dr}^n \left[\ln(1+x) + \frac{\alpha x}{1+x} \right], \qquad x = \left(\frac{I_{out}^n}{I_{max}^n} \right)^{\alpha} \end{aligned} \tag{4.40}$$

In (4.40), the symbol $(\widehat{\cdot})$ also denotes a variable perturbed around the operating point. Fig. 4.18 presents the equivalent diagram of the tested DC-MG. As shown in that figure, by accounting for the equivalent inductance and resistance of the lines and the equivalent lumped load model, Kirchhoff's laws can be derived and then linearized using a small-signal approximation:

$$\begin{aligned} \widehat{v}_{out}^n - \widehat{v}_{pcc} &= R_{line}^n \widehat{I}_{out}^n + l_{line}^n \frac{d\widehat{I}_{out}^n}{dt}, \\ \widehat{v}_{pcc} &= R_{load,eq} \sum_{n=1}^{N_u} \widehat{I}_{out}^n, \\ R_{load,eq} &= R_{resis} \parallel R_{CPL}. \end{aligned} \tag{4.41}$$

Substituting (4.40) into (4.41) yields:

$$\frac{d\widehat{I}_{out}^n}{dt} = -\frac{D_n + R_{load,eq} + R_{line}^n}{L_{line}^n} \cdot \widehat{I}_{out}^n - \frac{R_{load,eq}}{L_{line}^n} \sum_{\substack{j=1 \\ j \neq n}}^{N_u} \widehat{I}_{out}^j. \tag{4.42}$$

The above formulation can also be expressed in matrix form:

$$\frac{d\widehat{\mathbf{I}}_{out}}{dt} = A \widehat{\mathbf{I}}_{out} \tag{4.43}$$

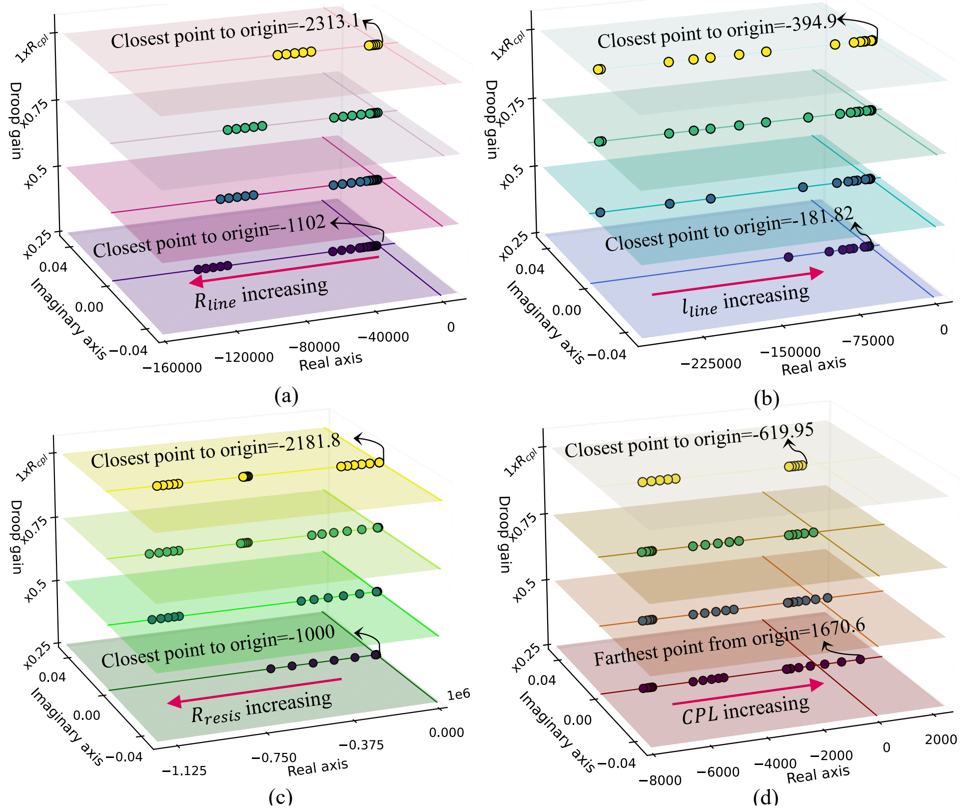

Figure 4.19: Family of root locus while changing different parameters. (a) Line resistance, (b) line inductance, (c) resistive loads, (d) CPLs.

where $\widehat{\mathbf{I}}_{out}$ is the column vector of perturbed output currents, and A is given by:

$$A = \begin{bmatrix} -\dfrac{D_1 + R_{load,eq} + R^1_{line}}{L^1_{line}} & -\dfrac{R_{load,eq}}{L^2_{line}} & \cdots & -\dfrac{R_{load,eq}}{L^n_{line}} \\ -\dfrac{R_{load,eq}}{L^1_{line}} & -\dfrac{D_2 + R_{load,eq} + R^2_{line}}{L^2_{line}} & \cdots & -\dfrac{R_{load,eq}}{L^n_{line}} \\ \vdots & \ddots & \vdots & \\ -\dfrac{R_{load,eq}}{L^1_{line}} & -\dfrac{R_{load,eq}}{L^2_{line}} & \cdots & -\dfrac{D_n + R_{load,eq} + R^n_{line}}{L^n_{line}} \end{bmatrix}$$

Figure 4.19 illustrates the root locus trajectories obtained under variations of key system parameters. Since the proposed control law adaptively adjusts the droop gain with the operating point, this effect is inherently captured in all plots. In Fig. 4.19(a), the eigenvalue distribution is shown as the line resistance is increased in ten increments of 10%. The additional resistance shifts the poles deeper into the left half-plane, thereby improving the overall stability margin. The opposite tendency is observed in Fig. 4.19(b), where larger line inductance drives the poles toward the right half-plane, reducing stability.

As shown in Fig. 4.19(c), increasing the resistive load from 15 Ω (light loading) alters the eigenvalue locations but does not compromise stability. In contrast, Fig. 4.19(d) highlights the destabilizing influence of CPLs: raising their power demand from 50 to 550 W moves the poles toward the right half-plane, gradually pushing the system toward instability. Importantly, the plots confirm that higher droop gains—up to $\times 24$—can effectively counteract this adverse effect.

It is worth noting that the destabilizing impact of CPLs is most pronounced under high-demand conditions, where their share of the total load is significant. In such scenarios, increasing the droop gain provides a practical stabilization mechanism, consistent with the adaptive nonlinear droop curve defined in (4.28) (see also Fig. 4.16). Overall, the results across all subfigures consistently demonstrate that larger droop gains enhance the robustness of the DC-MG small-signal response.

4.2.3 Performance Evaluation

In this section, the performance of the proposed scheme is assessed using the test DC-MG depicted in Fig. 4.15, modeled in the MATLAB® environment. The system includes three DG units: DG_1 and DG_2 emulate two PV arrays with identical power ratings, whereas DG_3 represents a smaller PV array that generates half the power of each of the other two units. The main parameters are summarized in Table 4.3. As discussed before, the ES employed in this study adopts a half-bridge inverter configuration, illustrated in Fig. 2.7, with detailed specifications provided in Table 2.3. The ES enhances overall system flexibility by participating in bus voltage support (i.e., through surplus energy provision) and demand-side management, by dynamically modulating NC loads under stressed conditions.

To validate the effectiveness of the proposed adaptive droop control, a comparative study is carried out against conventional droop control schemes with fixed low and high VR. These two benchmark cases are widely adopted in the literature and represent the inherent trade-off between voltage regulation and current-sharing precision in fixed-parameter approaches. The evaluation therefore focuses on whether the adaptive law can overcome the limitations of each extreme case.

The analysis considers four key performance metrics:

- PCC voltage regulation, to assess the ability of the controller to maintain bus voltage deviations within the admissible band;

- Current-sharing accuracy among heterogeneous DG units, ensuring proportionality to their rated capacities under both light and heavy loading;
- Total power losses associated with line resistances, reflecting the efficiency implications of different droop strategies; and
- The ES's capability to stabilize the PCC voltage under overload conditions, highlighting the contribution of storage and demand-side participation to system resilience.

This comprehensive framework enables a fair and transparent comparison of the proposed adaptive droop method against conventional approaches, providing quantitative evidence of its superiority in balancing voltage quality, current-sharing fairness, efficiency, and flexibility.

Two control strategies are compared in this study: (i) the proposed adaptive droop control and (ii) conventional droop control with constant VR. For the latter, two distinct gain settings are considered to reflect typical design trade-offs: low gains (0.3 for DG_1 and DG_2, 0.4 for DG_3, and 0.2 for ESs) and high gains (3 for DG_1 and DG_2, 4 for DG_3, and 2 for ESs). These cases will capture the inherent limitations of fixed-parameter droop control, where small gains lead to poor current sharing, while large gains improve proportionality at the expense of voltage quality.

An intermittent step-like demand profile is applied to evaluate the effectiveness of the proposed method. The total demand is assumed to remain within the generation capacity of the DGs, ensuring that no overloading occurs (i.e., $I_{out}^n \leq I_{max}^n$). This scenario serves as a benchmark to examine how the system reacts to abrupt load variations under normal conditions.

The analysis focuses on three critical aspects:

- PCC voltage recovery speed, as an indicator of the system's dynamic response and stability;
- Accuracy of current sharing among DG units, to assess fairness in load distribution relative to nominal capacities; and
- Prevention of unnecessary ES activation, which reflects the ability of the scheme to preserve stored energy for genuine contingencies rather than routine fluctuations.

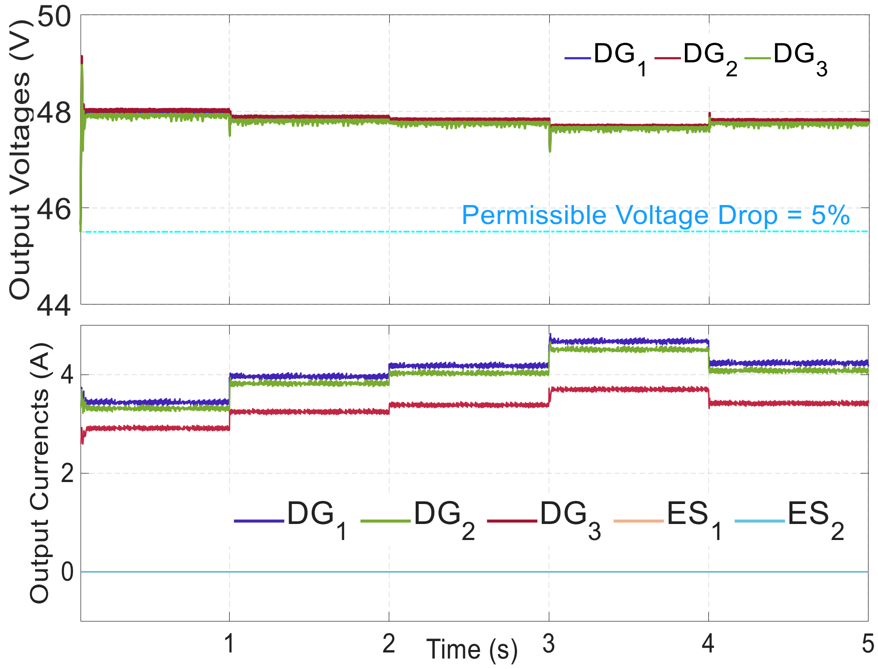

Figure 4.20: DG units' response to the variable demand profile using the proposed method.

The corresponding simulation outcomes are reported in Figs. 4.20-4.22 and are analyzed in detail in the following subsections.

Fig. 4.20 illustrates the terminal currents and voltages of the units under the proposed control strategy at different loading levels. The system demonstrates a rapid dynamic response to step changes, while PCC voltage deviations remain within the prescribed band. Furthermore, current distribution among the DG units follows their nominal ratings, ensuring accurate proportional sharing under both light and heavy loading. Since the terminal voltages never drop below the defined threshold, the ESs remain deactivated throughout the test. This behavior is desirable, as it preserves the stored energy of the ESs for future contingencies such as overloads or generation shortages.

For comparison, Fig. 4.21 presents the results of conventional droop control with low VR. In this case, voltage excursions do not exceed acceptable limits, indicating satisfactory regulation capability. However, current-sharing accuracy is poor: DG_1 and DG_2, despite having identical nominal capacities, supply noticeably different currents. This mismatch highlights the inadequacy of small fixed droop gains in ensuring fairness and voltage stability simultaneously.

A different behavior is observed when conventional droop control is applied with

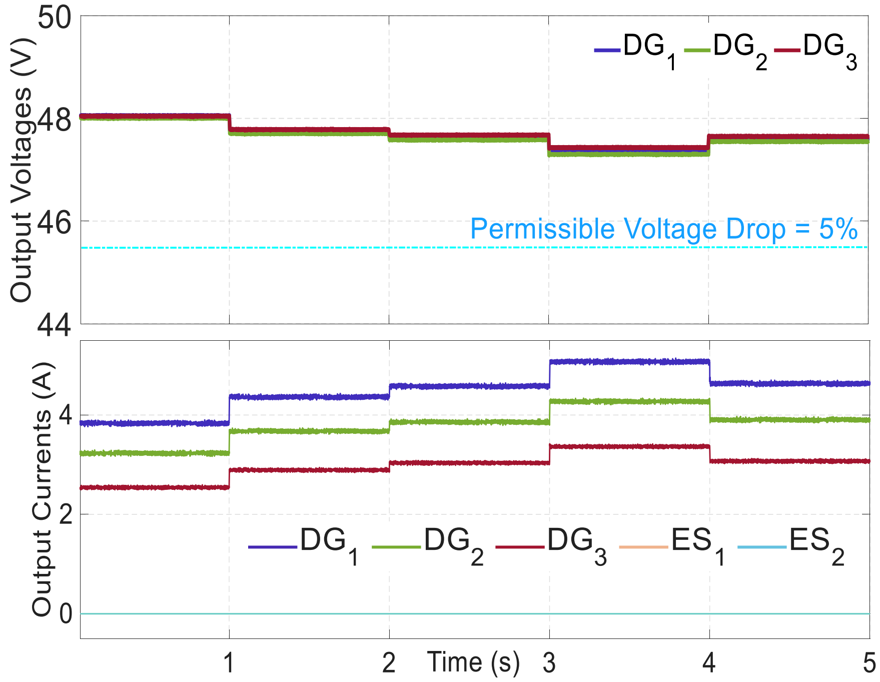

Figure 4.21: DG units' response to the variable demand profile using conventional droop control with low gains.

high VR, as shown in Fig. 4.22. Here, current-sharing accuracy is substantially improved compared to the low-gain case, as the steeper droop slopes enforce closer proportionality among units. However, this improvement comes at the expense of significant voltage violations, which in turn trigger the activation of the ESs. Nevertheless, it can be seen here that effective voltage correction is not achieved, even though the ESs' engagement is properly aligned with their characteristics (i.e., the unit with a lower SoC contributes less than that with a higher SoC). It is mainly due to the fact that the large droop gains introduce considerable deviations of the reference voltage (v_{ref}) from the nominal bus voltage (V_{nom}), as demonstrated in Fig. 4.16. As a result, the ES is forced into unnecessary operation, dissipating its energy without contributing meaningful stabilization. Such inefficient utilization of battery resources underscores the drawback of fixed high-gain droop control.

For a deeper analysis, the voltage regulation capability of the proposed control approach is benchmarked against conventional droop control with fixed small and large gains, irrespective of load conditions. To quantify this metric, the following general expression is employed:

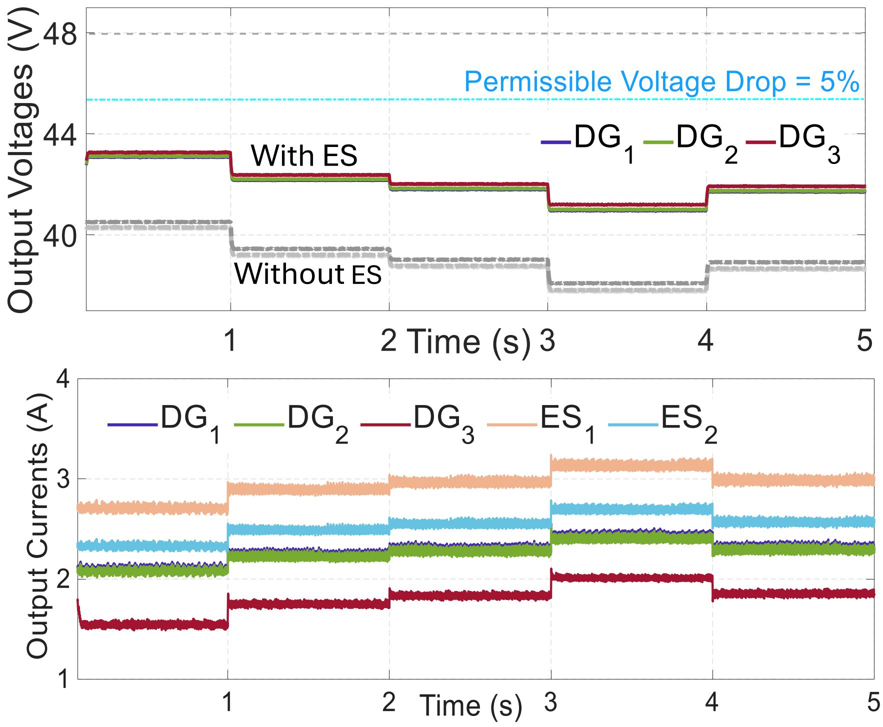

Figure 4.22: DG units' response to the variable demand profile using conventional droop control with high gains.

$$V_{reg}(\%) = \frac{V_{nom} - V_{pcc}}{V_{nom}} \times 100 \tag{4.44}$$

where V_{pcc} denotes the measured common bus voltage under varying load levels. The comparative results, shown in Fig. 4.23, confirm that the use of constant large droop gains significantly deteriorates voltage regulation by driving v_{ref} further away from V_{nom}. Conversely, the proposed adaptive scheme maintains the bus voltage within the prescribed permissible band while still yielding a sufficiently large equivalent droop gain at heavy loading. This demonstrates its ability to combine the strengths of both small- and large-gain strategies while avoiding their inherent drawbacks.

To further examine current-sharing performance, the following error index is defined:

$$I_{err}(\%) = \frac{|I^n_{des} - I^n_{out}|}{I^n_{des}} \times 100, \tag{4.45}$$

where the desired output current of the n-th unit is calculated as:

$$I^n_{des} = \frac{I^n_{max}}{\sum_{n=1}^{N_u} I^n_{max}} \times I_{Load}, \quad I_{Load} = \sum_{n=1}^{N_u} I^n_{out}, \tag{4.46}$$

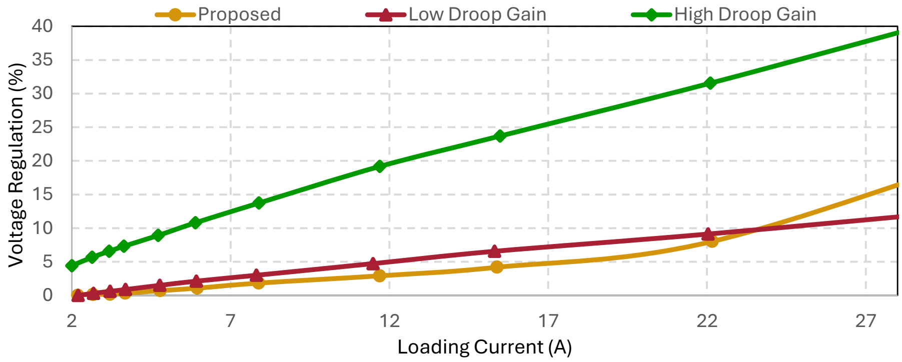

Figure 4.23: Voltage regulation comparison of proposed adaptive control approach and conventional droop control.

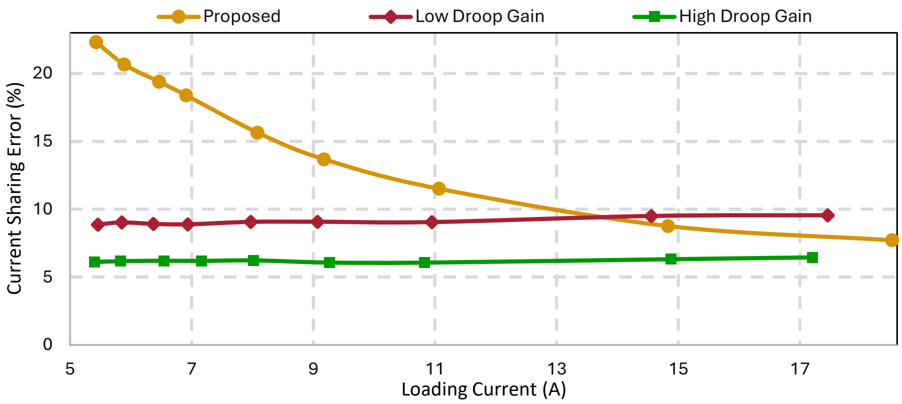

Figure 4.24: The comparison of the current-sharing error of the proposed control approach and that of the conventional droop control.

and N_u represents the total number of units.

Fig. 4.24 illustrates the average current-sharing accuracy across different operating modes. As observed, large droop gains provide relatively precise current distribution among multiple units across different demand levels, whereas small droop gains fail to guarantee fair distribution, leading to significant deviations even among units with identical nominal ratings. This imbalance may cause smaller DGs to approach their maximum generation limits while others operate well below capacity, thereby compromising the safe operation of the system under high-load conditions. In contrast, although the proposed adaptive method lacks sufficient accuracy in light loadings, it can achieve accurate proportional sharing, with notable improvements at high load levels, where precise distribution is most critical to prevent potential over-generation and mitigate thermal stress on small DGs. This result underscores the capability of the adaptive formulation to dynamically tune VR in a manner that balances current-sharing fairness with robust voltage regulation.

Fig. 4.25 illustrates the impact of three droop-based strategies on the total power losses

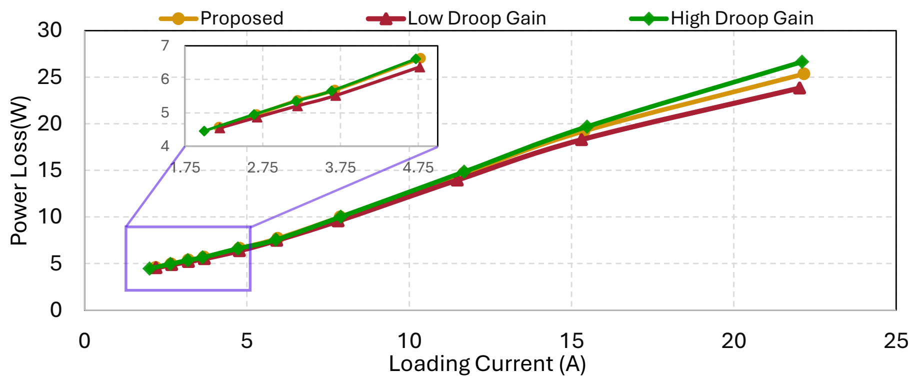

Figure 4.25: Total power losses in the DC-MG using the proposed control approach and conventional droop control.

of the DC-MG, which primarily originate from resistive dissipation along distribution lines. At light loading, the curves corresponding to all approaches nearly overlap, confirming that differences in VR settings have minimal influence when current levels are small. As the demand increases, however, discrepancies become more evident. In particular, smaller droop gains consistently yield lower power losses across all load levels, since the reduced voltage deviations translate into lower injected currents.

Nevertheless, the advantage of small fixed gains is offset by their inability to ensure fair current sharing, as shown earlier. Under heavy loading conditions—where higher droop gains are typically required to achieve proportional current distribution—the proposed adaptive method strikes an effective balance. Specifically, it achieves reduced total losses compared with the conventional case employing fixed large gains, while simultaneously maintaining accurate sharing and acceptable voltage regulation. This result highlights one of the key benefits of the adaptive strategy: it improves efficiency without compromising reliability, thereby reconciling two objectives that are typically in conflict under conventional droop control.

To investigate the role of the ES in enhancing MG flexibility and ensuring voltage stability under overloading conditions, an intermittent power profile is applied. During the first stage of the test, demand remains relatively constant and within the generation capacity of the RES units. At $t = 5$ s, however, an additional dynamic load is introduced to emulate an unscheduled surge that pushes the overall demand beyond the rated capacity of the DGs. This setup allows for a realistic evaluation of the ES's contribution under stressed operating conditions.

Fig. 4.26(a) confirms that the ESs remain inactive during the initial stage, since RES units are sufficient to support the baseline demand. Once the new load is applied,

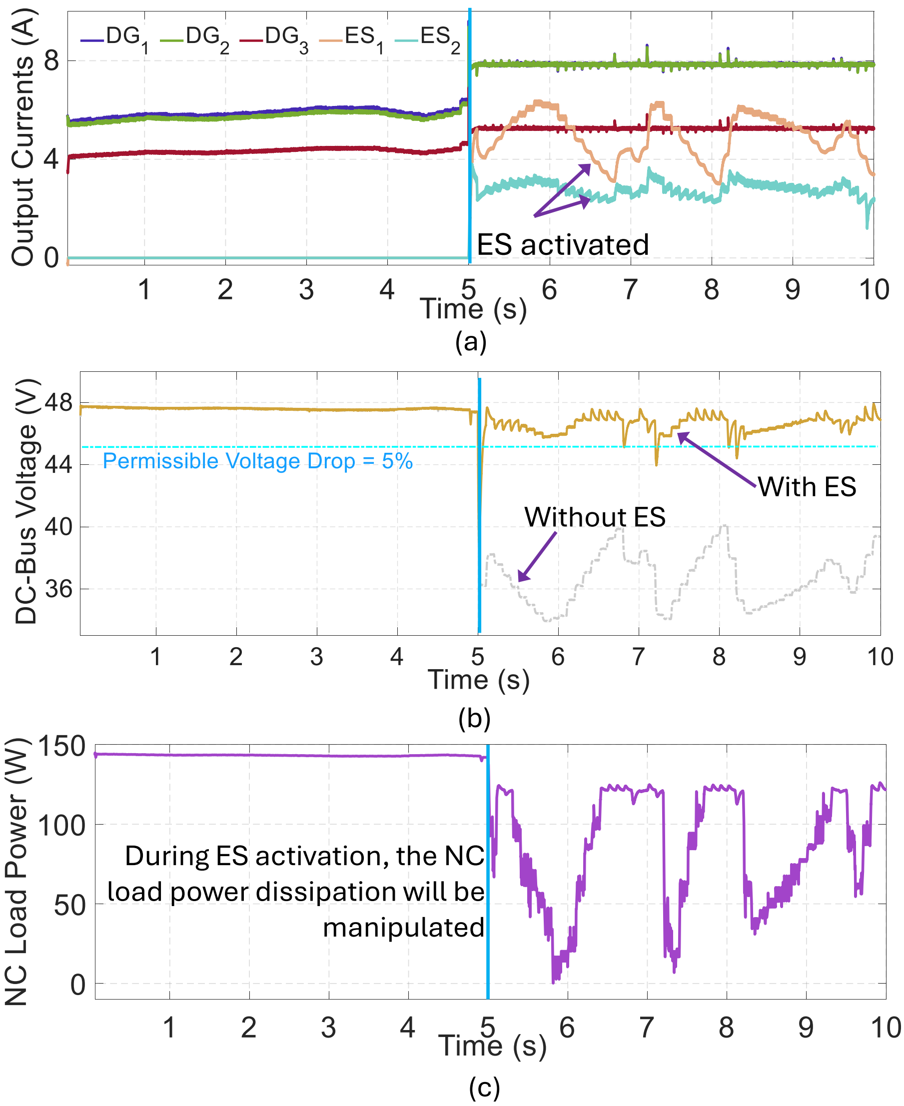

Figure 4.26: Simulation results over the impact of ES's bouncing reaction for voltage stability. (a) Terminal currents, (b) Terminal voltages, (c) Smart load power dissipation.

Fig. 4.26(b) shows that the ESs are promptly activated to compensate for the imbalance between generation and demand with respect to their unit-specific characteristics (i.e., SoCs), regulating the PCC voltage. It can be observed from Fig. 4.26(a) that the ES with higher SoC injects more current into the MG (please see Table 4.3). So, it can be said that the ES effectively behaves like a suspension spring, counteracting fluctuations and maintaining the voltage within the permissible band.

Beyond voltage stabilization, the ES also contributes to demand-side management. As illustrated in Fig. 4.26(c), the ES dynamically controls the power consumption of NC loads. Through its "bouncing" behavior, the ES modulates load dissipation in response to real-time conditions, thereby alleviating stress on generation units and preserving voltage stability. This dual functionality—supporting supply-side regulation and coordinating demand-side flexibility—reduces reliance on oversized BESS banks and enhances overall system efficiency. Consequently, the ES emerges as a valuable asset for improving the adaptability, resilience, and energy efficiency of DC-MG operation under uncertain and variable demand.

4.3 Cost-Based Coordination of Battery Energy Storage Systems

In the previous Sections, energy coordination among multiple ESSs was achieved through a SoC-based sharing mechanism. This strategy effectively balanced the energy levels of individual batteries, preventing overuse of particular units and thereby extending their overall lifespan. Nevertheless, although SoC balancing ensures technical fairness in energy utilization, it does not inherently guarantee economic optimality—especially in systems where batteries differ in type, capacity, or degradation behavior. In practice, each BESS exhibits a unique correlation between its charge–discharge cycles and degradation rate, leading to unequal aging patterns and replacement costs even when the supplied energy is the same. Given that battery degradation constitutes a major portion of a DC-MG's total capital cost, control strategies relying exclusively on SoC may inadvertently accelerate wear in more expensive or short-lived units, ultimately increasing long-term operating expenses.

To address this shortcoming, this work proposes a cost-oriented adaptive droop control strategy that allocates the power contribution of each BESS according to its degradation cost rather than its instantaneous SoC. The concept of *Incremental Cost* (IC) is adopted to the cost-benefit analysis as a real-time metric representing each battery's marginal degradation cost, derived from its cycle-life characteristics and capital investment. By enforcing an equal-IC condition across all BESSs, the proposed approach ensures an economically optimal distribution of power. Consequently, batteries with lower degradation costs are utilized more intensively, while the operation of costlier or shorter-lived units is moderated. This adaptive framework not only minimizes the total capital cost associated with energy storage but also extends the effective service life of the entire system, thereby enhancing both the economic efficiency and sustainability of isolated DC-MGs. So, it can be concluded that:

- **In previous approaches:** Adaptive droop control ensures *SoC balance* by solely equalizing energy utilization among storage units.
- **Now:** Adaptive droop control ensures *economic balance* by explicitly considering battery degradation cost and extending the control objective from BESSs' energy usage reduction to cost reduction.

It is also worth highlighting that in contrast to other previous sections, where the *Electric Spring* was incorporated as an active flexibility resource for balancing demand and supply, in this section the focus is placed solely on the BESS units. This simplification is intentional, as the primary objective here is not to enhance system-level flexibility, but rather to reduce the total usage and degradation cost of the batteries themselves. By considering the BESSs as the exclusive flexibility providers, the analysis directly targets the economic efficiency of energy storage utilization within the DC-MG.

The remainder of this section is organized as follows. Section 4.3.1 introduces the cost-based droop control design, where the fundamental principles of droop control for BESSs are reviewed and the formulation of the cost-based adaptive droop control is presented. The degradation characteristics of each battery are incorporated through an IC model derived from its cycle-life data and capital cost. The relationship between the IC, SoC, and output current is then established. Section 4.3.2 elaborates on the power contribution mechanism of the storage units and describes the overall control architecture of the DC-MG, including the hierarchical operation between renewable generation units and BESSs. Finally, Section 4.3.3 presents the performance evaluation, where the proposed approach is tested on a simulated DC-MG comprising multiple BESSs and renewable generators. Comparative results with conventional SoC-based droop methods are provided to demonstrate the superiority of the cost-based approach in minimizing total degradation costs, improving voltage regulation, and achieving balanced power sharing.

4.3.1 Cost-based Droop Control Design

In two previous Sections, the fundamentals of droop control and its adaptive extensions were examined within the framework of SoC-based coordination. In that approach, the droop slope was continuously adjusted to balance the SoC among multiple BESS units at different operating modes (i.e., in discharge mode, batteries with higher SoC are allocated

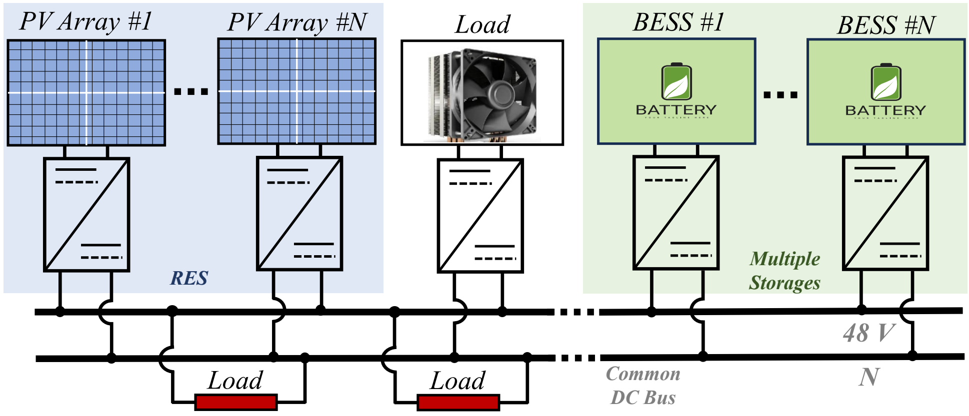

Figure 4.27: Generic configuration of a DC Microgrid.

lower VR to supply greater current, whereas in charging mode, units with lower SoC receive smaller VR to promote faster charging and achieve SoC balancing). Nevertheless, as previously discussed, maintaining identical SoC levels across heterogeneous batteries does not necessarily represent their actual economic condition or degradation dynamics. Units with different capacities, chemical structure, or cycle-life characteristics experience unequal wear and replacement costs, even when they supply equivalent amounts of energy.

To enhance the economic efficiency of the MG, the droop control formulation can be extended beyond energy-centric indicators by including cost-related data, in such a way that the VR of each storage unit is adaptively tuned based on its incremental degradation cost information.

For doing so, the proposed approach preserves the fundamental voltage–current droop principle but redefines the adaptive slope as a function of each battery's IC rather than its SoC. Under this configuration, batteries exhibiting lower degradation costs automatically contribute a larger share of current, while those with higher degradation costs proportionally reduce their participation. This behavior minimizes the overall operating and replacement costs of the energy storage system without compromising voltage stability or system reliability. The following subsections derive the mathematical formulation of the cost-based droop control, present the degradation-cost modeling as a function of Depth of Discharge (DoD) and SoC, and describe the implementation of the equal-IC condition that governs proper operation of the proposed scheme.

The rationale for employing a nonlinear droop curve with an adaptive slope—one that remains gradual under light loading and becomes progressively steeper as the load increases—has been established in earlier sections. In this context, an alternative nonlinear droop formulation is introduced, primarily aimed at achieving comparable adaptive behav-

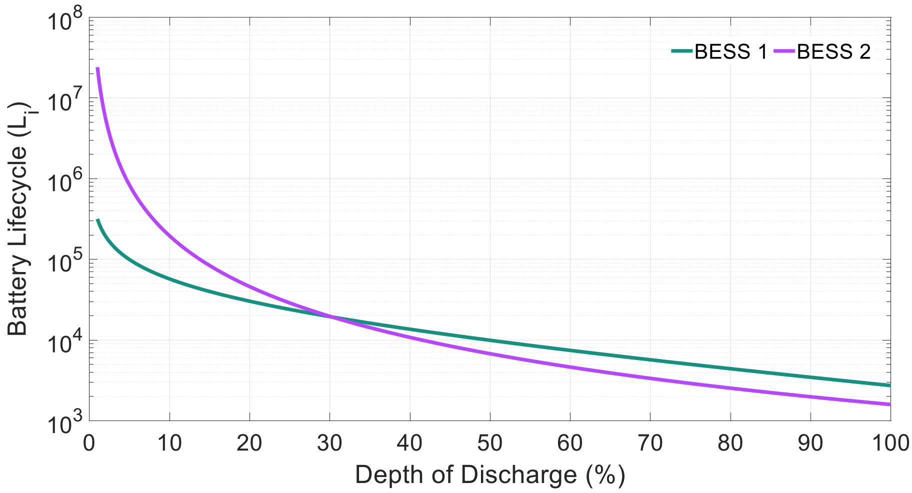

Figure 4.28: Lifetime cycles of a BESS versus depth of discharge.

ior while reducing the computational effort required to incorporate cost-related parameters into the droop gain calculation:

$$v_{ref,i} = V_{\text{nom}} - R_{\text{dr,i}}\, I_{\text{out,i}}^{\alpha} \tag{4.47}$$

In addition, the droop resistance $R_{\text{dr,i}}$ of the i-th storage unit can be constrained according to the permissible voltage deviation, ensuring that the terminal voltage remains within the predefined upper and lower limits (V_{max} and V_{min}) during charging and discharging, respectively. This constraint can be expressed as:

$$\left| R_{\text{dr},i}^{\text{char}} \right| \leq \frac{V_{\text{nom}} - V_{\text{max}}}{I_{\text{max},i}^{\alpha} \cdot SoC_i} \tag{4.48}$$

$$\left| R_{\text{dr},i}^{\text{dis}} \right| \leq \frac{(V_{\text{nom}} - V_{\text{min}}) \cdot SoC_i}{I_{\text{max},i}^{\alpha}} \tag{4.49}$$

where $R_{\text{dr},i}^{\text{char}}$ and $R_{\text{dr},i}^{\text{dis}}$ denote the effective droop resistances of the i-th unit during charging and discharging phases, respectively. The other parameters are the same as those already defined in similar equations.

Here, the parameter α for each battery unit is adjusted according to its individual degradation cost, ensuring a prolonged operational lifespan and minimizing the overall ESS expenditure. The subsequent discussion presents the methodology for determining this critical parameter.

A representative relationship between a battery's cycle life and its depth of discharge (DoD) is illustrated in Fig. 4.28. The cycle life denotes the maximum number of complete charge–discharge cycles a battery can undergo before reaching its End of Life (EoL). As shown, increasing the DoD—corresponding to deeper discharge levels—results in a substantial reduction in the attainable cycle count [139]. This inverse relationship highlights the critical trade-off between energy utilization and long-term durability in battery operation.

Even when identical energy exchanges occur among different BESS units, their degradation costs may vary significantly due to differences in intrinsic cycle-life characteristics. In addition to DoD, other aging-related factors—such as ambient temperature, charge/discharge rates, sustained operation at extreme SoC levels, and current ripple—can further influence degradation behavior. Nevertheless, these secondary factors can typically be mitigated through proper converter-level control, adequate thermal regulation, and optimized operating strategies. For this reason, the present analysis focuses exclusively on degradation mechanisms associated with DoD, which constitute the dominant contributor to long-term capacity fade and cost of ownership.

To embed the effect of battery cycle life into the proposed control scheme, it is first necessary to establish a mathematical relationship between the battery's lifetime and its depth of discharge (DoD). This dependence can be represented using an empirical model that approximates the typical cycle-life curve [172]:

$$L_i = \beta_{0,i} \times DoD_i^{-\beta_{1,i}} \times e^{\beta_{2,i}(1-DoD_i)} \tag{4.50}$$

where L_i denotes the cycle life of the i-th battery, and $\beta_{0,i}$, $\beta_{1,i}$, and $\beta_{2,i}$ are empirical coefficients determined from manufacturer data or experimental characterization. These parameters capture the specific degradation behavior of each battery type, thereby allowing the control strategy to account for heterogeneous lifetime characteristics among different BESS units.

In (4.50), the coefficients $\beta_{0,i}$, $\beta_{1,i}$, and $\beta_{2,i}$ are curve-fitting parameters specific to i-th battery type and are typically obtained from manufacturer data. Since the (DoD) is defined as DoD = 1 − SoC, a single discharge event—from full charge to a given SoC level—incurs a degradation cost that can be related to the Total Capital Cost (TCC) of the battery (C_{tot}) and its corresponding cycle life $L(SoC)$, which denotes the total number of charge–discharge cycles achievable when operating at that SoC level. When the SoC decreases from an initial value SoC_a to a lower value SoC_b, the degradation cost associated with this partial discharge (i.e., a half-cycle) can be estimated as

$$C_{\text{deg}} = \frac{1}{2}\left(\frac{C_{\text{tot}}}{L(\text{SoC}_b)} - \frac{C_{\text{tot}}}{L(\text{SoC}_a)}\right). \tag{4.51}$$

This relationship implies that deeper discharges (i.e., smaller SoC_b values) lead to higher degradation costs, since the achievable cycle life decreases exponentially with increasing DoD (See Fig. 4.28). Building on this concept, the *incremental cost* (IC) of BESS degradation can be derived as the derivative of the inverse cycle life with respect to SoC:

$$\begin{aligned} \text{IC}_i &= -\frac{C_{\text{tot},i}}{2C_{BAT,i}} \cdot \frac{d(1/L_i)}{d\text{SoC}_i} \\ &= \frac{C_{\text{tot},i}}{2C_{BAT,i}\beta_{0,i}} e^{-\beta_{2,i}\text{SoC}_i}\left[\beta_{1,i}(1-\text{SoC}_i)^{\beta_{1,i}-1} + \beta_{2,i}(1-\text{SoC}_i)^{\beta_{1,i}}\right] \end{aligned} \tag{4.52}$$

Equation (4.52) describes the degradation cost per unit of exchanged energy (i.e., in \$/kWh), which varies as a function of the battery's SoC. In other words, this equation quantifies how the instantaneous degradation cost of each battery evolves with its SoC. Batteries exhibiting lower IC values can therefore be assigned larger power contributions, enabling cost-effective operation and balanced degradation across the entire storage fleet. It is important to note that, although (4.51) and (4.52) are formulated for the discharge phase, the same relationships remain valid during charging, provided that the direction of the SoC variation is reversed.

On the other hand, the link between a battery's SoC and its output current can be established through the well-known Coulomb counting method, which expresses the SoC as a function of the accumulated charge exchanged over time. Note that the Coulomb counting equation is already defined in Subsection 4.1.2 (refer to equation (4.7)) According to (4.7), the SoC of each battery evolves as a function of its output current. Consequently, the IC can be expressed as a dynamic function of $I_{\text{out},i}$ by substituting the SoC variation into (4.52):

$$IC_i = f\left(I_{\text{out},i}\right) \tag{4.53}$$

In classical economic dispatch formulations, when transmission losses are negligible and DG outputs are unconstrained, the optimal operating condition is achieved when all generators exhibit identical incremental costs (ICs), ensuring that total generation precisely meets system demand. This is widely recognized as the equal incremental cost (equal-IC) principle [188]. In the context of small, isolated DC-MGs, distribution line losses are typically minimal due to short feeder lengths and low resistances. Moreover, as reported in [189], these resistances can be intentionally designed to maintain negligible loss levels through appropriate conductor sizing and layout optimization. Consequently, the equal-IC principle can be effectively extended to determine the optimal power (or current) allocation among BESSs [172].

In this framework, the IC of each BESS inherently represents its degradation-related cost, which depends on factors such as the SoC, DoD, and battery chemical nature. Therefore, equalizing the ICs across all units ensures an economically optimal discharge pattern, minimizing the overall degradation rate while maintaining energy balance. This condition is achieved provided that the aggregate output current of all BESS units collectively satisfies the system's required compensating current demand. The economic dispatch condition for optimal current sharing can thus be obtained provided that the following criterion is satisfied:

$$\begin{cases} IC_1 = IC_2 = \cdots = IC_i, \quad \forall i \in N_u, \\ \sum_{i=1}^{N_u} I_{\text{out},i} = I_{\text{req}} \end{cases} \tag{4.54}$$

where N_u represents the total number of in-service batteries, and I_{req} denotes the total required current that should be compensated by the storage units.

Fig. 4.29 presents the IC characteristics of the BESS units under various loading conditions. Due to inherent differences in their cycle-life profiles, capacity ratings, and installation costs, each battery exhibits a distinct IC curve. As depicted, one storage unit (e.g., BESS_2) may incur lower degradation costs within specific current ranges, whereas another unit (e.g., BESS_1) becomes more cost-effective under other operating conditions. These nonidentical IC profiles capture the practical heterogeneity of real-world storage systems, where variations in battery characteristics (e.g., age, type, usage history, etc.) affect the marginal cost of energy delivery.

In accordance with (4.54), the economically optimal operating point corresponds to the intersection where the aggregate output current of all batteries equals the system's required surplus demand. At this equilibrium, the incremental costs of all participating BESS units are equalized, and the corresponding optimal current contribution of each unit, denoted as $I_{\text{des},i}$, can be determined. This target current is then used to adapt the droop coefficient α dynamically, following the relation:

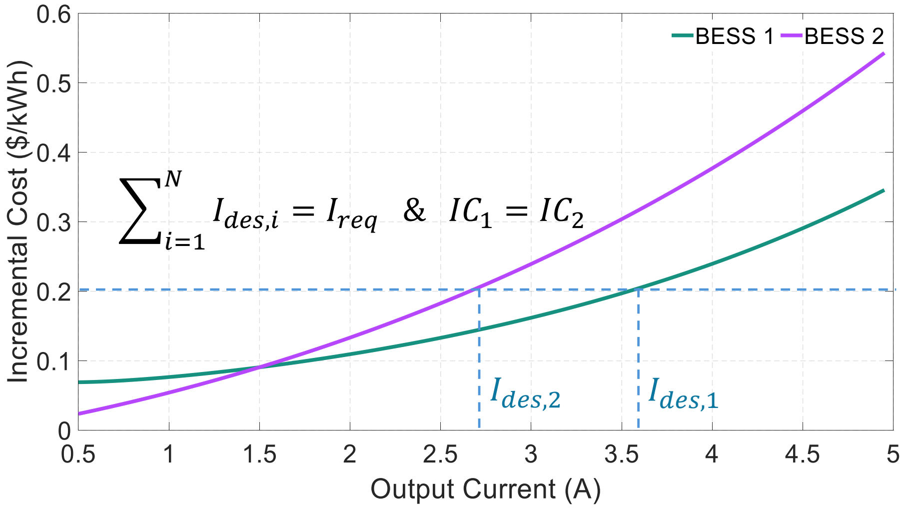

Figure 4.29: The concept of equal ICs for grid support.

$$\alpha = G_{\text{pi}} \frac{\left|I_{\text{des},i} - I_{\text{out},i}\right|}{I_{\text{des},i}}, \tag{4.55}$$

The PI action continuously minimizes the deviation between the desired ($I_{\text{des},i}$) and actual ($I_{\text{out},i}$) output currents of each BESS, thereby refining current-sharing accuracy while steering the system toward the economic equilibrium point [141]. This formulation enables decentralized implementation, as each unit locally adjusts its droop gain based on measurable current feedback and predefined cost characteristics.

It is important to emphasize that the economically optimal currents $I_{\text{des},i}$ derived from the equal-IC principle do not necessarily correspond to equal SoC levels across the storage units. This distinction highlights that, from an economic optimization perspective, enforcing uniform SoC among heterogeneous batteries may not yield the most cost-efficient operation for the overall ESS. Instead, each unit contributes according to its marginal cost characteristics, leading to an operation that minimizes total degradation and extends the collective lifetime of the BESS fleet.

4.3.2 Units' Power Contribution Mechanism

Based on the preceding formulations, the overall control framework for the DC-MG energy storage units is illustrated in Fig. 4.30. The proposed control system operates through two hierarchical layers that jointly ensure stable voltage regulation, efficient power sharing, and coordinated participation of distributed resources.

In the first layer, the RESs autonomously maintain the voltage at the PCC, taking into

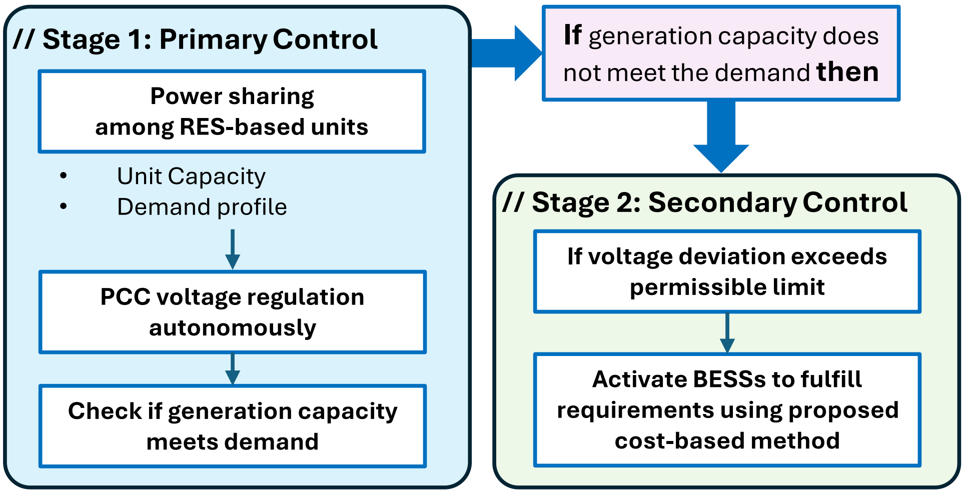

Figure 4.30: Flowchart diagram of the proposed control scheme.

account their generation capacities, the available solar irradiance, and the instantaneous demand profile. This stage constitutes the primary voltage regulation mechanism of the DC-MG. Power sharing among the RES units is achieved through a conventional droop-based approach, as described in [183], which adheres to the voltage–current characteristic defined in (1.1).

In the second layer, when the power delivered by the RESs becomes insufficient to meet the total demand—resulting in a PCC voltage drop below the lower permissible limit—the BESSs are automatically engaged. Once activated, these units operate under the proposed cost-based adaptive droop control strategy, dynamically adjusting their droop coefficients in response to real-time voltage and current measurements. This mechanism enables the BESSs to compensate for power imbalances, restore the DC bus voltage, and maintain system stability under variable load and generation conditions.

As summarized in Table 4.4, a voltage deviation within 5% of the nominal value is considered acceptable under the proposed hierarchical framework. The reference voltage v_{ref} for each BESS converter is determined using the adaptive droop formulation in (4.47), which incorporates both instantaneous system states and economic dispatch considerations.

4.3.3 Effectiveness Evaluation in Reducing Total Degradation Costs

To evaluate the effectiveness of the proposed control strategy, a test configuration of the DC-MG, illustrated in Fig. 4.27, was developed in the MATLAB®/Simulink environment. The system comprises two BESS units ($N_u = 2$) and three distributed generation (DG) units. Specifically, DG_1 and DG_2 emulate identical PV arrays, while DG_3 represents another

Table 4.4: DC Microgrid Parameters

Parameters	**Symbol**	**Value**
Nominal Voltage	V_{nom}	48 V
Permissible Voltage Variation	V_{per}	$\pm 5\% V_{nom}$
Max. Current (PV_1 & PV_2)	I_{max}	8 A
Max. Current (PV_3)	I_{max}	5 A
Max. Current ($BESSs$)	I_{max}	5 A
Initial SoC ($BESSs$)	SoC^0	% 80
Energy Cap. ($BESSs$)	Cap	10 kWh
Capital Cost ($BESSs$)	$C_{tot,1}$, $C_{tot,2}$	\$ 5500, \$ 2800
Line Res., Induc.(PV_1)	$R_{line,1}$, $l_{line,1}$	$0.15\ \Omega, 0.2$ mH
Line Res., Induc. (PV_2)	$R_{line,2}$, $l_{line,2}$	$0.1\ \Omega, 0.1$ mH
Line Res., Induc. (PV_3)	$R_{line,3}$, $l_{line,3}$	$0.3\ \Omega, 0.3$ mH
Line Res., Induc. ($BESSs$)	$R_{line,4;5}$, $l_{line,4;5}$	$0.25\ \Omega, 0.05$ mH
Total Resistive Load	R_{resis}	15 Ω

Table 4.5: Life Cycle Characteristics of Batteries

Battery No.	β_0	β_1	β_2
1	2732	0.68	1.64
2	1591	2.09	0

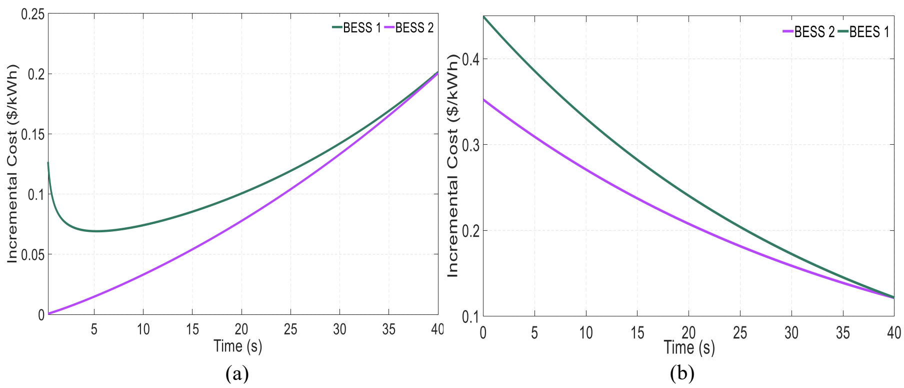

Figure 4.31: ICs convergence of two BESSs in (a) discharging and (b) charging.

photovoltaic panel with a generation capacity about half that of the others. The DC-MG operates at a nominal voltage of 48 V, with a permissible deviation of $\pm 5\%$. The principal system parameters are listed in Table 4.4, and the life-cycle characteristics of the BESS units are summarized in Table 4.5. These parameters were selected to reflect realistic ratings of small-scale renewable-based DC networks typically found in stand-alone or hybrid MG applications.

The convergence behavior of the IC for the BESS units during both discharging and charging phases is depicted in Figs. 4.31a and 4.31b, respectively. It can be observed that the IC values of the batteries progressively converge to a common value over time,

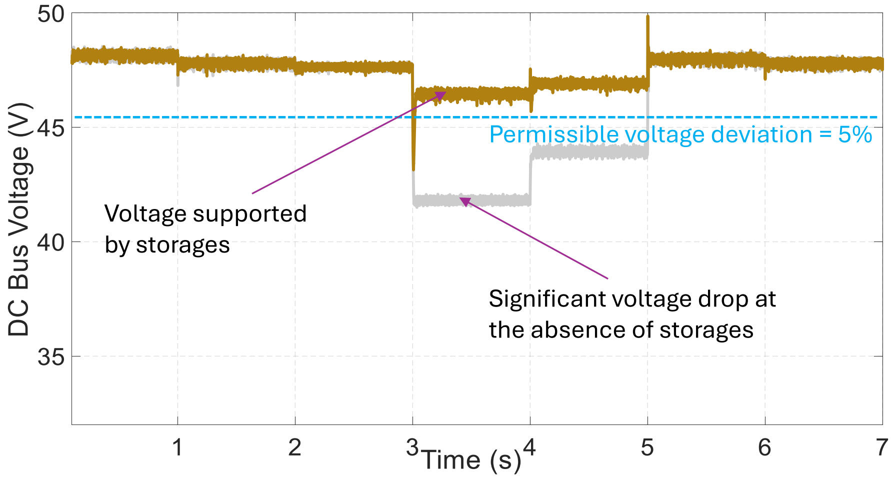

(a)

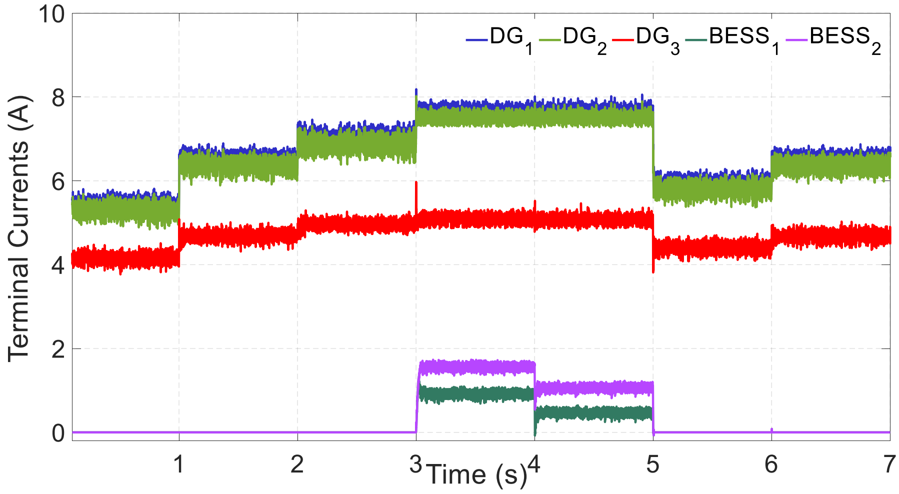

(b)

Figure 4.32: BESSs' response to the variable loading conditions using the proposed method. (a) DC bus voltage (b) Terminal currents.

demonstrating that the proposed adaptive droop-based control successfully enforces the equal-IC condition derived in (4.54). This convergence signifies that each storage unit autonomously adjusts its output current such that its marginal degradation cost matches that of the others, regardless of differences in capacity, cost coefficients, or aging characteristics.

The results confirm that the proposed control strategy achieves both technical coordination—by maintaining stable voltage regulation and balanced current sharing—and economic optimality—by distributing the total power exchange in proportion to each unit's degradation-related cost. Consequently, the method ensures fair utilization of heterogeneous BESS units, minimizes long-term degradation costs, and enhances the overall energy efficiency and lifetime of the DC-MG.

To further demonstrate the benefits of the proposed adaptive droop control strategy, a comparative study is carried out against the conventional droop method that employs fixed virtual resistances. As outlined before, the DG units are governed by the droop-based control framework described in [183], following the same formulation as in (1.1). For comparison, the conventional control approach is applied exclusively to the BESS units, where SoC balancing—rather than IC equalization—is adopted as the main coordination criterion [135]. Two gain configurations are examined to capture the behavior under extreme operating conditions: a low-droop gain (0.4 for each BESS converter) and a high-droop gain (4 for each BESS converter). The former prioritizes voltage regulation but compromises current-sharing precision, while the latter enhances current-sharing uniformity at the expense of larger voltage deviations.

To assess system performance, the net load is varied in a stepwise pattern while ensuring that total demand remains within the DG generation capacity (i.e., $I_{\mathrm{out},i} \leq I_{\mathrm{max},i}$), except during the interval $t = [3-5]$ s, when an intentional overload condition is introduced. This scenario allows evaluation of both steady-state and transient performance of the control strategy under realistic disturbances. The dynamic responses of the system under these varying load conditions are depicted in Fig. 4.32.

The simulation results reveal that the proposed adaptive control method responds rapidly to load variations while maintaining the PCC voltage within acceptable limits. The bus voltage recovers smoothly after each step change without exhibiting overshoot or oscillatory behavior, confirming the effectiveness of the adaptive droop mechanism in mitigating transient disturbances. Furthermore, the BESS units share the output current proportionally, consistent with the equal-IC principle established in (4.54) (see also Fig. 4.29). This proportional sharing ensures that each battery contributes according to its degradation-related cost, leading to an economically optimal discharge pattern.

It is also observed that the BESS units remain inactive as long as the PCC voltage exceeds the lower threshold, thereby conserving stored energy and avoiding unnecessary cycling. Once the voltage falls below the permissible limit during $t = [3-5]$ s, the BESSs are automatically activated and inject compensation currents that are adaptively modulated according to their IC characteristics. Minor deviations in current sharing can be attributed primarily to the influence of line resistances and parameter mismatches, which introduce slight voltage drops across feeders. Nonetheless, the system quickly restores equilibrium, validating the robustness and practical feasibility of the proposed approach under varying load and network conditions.

For comparison purposes, the same operating scenario is applied to the BESS units

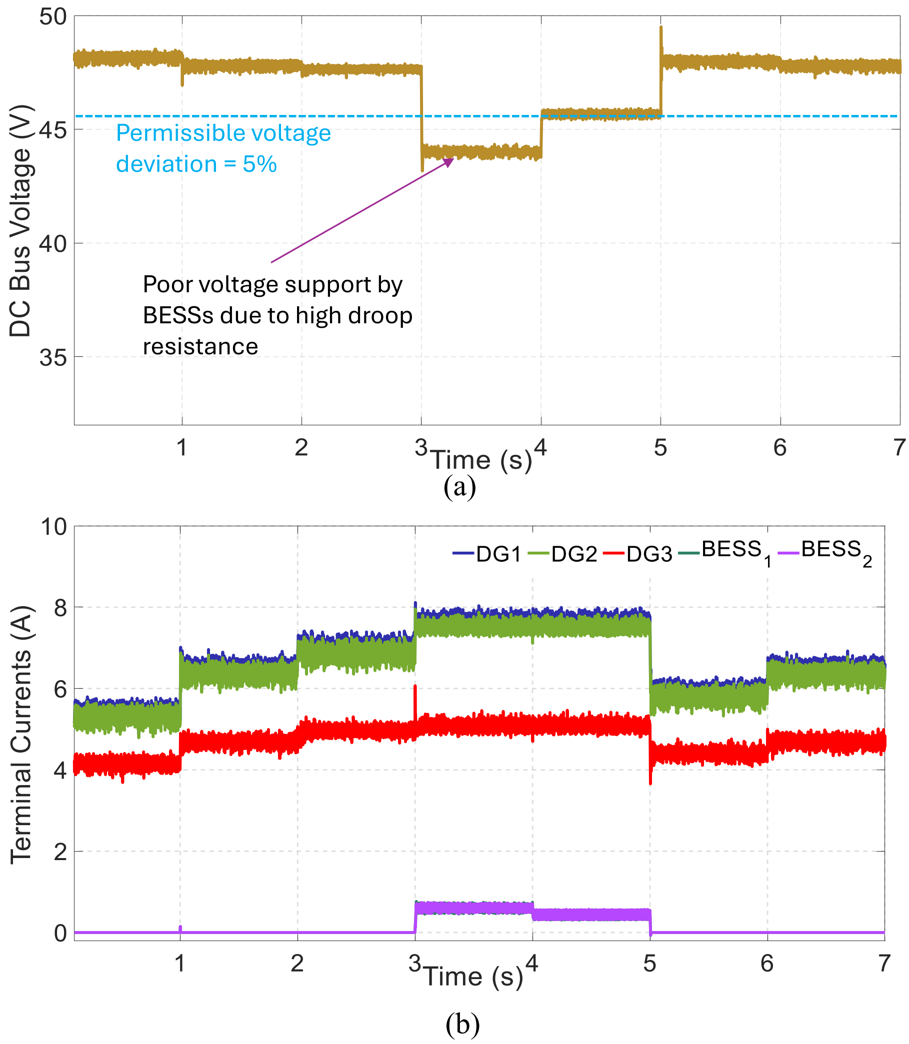

Figure 4.33: BESSs' response to the variable loading conditions using conventional droop control with high gains. (a) DC bus voltage (b) Terminal currents.

using a conventional droop control strategy with fixed high virtual resistances. In this configuration, the degradation characteristics of the batteries are disregarded, and the droop gains are assigned solely based on their SoC levels [183, 185]. Since both batteries possess identical electrical and capacity specifications, as summarized in Table 4.4, equal current contribution is expected under ideal conditions. This behavior is confirmed in Fig. 4.33, where the output currents of the two BESS units exhibit nearly perfect proportionality during the test period.

However, despite achieving accurate current sharing, the elevated droop gain significantly amplifies the deviation of the reference voltage (v_{ref}) from the nominal voltage (V_{nom}). As a result, the terminal voltage exceeds the permissible deviation range even after the BESSs are activated. This voltage violation indicates that while high droop gains

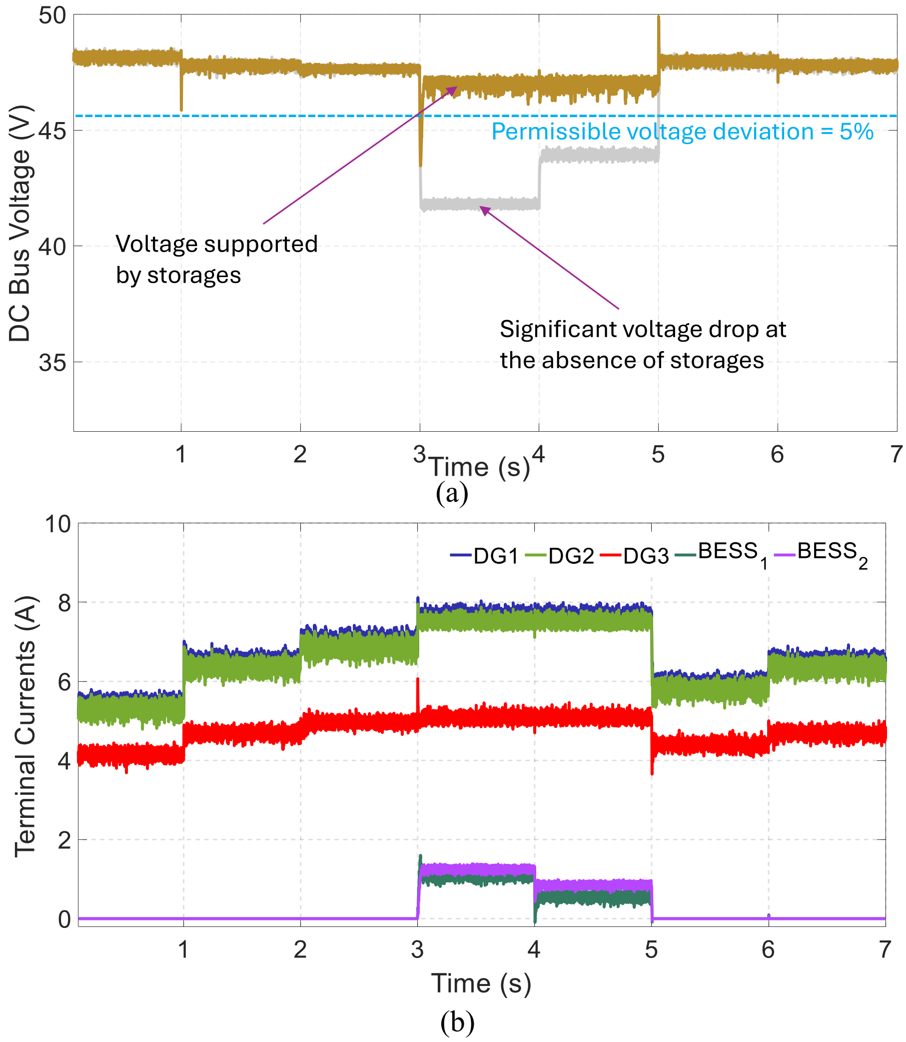

Figure 4.34: BESSs' response to the variable loading conditions using conventional droop control with low gains. (a) DC bus voltage (b) Terminal currents.

improve proportionality among storage units, they simultaneously deteriorate voltage regulation performance. The high virtual resistance effectively reduces the control sensitivity to voltage fluctuations, limiting the batteries' ability to compensate for power imbalances and undermining the overall stability of the DC-MG.

Conversely, when low virtual resistances are employed—as shown in Fig. 4.34—the PCC voltage remains within acceptable limits across all tested load conditions, confirming enhanced voltage regulation capability. Nevertheless, this improvement comes at the expense of degraded current-sharing precision. The two BESS units, despite identical ratings, display noticeable current mismatch as the load varies, resulting in unequal utilization and potential imbalance in charge–discharge cycles over time.

This comparative analysis highlights the inherent trade-off in conventional droop con-

Table 4.6: Comparison of annual degradation costs.

Battery No.	Degradation Cost (k$) Conv. low droop gain	Conv. high droop gain	Proposed
1	2.750	2.780	2.761
2	0.845	0.826	0.828
Total	**3,595**	**3,606**	**3,589**

trol strategies between maintaining tight voltage regulation and ensuring accurate current distribution among storage units. The inability to satisfy both objectives simultaneously underscores the need for an adaptive mechanism—such as the proposed IC-based droop approach—that dynamically tunes virtual resistances to preserve voltage stability while achieving economically coordinated power sharing.

For additional validation, Table 4.6 compares the annual degradation costs obtained from the control strategies discussed earlier under an excess-demand condition that follows the same pattern as in previous cases for a year. Although the degradation cost of individual BESS units may increase slightly in certain instances, the aggregate degradation cost across all batteries is notably lower when using the proposed approach. This outcome demonstrates that the cost-based adaptive droop control effectively minimizes the total degradation expenditure of the storage system, even when individual units contribute unevenly to power delivery. The results thus confirm the economic advantage and enhanced long-term sustainability of the proposed control strategy compared to conventional methods.

4.4 Summary of the Chapter

This chapter has presented a suite of innovative control frameworks for islanded DC microgrids, designed to enhance their autonomy, resilience, and cost-effectiveness. The research has progressively evolved from distributed coordination schemes requiring low-bandwidth communication, through fully decentralized configurations relying solely on local information, to a cost-oriented adaptive control strategy that integrates economic considerations directly into the power-sharing mechanism. Together, these developments form a coherent trajectory toward intelligent, self-organizing, and economically sustainable microgrid operation.

In Section 4.1.1, a distributed adaptive droop-based control strategy was introduced to achieve coordinated operation among DGs, BESSs, and controllable loads. The key innovation lies in the dynamic adaptation of droop gains based on each unit's SoC and capacity, exchanged via a lightweight communication layer. This mechanism enabled real-time balancing of energy resources, equitable current sharing, and bus voltage stabilization without reliance on a centralized controller. The inclusion of SoC-dependent energy sharing and capacity awareness also mitigated overcycling of storage units, extending their operational lifespan. In essence, this distributed framework established a communication-assisted yet fault-tolerant approach to flexible energy coordination in complex multi-unit microgrids.

Building on these foundations, Section 4.2.1 advanced the concept toward a fully decentralized adaptive droop control scheme, removing the dependency on any communication infrastructure. By relying solely on locally measured voltage and current signals, each unit autonomously regulated its power output while collectively maintaining voltage stability and accurate current distribution. The elimination of data exchange drastically simplified implementation, reduced cost, and enhanced reliability—particularly advantageous for rural and stand-alone DC microgrids where ICT infrastructure is limited. Despite its communication-free nature, the proposed control achieved comparable power-sharing accuracy to the distributed method through the design of adaptive droop laws that compensate for line impedances and nonlinearities. Hence, while the distributed strategy prioritized coordination accuracy and flexibility, the decentralized one emphasized robustness, modularity, and practical deployability. The comparison between these two schemes underscores the trade-off between communication-assisted precision and communication-free resilience.

Finally, Section 4.3.1 extended the technical discussion into the economic domain by incorporating battery degradation awareness into the control layer. The cost-oriented adaptive droop control introduced the concept of IC as a real-time indicator of each battery's marginal degradation expense. By enforcing an equal-IC condition among heterogeneous BESS units, the controller dynamically allocated power in a way that minimized total degradation cost and prolonged system lifetime. This represents a significant step beyond traditional SoC-based balancing, which ensures energy fairness but neglects economic heterogeneity among storage units. The cost-aware design therefore harmonizes technical fairness, economic rationality, and asset longevity—achieving optimal utilization of energy storage resources from both engineering and financial perspectives.

When viewed together, these three control paradigms illustrate a clear methodological evolution. The distributed strategy provides an intelligent cooperative framework leveraging limited communication for optimal coordination; the decentralized scheme achieves autonomy and fault tolerance through purely local decisions; and the cost-oriented control introduces an additional layer of intelligence by embedding economic self-optimization into the physical control loop. Their comparative evaluation reveals that increasing autonomy and economic awareness can be achieved without compromising stability or performance, provided that adaptive droop mechanisms are appropriately formulated. Collectively, the innovations presented in this chapter advance the state of the art in microgrid control by unifying distributed intelligence, communication independence, and cost-efficiency within a scalable and practical operational paradigm. These findings lay a robust foundation for future research aimed at integrating predictive optimization and cooperative energy management within interconnected multi-microgrid ecosystems.

Conclusion

In this thesis, some tools and methodologies have been proposed to facilitate the implementation of MGs in power systems, with a particular focus on increasing the hosting capacity of RESs in isolated or weakly connected networks. The work specifically addressed the operational and control challenges of small Italian islands, where high fuel costs, logistical constraints, and dependence on fossil-based generation impose significant economic and environmental burdens. Within this context, the study sought to identify and develop technical solutions that can accelerate decarbonization and improve system resilience while maintaining stability and cost efficiency. Given the suitable potential of solar irradiation in Italy, this thesis has focused on the deployment of solar systems as the main RES in this study.

Enabling greater penetration of renewable energy in isolated MGs requires a careful orchestration of distributed generation, storage, and demand-side resources. This thesis has presented a structured approach to achieving that goal, through contributions that span the entire control hierarchy—from long-term operational planning to real-time energy balancing and flexibility enhancement.

A major outcome of this research is the development of innovative adaptive control architectures designed to ensure the secure, autonomous, and economically sustainable operation of islanded DC MGs. The methodological evolution presented in Chapter 4 represents the core of this advancement.

First, a distributed adaptive droop-based coordination framework was introduced to enable real-time cooperation among distributed generators, BESSs, and controllable loads. This strategy dynamically adjusts droop parameters based on each unit's state of charge (SoC) and rated capacity, exchanged via a low-bandwidth communication network (LBC). The outcome is a communication-assisted yet decentralized control structure that achieves accurate current sharing, smooth voltage regulation, and improved battery lifetime. Validation through PHIL experiments confirmed the practical feasibility of this approach and its resilience under partial communication failures.

Building upon this foundation, a fully decentralized adaptive droop control method was proposed to remove any dependence on communication links. Relying solely on locally measured quantities, each unit autonomously modulates its droop coefficient to achieve power-sharing precision and voltage stability. Despite the absence of data exchange, the control design preserved performance parity with distributed architectures, demonstrating a significant leap in autonomy, modularity, and reliability. This communication-free strategy is particularly suited for rural and remote MGs, where robust operation with minimal infrastructure is essential.

The third innovation integrated an economic dimension into the control layer through a cost-oriented adaptive droop mechanism. By introducing the IC (Incremental Cost) index as a real-time indicator of each storage unit's degradation rate, the proposed controller achieved minimum total degradation cost across heterogeneous battery units. This design harmonized technical fairness, economic rationality, and asset longevity, marking a crucial step beyond traditional SoC-based balancing methods. The approach effectively minimized cumulative aging while preserving operational stability—offering a pragmatic solution for long-term sustainability of BESS fleets in isolated systems.

Together, these three frameworks—distributed, decentralized, and cost-aware—form a coherent trajectory toward next-generation MGs characterized by intelligence, self-organization, and cost efficiency. They collectively demonstrate that it is possible to achieve flexible coordination, resilience to faults, and economic optimization within the same control paradigm, thus bridging the gap between centralized intelligence and autonomous operation. Through comprehensive small-signal stability analyses, nonlinear simulations, and real-time experimental validation, this work has confirmed the robustness and scalability of the proposed methodologies.

Beyond their technical merits, the results of this research also provide actionable insights for policy and system planners targeting the transition of remote and islanded grids toward higher shares of renewables. The combination of flexibility resources, adaptive droop strategies, and HIL validation frameworks lays a strong foundation for extending these principles to multi-MG and interconnected MG environments, where communication, control, and economic interactions must coexist seamlessly.

Future developments stemming from this thesis may focus on integrating predictive optimization and learning-based coordination into the proposed adaptive control schemes. Moreover, the generalization of these frameworks to networked or hierarchical MG systems could enable cooperative energy exchange, resilience enhancement, and grid restoration capabilities following major contingencies.

In conclusion, the methodologies and control architectures developed in this work advance the state of the art in secure and flexible operation of isolated DC MGs, bridging the gap between theoretical modeling and practical implementation. By strengthening the stability, autonomy, and cost-effectiveness of MGs, the proposed solutions contribute to a sustainable energy transition, reducing the reliance on fossil fuels and supporting the decarbonization goals of isolated and weakly connected regions.

References

[1] M. Farrokhabadi, C. A. Canizares, J. W. Simpson-Porco, E. Nasr, L. Fan, P. A. Mendoza-Araya, R. Tonkoski, U. Tamrakar, N. Hatziargyriou, D. Lagos *et al.*, "Microgrid stability definitions, analysis, and examples," *IEEE Transactions on Power Systems*, vol. 35, no. 1, pp. 13–29, 2019.

[2] K.-T. Mok, M.-H. Wang, S.-C. Tan, and S. R. Hui, "Dc electric springs—a technology for stabilizing dc power distribution systems," *IEEE Transactions on Power Electronics*, vol. 32, no. 2, pp. 1088–1105, 2016.

[3] J. Su, K. Li, Y. Li, C. Xing, and J. Yu, "A novel state-of-charge-based droop control for battery energy storage systems to support coordinated operation of dc microgrids," *IEEE Journal of Emerging and Selected Topics in Power Electronics*, vol. 11, no. 1, pp. 312–324, 2023.

[4] A. Khorsandi, M. Ashourloo, and H. Mokhtari, "A decentralized control method for a low-voltage dc microgrid," *IEEE Transactions on Energy Conversion*, vol. 29, no. 4, pp. 793–801, 2014.

[5] X. Guillaud, M. O. Faruque, A. Teninge, A. H. Hariri, L. Vanfretti, M. Paolone, V. Dinavahi, P. Mitra, G. Lauss, C. Dufour *et al.*, "Applications of real-time simulation technologies in power and energy systems," *IEEE Power and Energy Technology Systems Journal*, vol. 2, no. 3, pp. 103–115, 2015.

[6] G. Lauss, Z. Feng, M. H. Syed, A. Kontou, A. De Paola, A. Paspatis, and P. Kotsampopoulos, "A framework for sensitivity analysis of real-time power hardware-in-the-loop (phil) systems," *IEEE Access*, vol. 10, pp. 101 305–101 318, 2022.

[7] M. O. Faruque, T. Strasser, G. Lauss, V. Jalili-Marandi, P. Forsyth, C. Dufour, V. Dinavahi, A. Monti, P. Kotsampopoulos, J. A. Martinez *et al.*, "Real-time simulation

technologies for power systems design, testing, and analysis," *IEEE Power and Energy Technology Systems Journal*, vol. 2, no. 2, pp. 63–73, 2015.

[8] E. Hossain, R. Perez, A. Nasiri, and S. Padmanaban, "A comprehensive review on constant power loads compensation techniques," *IEEE access*, vol. 6, pp. 33 285–33 305, 2018.

[9] S. Singh, A. R. Gautam, and D. Fulwani, "Constant power loads and their effects in dc distributed power systems: A review," *Renewable and Sustainable Energy Reviews*, vol. 72, pp. 407–421, 2017.

[10] M. R. Nasab, S. Bruno, M. Liserre, and M. L. Scala, "Adaptive Droop Control for Stability Enhancement in Islanded DC Microgrids with CPLs," in *2025 Power Tech Conference*. IEEE, 2025, pp. 1–6.

[11] M. R. Nasab *et al.*, "Cost-Based Adaptive Coordination of Battery Energy Storage Systems in DC Microgrid," in *2025 AEIT International Annual Conference (AEIT)*. IEEE, 2025, pp. 1–6.

[12] C. Iurlaro, M. R. Nasab *et al.*, "Fast frequency support in isolated distribution networks by means of distributed control of V2G electric vehicles," in *2025 IEEE International Conference on Environment and Electrical Engineering and 2025 IEEE Industrial and Commercial Power Systems Europe (EEEIC/I&CPS Europe)*. IEEE, 2025, pp. 1–6.

[13] M. R. Nasab, R. Cometa, C. Iurlaro, M. M. Islam, S. Bruno, and M. La Scala, "Stand-alone DC Microgrids for Rural Areas: A Decentralized Energy Management and Voltage Regulation Approach," in *2024 IEEE International Humanitarian Technologies Conference (IHTC)*. IEEE, 2024, pp. 1–7.

[14] M. Menga, C. Iurlaro, M. R. Nasab, S. Bruno, and M. La Scala, "Recursive predictive optimal dispatch for the reduction of fuel dependence in a multi-village power system," in *2024 IEEE International Humanitarian Technologies Conference (IHTC)*. IEEE, 2024, pp. 1–7.

[15] R. Cometa, A. Velini, M. R. Nasab, S. Bruno, and M. La Scala, "Optimal Transmission Grid Assets Maneuvering for Improving Voltage Profile in RES Scenarios," in *2024 IEEE International Humanitarian Technologies Conference (IHTC)*. IEEE, 2024, pp. 1–7.

[16] M. R. Nasab, R. Cometa, P. Ghalebani, S. Bruno, and M. La Scala, "Distributed adaptive droop control method for flexibility enhancement of islanded DC micro-grids including electric springs," in *2024 Energy Conversion Congress & Expo Europe (ECCE Europe)*. IEEE, 2024, pp. 1–6.

[17] M. R. Nasab, R. Cometa, S. Bruno, and M. La Scala, "Adaptive Scheme for Stability Margin Estimation of Grid-Connected DFIG Based Wind Turbines," in *2024 IEEE International Conference on Environment and Electrical Engineering and 2024 IEEE Industrial and Commercial Power Systems Europe (EEEIC/I&CPS Europe)*. IEEE, 2024, pp. 1–6.

[18] R. Cometa, M. R. Nasab, F. Lorusso, A. Velini, M. La Scala, and S. Bruno, "Integration of FDIR Practices in Distribution Optimal Network Reconfiguration Routines," in *2024 IEEE International Conference on Environment and Electrical Engineering and 2024 IEEE Industrial and Commercial Power Systems Europe (EEEIC/I&CPS Europe)*. IEEE, 2024, pp. 1–6.

[19] M. R. Nasab, P. Ghalebani, S. Bruno, R. Cometa, and M. La Scala, "Adaptive PI control of PMSM for electric vehicle application based on sliding-mode extremum seeking algorithm," in *2023 Asia Meeting on Environment and Electrical Engineering (EEE-AM)*. IEEE, 2023, pp. 1–6.

[20] A. Perrone, M. R. Nasab, and M. La Scala, "Draft animal power versus photovoltaic: A benchmark," in *2023 AEIT International Annual Conference (AEIT)*. IEEE, 2023, pp. 1–6.

[21] A. A. Darban, M. Rajabi Nasab *et al.*, "Anomaly detection in solar farms with a hybrid CNN-ViT model to enhance accuracy and efficiency," *International Journal of Ambient Energy*, vol. 46, no. 1, p. 2541270, 2025.

[22] M. R. Nasab, R. Cometa, S. Bruno, G. Giannoccaro, and M. La Scala, "Power systems simulation and analysis: A review on current applications and future trends in DRTS of grid-connected technologies," *IEEE Access*, 2024.

[23] M. M. Islam, T. Yu, G. Giannoccaro, Y. Mi, M. La Scala, M. N. Rajabi, and J. Wang, "Improving reliability and stability of the power systems: A comprehensive review on the role of energy storage systems to enhance flexibility," *IEEE Access*, 2024.

[24] CIGRÉ WG C6.22, *Microgrids 1 Engineering, Economics, & Experience*. Paris, France: CIGRÉ, 2015.

[25] U.S. Energy Information Administration (EIA), "International energy outlook 2016," 2016, license: CC BY 4.0. [Online]. Available: https://www.eia.gov/outlooks/ieo/pdf/0484(2016).pdf

[26] International Energy Agency (IEA), "World energy investment outlook," 2014, license: CC BY 4.0. [Online]. Available: https://www.iea.org/reports/world-energy-investment-outlook

[27] European Commission, "Directive (EU) 2018/2001 of the European Parliament and of the Council of 11 December 2018 on the promotion of the use of energy from renewable sources," 2018.

[28] E. Commission, "Communication from the commission to the european parliament, the council, the european economic and social committee and the committee of the regions: The european green deal," 2019.

[29] European Commission, "Delivering the European Green Deal," Brussels, Belgium, COM(2021) 640 final, 2021.

[30] E. Commission, "Communication from the commission to the european parliament, the council, the european economic and social committee and the committee of the regions: Repowereu plan," 2022.

[31] Council of the European Union, "Council regulation (eu) 2022/230 of 22 december 2022 on a temporary emergency measure to streamline permit-granting procedures for renewable energy projects and facilitate power purchase agreements," 2022.

[32] E. Commission, "Proposal for a council regulation on a temporary emergency measure to streamline permit-granting procedures for renewable energy projects and facilitate power purchase agreements," 2022.

[33] European Commission, "European green deal: Eu agrees stronger legislation to accelerate the rollout of renewable energy," Brussels, Belgium, COM(2021) 640 final, 2023.

[34] M. Carpintero-Rentería, D. Santos-Martín, and J. M. Guerrero, "Microgrids literature review through a layers structure," *Energies*, vol. 12, no. 22, p. 4381, 2019.

[35] D. T. Ton and M. A. Smith, "The u.s. department of energy's microgrid initiative," *The Electricity Journal*, vol. 25, no. 8, pp. 84–94, 2012. [Online]. Available: https://www.sciencedirect.com/science/article/pii/S1040619012002254

[36] N. Hatziargyriou, *Microgrids: architectures and control.* John Wiley & Sons, 2014.

[37] S. Parhizi, H. Lotfi, A. Khodaei, and S. Bahramirad, "State of the art in research on microgrids: A review," *IEEE Access*, vol. 3, pp. 890–925, 2015.

[38] F. Martin-Martínez, A. Sánchez-Miralles, and M. Rivier, "A literature review of microgrids: A functional layer based classification," *Renewable and Sustainable Energy Reviews*, vol. 62, pp. 1133–1153, 2016. [Online]. Available: https://www.sciencedirect.com/science/article/pii/S1364032116301356

[39] International Electrotechnical Commission, "IEC TS 62898-1:2017 Micro-grids—Part1:Guidelines for Microgrid Projects Planning and Specification," IEC Publications, Geneva, Switzerland, Technical Specification, 2017.

[40] IEEE, "IEEE Standard for the Specification of Microgrid Controllers," *IEEE Std 2030.7-2017*, pp. 1–43, 2018.

[41] G. Joos, J. Reilly, W. Bower, and R. Neal, "The need for standardization: The benefits to the core functions of the microgrid control system," *IEEE Power and Energy Magazine*, vol. 15, no. 4, pp. 32–40, 2017.

[42] J. F. Castro, R. A. Roncolatto, A. R. Donadon, V. E. Andrade, P. Rosas, R. G. Bento, J. G. Matos, F. A. Assis, F. C. Coelho, R. Quadros *et al.*, "Microgrid applications and technical challenges—the brazilian status of connection standards and operational procedures," *Energies*, vol. 16, no. 6, p. 2893, 2023.

[43] A. K. Arani, G. Gharehpetian, and M. Abedi, "Review on energy storage systems control methods in microgrids," *International journal of electrical power & energy systems*, vol. 107, pp. 745–757, 2019.

[44] T. Dragičević, J. M. Guerrero, J. C. Vasquez, and D. Škrlec, "Supervisory control of an adaptive-droop regulated dc microgrid with battery management capability," *IEEE Transactions on power Electronics*, vol. 29, no. 2, pp. 695–706, 2013.

[45] V. Nasirian, A. Davoudi, F. L. Lewis, and J. M. Guerrero, "Distributed adaptive droop control for dc distribution systems," *IEEE Transactions on Energy Conversion*, vol. 29, no. 4, pp. 944–956, 2014.

[46] Y. A.-R. I. Mohamed and E. F. El-Saadany, "Adaptive decentralized droop controller to preserve power sharing stability of paralleled inverters in distributed generation microgrids," *IEEE Transactions on Power Electronics*, vol. 23, no. 6, pp. 2806–2816, 2008.

[47] U. B. Tayab, M. A. B. Roslan, L. J. Hwai, and M. Kashif, "A review of droop control techniques for microgrid," *Renewable and Sustainable Energy Reviews*, vol. 76, pp. 717–727, 2017.

[48] J. M. Guerrero, J. C. Vasquez, J. Matas, L. G. De Vicuña, and M. Castilla, "Hierarchical control of droop-controlled ac and dc microgrids—a general approach toward standardization," *IEEE Transactions on industrial electronics*, vol. 58, no. 1, pp. 158–172, 2010.

[49] J. M. Guerrero, M. Chandorkar, T.-L. Lee, and P. C. Loh, "Advanced control architectures for intelligent microgrids—part i: Decentralized and hierarchical control," *IEEE Transactions on Industrial Electronics*, vol. 60, no. 4, pp. 1254–1262, 2012.

[50] T. Dragičević, X. Lu, J. C. Vasquez, and J. M. Guerrero, "Dc microgrids—part ii: A review of power architectures, applications, and standardization issues," *IEEE transactions on power electronics*, vol. 31, no. 5, pp. 3528–3549, 2015.

[51] Q. Shafiee, T. Dragičević, J. C. Vasquez, and J. M. Guerrero, "Hierarchical control for multiple dc-microgrids clusters," *IEEE transactions on energy conversion*, vol. 29, no. 4, pp. 922–933, 2014.

[52] A. Mohammed, S. S. Refaat, S. Bayhan, and H. Abu-Rub, "Ac microgrid control and management strategies: Evaluation and review," *IEEE Power Electronics Magazine*, vol. 6, no. 2, pp. 18–31, 2019.

[53] M. Barnes, A. Dimeas, A. Engler, C. Fitzer, N. Hatziargyriou, C. Jones, S. Papathanassiou, and M. Vandenbergh, "Microgrid laboratory facilities," in *2005 International Conference on Future Power Systems*, 2005, pp. 6 pp.–6.

[54] C. Papadimitriou, E. Zountouridou, and N. Hatziargyriou, “Review of hierarchical control in dc microgrids,” *Electric Power Systems Research*, vol. 122, pp. 159–167, 2015.

[55] C. Iurlaro, L. Barbato, G. Bianco, S. Bruno, G. Ceneri, M. La Scala, L. Mascolo, M. Menga, C. Micillo, F. Renna, and G. Sapienza, “Control Architecture and Algorithms for Isolated Microgrids,” in *CIRED 2023 - The 27th International Conference and Exhibition on Electricity Distribution*, Rome, Italy, 2023.

[56] IEEE, “IEEE Standard for the Testing of Microgrid Controllers,” *IEEE Std 2030.8-2018*, pp. 1–42, 2018.

[57] IEEE, “Ieee standard for interconnection and interoperability of distributed energy resources with associated electric power systems interfaces,” *IEEE Std 1547-2018 (Revision of IEEE Std 1547-2003)*, pp. 1–138, 2018.

[58] International Electrotechnical Commission, “IEC TS 62898-2:2018 Microgrids—Part1:Guidelines for Operation,” IEC Publications, Geneva, Switzerland, Technical Specification, 2018.

[59] N. M. Tabatabaei, E. Kabalci, and N. Bizon, *Microgrid architectures, control and protection methods*. Springer, 2019.

[60] S. Moussa, M. J.-B. Ghorbal, and I. Slama-Belkhodja, “Bus voltage level choice for standalone residential dc nanogrid,” *Sustainable Cities and Society*, vol. 46, p. 101431, 2019.

[61] K. Siraj and H. A. Khan, “Dc distribution for residential power networks: A framework to analyze the impact of voltage levels on energy efficiency,” *Energy Reports*, vol. 6, pp. 944–951, 2020.

[62] M. Anees, T. Moaz, S. Hussain, H. A. Khan, and M. Nasir, “Evaluation of system losses for 48v and 380v solar powered lvdc microgrids,” in *2020 IEEE Power & Energy Society General Meeting (PESGM)*. IEEE, 2020, pp. 1–5.

[63] L. Cassin, P. Melindi-Ghidi, and F. Prieur, “Confronting climate change: Adaptation vs. migration in small island developing states,” *Resource and Energy Economics*, vol. 69, p. 101301, 2022.

[64] E. Ali, W. Cramer, J. Carnicer, E. Georgopoulou, N. Hilmi, G. Le Cozannet, and P. Lionello, "Cross-chapter paper 4: Mediterranean region," *Climate change*, pp. 2233–2272, 2022.

[65] "Climate change 2022: Impacts, adaptation and vulnerability," contribution of Working Group II to the Sixth Assessment Report of the IPCC. [Online]. Available: https://www.ipcc.ch/report/ar6/wg2/

[66] I. Kougias, S. Szabó, A. Nikitas, and N. Theodossiou, "Sustainable energy modelling of non-interconnected mediterranean islands," *Renewable Energy*, vol. 133, pp. 930–940, 2019. [Online]. Available: https://www.sciencedirect.com/science/article/pii/S096014811831293X

[67] D. C. Major, P. Blaschke, V. Gornitz, E. Hosek, M. Lehmann, J. Lewis, H. Loehr, G. A. Major-Ex, M. Pedersen Zari, M. J. Vásquez Vargas, E. Watterson, and A. Wejs, "Adaptation to climate change in small island settlements," *Ocean & Coastal Management*, vol. 212, p. 105789, 2021. [Online]. Available: https://www.sciencedirect.com/science/article/pii/S0964569121002726

[68] United Nations Framework Convention on Climate Change, "Paris agreement," 2015. [Online]. Available: https://unfccc.int/process-and-meetings/the-paris-agreement/the-paris-agreement

[69] "NESOI | New Energy Solutions Optimized for Islands." [Online]. Available: https://www.nesoi.eu/

[70] Clean energy for EU islands secretariat. [Online]. Available: https://euislands.eu/index.php/.

[71] G. Frydrychowicz-Jastrzębska, "El hierro renewable energy hybrid system: A tough compromise," *Energies*, vol. 11, no. 10, 2018. [Online]. Available: https://www.mdpi.com/1996-1073/11/10/2812

[72] R. Godina, E. Rodrigues, J. Matias, and J. Catalão, "Sustainable energy system of el hierro island," in *International conference on renewable energies and power quality (ICREPQ'15)*, 2015, pp. 46–51.

[73] A. Mena-Nieto, C. Estay-Ossandon, and S. P. Dos Santos, "Will the balearics and the canary islands meet the european union targets for municipal waste? a comparative

study from 2000 to 2035," *Science of the Total Environment*, vol. 783, p. 147081, 2021.

[74] D. Curto, S. Favuzza, V. Franzitta, R. Musca, M. A. N. Navia, and G. Zizzo, "Evaluation of the optimal renewable electricity mix for lampedusa island: The adoption of a technical and economical methodology," *Journal of cleaner production*, vol. 263, p. 121404, 2020.

[75] J. R. S. Doorga, "Climate change and the fate of small islands: The case of mauritius," *Environmental Science & Policy*, vol. 136, pp. 282–290, 2022.

[76] F. Battistelli, A. Messina, L. Tomassetti, C. Montiroli, E. Manzo, M. Torre, P. Tratzi, M. Segreto, C.-Y. Chu, V. Paolini, A. Corsini, and F. Petracchini, "Assessment of Energy, Mobility, Waste, and Water Management on Italian Small Islands," *Sustainability*, vol. 15, no. 15, 2023. [Online]. Available: https://www.mdpi.com/2071-1050/15/15/11490

[77] Sustainable Islands - observatory on smaller Italian islands, "The challenges of ecological transition in the smaller islands - Issue 2023," Tech. Rep., 2023.

[78] E. Commission and D.-G. for Energy, *Clean energy for EU islands – Technology solutions booklet*. Publications Office of the European Union, 2021.

[79] Sustainable Islands - observatory on smaller Italian islands, "Energy, water, mobility, circular economy, sustainable tourism - Challenges for smaller islands and best practices from the world - Issue 2022," Tech. Rep., 2022.

[80] Ministry of Economic Development. Ministerial Decree of 14 February 2017. [Online]. Available: https://www.mise.gov.it/.

[81] Q. Lin, H. Huang, Y. Jing, H. Fu, P. Chang, D. Li, Y. Yao, and Z. Fan, "Flexible photovoltaic technologies," *Journal of Materials Chemistry C*, vol. 2, no. 7, pp. 1233–1247, 2014.

[82] G. Liu, J. Guo, H. Peng, H. Ping, and Q. Ma, "Review of recent offshore floating photovoltaic systems," *Journal of Marine Science and Engineering*, vol. 12, no. 11, p. 1942, 2024.

[83] Dragičević *et al.*, “DC microgrids—part I: A review of control strategies and stabilization techniques,” *IEEE Transactions on power electronics*, vol. 31, no. 7, pp. 4876–4891, 2015.

[84] A. Kaur *et al.*, “A review on microgrid central controller,” *Renewable and Sustainable Energy Reviews*, vol. 55, pp. 338–345, 2016.

[85] V. Nasirian, S. Moayedi, A. Davoudi, and F. L. Lewis, “Distributed cooperative control of dc microgrids,” *IEEE Transactions on Power Electronics*, vol. 30, no. 4, pp. 2288–2303, 2014.

[86] F. Gao, R. Kang, J. Cao, and T. Yang, “Primary and secondary control in dc microgrids: a review,” *Journal of Modern Power Systems and Clean Energy*, vol. 7, no. 2, pp. 227–242, 2019.

[87] S. Marzal, R. Salas, R. González-Medina, G. Garcerá, and E. Figueres, “Current challenges and future trends in the field of communication architectures for microgrids,” *Renewable and Sustainable Energy Reviews*, vol. 82, pp. 3610–3622, 2018.

[88] F. Salvadori, C. S. Gehrke, A. C. de Oliveira, M. de Campos, and P. S. Sausen, “Smart grid infrastructure using a hybrid network architecture,” *IEEE Transactions on Smart Grid*, vol. 4, no. 3, pp. 1630–1639, 2013.

[89] R. Madani, M. Ashraphijuo, J. Lavaei, and R. Baldick, “Power system state estimation with a limited number of measurements,” in *2016 IEEE 55th Conference on Decision and Control (CDC)*, 2016, pp. 672–679.

[90] B. Tamimi, C. Cañizares, and K. Bhattacharya, “System stability impact of large-scale and distributed solar photovoltaic generation: The case of ontario, canada,” *IEEE Transactions on Sustainable Energy*, vol. 4, no. 3, pp. 680–688, 2013.

[91] K. Kawabe and K. Tanaka, “Impact of dynamic behavior of photovoltaic power generation systems on short-term voltage stability,” *IEEE Transactions on Power Systems*, vol. 30, no. 6, pp. 3416–3424, 2015.

[92] L. Barbato, G. Bianco, L. Mascolo, M. Menga, F. Renna, G. Sapienza, C. Micillo, S. Bruno, C. Iurlaro, and M. L. Scala, “Power hardware-in-the-loop tests of a control

architecture for isolated microgrids in a co-simulation framework," in *2023 8th IEEE Workshop on the Electronic Grid (eGRID)*, 2023, pp. 1–6.

[93] H. K. Nguyen, A. Khodaei, and Z. Han, "Incentive mechanism design for integrated microgrids in peak ramp minimization problem," *IEEE Transactions on Smart Grid*, vol. 9, no. 6, pp. 5774–5785, 2018.

[94] J. Kumar, A. Agarwal, and V. Agarwal, "A review on overall control of dc microgrids," *Journal of energy storage*, vol. 21, pp. 113–138, 2019.

[95] R. Kumar and M. K. Pathak, "Distributed droop control of dc microgrid for improved voltage regulation and current sharing," *IET Renewable Power Generation*, vol. 14, no. 13, pp. 2499–2506, 2020.

[96] A. Khorsandi, M. Ashourloo, H. Mokhtari, and R. Iravani, "Automatic droop control for a low voltage dc microgrid," *IET Generation, Transmission & Distribution*, vol. 10, no. 1, pp. 41–47, 2016.

[97] Q. Yang, L. Jiang, H. Zhao, and H. Zeng, "Autonomous voltage regulation and current sharing in islanded multi-inverter dc microgrid," *IEEE Transactions on Smart Grid*, vol. 9, no. 6, pp. 6429–6437, 2017.

[98] M. J. Carrizosa, A. Iovine, G. Damm, and P. Alou, "Droop-inspired nonlinear control of a dc microgrid for integration of electrical mobility providing ancillary services to the ac main grid," *IEEE Transactions on Smart Grid*, vol. 13, no. 5, pp. 4113–4122, 2022.

[99] X. Lu, K. Sun, J. M. Guerrero, J. C. Vasquez, and L. Huang, "Double-quadrant state-of-charge-based droop control method for distributed energy storage systems in autonomous dc microgrids," *IEEE transactions on smart grid*, vol. 6, no. 1, pp. 147–157, 2014.

[100] F. Mihalič, M. Truntič, and A. Hren, "Hardware-in-the-loop simulations: A historical overview of engineering challenges," *Electronics*, vol. 11, no. 15, p. 2462, 2022.

[101] A. von Jouanne, E. Agamloh, and A. Yokochi, "Power hardware-in-the-loop (phil): A review to advance smart inverter-based grid-edge solutions," *Energies*, vol. 16, no. 2, p. 916, 2023.

[102] K. Sano, S. Horiuchi, and T. Noda, “Comparison and selection of grid-tied inverter models for accurate and efficient emt simulations,” *IEEE Transactions on Power Electronics*, vol. 37, no. 3, pp. 3462–3472, 2021.

[103] D. Baltensperger, S. Sanchez, S. D’Arco, and K. Uhlen, “Assessing hardware in the loop approaches for wide-area monitoring control and protection devices,” *IEEE Transactions on Power Delivery*, vol. 38, no. 4, pp. 2724–2734, 2023.

[104] X. Chen, Y. Hou, and S. R. Hui, “Distributed control of multiple electric springs for voltage control in microgrid,” *IEEE Transactions on Smart Grid*, vol. 8, no. 3, pp. 1350–1359, 2016.

[105] H. Gharibvand, G. B. Gharehpetian, and A. Anvari-Moghaddam, “A survey on microgrid flexibility resources, evaluation metrics and energy storage effects,” *Renewable and Sustainable Energy Reviews*, vol. 201, p. 114632, 2024.

[106] M. Z. Degefa, I. B. Sperstad, and H. Sæle, “Comprehensive classifications and characterizations of power system flexibility resources,” *Electric Power Systems Research*, vol. 194, p. 107022, 2021.

[107] Y. Gu, X. Xiang, W. Li, and X. He, “Mode-adaptive decentralized control for renewable dc microgrid with enhanced reliability and flexibility,” *IEEE Transactions on Power Electronics*, vol. 29, no. 9, pp. 5072–5080, 2013.

[108] O. M. Babatunde, J. L. Munda, and Y. Hamam, “Power system flexibility: A review,” *Energy Reports*, vol. 6, pp. 101–106, 2020.

[109] C. Eid, P. Codani, Y. Perez, J. Reneses, and R. Hakvoort, “Managing electric flexibility from distributed energy resources: A review of incentives for market design,” *Renewable and Sustainable Energy Reviews*, vol. 64, pp. 237–247, 2016.

[110] D. Rekioua, “Energy storage systems for photovoltaic and wind systems: A review,” *Energies*, vol. 16, no. 9, p. 3893, 2023.

[111] A. Emrani and A. Berrada, “A comprehensive review on techno-economic assessment of hybrid energy storage systems integrated with renewable energy,” *Journal of Energy Storage*, vol. 84, p. 111010, 2024.

[112] M. E. Şahin, F. Blaabjerg, and A. Sangwongwanich, “A comprehensive review on supercapacitor applications and developments,” *Energies*, vol. 15, no. 3, p. 674, 2022.

[113] R. T. Yadlapalli, R. R. Alla, R. Kandipati, and A. Kotapati, “Super capacitors for energy storage: Progress, applications and challenges,” *Journal of Energy Storage*, vol. 49, p. 104194, 2022.

[114] N. Vangapally, T. R. Penki, Y. Elias, S. Muduli, S. Maddukuri, S. Luski, D. Aurbach, and S. K. Martha, “Lead-acid batteries and lead–carbon hybrid systems: A review,” *Journal of Power Sources*, vol. 579, p. 233312, 2023.

[115] K. Yanamandra, D. Pinisetty, and N. Gupta, “Impact of carbon additives on lead-acid battery electrodes: A review,” *Renewable and Sustainable Energy Reviews*, vol. 173, p. 113078, 2023.

[116] N. Sharmili, R. Nagi, and P. Wang, “A review of research in the li-ion battery production and reverse supply chains,” *Journal of energy storage*, vol. 68, p. 107622, 2023.

[117] A. Y. S. Eng, V. Kumar, Y. Zhang, J. Luo, W. Wang, Y. Sun, W. Li, and Z. W. Seh, “Room-temperature sodium–sulfur batteries and beyond: realizing practical high energy systems through anode, cathode, and electrolyte engineering,” *Advanced Energy Materials*, vol. 11, no. 14, p. 2003493, 2021.

[118] Y. Chen, Y. Kang, Y. Zhao, L. Wang, J. Liu, Y. Li, Z. Liang, X. He, X. Li, N. Tavajohi *et al.*, “A review of lithium-ion battery safety concerns: The issues, strategies, and testing standards,” *Journal of Energy Chemistry*, vol. 59, pp. 83–99, 2021.

[119] X. Fan, B. Liu, J. Liu, J. Ding, X. Han, Y. Deng, X. Lv, Y. Xie, B. Chen, W. Hu *et al.*, “Battery technologies for grid-level large-scale electrical energy storage,” *Transactions of Tianjin University*, vol. 26, no. 2, pp. 92–103, 2020.

[120] L. F. Arenas, F. C. Walsh, and C. P. de León, “General aspects and fundamentals of flow batteries,” *Flow Batteries: From Fundamentals to Applications*, vol. 1, pp. 69–97, 2023.

[121] S. Bogdanov, M. Pugach, S. Parsegov, V. Vlasov, F. M. Ibanez, K. J. Stevenson, and P. Vorobev, “Dynamic modeling of vanadium redox flow batteries: Practical

approaches, their applications and limitations," *Journal of Energy Storage*, vol. 57, p. 106191, 2023.

[122] S. Wali, M. Hannan, M. Abd Rahman, H. A. Alghamdi, M. Mansor, P. J. Ker, S. Tiong, and T. I. Mahlia, "Usage count of hydrogen-based hybrid energy storage systems: An analytical review, challenges and future research potentials," *International Journal of Hydrogen Energy*, vol. 48, no. 89, pp. 34 836–34 861, 2023.

[123] G. Sadeghi, "Energy storage on demand: Thermal energy storage development, materials, design, and integration challenges," *Energy Storage Materials*, vol. 46, pp. 192–222, 2022.

[124] Z. Li, Y. Lu, R. Huang, J. Chang, X. Yu, R. Jiang, X. Yu, and A. P. Roskilly, "Applications and technological challenges for heat recovery, storage and utilisation with latent thermal energy storage," *Applied Energy*, vol. 283, p. 116277, 2021.

[125] S. Y. Hui, C. K. Lee, and F. F. Wu, "Electric springs—a new smart grid technology," *IEEE Transactions on Smart Grid*, vol. 3, no. 3, pp. 1552–1561, 2012.

[126] N. R. Chaudhuri, C. K. Lee, B. Chaudhuri, and S. R. Hui, "Dynamic modeling of electric springs," *IEEE Transactions on Smart Grid*, vol. 5, no. 5, pp. 2450–2458, 2014.

[127] Y. Shuo, S.-C. Tan, C. Lee, and S. R. Hui, "Electric spring for power quality improvement," in *2014 IEEE Applied Power Electronics Conference and Exposition-APEC 2014*. IEEE, 2014, pp. 2140–2147.

[128] J. Soni and S. K. Panda, "Electric spring for voltage and power stability and power factor correction," *IEEE transactions on industry applications*, vol. 53, no. 4, pp. 3871–3879, 2017.

[129] C. K. Lee and S. Y. Hui, "Reduction of energy storage requirements in future smart grid using electric springs," *IEEE Transactions on Smart Grid*, vol. 4, no. 3, pp. 1282–1288, 2013.

[130] A. Emadi *et al.*, "Constant power loads and negative impedance instability in automotive systems: definition, modeling, stability, and control of power electronic converters and motor drives," *IEEE Trans. on vehicular technology*, vol. 55, no. 4, pp. 1112–1125, 2006.

[131] C. K. Lee, N. R. Chaudhuri, B. Chaudhuri, and S. R. Hui, “Droop control of distributed electric springs for stabilizing future power grid,” *IEEE Transactions on Smart Grid*, vol. 4, no. 3, pp. 1558–1566, 2013.

[132] H. Yang, T. Li, Y. Long, C. P. Chen, and Y. Xiao, “Distributed virtual inertia implementation of multiple electric springs based on model predictive control in dc microgrids,” *IEEE Transactions on Industrial Electronics*, vol. 69, no. 12, pp. 13 439–13 450, 2021.

[133] M. Wang, Y. He, X. Xu, Z. Dong, and Y. Lei, “A review of ac and dc electric springs,” *IEEE access*, vol. 9, pp. 14 398–14 408, 2021.

[134] S. Anand and B. G. Fernandes, “Reduced-order model and stability analysis of low-voltage dc microgrid,” *IEEE Transactions on Industrial Electronics*, vol. 60, no. 11, pp. 5040–5049, 2012.

[135] X. Chen *et al.*, “Distributed cooperative control and stability analysis of multiple dc electric springs in a dc microgrid,” *IEEE Transactions on Industrial Electronics*, vol. 65, no. 7, pp. 5611–5622, 2018.

[136] A. M. Abdurraqeeb *et al.*, “Stabilization of constant power loads and dynamic current sharing in dc microgrid using robust control technique,” *Electric Power Systems Research*, vol. 230, p. 110258, 2024.

[137] Q. Zhou *et al.*, “Distributed control and communication strategies in networked microgrids,” *IEEE Communications Surveys & Tutorials*, vol. 22, no. 4, pp. 2586–2633, 2020.

[138] A. M. Rahimi and A. Emadi, “Active damping in dc/dc power electronic converters: A novel method to overcome the problems of constant power loads,” *IEEE Transactions on Industrial Electronics*, vol. 56, no. 5, pp. 1428–1439, 2009.

[139] C.-K. Lee, H. Liu, S.-C. Tan, B. Chaudhuri, and S.-Y. R. Hui, “Electric spring and smart load: Technology, system-level impact, and opportunities,” *IEEE Journal of Emerging and Selected Topics in Power Electronics*, vol. 9, no. 6, pp. 6524–6544, 2021.

[140] X. Lu, Guerrero *et al.*, “An improved droop control method for dc microgrids based on low bandwidth communication with dc bus voltage restoration and enhanced

current sharing accuracy," *IEEE transactions on power electronics*, vol. 29, no. 4, pp. 1800–1812, 2013.

[141] M. Z. Degefa *et al.*, "Comprehensive classifications and characterizations of power system flexibility resources," *Electric Power Systems Research*, vol. 194, p. 107022, 2021.

[142] S. Singer, "Realization of loss-free resistive elements," *IEEE Transactions on Circuits and Systems*, vol. 37, no. 1, pp. 54–60, 1990.

[143] A. B. Jusoh, "The instability effect of constant power loads," in *PECon 2004. Proceedings. National Power and Energy Conference, 2004.* IEEE, 2004, pp. 175–179.

[144] M. Cespedes, L. Xing, and J. Sun, "Constant-power load system stabilization by passive damping," *IEEE Transactions on Power Electronics*, vol. 26, no. 7, pp. 1832–1836, 2011.

[145] F. Gao, S. Bozhko, S. Yeoh, G. Asher, and P. Wheeler, "Stability of multi-source droop-controlled electrical power system for more-electric aircraft," in *2014 IEEE International Conference on Intelligent Energy and Power Systems (IEPS).* IEEE, 2014, pp. 122–126.

[146] C. H. Rivetta, A. Emadi, G. A. Williamson, R. Jayabalan, and B. Fahimi, "Analysis and control of a buck dc-dc converter operating with constant power load in sea and undersea vehicles," *IEEE Transactions on Industry Applications*, vol. 42, no. 2, pp. 559–572, 2006.

[147] Y. Li, K. R. Vannorsdel, A. J. Zirger, M. Norris, and D. Maksimovic, "Current mode control for boost converters with constant power loads," *IEEE Transactions on Circuits and Systems I: Regular Papers*, vol. 59, no. 1, pp. 198–206, 2011.

[148] M. Wu and D. D.-C. Lu, "A novel stabilization method of lc input filter with constant power loads without load performance compromise in dc microgrids," *IEEE Transactions on industrial electronics*, vol. 62, no. 7, pp. 4552–4562, 2014.

[149] Q. Shafiee, T. Dragicevic, J. C. Vasquez, and J. M. Guerrero, "Modeling, stability analysis and active stabilization of multiple dc-microgrid clusters," in *2014 IEEE international energy conference (ENERGYCON).* IEEE, 2014, pp. 1284–1290.

[150] S. F. Glover and S. D. Sudhoff, "An experimentally validated nonlinear stabilizing control for power electronics based power systems," *SAE transactions*, pp. 68–77, 1998.

[151] X. Liu, A. J. Forsyth, and A. M. Cross, "Negative input-resistance compensator for a constant power load," *IEEE Transactions on Industrial Electronics*, vol. 54, no. 6, pp. 3188–3196, 2007.

[152] X. Liu and A. Forsyth, "Input filter state feed-forward stabilising controller for constant power load systems," *IET Electric Power Applications*, vol. 2, no. 5, pp. 306–315, 2008.

[153] Y. A.-R. I. Mohamed, A. A. A. Radwan, and T. Lee, "Decoupled reference-voltage-based active dc-link stabilization for pmsm drives with tight-speed regulation," *IEEE Transactions on Industrial Electronics*, vol. 59, no. 12, pp. 4523–4536, 2011.

[154] P. Magne, B. Nahid-Mobarakeh, and S. Pierfederici, "General active global stabilization of multiloads dc-power networks," *IEEE Transactions on Power Electronics*, vol. 27, no. 4, pp. 1788–1798, 2011.

[155] P. Magne *et al.*, "Active stabilization of dc microgrids without remote sensors for more electric aircraft," *IEEE Transactions on Industry Applications*, vol. 49, no. 5, pp. 2352–2360, 2013.

[156] K. Inoue, T. Kato, M. Inoue, Y. Moriyama, and K. Nishii, "An oscillation suppression method of a dc power supply system with a constant power load and a lc filter," in *2012 IEEE 13th Workshop on Control and Modeling for Power Electronics (COMPEL)*. IEEE, 2012, pp. 1–4.

[157] M. S. Carmeli, D. Forlani, S. Grillo, R. Pinetti, E. Ragaini, and E. Tironi, "A stabilization method for dc networks with constant-power loads," in *2012 IEEE International Energy Conference and Exhibition (ENERGYCON)*. IEEE, 2012, pp. 617–622.

[158] O. Pizniur, Z. Shan, and J. Jatskevich, "Ensuring dynamic stability of constant power loads in dc telecom power systems and data centers using active damping," in *2014 IEEE 36th International Telecommunications Energy Conference (INTELEC)*. IEEE, 2014, pp. 1–8.

[159] J. Wang and D. Howe, "A power shaping stabilizing control strategy for dc power systems with constant power loads," *IEEE Transactions on Power Electronics*, vol. 23, no. 6, pp. 2982–2989, 2008.

[160] S. Kim and S. S. Williamson, "Negative impedance instability compensation in more electric aircraft dc power systems using state space pole placement control," in *2011 IEEE Vehicle Power and Propulsion Conference*. IEEE, 2011, pp. 1–6.

[161] J. Ciezki and R. Ashton, "The application of feedback linearization techniques to the stabilization of dc-to-dc converters with constant power loads," in *1998 IEEE International Symposium on Circuits and Systems (ISCAS)*, vol. 3. IEEE, 1998, pp. 526–529.

[162] A. M. Rahimi, G. A. Williamson, and A. Emadi, "Loop-cancellation technique: A novel nonlinear feedback to overcome the destabilizing effect of constant-power loads," *IEEE Transactions on vehicular technology*, vol. 59, no. 2, pp. 650–661, 2009.

[163] J. A. Solsona, S. G. Jorge, and C. A. Busada, "Nonlinear control of a buck converter which feeds a constant power load," *IEEE Transactions on Power Electronics*, vol. 30, no. 12, pp. 7193–7201, 2015.

[164] G. Sulligoi, D. Bosich, G. Giadrossi, L. Zhu, M. Cupelli, and A. Monti, "Multiconverter medium voltage dc power systems on ships: Constant-power loads instability solution using linearization via state feedback control," *IEEE Transactions on Smart Grid*, vol. 5, no. 5, pp. 2543–2552, 2014.

[165] S. Impram, S. Varbak Nese, and B. Oral, "Challenges of renewable energy penetration on power system flexibility: A survey," *Energy Strategy Reviews*, vol. 31, p. 100539, 2020. [Online]. Available: https://www.sciencedirect.com/science/article/pii/S2211467X20300924

[166] J. Song, X. Zhou, Z. Zhou, Y. Wang, Y. Wang, and X. Wang, "Review of low inertia in power systems caused by high proportion of renewable energy grid integration," *Energies*, vol. 16, no. 16, 2023. [Online]. Available: https://www.mdpi.com/1996-1073/16/16/6042

[167] A. Ulbig, T. Borsche, and G. Andersson, “Impact of low rotational inertia on power system stability and operation,” *IFAC Proceedings Volumes (IFAC-PapersOnline)*, vol. 19, 12 2013.

[168] S. Bruno, G. Giannoccaro, C. Iurlaro, M. La Scala, and C. Rodio, “Power Hardware-in-the-Loop Test of a Low-Cost Synthetic Inertia Controller for Battery Energy Storage System,” *Energies*, vol. 15, no. 9, 2022.

[169] N. Zhi, K. Ding, L. Du, and H. Zhang, “An soc-based virtual dc machine control for distributed storage systems in dc microgrids,” *IEEE Transactions on Energy Conversion*, vol. 35, no. 3, pp. 1411–1420, 2020.

[170] T. Dragičević, J. M. Guerrero, J. C. Vasquez, and D. Škrlec, “Supervisory control of an adaptive-droop regulated dc microgrid with battery management capability,” *IEEE Transactions on power Electronics*, vol. 29, no. 2, pp. 695–706, 2013.

[171] K.-T. Mok *et al.*, “Dc electric springs—a technology for stabilizing dc power distribution systems,” *IEEE Transactions on Power Electronics*, vol. 32, no. 2, pp. 1088–1105, 2017.

[172] M. Wang, Y. He, X. Xu, Z. Dong, and Y. Lei, “A review of ac and dc electric springs,” *IEEE access*, vol. 9, pp. 14 398–14 408, 2021.

[173] L. Liu, M. Shan, L. Qin, X. Wu, and K.-W. Lao, “Analysis of low-cost btb-dc electric spring in dc microgrid considering impedance ratio impact,” *IEEE Transactions on Power Electronics*, 2024.

[174] P. Ghalebani and M. Niasati, “A distributed control strategy based on droop control and low-bandwidth communication in dc microgrids with increased accuracy of load sharing,” *Sustainable cities and society*, vol. 40, pp. 155–164, 2018.

[175] N. N. A. Bakar *et al.*, “Microgrid and load shedding scheme during islanded mode: A review,” *Renewable and Sustainable Energy Reviews*, vol. 71, pp. 161–169, 2017.

[176] A. Visioli, “Modified anti-windup scheme for pid controllers,” *IEE Proce. Cont. Theory and App.*, vol. 150, no. 1, pp. 49–54, 2003.

[177] J. Liao, N. Zhou, Y. Huang, and Q. Wang, “Decoupling control for dc electric spring-based unbalanced voltage suppression in a bipolar dc distribution system,” *IEEE Transactions on Industrial Electronics*, vol. 68, no. 4, pp. 3239–3250, 2020.

[178] Y. Gu *et al.*, “Mode-adaptive decentralized control for renewable dc microgrid with enhanced reliability and flexibility,” *IEEE Transactions on power electronics*, vol. 29, no. 9, pp. 5072–5080, 2013.

[179] M. R. Nasab *et al.*, “Power systems simulation and analysis: A review on current applications and future trends in DRTS of grid-connected technologies,” *IEEE Access*, 2024.

[180] M. Menga *et al.*, “Geographically Distributed Real-Time Simulation of a Hierarchical Control Architecture for Isolated Microgrids,” *IEEE Open Journal of Power Electronics*, 2025.

[181] U. Krewer *et al.*, “Dynamic models of Li-ion batteries for diagnosis and operation: a review and perspective,” *Journal of the electrochemical society*, vol. 165, no. 16, p. A3656, 2018.

[182] M. M. Islam *et al.*, “Improving reliability and stability of the power systems: A comprehensive review on the role of energy storage systems to enhance flexibility,” *IEEE Access*, 2024.

[183] S. Y. Hui *et al.*, “Electric springs—a new smart grid technology,” *IEEE Tran. on Smart Grid*, vol. 3, no. 3, pp. 1552–1561, 2012.

[184] Q. Yang *et al.*, “Autonomous voltage regulation and current sharing in islanded multi-inverter dc microgrid,” *IEEE Transactions on Smart Grid*, vol. 9, no. 6, pp. 6429–6437, 2017.

[185] M.-H. Wang, K.-T. Mok, S.-C. Tan, and S. Hui, “Multifunctional dc electric springs for improving voltage quality of dc grids,” *IEEE Transactions on Smart Grid*, vol. 9, no. 3, pp. 2248–2258, 2017.

[186] L. Rundqwist, “Anti-reset windup for pid controllers,” *IFAC Proceedings Volumes*, vol. 23, no. 8, pp. 453–458, 1990.

[187] E. Espina *et al.*, “Distributed control strategies for microgrids: An overview,” *IEEE Access*, vol. 8, pp. 193 412–193 448, 2020.

[188] H. Yang, T. Li, Y. Long, C. P. Chen, and Y. Xiao, “Distributed virtual inertia implementation of multiple electric springs based on model predictive control in

dc microgrids," *IEEE Transactions on Industrial Electronics*, vol. 69, no. 12, pp. 13 439–13 450, 2022.

[189] J.-O. Lee and Y.-S. Kim, "Novel battery degradation cost formulation for optimal scheduling of battery energy storage systems," *International Journal of Electrical Power & Energy Systems*, vol. 137, p. 107795, 2022.

Acronyms

AC Alternating Current. 14, 25, 68, 70, 75, 76, 78, 79, 97, 99, 114

APF Active Power Filter. 115

BDC Bidirectional DC–DC converters. 68, 116

BESS Battery Energy Storage System. 13, 28, 45, 62, 63, 68–74, 77, 80, 81, 95, 123–126, 154, 173, 174, 177–188, 190, 191

BMS battery management system. 59, 69

CAES Compressed Air Energy Storage. 62, 65

CAESS Compressed Air Energy Storage System. 61, 62, 68

CBA cost-benefit analysis. 173

CESS Chemical Energy Storage System. 63

CHIL Control-Hardware-In-the-Loop. 35, 36, 38

CL Critical Load. 75, 80, 88, 128

CPL Constant Power Load. 10, 76, 79, 82, 84–86, 89, 90, 92, 94, 96–100, 102, 105, 108–119, 121, 122, 125, 140, 153–157, 165

CPS Constant Power Sources. 129

CVS Constant Voltage Source. 109

DC Direct Current. vi, 7–9, 13, 14, 16, 20, 25, 28–32, 34, 35, 38, 39, 42–46, 48–51, 54, 56–63, 66, 68–84, 86–88, 92, 95–99, 107–119, 122–128, 136, 138, 140, 144–146, 148, 150–155, 157–162, 165, 171, 173, 174, 179–183, 186–188, 190, 192

DC-ES DC Electric Spring. 77, 79–82, 84–88, 91–95

DER Distributed Energy Resource. 17, 18, 20, 32, 35, 39, 49

DG Distributed Generation. 11, 24, 25, 30, 50, 69, 72, 77, 95, 98, 125, 152, 154, 160, 161, 165–167, 170, 171, 178, 181, 184, 187

DMS Distribution Management System. 46

DoD Depth of Discharge. 175–179

DPS Distribution Power System. 118

DR Demand Response. 73–75

DRTS Digital Real-Time Simulation. 29–36, 42, 44, 46

DSM Demand-Side Management. 52, 74

DSO Distribution System Operator. 25

DSR Demand-Side Response. 52

DUT Device Under Test. 29, 33, 34

EcES Electrochemical Energy Storage. 59

EES Electrical Energy Storage. 57, 58, 99

EIA Energy Information Administration. 11

EMS Energy Management System. 20, 30, 72, 74, 77

EMT Electromagnetic Transient. 31–33

EoL End of Life. 177

ES Electric Spring. v, 48, 73, 75, 78–80, 82, 84, 85, 94, 96, 126–130, 132–135, 138, 144, 146–148, 150, 154, 155, 158–160, 165–168, 171–174

ESS Energy Storage System. 24, 25, 45, 48–50, 53, 54, 56, 57, 59, 65, 66, 81, 88, 95, 152, 154, 158, 160, 161, 173, 176, 180

EU European Union. 12, 47

EV Electric Vehicle. 97

FC Fuel Cell. 63, 75

FESS Flywheel Energy Storage System. 61, 68–71

FLC Feedback Linearization Control. 118

HESS Hybrid Energy Storage System. 59

HEV Hybrid-Electric Vehicle. 30

HIL Hardware-In-the-Loop. 13, 29–36, 38–40, 42, 45–47, 191

HT-TESS High-Temperature Thermal Energy Storage. 64, 65

HTS High-Temperature Superconducting. 58

HUT Hardware Under Test. 29, 34–36, 38, 39, 44

IC Incremental Cost. 173–175, 178–180, 182–184, 187, 188, 191

ICT Information and Communication Technologies. 152, 188

IEA International Energy Agency. 11

IoT Internet of Things. 25

KCL Kirchhoff's current law. 98, 100, 103, 119

KVL Kirchhoff's voltage law. 98, 99, 103, 119

LBC Low-Bandwidth Communication. 128, 190

LFR Loss-Free Resistor. 113

Li-ion Lithium-ion. 59, 60, 69–71, 80

LSF Linearization via State Feedback. 119

LV Low Voltage. 11, 13, 20

MESS Mechanical Energy Storage System. 61

MG Microgrid. iv, vi, 6–9, 12–14, 16–20, 24, 25, 28–35, 38, 39, 42–44, 46, 50, 51, 56–63, 66, 68–75, 77–79, 81, 82, 86, 95–109, 113, 114, 117–119, 122–127, 129, 136, 138, 140, 144–146, 148, 150–155, 157–162, 165, 171–175, 179–183, 186, 190–192

MGC Microgrid Controller. 13

MIL Model-in-the-Loop. 34

MMC Modular Multilevel Converter. 33

MPPT Maximum Power Point Tracking. 121, 126, 127, 129, 130, 134–137, 139, 146, 148

MV Medium Voltage. 11, 13, 20

Na–S Sodium–Sulfur. 60, 65, 68, 69, 71

NC Non-Critical. 75, 80–84, 88–90, 92, 94, 128, 154, 165, 172

Ni–Cd Nickel–Cadmium. 60, 68

Ni–MH Nickel–Metal Hydride. 60, 68

NIRC Negative Input Resistance Compensator. 115

NSSC Nonlinear System Stabilizing Controller. 115

PCC Point of Common Connection. 109, 122, 128, 135, 157, 159–161, 165–167, 172, 180, 181, 184, 186

PCM Phase Change Material. 64

PD Proportional–Derivative. 119

PEC Power Electronic Converter. 68, 72, 98, 99

PHESS Pumped Hydro Energy Storage System. 61, 62, 68

PHIL Power-Hardware-In-the-Loop. ii, v, 35, 36, 38, 39, 43–45, 126, 127, 144–146, 190

PI Proportional–Integral. 161

PIL Processor-in-the-Loop. 34

PMU Phasor Measurement Unit. 46

PSC Power Shaping Control. 116, 117

PV Photovoltaic. 22, 24, 45, 48, 69, 70, 75, 86, 99, 127, 129, 130, 154, 165, 181

RES Renewable Energy Source. 6–8, 11, 12, 14, 15, 20–22, 24, 30, 33, 45, 47–49, 51, 56, 71, 72, 74, 80, 92, 95, 122, 123, 126, 154, 155, 159, 171, 180, 181, 190

RP Rapid Prototyping. 33

RT Real-Time. 126, 129, 145

RTS Real-Time Simulator. 29, 32, 33, 38, 39

RVC Reference Voltage–Based Compensator. 115

SC Supercapacitor. 57–59, 62, 63, 68–71

SCADA Supervisory Control And Data Acquisition. 46

SEP Stable Equilibrium Point. 110

SFSC State Feedforward Stabilizing Controller. 115

SI Synthetic Inertia. 68, 70

SIL Software-in-the-Loop. 34

SMES Superconducting Magnetic Energy Storage. 57, 58, 68

SoC State of Charge. 25, 69–73, 97, 122, 124, 126, 128–130, 132–137, 139, 158–160, 168, 173–175, 177–180, 184, 185, 188, 190, 191

STATCOM Static Synchronous Compensator. 44, 75

TCC Total Capital Cost. 177

TESS Thermal Energy Storage System. 63

UEP Unstable Equilibrium Point. 110

VPN Virtual Private Network. 42

VR Virtual Resistances. 119, 130, 165–168, 170, 171, 175

VRF Vanadium Redox Flow. 60, 68

VSC Voltage Source Converter. 100

WAMPAC Wide-Area Monitoring and Control. 44, 46